



HAL
open science

Photoluminescent diamond nanoparticles as labels in cells: study of their optical properties and investigation of their cellular uptake mechanism

Orestis Faklaris

► **To cite this version:**

Orestis Faklaris. Photoluminescent diamond nanoparticles as labels in cells: study of their optical properties and investigation of their cellular uptake mechanism. Atomic Physics [physics.atom-ph]. École normale supérieure de Cachan - ENS Cachan, 2009. English. NNT: . tel-00439561

HAL Id: tel-00439561

<https://theses.hal.science/tel-00439561>

Submitted on 7 Dec 2009

HAL is a multi-disciplinary open access archive for the deposit and dissemination of scientific research documents, whether they are published or not. The documents may come from teaching and research institutions in France or abroad, or from public or private research centers.

L'archive ouverte pluridisciplinaire **HAL**, est destinée au dépôt et à la diffusion de documents scientifiques de niveau recherche, publiés ou non, émanant des établissements d'enseignement et de recherche français ou étrangers, des laboratoires publics ou privés.



Ecole Normale Supérieure
de Cachan



Laboratoire de Photonique
Quantique et Moléculaire

THESE DE DOCTORAT
Spécialité: Sciences Physiques

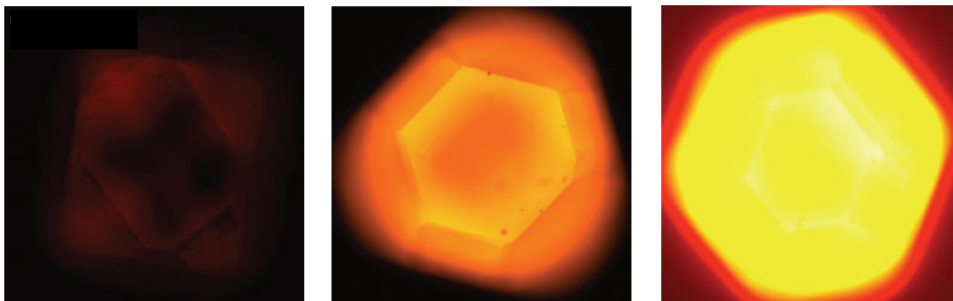
présentée par

Orestis FAKLARIS

pour obtenir le grade de
Docteur de l'Ecole Normale Supérieure de Cachan

Sujet:

**Photoluminescent diamond nanoparticles as
labels in cells: study of their optical
properties and investigation of their cellular
uptake mechanism**



soutenue le 19 octobre 2009
devant le jury composé de:

M. Hervé RIGNEAULT
Mme Antigoni ALEXANDROU
M. Benoit DUBERTRET
M. Patrick CURMI
M. Claude MALVY
M. Huan-Cheng CHANG
M. François TREUSSART

Président
Rapporteur
Rapporteur
Examineur
Examineur
Examineur
Directeur de thèse

*“As you set out for Ithaka
hope the voyage is a long one,
full of adventure, full of discovery. [...]
But do not hurry the journey at all.
Better if it lasts for years,
so you are old by the time you reach the island,
wealthy with all you have gained on the way,
not expecting Ithaka to make you rich.”*

Ithaka, Konstantinos Kavafis

Acknowledgements

A great part of this work was carried out in “Laboratoire de Photonique Quantique et Moléculaire” (LPQM) at Ecole Normale Supérieure de Cachan. I would like to thank the director of the laboratory, Isabelle Ledoux-Rak, for giving me the opportunity to be a member of LPQM during my PhD thesis.

The experiments and results of this thesis were obtained in the frame of the Quantum Nanophotonics team. First and foremost, I want to thank my supervisor, François Treussart. The journey started in 2006, when he proposed me a master training work on photoluminescent nanodiamonds for biology. A brand new research topic at that time, presenting for me a great challenge but multiple obstacles to overpass as well. I want to thank François for the confidence he had in me. The high degree of autonomy allowed me to take initiatives, and at the same time, although highly occupied with overcharged timetables, he was every time available to give his advice. The joy and enthusiasm he has for experimental physics and optics was contagious and motivational for me. His dynamism and efficiency to solve problems, his critical thinking to the experimental results, his perpetual desire to perform with no delay new experiments, his organization skills and his honest behavior towards the others (and much more towards the scientific community) are elements that have influenced me.

I would like also to thank the other members of the Quantum Nanophotonics group. In particular, special thanks to the leader of the group, Jean-François Roch, for the continuous support, the helpful suggestions and the constant encouragement during the course of this work. I was particularly overwhelmed by his optimism, his pedagogic skills and his human generosity.

At the beginning of my PhD I had the chance to work for one year with Damien Garrot, who was doing his ATER in LPQM. Part of the experimental results is the fruit of our creative commun work. As usually happens, the research work is characterized by long periods of experimental troubleshoots. His contribution was more than important to the efficient resolution of such issues, especially the informatics ones. I gratefully thank him for the year that we worked together.

Due to the interdisciplinarity of my PhD topic, many experiments of my work took place in other laboratories. Regarding the biological applications of nanodiamonds, most of the cell biology experiments were carried out in “Laboratoire Structure et Activité des Biomolécules Normales et Pathologiques” (Université d’Evry - Val d’Essonne), with supervisor Patrick Curmi. I would like to specially thank him for accepting me in his research group during the four months of my master training and later on for providing me the opportunity to work within his laboratory. His enthusiasm for the biological applications of photoluminescent nanodiamonds was a decisive factor of undertaking my PhD on this topic. I appreciate all his contribution of time, ideas as well as his valuable suggestions and constructive advice on the biological aspects of my work. I equally thank him for accepting being a member of my PhD defense committee.

My stay in this group and the willingness of the research members to show me and introduce me to the world of biology has allowed me to obtain a biology background, necessary condition in order to planify and carry out the biology experiments with nan-

odiamonds. I wish to express my gratitude to Vandana Joshi, for her continuous availability to perform experiments with nanodiamonds. Her contribution was decisive for the progress of the biological part of my thesis. Additionally, I thank Anne Tarade for her availability to prepare the nanodiamond-cell samples for the transmission electron microscopy observations. Special thanks go to David Pastré, for his help with the AFM experiments of DNA with nanodiamonds. The fruitful discussions we had, his numerous ideas and his pedagogic sense transmitted to me during our common laboratory exercises on Optics when I was “moniteur” at the University of Evry-Val d’Essonne are elements that will stay deeply in my memory.

Part of the size and shape characterization of nanodiamonds and their observation in cells was carried out in “Laboratoire Pierre-Marie Fourt”, Centre des Matériaux de l’Ecole des Mines de Paris. I would like to thank Mohamed Sennour and Alain Thorel for performing the Transmission Electron Microscopy experiments.

Special thanks also to Patrick Tauc (Laboratoire de Biologie et de Pharmacologie Appliqué, ENS Cachan) and Theano Irinopoulou (Institut du Fer Moulin), for their help and availability of the commercial confocal microscopes, of the imaging platforms for which they are responsible, for nanodiamond intracellular imaging.

Part of this work and especially the time-gated imaging and the discovery of the quenching effect of the NV center in nanodiamonds could not be possible without the use of a mode-locked picosecond laser. This laser was developed in the team of Patrick Georges at Institut d’Optique (Laboratoire Charles Fabry) by Frédéric Druon and Dimitris Papadopoulos. I sincerely thank them for putting at our disposal the laser and for their continuous availability, whenever we faced problems with the laser alignment.

Regarding the members of LPQM, I would like to thank Abdallah Slablab, for carrying out the time-consuming but necessary size-photoluminescence characterization experiments of nanodiamonds with his unique (in our laboratory) AFM setup coupled to a confocal microscope.

Special thanks to Dominique Chauvat and Marcin Zielinski, for the availability of their experimental setup and their participation in the investigation of the two-photon excitation properties of the NV centers.

The implication of Dingwei Zheng and Ngoc Diep Lai with the end of my thesis in the quenching effect of the NV center under excitation with pulsed infra-red light gave a new dynamic and clear explanations of this phenomenon. I would like to thank them for having continued with the experiments.

Moreover I am grateful to Frédéric Grosshans and Vincent Jacques for the fruitful discussions we had during all these years of my PhD on the photophysics of the NV center in diamond.

I specially thank André Clouqueur for the realisation of the appropriate electronic interfaces for the experimental setup.

The surface characterization and the zeta potential measurements of the nanodiamonds was carried out by Geraldine Dantelle and Hugues Girard in “Laboratoire de la Physique de la Matière Condensée” (Ecole Polytechnique), persons who I would like to acknowledge. In addition, I would like to thank Celine Gesset and Jean-Charles Arnault (Diamond Sensor Laboratory, CEA-LIST) for their implication in the studies of the attachment of nanodiamonds with serum proteins.

In this work we used photoluminescent nanodiamonds. I am grateful to Thierry Sauvage, who was responsible for the proton irradiations of nanodiamonds in the Laboratory of “Conditions Extrêmes et Matériaux : Haute Température et Irradiation”, in Orléans. I also wish to express my cordial appreciation to Jean-Paul Boudou, for the annealing of the irradiated material, his valuable suggestions and willingness to provide a complete bibliography on the material science issues of nanodiamonds.

For the individual tracking of photoluminescent nanodiamonds in cells, apart from the traditional methods of calculating the diffusion coefficient (like the Mean Square Displacement), we used the interference method, which was provided by Silvan Türkcan and Antigoni Alexandrou (Laboratoire d’Optique et Biosciences, Ecole Polytechnique). I would like to particularly thank Silvan for this constant willingness to help regarding software issues of the interference program and Antigoni Alexandrou for providing us the program and for accepting being a reading committee member of my PhD thesis as well. Her thorough lecture of this manuscript and her comments have improved its scientific clarity.

I would also like to gratefully acknowledge Karen Perronet (Laboratoire Charles Fabry, Institut d’Optique) for on the one hand the loan of the CCD array, which enabled us to record the nanodiamond trajectories in cells, and on the other hand her critical lecture of this PhD manuscript and her valuable remarks, especially during the difficult period of the summer vacations.

I gratefully acknowledge the funding source that made this PhD work possible. I was funded by a “Ile-de-France” Region C’Nano three year scholarship under the project “Biodiam”.

For this dissertation I would like to thank Benoit Dubertret for accepting being a reading committee member and for his time, interest, and helpful comments on this work. I would also like to thank the other members of my oral defense committee for their time and insightful questions; Hervé Rigneault for accepting being the president of the committee, Claude Malvy for his critical biological approach, and Huan-Cheng Chang, for his long journey from Taiwan to attend to my defense.

In parallel to my PhD, I followed 3-year courses organized by the “Institut de Formation Supérieure Biomédicale” of “Institut Gustave Roussy”, at Villejuif, to obtain at the end a university diploma. These courses allowed me to obtain the basic knowledges on biology and biomedicine, which helped me a lot for my PhD thesis. I would therefore like to thank the persons responsible for the courses: Claude Malvy, Luis Villanueva, Liliane Massade, Christine Ho, my tutor Patrick Couvreur, and of course the students who I had the chance to meet: Stéphanie, Aurélien, Jérôme, Pierre, Matthias, Makrina, Simon, and all the others. These 3 year courses were also the starting point for fruitful scientific collaborations. I would like to acknowledge Jean-Remi Bertrand and Anna Haddad (Laboratoire Vectorisation et Transfert de Gènes, IGR) for their implication in the vectorization experiments of siRNA using nanodiamonds.

The accomplishment of this thesis would not be possible if I did not have the support of the friends and the family. My time at the region of Paris was made enjoyable to a high degree due to the friends I met during these three years. I am grateful for the time spent and the deep conversations I had, scientific and non-scientific, with Dimitris, Giorgia,

Fred, Petros, Elli, Kostas, Vangelis, Aris, Dimitra, Andy, Michalis, Justine, Marie Pia, and all the others who I have forgotten.

I am also grateful to Michelle and Alain, for their warm care and affection since I moved to the Paris region.

Finally, I would like to deeply thank my mother, for all she has done for me and her encouragement during all these years, and Sophie for her endless comprehension and continuous support. Thank you.

Contents

1	Introduction	9
1.1	Photoluminescence	9
1.2	Fluorescent probes for biology	11
1.2.1	Organic fluorescent probes	11
1.2.2	Inorganic fluorescent probes	12
1.3	NV color centers in diamond	14
1.4	Photoluminescent diamond nanoparticles for biological applications - state of the art	16
1.4.1	Photoluminescent diamond nanoparticles as cellular or biomolecular labels	16
1.4.2	Nanodiamond detection by backscattered light or Raman scattering	17
1.4.3	Surface functionalization of nanodiamonds	18
1.4.4	Diamond nanoparticles as drug delivery devices in cells	20
1.4.5	Biocompatibility of nanodiamonds	20
1.4.6	Conclusion	21
I	Optical properties of NV color centers in nanodiamonds	23
2	Production and characterization of NV centers embedded in nanodiamonds	25
2.1	Production of colloidal photoluminescent nanodiamonds	25
2.1.1	Diamond synthesis and nanodiamonds production	26
2.1.2	Creation of NV centers in diamond	27
a	Some theoretical elements on NV creation	28
b	Experimental results	29
2.1.3	Preparation of colloidal suspensions	32
2.1.4	Photoluminescence studies of nanodiamonds	36
2.1.5	Discussion	38
2.2	Experimental setup	40
2.2.1	The confocal microscopy	40
2.2.2	The home-built confocal setup	40
2.2.3	The scanning setup	44
2.2.4	The intensity-time correlation measurement setup	44
2.3	Optical properties of single photoluminescent nanodiamonds and comparison with single fluorescent bioprobes	47

2.3.1	Single NV centers in type N nanodiamonds	47
2.3.2	Single dye molecules	49
2.3.3	Individual commercial Quantum Dots	50
2.3.4	Comparison of single photoluminescent nanodiamond, dye molecule and quantum dot photoluminescent properties	53
2.4	Optimization of the photoluminescent nanodiamond fluorescence yield . .	55
2.4.1	Diamond microcrystals	55
2.4.2	Diamond nanocrystals	57
2.4.3	Discussion	58
2.5	Detonation nanodiamonds	60
2.5.1	Production and de-agglomeration of detonation nanodiamonds . .	60
2.5.2	Optical properties	61
2.5.3	Discussion	62
3	IR pulsed excitation of NV centers in diamond micro- and nanocrystals	65
3.1	Two photon excitation of NV centers	65
3.1.1	Introduction	65
a	Basic principles of two photon fluorescence microscopy .	65
b	Two photon excitation of NV centers - state of the art .	68
3.1.2	Two Photon Excitation properties of NV centers in bulk diamond	69
a	Experimental Setup	69
b	Two Photon Excitation photoluminescence spectra of NV centers in diamond microcrystals	72
c	Two Photon Excitation spectra of NV centers in diamond microcrystals	73
d	Corrections for the optical setup transmission	74
3.1.3	Two Photon Excitation properties of NV centers in nanodiamonds	75
a	Two Photon Excitation spectra of NV center photolumi- nescence in diamond nanocrystals	75
b	Two Photon Excitation Photoluminescence properties of NV centers in nanodiamonds	76
3.1.4	Conclusion	79
3.2	Quenching of the NV center photoluminescence and applications	80
3.2.1	State of the art	80
3.2.2	Quenching effect of NV center with green - infrared light	84
a	Experimental setup	84
b	Results	84
c	Discussion	89
3.2.3	Super Resolution imaging of NV centers in nanodiamonds	90
a	Experimental validation of the resolution enhancement by simultaneous fundamental (1064 nm) and frequency- doubled beam illumination	91
b	Sub-diffraction imaging limits with IR+green light exci- tation	93
3.2.4	Conclusion	94

II Applications of photoluminescent nanodiamonds in Biology	97
4 Internalization of photoluminescent nanodiamonds in cells	99
4.1 Introduction	99
4.2 Spontaneous internalization of photoluminescent nanodiamonds in HeLa cells	101
4.2.1 Experimental process	101
4.2.2 Internalization of photoluminescent nanodiamonds in cells	101
4.2.3 Detection of individual photoluminescent nanodiamonds in cells	103
4.3 Tracking of single photoluminescent nanodiamonds in cells	105
4.3.1 Techniques of individual nanoparticle tracking	105
4.3.2 Experimental Setup	107
4.3.3 Wide-field microscopy observations of freely diffusing nanodiamonds	108
4.3.4 Diffusion of photoluminescent nanodiamonds in living cells	109
4.4 Conclusion	113
5 Uptake mechanism and biocompatibility of nanodiamonds	115
5.1 Introduction	115
5.2 Determining the cellular uptake pathway of photoluminescent nanodiamonds	118
5.2.1 Study of the endocytosis mechanism	118
5.2.2 Study of receptor-mediated uptake mechanisms	120
5.2.3 Surface characterization of photoluminescent nanodiamonds in serum supplemented culture medium	121
5.3 Intracellular localization of photoluminescent nanodiamonds	123
5.3.1 Colocalization experiments of PNDs with endocytotic vesicles	123
a Immunofluorescence experiments and optical setup	123
b Experimental results and discussion	124
5.3.2 TEM Microscopy observations of PNDs in cells	126
5.4 Cell morphology after incubation with nanodiamonds	127
5.4.1 Experimental conditions	128
5.4.2 Results and Discussion	129
5.5 Biocompatibility assessment	129
5.5.1 Experimental conditions	129
5.5.2 Results and Discussion	131
5.6 Conclusion	131
6 Conjugation of nanodiamonds with plasmid DNA	133
6.1 Introduction	133
6.2 DNA- Nanodiamond coupling	134
6.2.1 Nanodiamond size selection	134
6.2.2 Nanodiamond surface coating by polycations : poly-L-lysine	135
a DNA - ND complex examination by Electrophoresis	136
b DNA - ND complex observation by AFM	137
6.2.3 Nanodiamond surface coating by polycations: polyallylamine hydrochloride (PAH)	138

6.2.4	Nanodiamond surface coating by divalent cations - Nickel	138
a	DNA - ND complex examination by Electrophoresis	139
b	DNA - ND complex observation by AFM	140
6.3	Transfection experiments of DNA - ND complex in HeLa cells	140
6.4	Conclusion	142
7	Conclusion	143
A	H3 color center in diamond	147
A.1	Introduction	147
A.2	H3 color center in micro-diamonds	147
A.3	Conclusion	149
B	Time Gated Imaging of photoluminescent nanodiamonds in cells	151
B.1	Introduction	151
B.2	NV color center radiative decay lifetime	151
B.2.1	Experimental setup	151
B.2.2	Measurement of NV decay lifetime in bulk diamond	152
B.2.3	NV decay lifetime in nanodiamonds	153
a	Influence of the emitters environment on the decay lifetime	153
b	Measurement of the decay lifetime of nanodiamonds	154
B.2.4	Discussion	155
B.3	Time-gated imaging of photoluminescent nanodiamonds internalized by cells	157
B.3.1	Cell preparation and PNDs uptake	157
B.3.2	Improving intracellular PNDs image contrast	157
B.4	Conclusion	159
C	Elements for doughnut-shaped intensity patterning	161
C.1	Liquid Crystal Polarization Converter	161
C.2	Helical $0-2\pi$ phase mask	162
D	Optical elements transmission	165
D.1	Collection efficiency	165
D.2	Transmission spectra of optical elements	167
D.2.1	Dichroic mirrors	167
D.2.2	Long-pass filters	169
D.2.3	Band-pass filters	170
D.2.4	Short-pass filters	171

Introduction

Ce manuscrit contient le travail de recherche effectué pendant mes trois ans de thèse (octobre 2006 - octobre 2009). La majorité de ce travail a été faite au sein de l'équipe de Nanophotonique Quantique du "Laboratoire de Photonique Quantique et Moléculaire" (LPQM, Ecole Normale Supérieure de Cachan and CNRS UMR8537), sous la direction de François Treussart. Un des sujets de recherche de cette équipe est l'utilisation de centres colorés NV uniques (NV étant une impureté d'azote à côté d'une lacune) dans le diamant pour l'optique et la cryptographie quantique. La stabilité du centre coloré NV a plus particulièrement permis de construire une source de photon unique qui a été utilisée pour la distribution quantique de clés cryptographiques et pour réaliser des expériences d'interférences à photon unique. Mon sujet de recherche a porté sur l'utilisation des nanoparticules de diamant contenant un grand nombre des centres colorés NV pour des applications en bio-imagerie, en mettant à profit leur photostabilité parfaite.

En biologie les nanoparticules sont couramment utilisées comme sondes fluorescentes pour marquer des biomolécules et suivre leurs déplacements. Parallèlement, elles offrent la possibilité du transport de molécules-médicaments dans des cellules, en servant de plateformes pour des réactions chimiques permettant l'accroche des biomolécules actives.

La nanoparticule photoluminescente idéale doit disposer d'une photostabilité parfaite et être non-toxique. De plus, si la même particule est utilisée pour des applications de délivrance des médicaments dans des cellules, elle doit disposer d'une composition chimique de la surface avec un potentiel élevé de fonctionnalisation.

Dans ce travail, nous nous sommes d'abord concentrés sur les propriétés optiques des nanoparticules pour la biologie. Nous avons comparé les propriétés optiques des nanodiamants photoluminescents avec celles des fluorophores les plus utilisés en bio-imagerie, tels que les fluorophores organiques. Ces derniers sont cependant caractérisés par un photoblanchiment, ce qui empêche leur suivi efficace sur de longues périodes d'observation. Les nanoparticules semiconductrices (Quantum Dots, QDs) possèdent une meilleure photostabilité et une brillance plus élevée. Cependant leur photoluminescence est encore marquée par un clignotement et elles sont caractérisés par une toxicité (pas encore bien étudiée).

Ainsi, le système constitué des nanoparticules de diamant contenant des centres colorés NV ayant une photoluminescence parfaitement stable dans le temps, avec une brillance équivalente à celle de QDs, comme il sera démontré dans ce travail, s'avère une alternative intéressante.

Ce manuscrit est divisé en deux parties. La première partie se concentre sur l'étude des **propriétés optiques des centres colorés NV des nanodiamants**. Différents types de nanodiamants, provenant de procédés de production différents ont été étudiés et caractérisés en particulier du point de vue de leurs propriétés optiques. Afin de produire des nanodiamants plus brillants, qui contiennent une densité plus élevée de centres NV, nous avons étudié les effets de différentes conditions d'irradiation (en variant les doses et les types de faisceaux des particules) et nous avons comparé les résultats expérimentaux aux estimations théoriques.

Dans la deuxième partie de cette thèse, nous avons étudié les **applications des**

NanoDiamants Photoluminescents (NDPs) en bio-imagerie. Nous avons observés que les NDPs sont internalisés spontanément par des cellules en culture et nous avons étudié leur localisation intracellulaire. Dans le but d'utiliser ces NDs comme véhicules de biomolécules-médicaments dans des cellules, nous avons étudié les mécanismes d'internalisation des NDPs, en les bloquant séparément. Nous avons étudié leur localisation intracellulaire par des méthodes d'immunofluorescence et de microscopie confocale et électronique en transmission. De plus, pour des applications biologiques le matériau utilisé ne doit pas être toxique. Comme la cytotoxicité dépend fortement du type de nanoparticules utilisées, nous avons comparé la cytotoxicité de tous des NDPs utilisés dans les expériences de cette thèse.

Afin d'améliorer le contraste d'imagerie des NDPs internalisés par des cellules, nous avons étudié les propriétés d'excitation à 2-photons des centres NV dans des micro- et nanodiamants à l'aide d'une excitation laser impulsionnelle. Lors de ces expériences, nous avons découvert une forte diminution du signal de photoluminescence des NDPs lorsque les impulsions visibles et infrarouges excitent les NDPs simultanément. Cet effet pourrait servir pour l'imagerie de super-résolution des centres NV dans des nanodiamants. Des résultats préliminaires ont été obtenu pendant cette thèse. Une autre méthode pour améliorer le contraste intracellulaire est la technique d'imagerie résolue en temps. Nous avons appliqué cette technique pour des NDPs, en tirant profit de leur durée de vie radiative relativement longue (~ 20 ns), par rapport à celle de l'autofluorescence du milieu intracellulaire (~ 2 ns).

Dans le domaine des applications à la vectorisation de biomolécules, nous avons utilisé les NDs pour transporter de l'ADN plasmidique dans le noyau de la cellule. Les expériences de transfection réalisées avec cet hybride ont initié l'une des directions de recherche prise à l'issue de ce travail de thèse.

En raison de l'interdisciplinarité de ce travail, nous avons effectué une partie des expériences dans de nombreux laboratoires partenaires. Les expériences de biologie cellulaire, y compris le marquage cellulaire, les tests de cytotoxicité et de transfection, ont été effectués dans le "Laboratoire Structure et Activité des Biomolécules Normales et Pathologiques" (Université d'Evry - Val d'Essonne and INSERM U829), dirigé par Patrick Curmi. Pour l'imagerie des NDPs dans des cellules par des microscopes standards, commerciaux, nous avons utilisé les microscopes de deux plateformes d'imagerie, dans le "Laboratoire de Biologie et de Pharmacologie Appliquée" (LBPA, Ecole Normale Supérieure de Cachan et CNRS UMR 8113) supervisé par Patrick Tauc et dans l' "Institut du Fer Moulin" (INSERM UMR-S 839 et Université Pierre et Marie Curie, Paris) supervisé par Theano Irinopoulou.

Une partie de la caractérisation de la taille et de la morphologie des NDs, ainsi que l'étude de la localisation précise des NDs dans des cellules, ont requis des expériences de Microscopie Electronique en Transmission (MET), que nous avons effectuées dans le "Laboratoire Pierre-Marie Fourt" (Centre des Matériaux de l'Ecole des Mines de Paris et CNRS UMR 7633).

Introduction

This manuscript contains the research work carried out during my three years of PhD (October 2006 - July 2009). The majority of this work was carried out in the Quantum Nanophotonics team of “Laboratoire de Photonique Quantique et Moléculaire” (LPQM, Ecole Normale Supérieure de Cachan and CNRS UMR8537), under the direction of François Treussart. One of the main research topics of the team is the use of single nitrogen-vacancy (NV, a nitrogen impurity next to a vacancy) color centers in diamond nanoparticles for quantum optics and quantum information processing. In particular, the NV color center photostability allowed to build a reliable single photon source that was used for quantum key distribution and single photon interferences. My research topic was focused on using nanodiamonds containing a big number of NV color centers for bio-imaging applications, taking advantage of their perfect photostability.

In biology nanoparticles are used as fluorescent probes to monitor interactions and study the dynamics at the single molecule level. They also provide the opportunity to improve drug delivery in cells, serving as a biochemical platform to which active biomolecules can be attached.

An ideal nanoparticle should have a perfect photostability and be biocompatible. Additionally, if the same particle is used for drug delivery applications, it should have a surface chemical composition with a high potential of functionalization.

In this work, we mainly concentrated on the fluorescence properties of nanoparticles. Therefore, we compared photoluminescent nanodiamonds to widely used fluorophores. Organic dye molecules are widely used over the last years in bio-labeling applications, but they suffer from photobleaching, which precludes tracking over a long observation time. Quantum Dots (QDs) overcome this problem by a better photostability and a higher brightness. Blinking effects and toxicity reasons increase however the need of examining other alternative systems.

In comparison, the alternative system consisting of diamond nanoparticles containing NV color centers, is perfectly stable in time with a similar brightness, as it will be shown in this work.

The manuscript is divided in two parts. The first part concerns the study of the **optical properties of NV color centers in nanodiamonds**. Different types of nanodiamonds, coming from different production processes are studied, characterized and their optical properties are compared. In order to produce brighter nanodiamonds, which contain a high density of NV centers, we examine nanodiamonds made photoluminescent under different irradiation conditions (doses and types of particle beams) and compare the experimental data to the theoretical estimates.

In the second part of this thesis we study the **applications of Photoluminescent NanoDiamonds (PNDs) to bio-imaging**. PNDs are spontaneously internalized by cells and we study their intracellular localization. In the prospect of applications of NDs as drug delivery vehicles, we study the uptake mechanisms of PNDs in cells, by blocking different entry mechanisms. By immunofluorescence methods and transmission electron microscopy as well we elucidate their intracellular localization. Moreover, for biological applications one has to ensure that the material used is biocompatible. As cytotoxicity

depends strongly on the type of PNDs, we compare the cytotoxicity of all PNDs used for the experiments of this thesis.

To enhance the imaging contrast of internalized PNDs, we study the 2-photon excitation properties of NV centers in micro- and nanodiamonds. While implementing a pulsed excitation laser system to realize these experiments, we discover another non-linear phenomenon that “quenches” the photoluminescence signal of PNDs. This effect could serve for sub-resolution imaging of NV color centers in nanodiamonds. Preliminary results are obtained in the course of this thesis. Additionally, an alternative way to improve the intracellular contrast of PNDs is by time-gated imaging. We applied this technique for PNDs, taking advantage of their long decay lifetime (~ 20 ns) in comparison to the short decay lifetime of the cell medium autofluorescence (~ 2 ns).

In the field of vectorization applications, as a first try we examine the possibility of using NDs to deliver plasmid DNA in the cell nucleus. These transfection experiments allowed us to plan further vectorization applications, which are the eventual continuity of this PhD work.

Due to the interdisciplinarity of this work, we executed part of our experiments in numerous laboratories. The cell biology experiments, including cell staining, cytotoxicity and transfection tests were carried out in “Laboratoire Structure et Activité des Biomolécules Normales et Pathologiques” (Université d’Evry - Val d’Essonne and INSERM U829), directed by Patrick Curmi. Additionally, for the imaging of photoluminescent nanodiamonds in cells with standard commercial confocal microscopes we used the microscopy facilities of two imaging platforms, in “Laboratoire de Biologie et de Pharmacologie Appliquée” (LBPA, Ecole Normale Supérieure de Cachan and CNRS UMR 8113) supervised by Patrick Tauc and in “Institut du Fer Moulin” (INSERM UMR-S 839 and Université Pierre et Marie Curie, Paris) supervised by Theano Irinopoulou.

Part of the nanodiamonds size and morphology characterization, and the study of the precise localization of nanodiamonds in cells, required Transmission Electron Microscopy experiments, which we carried out in “Laboratoire Pierre-Marie Fournier” (Centre des Matériaux de l’Ecole des Mines de Paris and CNRS UMR 7633).

Chapter 1

Introduction

In this chapter we make a brief review of the main fluorescent probes used in biology. We provide an introduction to the Nitrogen-Vacancy color centers in diamond crystals and summarize their broad range of applications, in particular in quantum information processing as single photon sources and sensitive magnetic sensors. Finally, we present a state of the art of the use of photoluminescent nanodiamonds as markers for biology, which is the main topic of this work.

1.1 Photoluminescence

Light is very important for our understanding of matter because both can interact with each other and reveal a lot of information about the material properties.

Here we are interested in the photoluminescence phenomenon, which is the emission of light caused by the irradiation of matter with light [1]. The term embraces both fluorescence and phosphorescence, which differ in the after irradiation time over which the luminescence occurs. Fluorescent materials absorb and then re-emit light at a longer wavelength, within nanoseconds to milliseconds after irradiation, by spontaneous emission.

The absorption and emission phenomena of fluorescent molecules are described with an energy diagram, the so-called Jablonski diagram (from Alexander Jablonski, 1898-1980). Figure 1.1 illustrates a simplified version of this diagram. To allow an excitation from the ground state S_0 to the first excited state S_1 , a photon of energy at least equal to the energy difference between the lower vibrational energy level of S_1 state and the lower vibrational level of state S_0 has to be absorbed. Due to a vibrational relaxation the de-excitation of the system is followed by an emission of a photon of energy lower than the one needed for the excitation. The energy difference corresponds to the so-called Stokes shift, which is characteristic of the material.

The phenomenon of phosphorescence comes from the de-excitation of the emitter from a metastable electronic state (triplet state, in the case of organic dyes), exhibiting only forbidden transitions towards the ground state. The stored energy is therefore released only through relatively slow processes (10^{-5} to 1 s) compared to the fluorescence process.

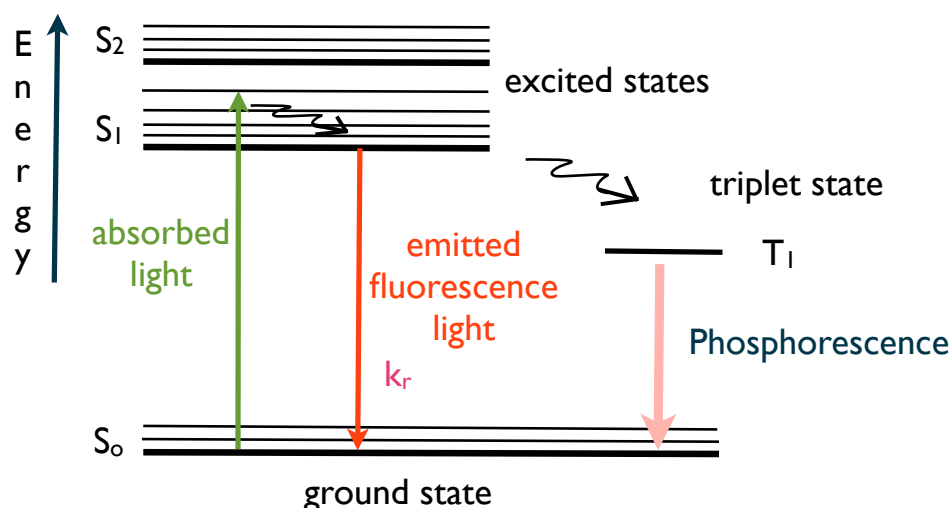


Figure 1.1: Simplified Jablonski diagram.

All kinds of fluorophore probes can be characterized by the following properties that we briefly define:

Absorption, emission and excitation spectra: they are the “fingerprints” of each material. The absorption spectrum is the continuous spectrum or pattern of lines or bands distinguished when electromagnetic radiation (i.e. light) is absorbed by the fluorophore over a spanning frequency range of the excitation source. The emission spectrum is the continuous spectrum or pattern of bright lines or bands formed when light is emitted by the fluorophore for a given excitation wavelength. The *excitation spectrum* is obtained by monitoring the fluorescence intensity at a given wavelength (usually the one of the maximum intensity of the fluorophore) while the fluorophore is excited over a spanning frequency range. Excitation is induced at various excitation wavelengths and the intensity of the emitted fluorescence is measured as a function of the wavelength.

Quantum Yield: it is the relative efficiency of the fluorescence (described by the radiative decay rate k_r) compared to other de-excitation processes (described by the non-radiative decay rate k_{nr}). It can also be seen as the ratio of the emitted to the absorbed photons. The quantum yield is defined as:

$$\phi = \frac{k_r}{k_r + k_{nr}} \quad (1.1)$$

Its maximal value can be 100%, when there is absence of non radiative de-excitation processes.

Extinction coefficient (or molar absorption coefficient, ϵ): For light propagating through a solution of fluorophore molecules M , its intensity at a distance L is described by the Beer-Lambert law: $I(L) = I(0)\epsilon[M]L$, with $I(0)$ the initial intensity, $[M]$ the concentration of the fluorophore M in solution. Thus the extinction coefficient ϵ is the quantity of light absorbed for a specific wavelength and is measured in $M^{-1}cm^{-1}$. The molar absorption coefficient is related to the absorption cross section σ (cm^2) as: $\sigma = 3.82 \times 10^{-21} \epsilon$ [1].

Fluorescence decay lifetime: the fluorescence decay time is the characteristic duration that a fluorophore remains in its excited state after excitation, and is defined as:

$\tau = \frac{1}{k_r + k_{nr}}$. This decay lifetime depends strongly on the environment of the fluorophore molecule, i.e. pH, dipole orientation, medium surrounding the molecule.

Photostability: it characterizes the stability of the fluorescence signal under continuous excitation. Common fluorophores photobleach (i.e. lose permanently their fluorescence) after some time of illumination. The reasons of photobleaching vary, the most common one being the reaction of the fluorophore in its triplet state with oxygen molecules. Photoblinking is another phenomenon related to photostability. Here the fluorescence is interrupted by dark periods during which no emission occurs.

An ideal fluorescent probe should have well separated absorption and emission spectra, a not too broad emission spectrum (to avoid overlap), a quantum efficiency near unity (with absence of non radiative de-excitation processes), a large extinction coefficient (to avoid high excitation powers) and a perfect photostability.

1.2 Fluorescent probes for biology

1.2.1 Organic fluorescent probes

Organic fluorescent probes are nowadays the most widespread probes for fluorescence microscopy in biology.

Organic fluorescent molecules can be specifically “coupled” to biomolecules (peptides, proteins, oligonucleotides) or to cell compartments in three different ways : i) by a covalent coupling (direct chemical reaction), ii) by an intermediate attachment to an antibody, which is specific to the biomolecule or with the attachment to a secondary antibody specific to the primary antibody, which in its turn is specific to the biomolecule (immunofluorescence technique), iii) by cloning a fluorescent protein. For the first two methods, the most common probes are organic dye molecules, which can be synthesized and are commercially available. They are widely used in routine procedures and well established protocols [2].

The technique of immunofluorescence (see Ref. [3] for the first report of this method and its application with fluorescence microscopy [4]) opened the way to the commercialization of organic dye molecules. It allows to attach several fluorophores at the same time on the molecule of interest, enhancing the emitted fluorescence signal.

Figure 1.2 shows a typical labeling of different cell compartments with the use of Alexa Fluor, a commonly used organic fluorophore. As seen on the images, after some minutes of illumination the dyes photobleach, leading to an irreversible loss of fluorescence. Although methods have been developed to reduce this effect (by a weak excitation power, or by using oxygen scavenger systems) the phenomenon still exists and makes organic dyes not the appropriate fluorescence probes for long-time observations (Table 1.1).

Apart from the organic dye molecules, the genetically encoded fluorescent proteins constitute another category of organic fluorophores widely used for bio-imaging. The first discovered fluorescent protein was the Green Fluorescent Protein (GFP), originat-

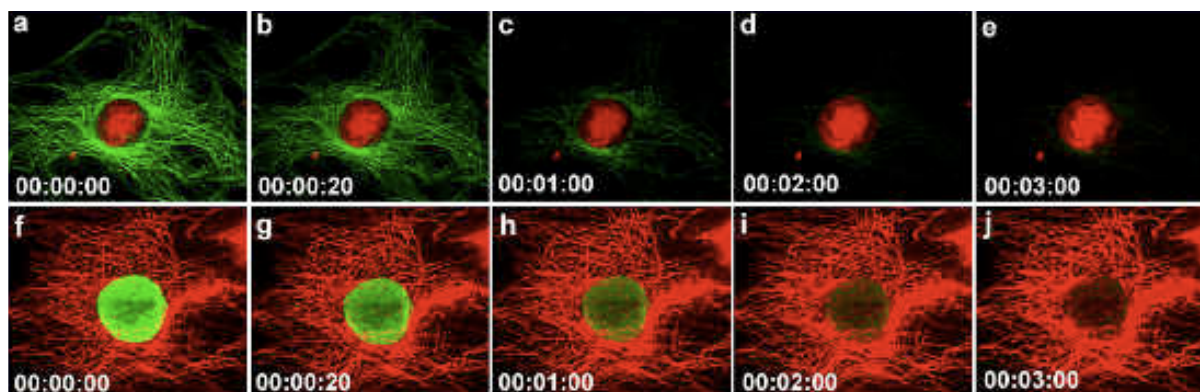


Figure 1.2: Simultaneous cell labeling with organic dye molecules and quantum dots. In the upper panels the actin filaments are stained in green with Alexa Fluor 488 and the nucleus is stained in red with QDs 605 - streptavidin conjugate. In the lower panels the labeling is reversed. Images on both lines are taken every 20 s. The dye molecules photobleach rapidly, in contrast to QDs. Image is extracted from Ref. [5].

ing from jellyfish. It emits green fluorescence light under blue light excitation. It was discovered by Osamu Shimomura, in 1962, who purified it from the *Aequorea victoria* jellyfish [6]. It was only in 1992 that Douglas Prasher cloned the sequence of GFP and Martin Chalfie expressed this sequence *in vivo* [7]. Later on, the group of Roger Tsien reported the first crystal structure of GFP, showing the way for the creation of GFP mutants, to finally obtain different color variants and improve the fluorescence signal and photostability [8–10]. Shimomura, Chalfie and Tsien were awarded in 2008 with the Nobel Prize in Chemistry for their work on the genetically encoded fluorescent proteins.

The reason why GFP became so popular in biology is that with no external labeling, one can label cell compartments, or even whole cells, tissues or organisms, with the appropriate introduction of the GFP-cDNA¹ into the cell or organism under study. Although convenient for intracellular bio-imaging, GFP and its derivatives lose their fluorescence properties under a continuous illumination time period.

1.2.2 Inorganic fluorescent probes

During the past 15 years new inorganic fluorescent probes have been proposed, as alternatives to organic fluorophores, with the aim to achieve higher fluorescence yield and lower photobleaching. Inorganic fluorescent nanocrystals include Quantum Dots (QDs) [5], silicon nanoparticles [18], core-shell fluorescent silica nanoparticles (or C dots) [19], lanthanide-doped oxide nanoparticles [20], etc. Some of the above systems are already commercialized and widely used, some others are new and under development.

The most widely used inorganic nanoparticles are the quantum dots. They are nanocrystals made of semiconductors of the II/VI or III/V family. These nanocrystals are made of a few hundreds to some thousands atoms and the electron motion is confined by potential barriers in the three dimensions, forming a “point-like” structure. In such small size nanocrystals the energy levels are quantized, with values directly related to the particle size; an effect called quantum confinement [21]. This confinement allows a

¹cDNA: complementary DNA

Property	Dye molecule	QD	nanodiamond with NV centers
Absorption spectra (FWHM)	30-100 nm ^a	broadband ^b increase at low λ	broad (>100 nm) ^c
ϵ (M ⁻¹ cm ⁻¹)	10 ⁴ -10 ⁵ ^a	10 ⁵ -10 ⁶ ^a	10 ⁴ ^d
Emission spectra (FWHM)	35-100 nm ^a	<50 nm ^b	≈110 nm
Quantum efficiency	0.1-1 ^a	0.3-1 ^a	in bulk diamond ~ 1 ^e
τ_{rad} (ns)	1-10 (monoexp.) ^a	10-100 (multiexp.) ^a	10-40 (multiexp.)
Size (nm)	0.5	6-60 ^a	5-100 ^{f,g}
Photostability	low	good but photoblinking	perfect

Table 1.1: Comparison of the photophysical properties of dye molecules, QDs and NV centers in nanodiamonds, for the visible wavelength range. Corresponding references: a: [11], b: [12], c: [13], d: [14], e: [15], f: [16], g: [17]

tunable emission wavelength of the QDs by varying their size. Colloidal QDs were first used in bio-imaging in 1998 [22, 23], and since then they have become well established biological markers.

The most widely used QDs are CdSe and CdTe particles (II/VI family), which are commercially available (Invitrogen, Evident Technologies, etc.). Recently new particles appeared as very promising systems, like InP or InGaP (III/V family) [5, 12].

The core size of typical QDs is 2-10 nm. A shell, usually made of ZnS is necessary to stabilize the fluorescence properties. For their solubilization the particles are further coated with various polymers, which have the necessary chemical groups for biomolecule attachment. At the end, the total size of the particles is in the range of 20-50 nm. This is one or two orders of magnitude larger than the equivalent system using a single dye molecule as the fluorophore, but is still in the nanometric scale.

The advantages of this kind of particles is that their fluorescence signal is brighter than the equivalent of organic dye molecules and they present a better photostability allowing observations and tracking over an extended period of time with confocal microscopy or wide-field epifluorescence microscopy (Figure 1.2). Additionally, QDs present a large two-photon absorption cross section, so two-photon microscopy experiments are possible [24].

However, QDs present also some drawbacks for biological applications. Their photoluminescence blinks alternating bright and dark periods [25]. This prevents reliable long term single particle tracking. A large amount of work has been carried out to overcome this effect, and very recent reports show that blinking can be reduced or even suppressed [26–28], but at the expense of a higher bleaching yield [28]. Finally, QDs may appear cytotoxic on the long term due to their core chemical composition, composed of cadmium, a very toxic heavy metal element [29, 30]. Little is known for the moment on this issue and further investigations are necessary.

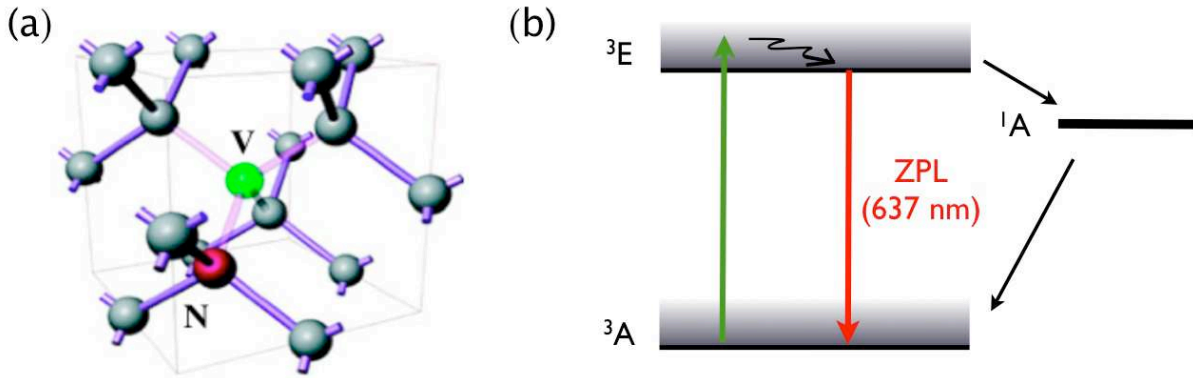


Figure 1.3: Nitrogen Vacancy color center in the diamond matrix. (a) One substitutional Nitrogen atom next to a Vacancy form a NV color center. (b) Schematic description of the energy levels of the NV^- center. The ground and excited states of multiplicity type ^3A and ^3E respectively are triplet spin states. There is also a metastable singlet state of lower energy and multiplicity type ^1A . When a photon is absorbed by the NV^- center the system is excited to the ^3E state. From this state, either the system falls back to the ground state, with a broad emission spectrum (due to the vibrational levels) and a Zero Phonon Line at 637 nm, or the system is trapped in the ^1A state, after having undergone an inter-system crossing transition. The decay rate to this state (0.005 ns^{-1}) is very low in comparison to the decay rate of the $^3\text{E} \rightarrow ^3\text{A}$ transition (0.083 ns^{-1}) [32]) so de-excitation mostly occurs through the $^3\text{E} \rightarrow ^3\text{A}$ photoluminescent transition.

1.3 NV color centers in diamond

Some impurities in the diamond lattice form color centers, which can emit a photoluminescence signal. There are more than 500 optically active defects in diamond [15, 31]. In this work we are interested in the Nitrogen-Vacancy (NV) color center. Nitrogen is the most abundant impurity in diamond. It exists either as a single substitutional atom or in aggregated form. The NV center is created when a carbon vacancy is positioned next to a substitutional nitrogen atom (Figure 1.3a). Its photoluminescence has the remarkable property of being perfectly photostable at room temperature.

The NV defect can exist in two charge states, the neutral state NV° and the negatively charged state NV^- . At low temperature the absorption is marked by a narrow optical resonance line (Zero Phonon Line, ZPL) at 575 nm and 637 nm respectively. The absorption and emission spectra of the NV^- center are relative broad [13], providing a wide range of excitation wavelengths (most typically 488 to 532 nm). At room temperature vibronic side bands are also visible.

The perfect photostability has been used to design a reliable single photon source, based on pulsed excitation of the NV^- color center [33]. Such a source was then used to realize the first single photon Quantum Key Distributor [34].

Electron spin resonance measurements have indicated that the NV^- center has an electron paramagnetic ground triplet state with $S = 1$, opening the way for applications using the spin states properties. Hole burning [35] and magnetic resonance experiments [36] indicate that the excited state is also a spin triplet. The most dominant theory is that

the ground state has 3A symmetry and the excited state a 3E symmetry (the number 3 means that these levels are triplets, Figure 1.3b). The existence of at least one metastable state between the ground and excited states has been proposed. This state is a singlet 1A state where the system can be found after an inter-system crossing $^3E \rightarrow ^1A$.

Numerous applications exist or are under development using the spin states of the NV^- center (similar states do not exist in other nanoparticles, like QDs), like in quantum information processing. The possibility to detect the spin state of the NV center optically (via the photoluminescence intensity) facilitates the use of the NV center as a spin qubit [37] and/or its coupling with nearby electron and nuclear spins [37, 38]. Moreover, nanodiamonds doped with NV centers can be used as magnetic field sensors with high sensitivity, reaching atomic spatial resolution [39].

Another field of applications is the use of nanodiamonds as near-field single photon probes. Schietinger et al. have reported an enhancement of the single NV center photoluminescence intensity, when a PND approaches metal structures (i.e. gold nanospheres) [40]. Cucho et al. have recently attached a 20 nm PND containing a single NV center on a Near-field Scanning Optical Microscope (NSOM) tip and imaged metallic nanostructures in the near-field, achieving stable room temperature near-field scanning single-photon microscopy [16, 41]. The attachment of NDs with single NV centers on an AFM (Atomic Force Microscope) or NSOM tip and the control of this procedure, opens up new possibilities for some emerging branches of nanophotonics, such as for example quantum plasmonics [40, 42] or high-resolution high-sensitivity magnetometry [39, 43, 44].

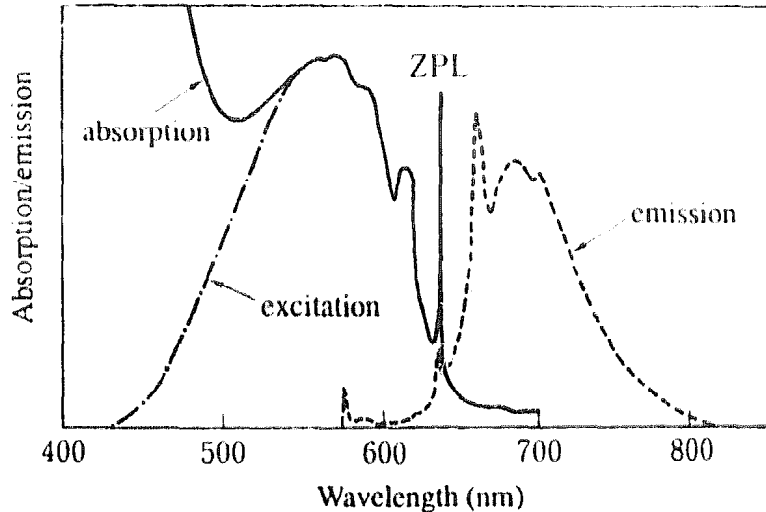


Figure 1.4: The one-photon absorption, emission and excitation spectra of NV^- center. Note the sharp zero phonon line at 637 nm [13].

Regarding the optical characteristics of the NV center, the quantum yield of the NV^- center has been found equal to unity in bulk diamond [15], but has never been measured for diamond nanoparticles.

The absorption cross section of the NV^- center was recently measured by Wee et al. [14] and found equal to $3 \times 10^{-17} \text{ cm}^{-2}$. As we will see in more details in the following

chapters, the fluorescence decay lifetime of this type of color center is ~ 12 ns in bulk diamond and dispersed between 10-40 ns for nanodiamonds (Table 1.1). The absorption spectrum has also been reported in the blue-green wavelength region [13, 45].

NV centers can be present or be introduced in diamond particles, of micro- or nanometric size. Traditionally, NV centers are created in the diamond lattice by high energy electron (2-10 MeV) [33, 46] or proton (2-3 MeV) irradiation [47, 48], a process which creates more vacancies in the lattice. A subsequent annealing (usually at 800°C for 2 hours) is necessary, to make vacancies migrate next to substitutional nitrogen atoms. An alternative way to produce NV centers in diamond is by the use of a low energy (40 keV) alpha-particle irradiation beam [47]. Such experiments were carried out by the team of Huan-Cheng Chang at the Institute of Atomic and Molecular Science (IAMS, Academia Sinica, Taipei).

Given the perfect photostability of NV centers embedded in diamond nanoparticles, one can envision to use NV centers for biological labeling. In addition to the absence of photobleaching, NV centers do not photoblink. Their emission maximum is in the red and near infrared spectral region; a spectral window of low absorption in biology, allowing deeper photon penetration in tissues [49]. Moreover, diamond is characterized by a pure sp^3 carbon composition², rendering nanodiamonds chemically inert.

1.4 Photoluminescent diamond nanoparticles for biological applications - state of the art

1.4.1 Photoluminescent diamond nanoparticles as cellular or biomolecular labels

The first use of photoluminescent nanodiamonds as biological labels was reported in 2005. The team of Huan-Cheng Chang showed that PNDs are spontaneously internalized in HeLa cells and seem to be non-toxic for *in vitro* experiments [50]. These results, combined with the intense and perfect photostability of the NV color center emission in 100 nm nanodiamonds, opened the way for the use of PNDs for bio-imaging.

At the same time, a group of european laboratories gathered their skills in the European project Nano4Drugs, *A Multidisciplinary Effort for Protein-Based Drugs Delivery using Fluorescent Nanodiamond*. The project lasted 3 years (2006-2009). The project manager was Patrick Curmi (Laboratoire Structure et Activité des Biomolécules Normales et Pathologiques, Université d'Evry) and a participating group was the Quantum Nanophotonics team of Jean-François Roch (ENS de Cachan). Part of this thesis work benefitted from the inter-disciplinary cooperations with the other partners of the project.

For biological applications and intracellular labeling, one has to examine the internalization of the probes in the cell. Many reports indicate the spontaneous internalization and efficient detection³ of such photoluminescent nanodiamonds in cells [48, 51–53].

²Carbon atoms in diamond have four valence electrons in the following configuration: $1s^2 2s^1 2p^3$, forming a sp^3 state.

³detectable with fluorescence microscopy and flow cytometry techniques

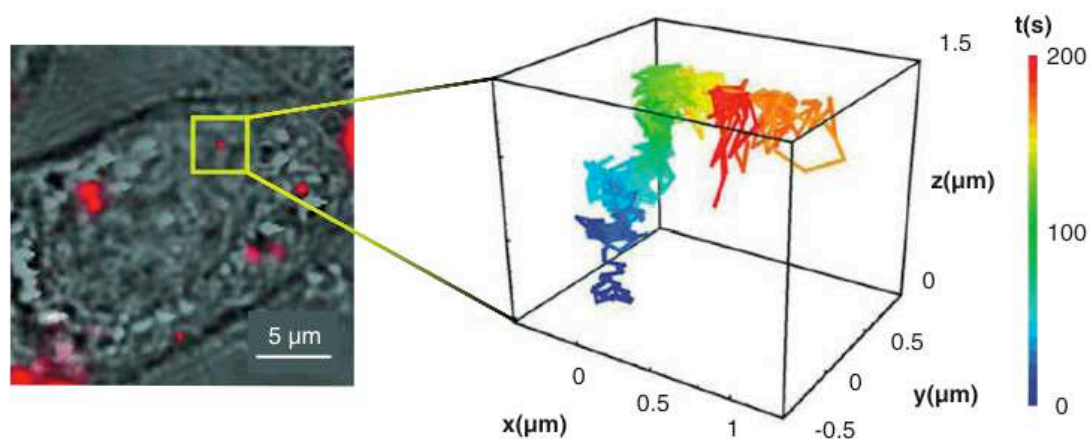


Figure 1.5: Three dimensional tracking of a single PND in a live cell. Merge of bright-field and epifluorescence images shows a PND in the cytoplasm. Since the photoluminescence is stable, a 3D trajectory of the selected particle in the cell can be followed for about 200 s [47].

Small in size and bright enough PNDs are perfect candidates for bio-imaging and long-term tracking experiments. Fu et al. incubated PNDs with HeLa cells at 37°C and observed their intracellular diffusion. Thanks to their perfect photostability, PNDs were individually tracked for more than 200 s in cells, in three dimensions, using a wide-field fluorescence microscope, an electron-multiplier CCD detection camera (Andor Technology) and a home-made setup that allowed the movement of the microscope objective according to the nanoparticle trajectory on the z axis (Figure 1.5) [47].

Thanks to PNDs perfect photostability, one can use PNDs for labeling and tracking the cell division and differentiation of cancer and stem cells [54]. Apart from cell labeling, with the appropriate surface functionalization, nanodiamonds attached to antibodies can target specifically intracellular structures, like mitochondria[55].

Additionally, like for QDs, one can improve the imaging contrast of PNDs in the cellular medium, either by detecting the 2-photon emission of the NV centers [47] or by time-gated imaging techniques [48].

1.4.2 Nanodiamond detection by backscattered light or Raman scattering

NDs can be detected in cells by a few other alternative methods than photoluminescence. Since diamond refractive index (2.42) is about twice larger than the one of endocellular medium, diamond can yield a higher back-scattered intensity of the excitation laser light than the cell compartments. Such a scattering signal can then be used to image 50 nm nanodiamonds in cells with a good contrast [52, 56, 57].

Moreover, due to the diamond structure, nanodiamonds can be detected by the Raman scattering of the diamond matrix with a sharp and narrow peak at 1332 cm^{-1} of the sp^3 bonding carbons. This method was applied and gave an intense signal for >50 nm nanodiamonds in cells, while for NDs of size <50 the signal is low and the detection more difficult [58–60].

1.4.3 Surface functionalization of nanodiamonds

Interestingly, a lot of work has been carried out the last years on the surface chemistry of diamond [61]. For biology, the conjugation with active agents on the particles surface is of crucial importance. Depending on the fabrication process, diamond can be produced either by Chemical Vapor Deposition (CVD) or under High Pressure High Temperature (HPHT) conditions. For the former case, diamond surfaces (i.e. diamond films) have been efficiently functionalized for coupling with various chemical or biological molecules (for example with DNA for bio-sensor applications [62]).

Regarding HPHT diamond, many efforts are made to apply the outstanding functionalization results achieved for diamond films to nanodiamonds. For instance, a major point is to induce stable C-H bonds homogeneously at the nanodiamond surface, bonds that constitute the starting point for a large amount of further surface chemistry. The most suitable method for that is by hydrogenation. Diamond hydrogenated films exhibiting particular surface electronic properties can be obtained by microwave plasma (MPCVD) exposure [63]. With plasma temperatures close to 2000°C, the surface is exposed to very reactive species (atomic hydrogen). An accurate knowledge and control of the reactions at the nanodiamond surface under plasma exposure could lead to a controlled surface hydrogenation. Although ND hydrogenation is reported for diamond powder in a H_2/N_2 gas mixture at 800°C for 2 h [64], the control of the process to obtain a homogeneous hydrogenated nanodiamond surface is an open challenge for chemists.

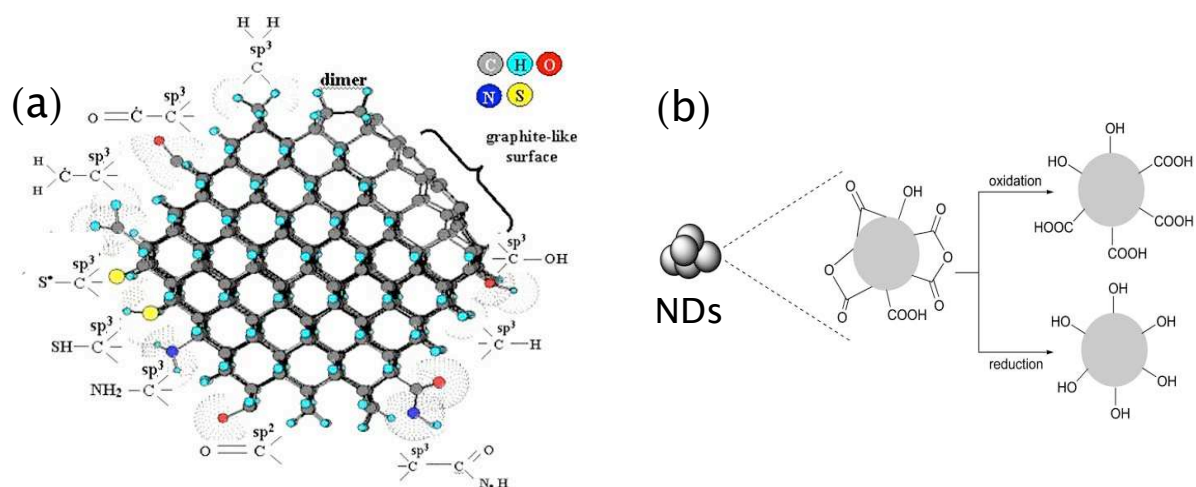


Figure 1.6: Nanodiamond surface chemical groups. (a) Different possible functional groups on nanodiamond surface. The nature of the tetrahedral carbon arrangement leads to the loss of at least one valence on the surface of the material, implying the presence of radical species, incorporation of hydrogen, or hetero-atoms of the surface (CH, COH, COC ...) [65]. (b) Pre-functionalization of the ND surface by an oxidation or reduction process [66].

Classical pre-functionalization⁴ methods of nanodiamonds include treatment in strong oxidative-acids ($HNO_3 - H_2SO_4$ [67, 68], oxidation in air [69] to form carboxyl groups)

⁴with “pre-functionalization” we mean the cleaning of the diamond surface of the various initial chemical groups and its functionalization with a specific group

1.4.4 Diamond nanoparticles as drug delivery devices in cells

The possibility of modifying the nanodiamond surface and grafting bioactive moieties has opened the way for drug delivery applications.

Huang et al. demonstrated that detonation NDs can serve as chemotherapeutic drug carriers, by loading them with an apoptosis inducing drug, the doxorubicin hydrochloride (DOX) [74]. NDs are negatively charged (carboxylated) and doxorubicin ions ($D-NH_3^+$) are cationic but the non-covalent adsorption is not straightforward (due to their high dispersibility). Thus, they added salt (NaCl), which promotes the adsorption of DOX on the NDs surface. They observed transport of the ND-DOX complex in living cells (human colorectal carcinoma cells and murine macrophages), release of the drug and subsequent cell death (Figure 1.8a).

Very recently, the same team demonstrated the application of carboxylated NDs towards the enhancement of the water dispersion of poorly water-soluble therapeutic molecules, like Purvalanol A (a chemotherapeutic for liver cancer) or dexamethasone (an anti-inflammatory addressing a wide spectrum of diseases) [75]. The attachment was achieved electrostatically, the drugs were water-dispersed and experiments with cells verified that the drugs maintained their functionalities.

To conclude, all the existing reports show that nanodiamonds are medically significant nanomaterials, which can serve as platforms for controlled delivery of therapeutic agents in cells.

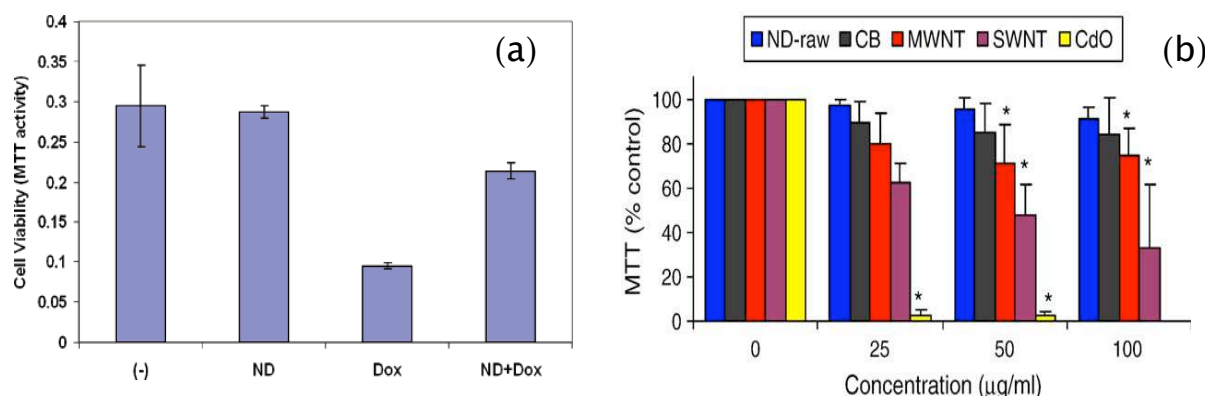


Figure 1.8: Drug delivery of chemotherapeutics in cells by 5 nm NDs and cytotoxicity evaluation of NDs. (a) Cytotoxicity evaluation (MTT) of HT-29 human colorectal adenocarcinoma cells grown alone (-), with 25 $\mu\text{g/ml}$ NDs, with 2.5 $\mu\text{g/mL}$ doxorubicin (DOX) or with 25 $\mu\text{g/ml}$ NDs conjugated with 2.5 $\mu\text{g/ml}$ DOX [74]. (b) Cell viability assay (MTT) after 24 h of incubation of NDs, Carbon black (CB), Multi-wall Nanotubes (MWNT), Single-wall Nanotubes (SWNT) or CdO particles with neuroblastoma cells [76].

1.4.5 Biocompatibility of nanodiamonds

Nanoparticles, according to the American Society for Testing and Materials standard definition of 2006, are particles with lengths that range from 1 to 100 nanometers in two or three dimensions [77]. The diamond material used for our studies fulfills this criterion, as it varies from 5 nm (detonation NDs) to 100-150 nm (typical HPHT diamond).

Despite the increase in manufacturing of nanoparticle-containing systems along with the constant discovery of new applications of nanoparticles, knowledge on the health effects of nanoparticle exposure is still limited.

Carbon nanoparticles are expected to be more biocompatible compared to inorganic materials. Nevertheless, among carbon nanoparticles a differentiation in biocompatibility is observed, depending on the purity, size, shape and surface functional groups of the nanoparticles. For example pure fullerenes were found more biocompatible than carbon nanotubes in alveolar macrophages [78]. Regarding nanodiamonds, Schrand et al. reported that single-walled carbon nanotubes show the highest toxicity for neuroblastoma cells and alveolar macrophages, followed by multi-walled nanotubes, carbon black and at last nanodiamonds, which were shown to be non toxic for this kind of cells (Figure 1.8b) [79]. Moreover, cells grown on 5 nm ND-coated substrates exhibit high viability and preserve their morphology and functions [76].

Other studies on 5 nm and 100 nm primary size NDs in lung cells for up to 24 h showed similar results of biocompatibility [80]. The results for the biocompatibility of NDs are encouraging. The understanding of possible long-term adverse effects of internalized nanodiamonds on cells will require more, long-term, toxicology experiments on animal models; a work just started in different laboratories worldwide.

1.4.6 Conclusion

Diamond nanoparticles for biological applications is a particularly active field of research, because of the photoluminescence, surface chemistry and biocompatibility properties of this material. However, there are only a few reports that combine all these properties, in order to be able to use nanodiamonds as drug delivery devices and at the same time visualize the internalization route and follow the interactions of the transported biomolecules with their target.

The starting idea of this thesis was to use photoluminescent nanodiamonds as markers and vectors of biomolecules. Although very promising and innovative, this requires the synergy of many different disciplines, including materials science, optics, biochemistry, cellular biology. Some aspects of the initial plan were well developed, with often unexpected findings and results (like the ground state depletion of the NV center or the intracellular localization of nanodiamonds), while other were blocked by interdisciplinary problematics (like the efficient transfection of DNA in cells using nanodiamonds as the cargo device). All that work is extensively presented in the following chapters.

Part I

Optical properties of NV color centers in nanodiamonds

Chapter 2

Production and characterization of NV centers embedded in nanodiamonds

This chapter describes the methods used to obtain nanodiamonds containing NV color centers and the optical setup used to characterize their optical properties. Photoluminescent nanodiamonds are obtained by two methods, which are thoroughly explained. We then study the photoluminescence properties of nanodiamonds containing NV centers. We compare them with the ones of single carbocyanine molecules or of single CdSe/ZnS Quantum Dots which are common fluorescent probes in bio-imaging and we extract useful conclusions on the prospect of using PNDs as fluorescent biological probes. By changing a parameter of the NV creation process, we obtain nanodiamonds characterized by different photoluminescence intensity, which we quantify and compare to the values expected from the theory. Finally, we study the photoluminescence properties of another type of nanodiamonds, the so-called detonation nanodiamonds, with the tiny sizes of 5 nm.

2.1 Production of colloidal photoluminescent nanodiamonds

The applications of nanoparticles as fluorescent probes in biology, require that the latter meet the following conditions:

- *Small size.*
The intracellular medium of cells is a viscous region. Small size renders nanoparticles highly mobile, a necessary requirement for fast diffusion in the cytosol. Additionally, for biomolecule tracking, the fluorescent probe must have a tiny size in comparison to the stained biomolecule, so that it does not influence its motion.
- *High brightness.*
The cytoplasm contains a lot of components that present autofluorescence. The signal-to-background ratio of the fluorescent nanoprobe should be high.
- *Possibility of functionalization.*
For all kinds of applications, a well defined surface function is desirable. It can be

used to chemically couple the nanoparticle to the biomolecule of interest.

- *Biocompatibility.*

The fluorescent probes should of course be non-toxic for the cell and/or the organism.

In the following section we summarize the different methods of nanodiamonds synthesis. We describe the procedure of NV center creation in the diamond matrix and the way to obtain strongly Photoluminescent and small size NanoDiamonds (PNDs). After the photoluminescence activation, the nanoparticles are acid treated, to obtain acid functions on their surface and form stable colloidal suspensions in water. We optimise the NV center creation to increase PND brightness (section 1.4). The biocompatibility issue will be discussed in chapter 5.

2.1.1 Diamond synthesis and nanodiamonds production

Diamond, from the greek word “ $\alpha\text{-}\delta\alpha\mu\alpha\varsigma$ ” (a-damas, meaning unbeatable, because of its robustness) is a material with a vast range of applications, due to its hardness, electrical and thermal conductivity properties. It exists under natural and synthetic form. For the majority of the applications synthetic diamond is used ($\sim 75\%$ of diamond used is synthetic).

There exist three different ways of creating synthetic diamond, and in particular diamond nanoparticles. Figure 2.1 is a summary of the most common synthesis methods.

I. The most widely used method for diamond synthesis is the **High Temperature High Pressure, (HPHT)** method. It involves large presses that produce high pressures (~ 6 GPa) at high temperatures ($\sim 1500^\circ\text{C}$). Graphite and metallic catalysts are placed in hydraulic presses. Under high temperatures and pressures conditions over the period of a few hours the graphite is converted into diamond. For nanodiamond production, the micrometer sized faceted crystals ($100\text{-}200\ \mu\text{m}$) coming out of the press (Figure 2.3a) are milled, purified and graded, to obtain nano-sized powders. A way to avoid the use of catalysts, that contaminate the sample, is to synthesize diamond starting from exotic precursor materials such as fullerenes [81] as well as carbon nanotubes [82].

Another way to produce diamond nanoparticles under high pressure high temperature conditions is by using explosives (see section 1.5).

II. An alternative method for nanodiamond formation includes **direct transformation of carbon solids into nanodiamond**. Recent experiments have shown that heavy ion or electron irradiation ($1.2\ \text{MeV}$, doses $> 10^{24}\ \text{e}^-/\text{cm}^2$, $100\ \text{dPa}$) successfully convert the cores of concentric-shell graphitic nanoparticles into nanometer-size diamonds at temperatures above $900\ \text{K}$ [83, 84]. Other carbon materials can also be transformed into nanodiamonds by laser pulses, electron, or ion beams. Nanodiamond particles have been synthesized from fine particles of carbon black exposed to intense laser irradiation [85] or from carbon nanotubes [86]. Very recently luminescence of nanodiamonds produced by this method was reported as well [87].

III. Another method to produce diamond, uses low pressure and moderate tempera-

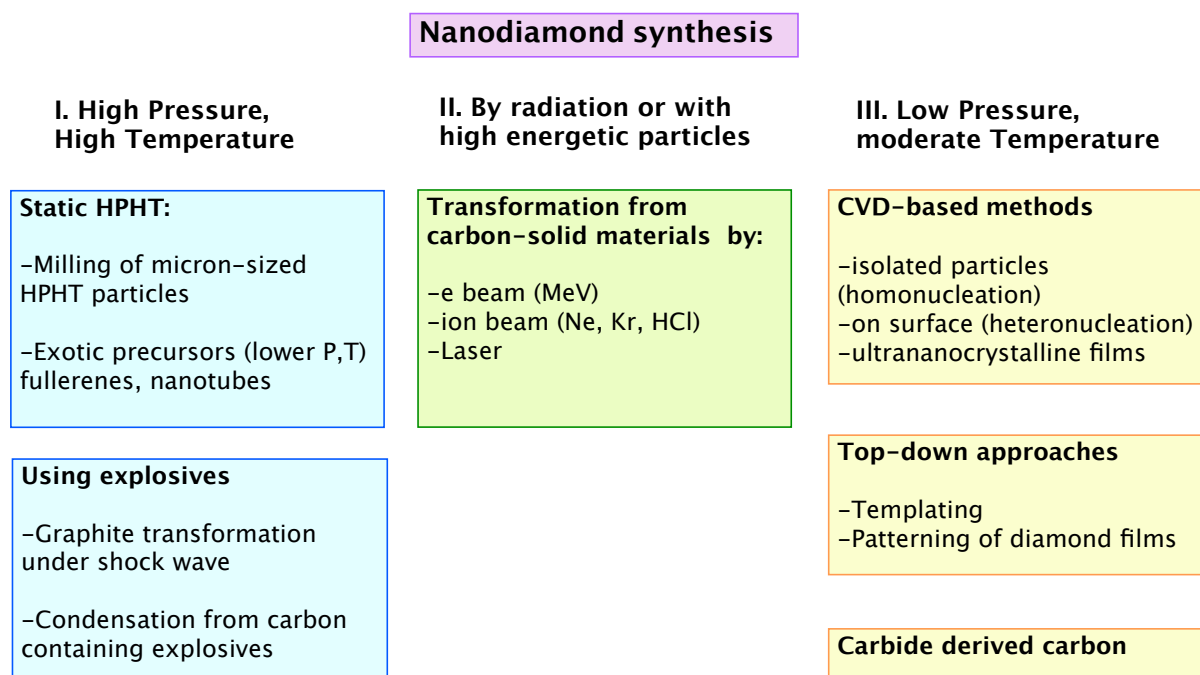


Figure 2.1: Summary of the different methods to produce diamond nanoparticles, adapted from [65].

ture conditions. The most common way is by **Chemical Vapor Deposition, (CVD)**. In a microwave plasma reactor, containing a CH_4 and H_2 mixture, diamond is grown on substrates. This method allows a fine control of the crystal formation, like the amount of chemical impurities in diamond. The production of very thin nanometer sized films is also possible [88].

In all our studies requiring photoluminescence we used HPHT diamond. We either used already milled and nanometer size particles, in which we subsequently created color centers, or color centers were created in micron size HPHT diamond crystals, which were then milled and grinded to obtain photoluminescent nanoparticles.

2.1.2 Creation of NV centers in diamond

Nitrogen is one of the most common impurities in the diamond matrix. Diamond classification is based on its nitrogen content and its optical absorption as follows [31]:

Type I

In type I diamond the paramagnetism and optical absorption is due to the nitrogen impurities. This type is divided in two categories, denoted type Ia and type Ib. In type Ia nitrogen forms clusters and the optical absorption of diamond is not due to an individual nitrogen atom. Most of the natural diamond belongs to this type. In type Ib diamond (i.e. most of the synthetic diamonds) the nitrogen atoms are positioned in substitutional sites. It is the category of diamond that we use in our experiments.

Type II

In this category the nitrogen concentration in diamond is very low ($<10^{20}$ atoms/cm³). It is divided in two sub-categories, the type IIa and IIb. The first one is the purest diamond, colorless and free from all impurities, while the second one contains high quantities of boron atoms, which give to diamond some semi-conductor properties.

a Some theoretical elements on NV creation

Creation of NV centers in diamond crystals can be achieved by two ways:

i) with **radiation damage** from various particle sources (electron, neutrons, ions) and subsequent annealing of type Ib diamond.

ii) with **direct implantation** of nitrogen in pure (type IIa) diamond and subsequent annealing.

For biological applications a high density of NV centers per nanoparticle is desired, so the first method is preferred. On the contrary, for quantum applications and isolated qubits in diamond, low density of NV centers is the ideal option, thus the latter technique is more adequate.

In our case, active NV centers were created in nitrogen-rich type Ib diamond crystal by a two-step procedure, involving the generation of vacancies by electron or proton beams followed by thermal annealing of vacancy defects at temperatures $>600^{\circ}\text{C}$.

Irradiation

As a charged particle passes through matter, part of the particle kinetic energy can be transferred by collisions to the material nuclei and to excited electronic orbitals. An elastic collision can remove an atom from its normal lattice position. The ejected atom is known as a primary knock-on, which may cause a cascade of atomic displacements before eventually losing its kinetic energy and stop moving. The knock-on effect is significant when the incident particle is heavy (proton or alpha particle) or has a high energy (a few MeV for electrons), energy higher than the displacement energy of the atoms. Figure 2.2 illustrates the creation of a vacancy consecutive to the collision of a charged particle with an atom. The displaced atom ends up in an interstitial position.

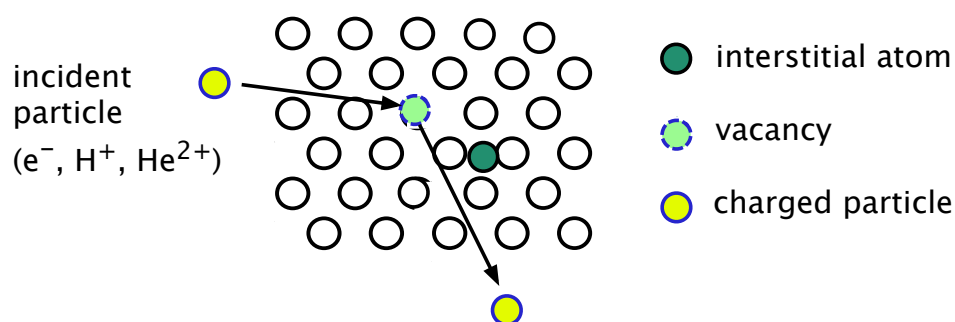


Figure 2.2: Atom displacement due to collision with a high energy charged particle and creation of a vacancy.

Single defects (vacancies, interstitials, dislocations) are produced along the trajectories of the particles and form clusters at the end of the particle trajectory, where they deposit most of their energy.

Depending on the particle type and its energy, the defect creation efficiency varies. SRIM Monte Carlo simulations¹ allow the exact calculation of the penetration depth of the particles and the number of vacancies created along their track, taking into account the amount of displaced atoms.

For NV creation in the diamond lattice, neutrons [45], alpha particles [47, 89], protons [47, 48] or electrons [33, 46, 90] have been used. In our experiments we used proton and electron irradiation.

Annealing

A subsequent thermal annealing of vacancy defects at temperatures $>600^{\circ}\text{C}$ is necessary for NV creation. At such temperatures the vacancies start migrating and are stabilized in the adjunct site of the nearest substitutional nitrogen atom. This position is the most favorable one, thermodynamically speaking [91, 92].

The optimal value of temperature and timing of the annealing process are still open questions. Annealing at too high temperatures may graphitize diamond.

Both vacancies and interstitials are mobile at sufficiently high temperature and annealing facilitates their recombination. At high temperatures, the vibration of the atoms in the lattice increases, thereby providing a mechanism by which an interstitial atom (carbon or nitrogen) can migrate to a vacancy and fix the defect. For NV creation, recombination effects should be avoided and a single substitutional nitrogen atom should be positioned next to a vacancy.

b Experimental results

In our experiments we used both proton and electron irradiation. For electron irradiation, we irradiated and annealed diamond microcrystals, which were then transformed to nanoparticles by milling and grinding processes. This is what we will call **type M** (obtained from Microdiamonds) nanodiamonds. **Type N** nanodiamonds consist of nanoparticles already provided in nanometer sizes, which were irradiated by protons and annealed.

Type M photoluminescent diamond microcrystals

The starting material was type Ib diamond synthetic micron size powder (PDA999, Element Six, Netherlands) with a specified size of 150-200 μm . NV centers were created by electron irradiation. The electron beam energy was 2 or 8 MeV and we tried different irradiation doses, in the range of $2 \times 10^{17}\text{e}^-/\text{cm}^2$ to $2 \times 10^{19}\text{e}^-/\text{cm}^2$ (at *Herotron Technologies GmbH*, Germany, or at *Ionmed*, Spain).

Annealing of the samples was carried out at 800°C under vacuum ($\sim 10^{-8}$ Torr) during 2 hours. As seen in Figure 2.3a by bright field illumination in a fluorescence microscope, the color of the microcrystals changes, due to the different optical absorption after the vacancy creation and migration.

A nice illustration of the NV creation in diamond microcrystals is depicted on Figure 2.3b. Here the microdiamonds are excited in the range of 500-550 nm (filtered from a halogen high power white lamp) in a standard fluorescence microscope. We observe

¹Stopping and Range of Ions in Matter - SRIM software is available from the website, <http://www.srim.org/>

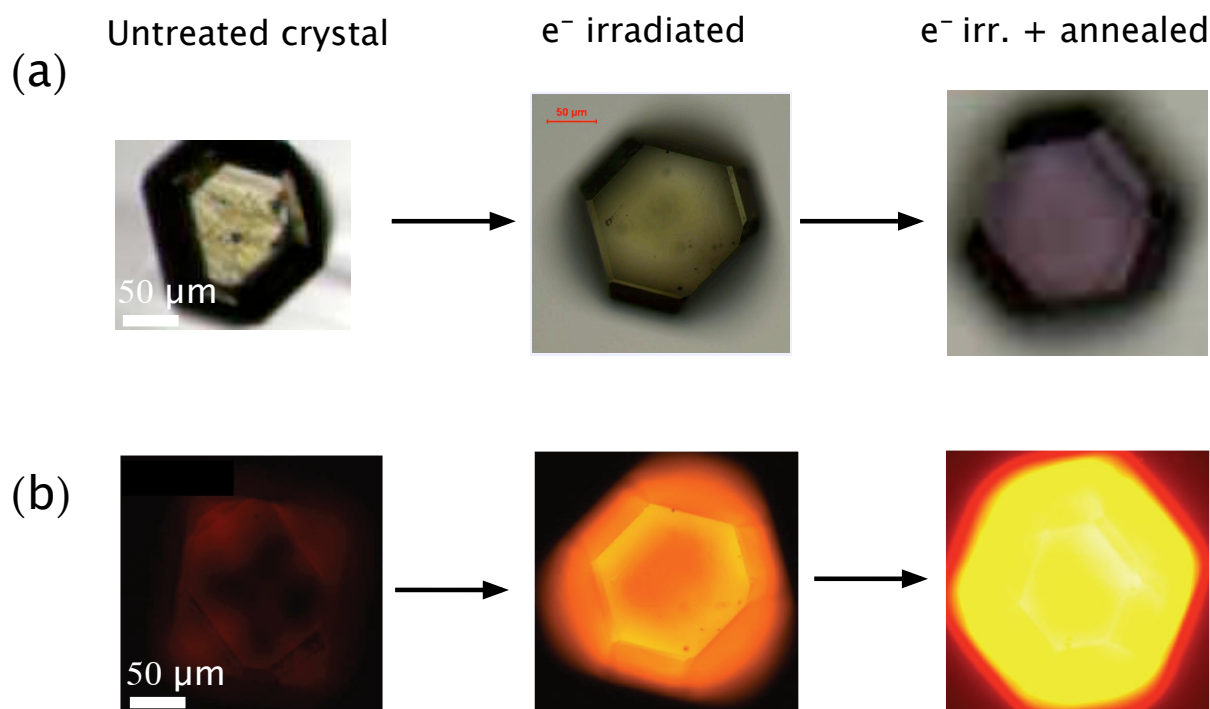


Figure 2.3: NV center creation process in type Ib diamond microcrystals. (a) Bright field observations in transmission recorded on a CCD array of single $\sim 150 \mu\text{m}$ diamond crystals. From left to right: untreated (non-irradiated) crystal under white light illumination (slight yellow color due to high concentration in nitrogen), electron irradiated crystal at a dose $2 \times 10^{18} \text{e}^-/\text{cm}^2$ at 8 MeV (green color, due to the high vacancy concentration), annealed for 2 h at 800°C after the electron irradiation (pink color due to the migration of vacancies near nitrogen atoms). (b) Photoluminescence image of the same type of microcrystals as in (a). From left to right the same conditions as in (a); for the annealed crystal after irradiation the image is saturated; excitation and collection wavelengths for the photoluminescence image are respectively 500-550 and 600-700 nm. CCD exposure time is 1.5 s.

the fluorescence signal in the wavelength range 600-700 nm (used Texas Red filter). An almost zero signal is recorded for non-irradiated diamond crystals, while with irradiation and subsequent annealing the photoluminescence intensity increases drastically.

For biological applications one should use stable fluorescent probes. We tested the photostability of the crystals, before and after the annealing process. While before annealing the photoluminescence vanishes after some hours of illumination, after annealing the crystals are perfectly photostable under more than six hours of illumination (Figure 2.4).

Type N photoluminescent diamond nanocrystals

For the type N diamond crystals, the starting material was synthetic type Ib diamond powder (SYP 0-0.05, Van Moppes, Geneva) with a specified size smaller than 50 nm. NDs were rendered photoluminescent by proton irradiation and subsequent annealing.

The proton irradiation doses were either $5 \times 10^{15} \text{H}^+/\text{cm}^2$ or $5 \times 10^{16} \text{H}^+/\text{cm}^2$, with

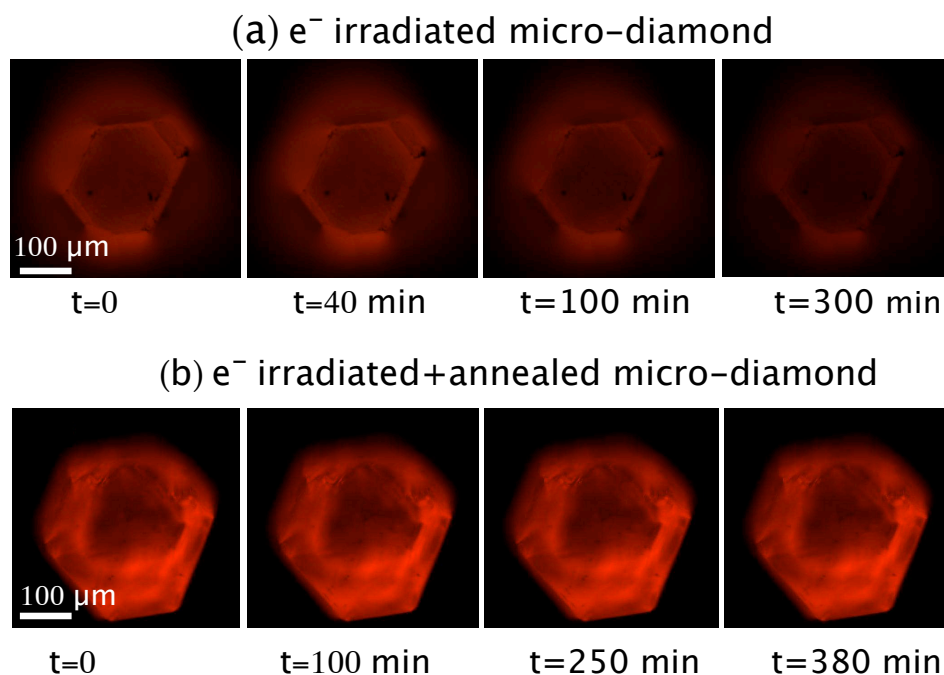


Figure 2.4: Photoluminescence intensity over time for a diamond microcrystal. (a) The crystal was irradiated but not annealed ($2 \times 10^{18} e^- / \text{cm}^2$, energy 8 MeV). (b) The crystal was irradiated and annealed (2 h at 800°C). It presents a perfect photostability for more than 6 h of illumination. Excitation wavelength 500-550 nm, exposure time 5 ms.

a proton energy of 2.4 MeV. In the sample plane the proton beam had dimensions of $10 \times 10 \text{ mm}^2$. We prepared diamond thin films deposited on Si wafers. As the penetration depth for protons of 2.4 MeV is $35 \mu\text{m}$ (calculated by SRIM simulations), we sought to have an homogeneous vacancy creation in the diamond film, i.e. creation of a diamond film with thickness $< 35 \mu\text{m}$. We put a drop of nanodiamond aqueous solution (SYP 0-0.05-GAF, concentration 81 carats/kg²) on the square wafer and put it for ~ 3 hours in an oven at 75°C , so that the water of the solution evaporates. After this time, a dense diamond film was formed. The thickness of the film was $15\text{-}30 \mu\text{m}$, verified by stylus surface profiler (DekTak, Veeco).

The irradiations were realized at the proton Van de Graaff accelerator of CEMHTI Laboratory (Laboratoire des Conditions Extrêmes et Matériaux : Haute Température et Irradiation, UPR CNRS 3079) in Orleans (France), under the supervision of Dr. Thierry Sauvage. For each dose and each square wafer the irradiation lasted for 86 min.

Annealing of the samples was carried out by Dr. Jean-Paul Boudou, at “Université Pierre et Marie Curie”, Paris. After scratching the substrates with a razor to collect the diamond irradiated powder, the powder was placed in a 1/4 inch quartz tube. The tube was placed in an oven (electrical resistance type), with a Helium + 5% hydrogen flow. The annealing lasted for 2 hours, at 750°C .

For the following applications of photoluminescent NDs, they had to be dispersed in water solutions.

²Since 1907, 1 carat equals to 200 mg (i.e. the approximate weight of 1 carob tree seed or 4 wheat grains).

2.1.3 Preparation of colloidal suspensions

Type M diamond nanocrystals

Diamond photoluminescent microcrystals (8 MeV , $2 \times 10^{18} \text{ e}^- \text{ cm}^{-2}$) were reduced in size by nitrogen jet milling to obtain submicron crystals (Hosokawa - Alpine, Germany). This work was carried out by Dr. Jean-Paul Boudou. The following process is similar to the method described in Ref. [90], with some small differences.

After nitrogen jet milling, further size reduction to nanoparticles was achieved using a planetary ball mill under argon with hard alloy WC (tungsten carbide) + 6% Cobalt bowls and 10 mm balls made with the same WC-Co cemented carbide (Vario-Planetary Mill, Fritsch, Germany). After the 24 h effective grinding time, the milled powder was sieved and treated with strong acids (hydrofluoric and nitric acid mixture 2:1 v/v for 24 h, at 80°C , under strong sonication), in order to remove the contaminations of the tungsten-carbide beads. An excess of Milli-Q ultrapure water (resistivity $18.2 \text{ M}\Omega \text{ cm}$, at 25°C) was added to the sample, which was then centrifuged at 4000g, for 30 min. The strongly acid supernatant was discarded, the pellet was suspended in ultrapure water and the suspension was neutralized, with addition of aqueous ammonia solution. The solution, with a pH 7, contained nanoparticles, mostly in form of aggregates. Dynamic Light Scattering (DLS) measurements (apparatus: *BI-200M*, Brookhaven Instruments Corp., USA) showed the majority of nanoparticles with a mean size at 164 nm ³ with a distribution width of $\pm 32 \text{ nm}$, but with a very small population around 26 nm (Figure 2.5a-(i)). As examined closer by Atomic Force Microscopy (AFM, apparatus: *Nanoscope IIIa*, Veeco Instruments Inc., USA) and High Resolution Transmission Electron Microscopy (HR-TEM, apparatus: *Tecnai F20*, operating at 200 keV) nanodiamonds of primary size 5-50 nm are aggregated in clusters of 150-200 nm (Figure 2.5b). We will call this solution *Aq164nm-Me18*⁴.

The solution was further centrifuged (4000g, 30 min) and the supernatant was collected. Further centrifugation (5000g, 15 min) and sonication (ultrasonic bath, 30 min) gave a solution of smaller nanoparticles. As observed by DLS (Figure 2.5a-(ii)) there are also two populations in the solution, one with mean size at 45 nm (with size distribution $\pm 14 \text{ nm}$) and the other with size around 204 nm (and size distribution $\pm 43 \text{ nm}$). In comparison to solution *Aq164nm-Me18* (Figure 2.5a-(i)), now the signal from the population of the smaller PNDs is stronger. DLS measurements of the same sample with a device that allows Mie scattering correction⁵ showed that the nanodiamonds have a mean size of 46 nm (DLS apparatus: *DL135* particle size analyzer from Cordouan Technologies, France). Thus we will refer to this sample as *Aq46nm-Me18*. AFM microscopy reveals the large size dispersion of this type of PNDs. A remarkable proportion of PNDs has

³DLS devices calculate the hydrodynamic radius R_H , which is the effective radius of a diffusing particle, calculated by the Stokes-Einstein relation, $D = kT/6\pi\eta R_H$, where D the diffusion coefficient of the particle, T the temperature, η the dynamic viscosity of the medium.

⁴*Aq164nm-Me18* stands for: Aq: Aqueous solution
164nm: mean diameter
M: type of diamond (Microcrystals the irradiated material)
e: electron irradiation

18: irradiation dose $2 \times 10^{18} \text{ e}^- \text{ cm}^{-2}$

⁵The “inconvenience” of Mie scattering is that big particles cover the scattered signal of the smaller ones.

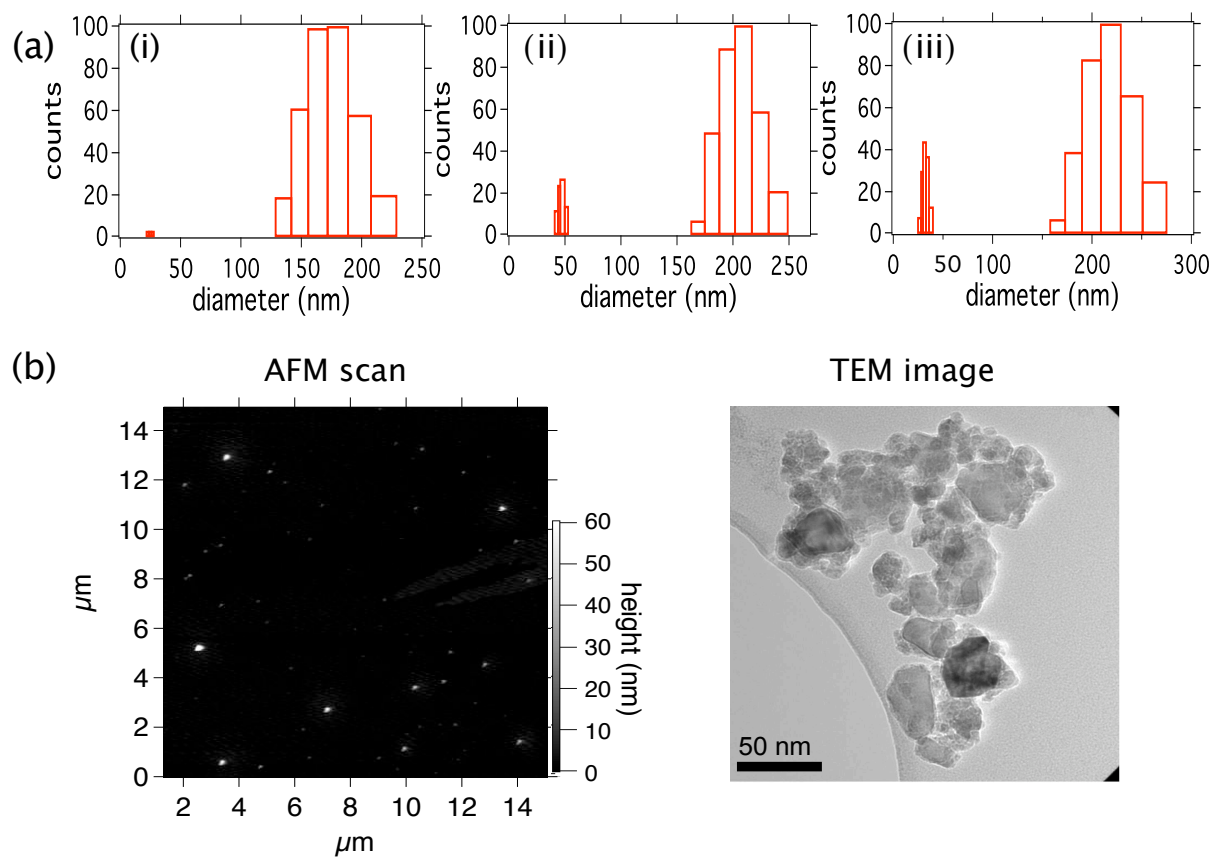


Figure 2.5: Size and photoluminescence characterization of type M nanodiamonds. (a) DLS measurements of (i) the initial solution of PNDs (just after the neutralization process), with a dominant population at 164 nm, sample *Aq164nm-Me18*; (ii) solution of PNDs which is the supernatant of successive centrifugations of (i), solution *Aq46nm-Me18*; (iii) supernatant of an aliquot of (ii) which is further centrifuged, sample *Aq29nm-Me18*. (b) AFM scan and TEM image of PNDs of *Aq164nm-Me18* solution, the AFM image is saturated to make smaller PNDs distinguishable, maximum height observed on this scan is 178 nm, the sample is spin coated on a glass substrate. For TEM experiments a droplet of the aqueous suspension *Aq164nm-Me18* was initially dried on a carbon grid.

sizes <15nm (Figure 2.8a).

The zeta potential of the *Aq46nm-Me18* was measured at -43 mV (Zetasizer Nano ZS, Malvern), highly negative, ensuring the stability of the solution⁶. Mass spectroscopy measurements reveal the functional groups on the PNDs surface (Figure 2.7a), an issue that we will discuss in more detail in the following.

After further centrifugation (6000g, 15 min) and subsequent strong ultra-sonication (15 min, with a sonotrode in the PNDs solution, 27% of 750 W total power) of an aliquot of the *Aq46nm-Me18* solution, we obtained a suspension with even smaller PNDs, of mean size 29 nm, named as the *Aq29nm-Me18* sample (Figure 2.5a-(iii)).

⁶The zeta potential characterizes the overall particle surface charge and indicates its colloidal stability. It is defined as the potential difference between the dispersion medium and the stationary layer of fluid attached to the dispersed particle.

For biological applications, we will use the *Aq46nm-Me18* sample.

Type N diamond nanocrystals

Deagglomeration of type N diamond nanocrystals was achieved by hydrolysis of the sample in a 50/50 mixture of $\text{HNO}_3:\text{H}_2\text{SO}_4$, after their irradiation+annealing process [16, 51, 71]. The solution was put in a Teflon autoclave in a ultrasonic bath (25 kHz, 300 W, working at 80% of its total power) under a temperature of 80°C for 24 h.

After the 24 h acid treatment time, we passed the solution of diamond crystals mixed with acids through a filter (3 μm pore diameter), to get rid of the majority of the acids. Most of the particles, which were aggregated, were blocked on the pores of the filter.

The following of the dispersion process in water consisted of three consecutive washings with pure water (Milli-Q) each one followed by a centrifugation (20,000g, 15 min) and selection of the pellet, to get rid of the acids. Finally, the solution was ultra-sonicated by a sonotrode placed in the solution (working at 20% of its total 750 W power) for one hour.

The solution remained stable for months. The zeta potential of the suspension in aqueous solution was measured at -41.3 mV (Zetasizer Nano ZS, Malvern). This value is negative enough to ensure the stability of the solution.

The mean size of the solution is 35 ± 8 nm (measured by DLS, apparatus: *BI-200M*, Brookhaven Instruments Corp., USA) (Figure 2.6a). A TEM image of the initial non-irradiated solution SYP0.05 shows the shapes and sizes of the nanodiamonds (Figure 2.6b). In contrast to type M PNDs, here the nanoparticles have edge shapes, due to their different production method. With AFM measurements we characterize the mean size of PNDs by spin-coating a ≈ 100 ml (3,000 rounds/min, initial acceleration 200 g, during 30 s).

The AFM observations (apparatus: *Nanoscope IIIa*, Veeco Instruments Inc., USA) give a mean size of 23 ± 9 nm for ~ 60 nanoparticles (Figure 2.10a). The discrepancy of the AFM and DLS measurements is mainly due to the fact that PNDs have angular shapes and DLS calculates the hydrodynamic radius, considering the particles spherical,

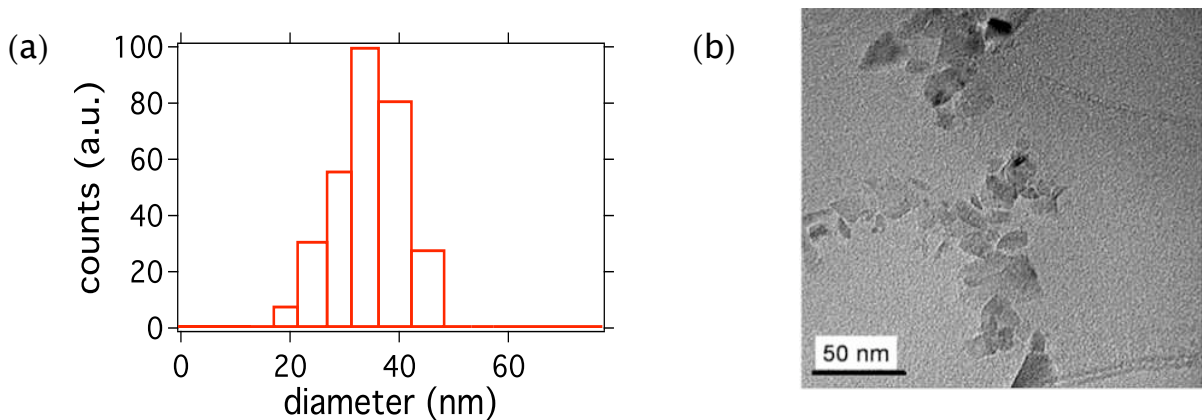


Figure 2.6: Size and shape characterization of type N PNDs. (a) Dynamic Light Scattering measurement of *Aq30nm-Np16*; (b) TEM image of type N PNDs, deposited on a carbon grid.

which is not the case for this type of PNDs. Moreover, the smallest particles (10-15 nm) observed by AFM are not observed by DLS, due to their low scattering efficiency. By taking into account both AFM and DLS measurements we infer a mean value of 30 nm (hence *Aq30nm-Np16* sample ⁷). For the 10 times lower irradiation dose PND solution (i.e. dose $5 \times 10^{15} \text{ H}^+/\text{cm}^2$) the size distribution is similar, centered at 30 nm (sample *Aq30nm-Np15*).

Measurements by temperature-programmed desorption mass spectrometry (carried out by Jean-Paul Boudou, for details on the experimental procedure look at Ref. [90]) revealed an important concentration of carboxylic groups on the diamond surface.

In comparison with type M nanodiamonds, the surface of type N PNDs contains more functional groups, as seen on Figure 2.7. Type M nanodiamonds seem to contain a few carboxyl groups. Indeed, previous studies report a percentage of 7% of carboxylic groups after similar oxidative acid treatment of nanodiamonds [93]. In those cases NDs present high affinity for proteins. The quantity of COO^- is sufficient for further conjugation (covalent or non-covalent) with other chemical moieties.

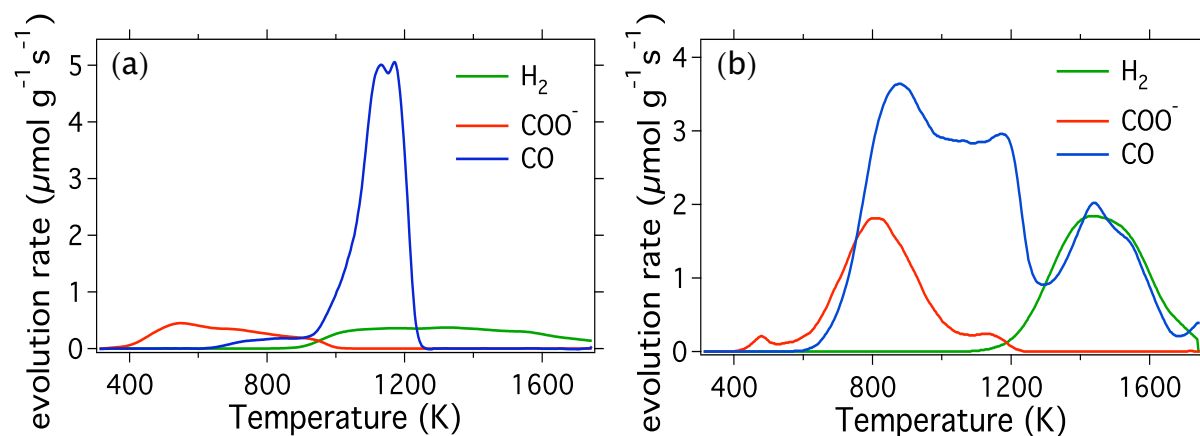


Figure 2.7: Thermal desorption profiles of H₂, COO⁻ and CO for (a) type M nanodiamonds and (b) type N nanodiamonds.

⁷*Aq30nm-Np16* stands for an Aqueous solution, 30nm mean diameter, N type diamond (Nanocrystal irradiated material), proton irradiated, dose $5 \times 10^{16} \text{ H}^+/\text{cm}^2$.

Table 2.1 illustrates the produced PND solutions.

solution name	diameter (nm)	irradiated material	shape	irradiation dose	ζ -potential (mV)
<i>Aq164nm-Me18</i>	164	Microcrystals	round edges	$2 \times 10^{18} \text{ e}^-/\text{cm}^2$	–
<i>Aq46nm-Me18</i>	46	Microcrystals	round edges	$2 \times 10^{18} \text{ e}^-/\text{cm}^2$	-43
<i>Aq29nm-Me18</i>	29	Microcrystals	round edges	$2 \times 10^{18} \text{ e}^-/\text{cm}^2$	–
<i>Aq30nm-Np15</i>	30	Nanocrystals	angular edges	$5 \times 10^{15} \text{ H}^+/\text{cm}^2$	–
<i>Aq30nm-Np16</i>	30	Nanocrystals	angular edges	$5 \times 10^{16} \text{ H}^+/\text{cm}^2$	-41.3

Table 2.1: Types of PNDs used. The dash “–” at the ζ -potential row means that the potential was not measured.

2.1.4 Photoluminescence studies of nanodiamonds

Type M nanodiamonds

A home-built confocal microscope similar to the one described in the following section was coupled with an Atomic Force Microscope (AFM, *MFP-3D* Asylum Research) to correlate the size to photoluminescence signal. A droplet of the PND aqueous suspension was deposited by spin-coating on a glass coverslip which was then simultaneously imaged in both AFM and photoluminescence modes (Figure 2.8). Among 200 nanodiamonds identified on the AFM scan, 115 display some photoluminescence signal, i.e. about 58% of the NDs are photoluminescent. Among the photoluminescent nanoparticles a fraction consists of 10-15 nm diameter PNDs, but the majority of the PNDs appears as nano-objects of size 40-50 nm.

Type N nanodiamonds

Figure 2.9 shows a photo of a solution of nanodiamonds (*Aq30nm-Np16*) excited by a 532 nm laser. Without filter we observe the diffusion of the laser beam in the solution (demonstrating that the solution is diffusive and contains nanoparticles). With a longpass filter, $\lambda > 580 \text{ nm}$ (*HQ580LP*, Chroma) in front of the camera we cut selectively the green excitation color, and the red photoluminescence is revealed.

By the home-built confocal setup we ensure that the sample studied by the AFM contains photoluminescent nanodiamonds (Figure 2.10). This time the confocal system was not coupled with the AFM, as for type M nanodiamonds characterization.

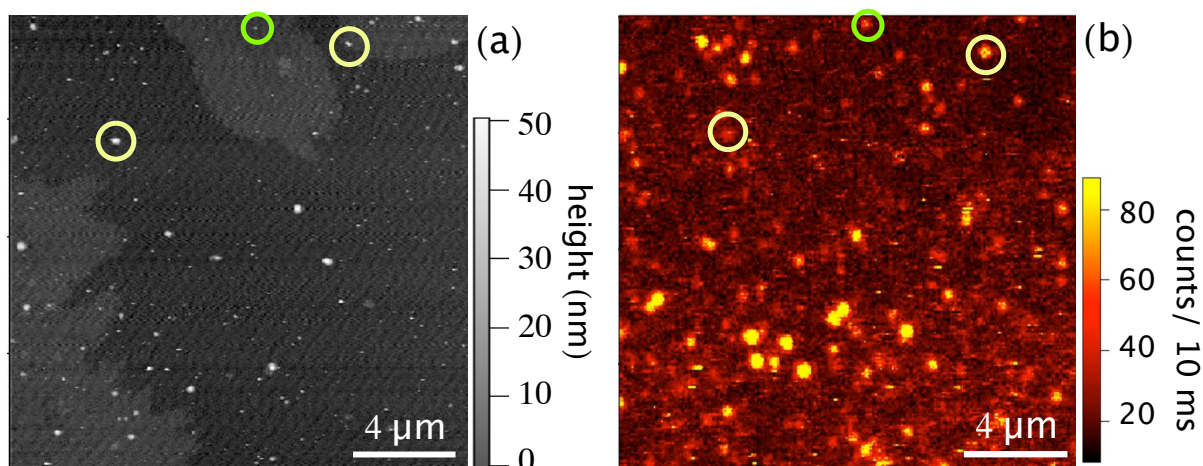


Figure 2.8: Simultaneous size and photoluminescence characterization of type M nanodiamonds. (a) AFM scan of *Aq46nm-Me18* sample spin-coated on a glass coverslip. (b) Confocal raster-scan of (a). Excitation at 532 nm, under 200 μW. The photoluminescence intensity scale bar maximum is set to 90 counts/10 ms, enabling the observation of the less intense PNDs (the brightest spot yields 367 counts/10 ms). Two PNDs with 40 nm height are in yellow circles, while a single 12 nm PND is in green, displaying still an intense photoluminescence signal.

According to measurements carried out by Near Field Optical Microscopy by the team of Serge Huant, of Institut Néel in Grenoble, we found that for this type of PNDs and for the *Aq30nm-Np15* sample, approximately 30% of the particles are photoluminescent [16]. By AFM coupled to confocal microscope measurements on the *Aq30nm-Np16* sample this proportion was increased, and reached ~50%. This indicates that the proportion of NDs that are rendered photoluminescent depends highly on the sample preparation conditions (e.g. thickness of diamond film on Si wafer for irradiation process). For the first case we observed that the measured thickness of the diamond film was very irregular

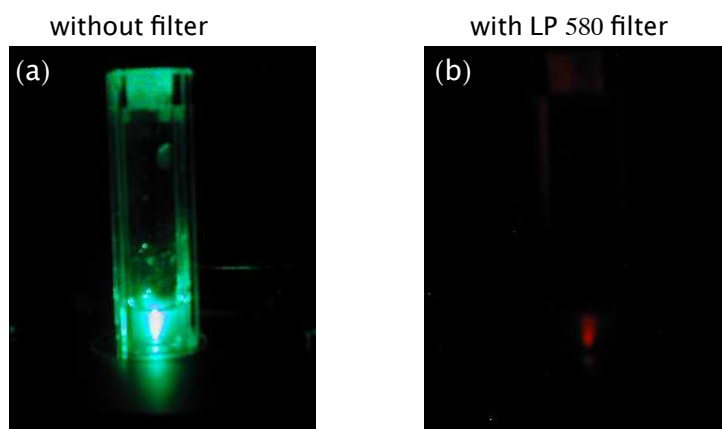


Figure 2.9: Photoluminescence of PNDs (*Aq30nm-Np16*) dispersed in aqueous solution. (a) Without filter and (b) with a longpass ($\lambda > 580$ nm) filter to cut the excitation laser. The red photoluminescence signal of nanodiamonds is observed.

and sometimes superior to the proton penetration depth, while in the second case the thickness was more homogeneous and in the limits of the proton penetration depth of $35\ \mu\text{m}$.

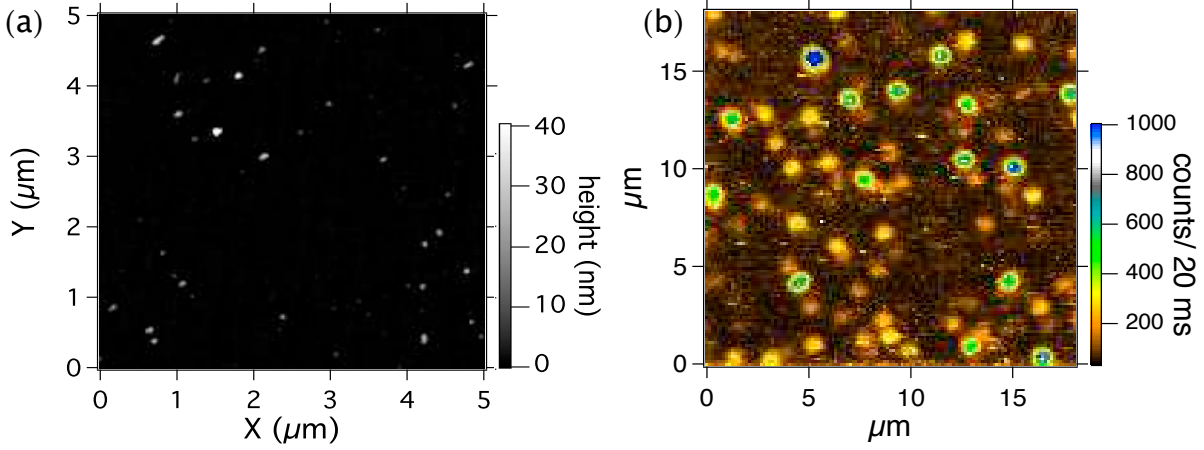


Figure 2.10: Size and photoluminescence characterization of 30 nm type N PNDs. (a) AFM scan of Aq30nm–Np16 solution, spin-coated on a glass coverslip. (b) Confocal raster-scan of the same sample as in (a), excitation at 532 nm, power 0.5 mW.

2.1.5 Discussion

We have herein described the two different processes that we applied to obtain nanometer size photoluminescent diamond nanoparticles. Each method presents some advantages and drawbacks as well.

Regarding the irradiation method, high energy electrons can penetrate deep in matter (some mm), creating homogeneously vacancies in a whole crystal or a few grams of powder. Electrons have a small mass (i.e. carry a low amount of momentum) and so have a low probability to knock out carbon atoms, resulting however in a deeper penetration depth in matter. For instance, electrons with energy 1.9 MeV at a dose of 2×10^{18} penetrate 2 mm in diamond and the efficiency is 10 electrons for the creation of one vacancy [91]. For our experiments we used 8 MeV electron energy, which penetrates even deeper in diamond (~ 25 mm). Additionally, the way electron irradiation is carried out (diamond in powder) allows irradiation of large quantities of diamond micro-(or nano) crystals.

Irradiation by protons on the other hand enables a more drastic creation of vacancies, due to their larger mass. As we will examine in detail in the following section, a 2.4 MeV proton beam can penetrate into $35\ \mu\text{m}$ depth, with an efficiency of one proton creating about 10 vacancies. Thus, protons are much more efficient in vacancy creation than electrons, of the same energy. However, the proton drawback is that the proton beam is focused on a small surface ($10\ \text{mm} \times 10\ \text{mm}$ in our case), so the irradiated sample occupies a rather small surface. Considering the small penetration depth, the irradiated diamond quantity is of the order of one mg per run, very small in comparison to the electron irradiation method.

Regarding the nanodiamond synthesis method, irradiating nanometer size powder is a fast (and cheap) solution. However, phase changes can occur during the grinding process, leading to partial amorphization, carbonization or burning of the diamond surface [94–96]. Additionally, the shape of the nanodiamonds produced is rather edged.

By producing photoluminescent nanodiamonds from irradiated and annealed microcrystals we obtain round shape nanocrystals. The round shape of the particles is still difficult to explain. One reason could be the starting material, which consists of uniform cubo-octahedral diamond microcrystals (*PDA999*, Element Six, highly crystalline synthetic diamond crystals, with a high impact strength and uniform particle shape). For commercial nanodiamonds production, the starting material is microdiamonds characterized by an irregular shape and structure, with many defects distributed in a heterogenous way in the crystals, an irregularity that probably remains until the nanometer size particles. Commercial methods use this kind of microdiamonds, because they are easy to be milled with steel beads, a process less expensive than with the WC beads.

For the production of nanometer size crystals, a vario-planetary ball milling is used [90, 97]. The particularity here (in comparison with the traditional commercial method) is that one can control the frictional and impact pressures of the grinding process and thus control the final size of the nanocrystals.

It has been observed that for this kind of PNDs, nanodiamonds of 12 nm size can contain up to 12 NV centers. Although it is probably a singular event, this is a relatively high concentration in NV centers, in comparison with the up to 3 NV centers per particle concentration for the other method of PND creation (see section 2.4).

It is reported that the probability of NV center creation in nanocrystals decreases when the particles have sizes < 50 nm because more vacancies are expected to anneal to the surface [98]. As the surface comes closer to the core of the nanoparticle, the probability of vacancies forming NV centers decreases with the square of the particle radius for particles < 10 nm (Figure 2.11). Thus, the NV formation yield is lower in small nanodiamonds compared to bulk diamond.

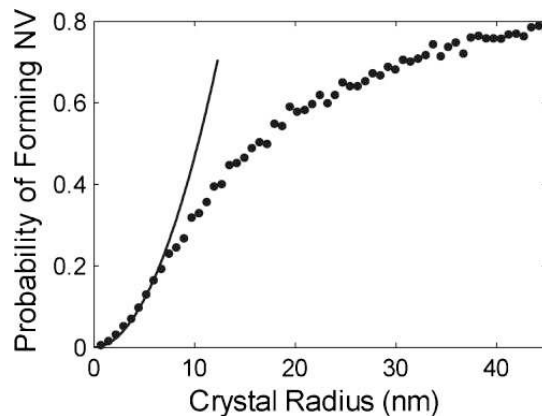


Figure 2.11: NV center creation dependence on the ND size. In circles the Monte Carlo simulation of the probability of vacancies forming NV centers in NDs with 300 ppm nitrogen concentration. The probability decreases with the square of the particle radius for $r < 10$ nm. The solid line is the fit of the probability $P = 4.8 \times 10^{-3} \text{ nm}^{-2} r^2$, extracted from [98].

2.2 Experimental setup

For the observation of the photoluminescence signal of single nanodiamonds, which are either deposited on glass coverslips or internalized in cells, we used a home-built confocal microscope. This microscope allows recording of optical cross section scans of PNDs in cells and hence we can reconstruct the three dimensional image. Moreover, this system coupled with an intensity autocorrelation Hanbury-Brown and Twiss setup, allows us to study and characterize the number of NV color centers in single nanodiamonds.

2.2.1 The confocal microscopy

Confocal microscopy was pioneered by Minsky in 1955 [99]. The confocal microscope incorporates the ideas of point-by-point illumination of the specimen and rejection of the out of focus light coming from the sample, e.g. fluorescence (look at Ref. [100] for a complete description of the principle). As seen on Figure 2.12 the sample is illuminated by a laser source. The excitation light reflects on a dichroic mirror, which directs it to the sample through a microscope objective. The fluorescence light emitted by the sample is collected by the same objective and focalized on a pinhole. The pinhole filters spatially the collected light, so that the recorded signal comes only from the focal plane of the objective, an effect referred to as optical sectioning. Out-of plane unfocused light is rejected, resulting in a sharper image, with highest signal-to-noise ratio. A detector placed after the pinhole records the incoming (e.g. fluorescence) signal.

The ability of a confocal microscope to create sharp optical sections makes it possible to build 3D images of the specimen, with the use of specific software.

It should be mentioned that confocal microscopy is a point-to-point technique. This means that the sample has to be scanned by the illumination laser beam point-per-point (actually pixel per pixel), to form at the end a 2-dimensional image. By that way the formation of a whole image takes more time than the classical wide field microscopy techniques (where the signal is recorded on a CCD array), but the axial resolution and the contrast are better.

2.2.2 The home-built confocal setup

For both three dimensional images of PNDs in cells and single emitter detection, a confocal setup was used. The experimental setup of the microscope system is illustrated on Figure 2.13.

The excitation laser for one photon fluorescence excitation is either a 532 nm cw laser (*Torus Laser*, Laser Quantum, UK) or a 488 nm cw laser (*Sapphire 488-50 LP*, Coherent Inc., USA), depending on the application. It is guided through a single mode optical fiber to the entrance of the microscope, which induces the additional advantage of spatial filtering. A beam expander ensures the increase of the beam diameter so that it covers the objective pupil.

An interferential filter (F) purifies spectrally the excitation light after its pass through the fiber. In the fiber non-linear effects can occur (Raman type), creating parasitic light, in the 560-590 wavelength range, increasing the background in the scans.

The excitation light passes through a half-wave plate and a polarizing beam-splitter

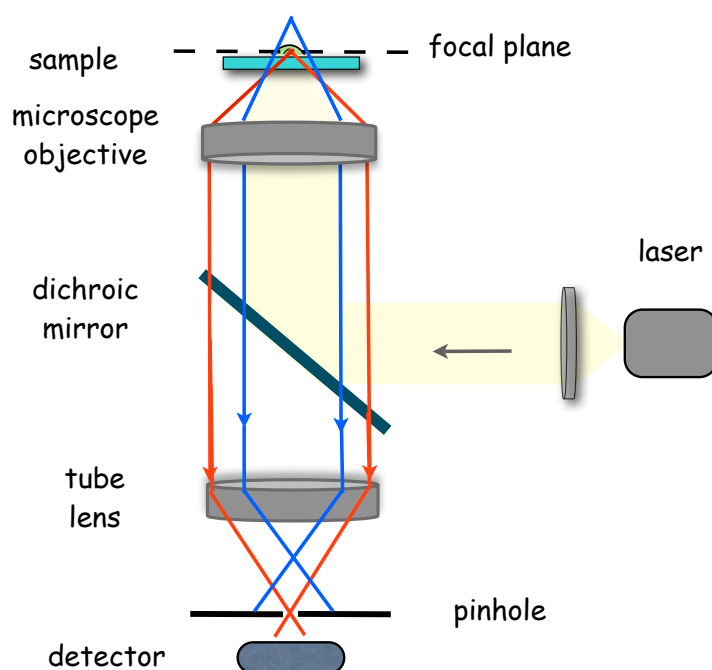


Figure 2.12: Schema of the confocal microscope principle. The microscope objective is inverted and corrected to infinity. The tube lens converges light to the pinhole, whose plane is conjugated with the microscope objective focal plane.

50/50, to adjust the laser power. The excitation laser beam is circularly polarized with a quarter-wave plate, so that its absorption efficiency by the fluorescent probe does not depend on the dipole orientation in the sample plane, which could have led to some artifact.

The home-built confocal microscope relies on a Nikon TE300 stand, equipped with a closed loop piezoelectric three-axis scanner stage (*Tritor 102*, Piezोजना, Germany). After its reflection on the dichroic mirror the excitation laser beam is focused by an oil immersion objective (Nikon Apochroma, $\times 60$, $NA=1.4$) onto the sample. To obtain a minimum excitation volume and a maximum signal collection, a microscope objective with a high numerical aperture is necessary. The fluorescence is collected by the same objective making a collimated beam; which then goes through the 200 mm focal length microscope lens tube (LT).

We modified the Nikon TE300 microscope in order to get a collimated beam at its output port. This modification consists in the addition of a diverging lens DL (focal length: -125 mm) after the lens tube turning the beam back into a collimated one, easier to handle. The collimated output beam is then focused by the L1 lens (100 mm focal length) into the pinhole (PH).

The residual excitation laser light is removed with the long-pass filter (LPF) having a transmission of 97% in the range of 539-1200 nm (*RazorEdge LP03-532RU-25*, Semrock, USA) for 532 nm excitation or a LPF filter with transmission of 97% in the range of 494-1100 nm (*RazorEdge LP02-514RU-25*, Semrock, USA) for 488 nm excitation.

To increase the imaging resolution we work with an oil-immersion objective. To decrease the background level, one has to use a special oil, with a low autofluorescence signal. The oil we use is Cargille (USA), with a refractive index 1.51.

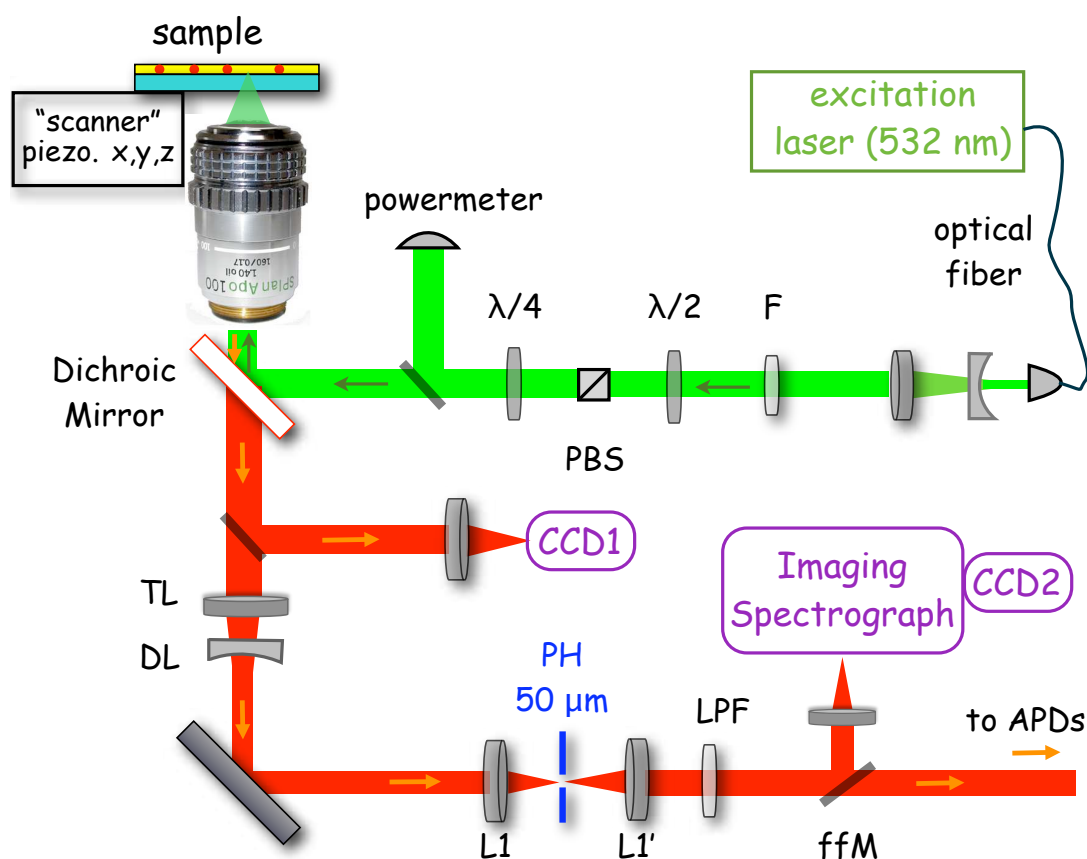


Figure 2.13: Experimental scheme of the confocal home-built microscope.

The photoluminescence spectrum is acquired with the addition of an imaging spectrograph (beam intercepted with a flip-flop Mirror (ffM)), simply relying on a concave grating (30% maximum efficiency in its first diffraction order) coupled to a cooled CCD array (CCD2, back-illuminated array *DU-420-BV*, Andor Technology, Ireland).

The image of the focal plane of the microscope objective is obtained via another CCD camera (CCD1). This CCD is used for wide (bright) field imaging of the sample (or for phase contrast images when imaging cells).

The phase contrast mode

For cells observations, bright field illumination cannot reveal many details of the cell morphology. Many objects are transparent to light, so there is no high contrast when they are observed by bright field illumination. However, due to their thickness and their different refractive index, they induce an optical path difference (i.e. phase difference) between the light passing through them and the source light. Our eyes or the cameras cannot detect these phase differences. Thus, if somehow one could transform this phase difference in intensity difference, we could observe more details of the sample.

The phase contrast technique is widely used to enhance the image contrast between the different cell components. It was introduced in the 1930s by Frits Zernike [101, 102]. Zernike introduced a phase plate in the form of a ring at the microscope back focal plane, which induces an additional $\lambda/4$ optical path to light passing through it. To ensure that

2.2 Experimental setup

only direct light (i.e. undeviated from the sample light) passes through the phase plate ring, a ring is placed before the microscope objective (in the focal plane of the condenser lens, Figure 2.14), conjugated with the objective back focal plane.

The deviated light passing through the sample will pass through the phase plate, but not through its phase ring, so no phase difference is induced. However, the deviated light has already a phase difference compared to the direct light (it is “behind” in phase for objects with higher refractive index), induced by the thickness and the refractive index difference of the sample. Thus, the phase difference between the two beams is enhanced leading to destructive interferences in the image plane of the eyepiece, improving the image contrast. If the interferences are destructive, the details of the image appear darker against a lighter background. The crucial point here for a maximum contrast is the exact positioning of the ring (condenser annulus) in relation to the phase plate position.

In our case, we had to make a custom phase contrast illuminating system. We designed a mounting tube in which we placed the ring annulus, at 10 cm above the condenser (x_1 on Figure 2.14). The condenser has a working distance of 52 cm. Light coming from a halogen lamp passes through the ring and illuminates the sample through the condenser. Light is collected by a special condenser microscope objective, containing a phase plate (NA 1.4, oil immersed, $\times 60$). A CCD camera conjugated to the focal plane of the objective records the image of the sample.

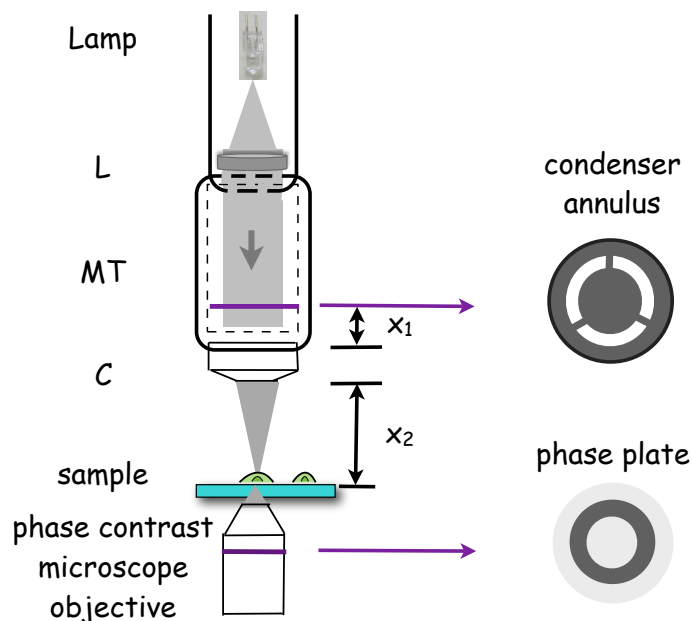


Figure 2.14: Experimental scheme of the phase contrast mode. Light coming from a halogen lamp is collimated by a lens (L) and passes through the condenser annulus placed 10 cm above the condenser lens (x_1). The condenser is placed 52 cm above the sample plane (x_2). The undeviated and diffracted light from the specimen are collected by the microscope objective. The undeviated light is ahead in path difference by $\lambda/4$ by a phase plate incorporated in the microscope objective.

2.2.3 The scanning setup

For point-to-point scanning of the samples, we are equipped with a closed loop piezoelectric three-axis stage (*Tritor 102*, Piezोजना, Germany). By applying a voltage between -30 and 120 V one achieves displacements up to 107 μm along the 3 axes. The maximum hysteresis for all axes is 12%. This means that there is a 12% positioning difference between an increasing applied voltage (-30 to 120 V) and a decreasing one. To minimize the hysteresis effect, a feedback system is used.

Through a PC and a Labview program, a PCI card interfaces a home-made electronic system controlling the counting of photons and the scanner driver (home-made too).

2.2.4 The intensity-time correlation measurement setup

To characterize the number of NV centers per nanodiamond, we used the *intensity-time correlation* measurement. It relies on the intensity-time correlation of the emitted signal, by measuring the normalized intensity $I(t)$ second order correlation function $g^{(2)}(\tau)$ defined by :

$$g^{(2)}(\tau) = \frac{\langle I(t) I(t + \tau) \rangle}{\langle I(t) \rangle^2} \quad (2.1)$$

The intensity correlation function gives the probability to detect a photon at the time τ , knowing that a photon is detected at $t = 0$. More details on this function can be found in Ref. [103, 104]. Briefly, in quantum physics, the emission of one photon by a single quantum emitter reduces the probability that another photon will be emitted immediately afterwards (particle nature of light). This is the so-called antibunching effect. Antibunched light behaves such as to have $g^{(2)}(0) < 1$.

For our measurements we used a typical Hanbury-Brown and Twiss setup, depicted on Figure 2.15 [105]. The *Hanbury-Brown and Twiss* intensity-time correlation setup consists of two avalanche photodiodes (2 APDs; *SPCM-AQR14*, Perkin-Elmer, Canada) in the single-photon counting mode. Their active surface has a 180 μm diameter and they have a very low dark count (<100 counts/s). They are placed on both sides of a non-polarizing 50/50 beam-splitter (BS) and are connected to a time-correlation electronics: a Time to Amplitude Converter (*Ortec Model 566*, Ametek Inc., USA) with its output linked to a multichannel analyzer (*Ortec 926-M32-USB*, Ametek Inc., USA).

A single photon source cannot emit two photons at a time. The setup records the time interval histogram between two consecutive detections, on the first and then on the second photodiode. After the emission of a first photon it takes a finite time for a single emitter to be excited again and then spontaneously emit a second photon. Thus in the normalized autocorrelation function $g^{(2)}(\tau)$ the antibunching effect appears as a dip around the zero delay $\tau = 0$.

This means that a photon cannot be detected simultaneously by the two detectors. The time lapse between 2 consecutive detections will be similar to the decay lifetime of the excited state of the emitter. The dead time for each photodiode is about 40 ns and the jitter due to the detector and the electronics is about 600 ps. By using one photodiode we are limited by the 40 ns dead time, so by using two photodiodes we are limited temporally at 600 ps, a time resolution much better than the decay lifetime of the NV center (>10 ns).

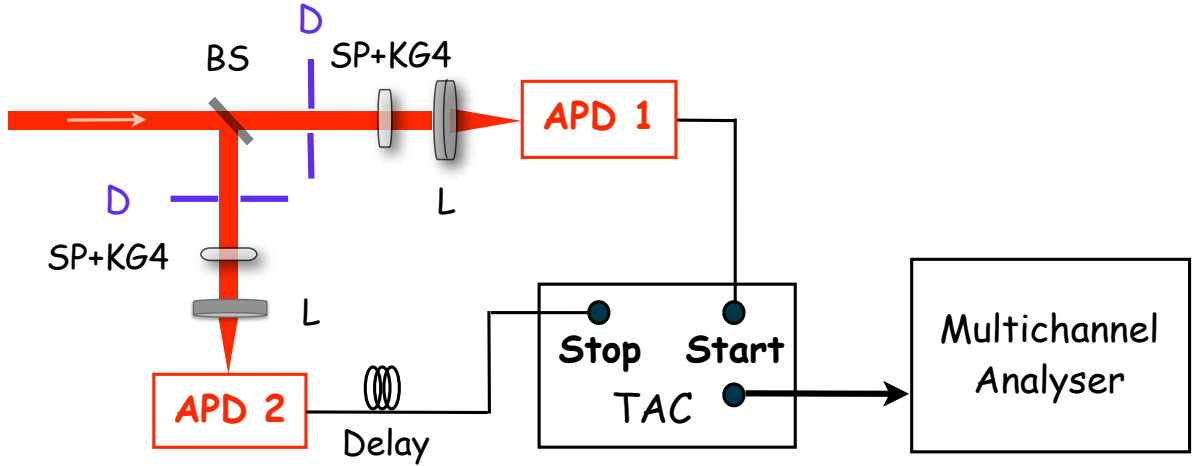


Figure 2.15: The Hanbury-Brown and Twiss setup used in our experiment. The fluorescence signal, after passing through the pinhole of the confocal setup (Figure 2.13) is divided by a non-polarizing 50/50 beam-splitter (BS) and directed towards the two avalanche photodiodes (APD). A diaphragm, a short-pass (SP) filter (Melles Griot *03SWP418*) and a KG4 glass filter suppressing IR light (about >800 nm) are used on the pathways for each photodiode to eliminate the optical cross-talk effect of the breakdown flash of the APDs [106]. Once the signal is detected by the APD1 connected to the Start of the TAC, it launches a voltage ramp. When the signal from the APD2 (Stop) is recorded, the TAC sends voltage, proportional to the time-delay value, to the MCA which yields the histogram of the time delay τ between two consecutively detected photons.

The signal from the avalanche photodiodes is distributed to the autocorrelation electronic setup and simultaneously to the counting system. More precisely, with the use of a signal splitter the signal coming from one APD is distributed to the Start input of the Time to Amplitude Converter (TAC) and to the photon counter. The latter counts the exact number of photons during the measurements duration, a necessary element for the proper normalization to unity of the intensity correlation function [32]. The detection of the signal on the Start input of the TAC device launches a voltage ramp, which is stopped when the second APD (connected to the Stop) detects a photon. The voltage value recorded by the TAC is proportional to the time interval between the two consecutive detections on the Start and Stop APD. The voltage values recorded by the TAC are stored in a multichannel analyzer (MCA) which in real time yields the histogram of the time delay τ between two consecutively detected photons. The acquisition window of the TAC can be adjusted in the range of 50 ns to 1 ms.

In practice, for single color center measurements, it is common that the $g^{(2)}(\tau)$ function does not have a zero value for zero delay. This is due to the background luminescence coming from the sample, which is not antibunched. One should record the value of the noise level and subtract it from the recorded signal.

Moreover, the instrumental response function (IRF) of the acquisition system (photodiodes+TAC) is responsible for a non-zero value of the $g^{(2)}(\tau)$ function at zero delay. The IRF function can be measured by autocorrelation of an ultra short pulsed laser (femtosecond) and it is of the order of 0.6 ns (FWHM of the gaussian fit). In order to fit the

autocorrelation function properly at zero delay, one has to consider the convolution of the IRF with the measured $g^{(2)}(\tau)$ function as the fit function.

Counting NV centers per nanodiamond

A simple two-level quantum system can emit only one photon at a time (photon - antibunching), and the probability of emitting two consecutive photons gradually drops to zero as the time-lag between them decreases. This results in a dip at the zero lag time of the normalized second order time-intensity correlation function ($g^{(2)}(\tau)$). When we excite the fluorescence of n emitters, the latter function displays a smaller dip of depth $1/n$ allowing the determination of the number n of emitters [107]. By a simple exponential fit of the intensity autocorrelation function, one can determine the number n of the emitters (Figure 2.16).

If we describe the NV center system as a two-state system and we consider only the case of low excitation intensities $I < I_{sat}$, for the short times after the zero time delay the intensity autocorrelation function for n independent emitters can be written as:

$$g_n^{(2)}(\tau) = 1 - \frac{1}{n} e^{-(k_{12}+k_{21})|\tau|} \quad (2.2)$$

with k_{12} the pumping rate and k_{21} the spontaneous emission rate. For $n = 1$ (single emitter), at zero delay $g^{(2)}(0)=0$ and at $\tau \rightarrow +\infty$, $g^{(2)}(\tau) \rightarrow 1$, whatever the number of emitters, in accordance to quantum theory. Note also that $g_n^{(2)}(\tau) \rightarrow 1$ for $n \rightarrow +\infty$, for any τ (a source containing a large number of emitters is characterized by poissonian statistics).

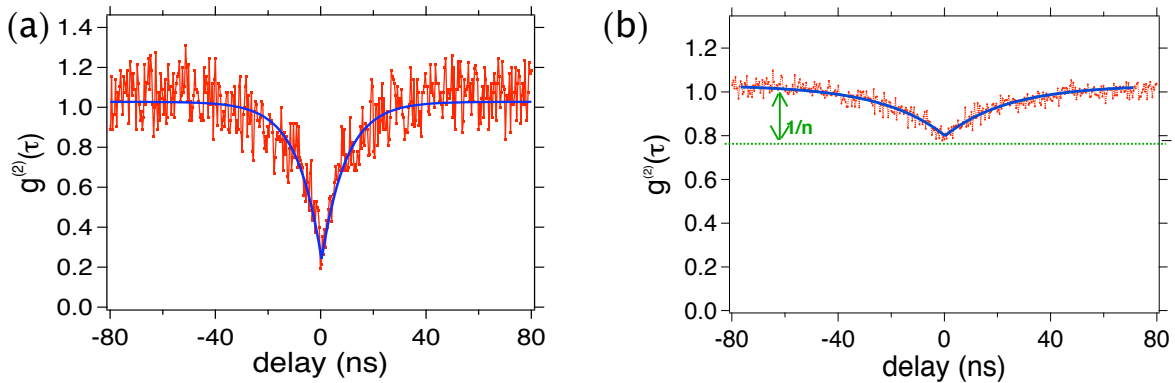


Figure 2.16: Typical intensity-time correlation functions of NV centers. The antibunching dip is (a) 0.19 and (b) 0.78 for zero delay, indicating $n=1$ and $n=4$ respectively. In blue plain: fit curve of a symmetric exponential function. Excitation at 532 nm, intensity 120 kW/cm².

2.3 Optical properties of single photoluminescent nanodiamonds and comparison with single fluorescent bioprobes

In the following, we study the optical properties of NV centers in nanodiamonds and compare them with the ones of single molecules and single Quantum Dots.

2.3.1 Single NV centers in type N nanodiamonds

Single NV center for comparison with single molecules

To study the photoluminescence properties of NV centers in nanodiamonds we spin coated *Aq30nm-Np15* on glass substrates. The substrates were exposed to oxygen plasma, to remove their organic impurities, which contribute to a high parasitic fluorescence signal. For a more controlled deposition of PNDs on the substrate, we add in the PNDs solution 0.5% weight of a polymer (polyvinyl alcohol, PVA). At the end we have a thin polymer film (thickness \approx nm) in which diamond nanocrystals are attached to the coverslip and are well dispersed.

We examined the photoluminescence of these PNDs. Figure 2.17a shows a confocal raster scan, where we observe many photoluminescent spots with different intensities, due to an inhomogeneous number of NV centers per nanocrystal.

By performing intensity-time correlation measurements we can quantify the number of NV center per nanocrystal. We considered a nanodiamond containing a single NV⁻ center from its Zero Phonon Line (ZPL) at 637 nm (Figure 2.17b). We recorded its photoluminescence intensity saturation curve (Figure 2.17c)⁸. The dichroic mirror was a 530DCLP (Chroma).

As emission rates depend on the environment of the NV center and the NV dipole orientation, we recorded the saturation curve for 3 single NV centers (marked with yellow squares on the scan) and then calculated the mean value (blue plain of Figure 2.17c). The counting rates of the 3 NV centers are the sum of the two APD recorded signals.

The laser excitation power at saturation for the mean curve is $P^{\text{sat}}(\text{NV}) = 0.44$ mW, which corresponds to an intensity of $I_{\text{exc}}^{\text{sat}}(\text{NV}) = 530$ kW/cm² (for the 532 nm laser beam the surface in the focal plane of the microscope objective of our setup is 0.6 μm^2)⁹.

At saturation intensity, the counting rate is found 31 kcounts/s.

After fitting the autocorrelation function measurement of a PND having more than 1 emitter (in square blue of Figure 2.17a) with the fit function described by equation 2.2, we find that this particle contains 4 NV centers (Figure 2.17d).

The photoluminescence signal of both particles with one or 4 NV centers is perfectly

⁸For the spectra recording a KG5 filter was in front of the spectrograph. This filter has a 50% cut-off wavelength at 700 nm and cuts totally light with wavelength >800 nm. It was left in front of the spectrograph to cut the excitation at 1064 nm of two photon experiments, carried out at the same period on the confocal setup. For the single molecule studies the filter was not removed, so a direct comparison with the NV measurements is still possible.

⁹The intensity saturation value is found by fitting the experimental data with the function $R(I) = \frac{A}{1 + \frac{I}{I_{\text{sat}}}}$, where $R(I)$ the counting rate, A a constant, I_{sat} the saturation intensity, I the excitation intensity. It corresponds to the intensity value for which $R^{\text{sat}}(I) = R \lim_{I \rightarrow \infty} / 2$

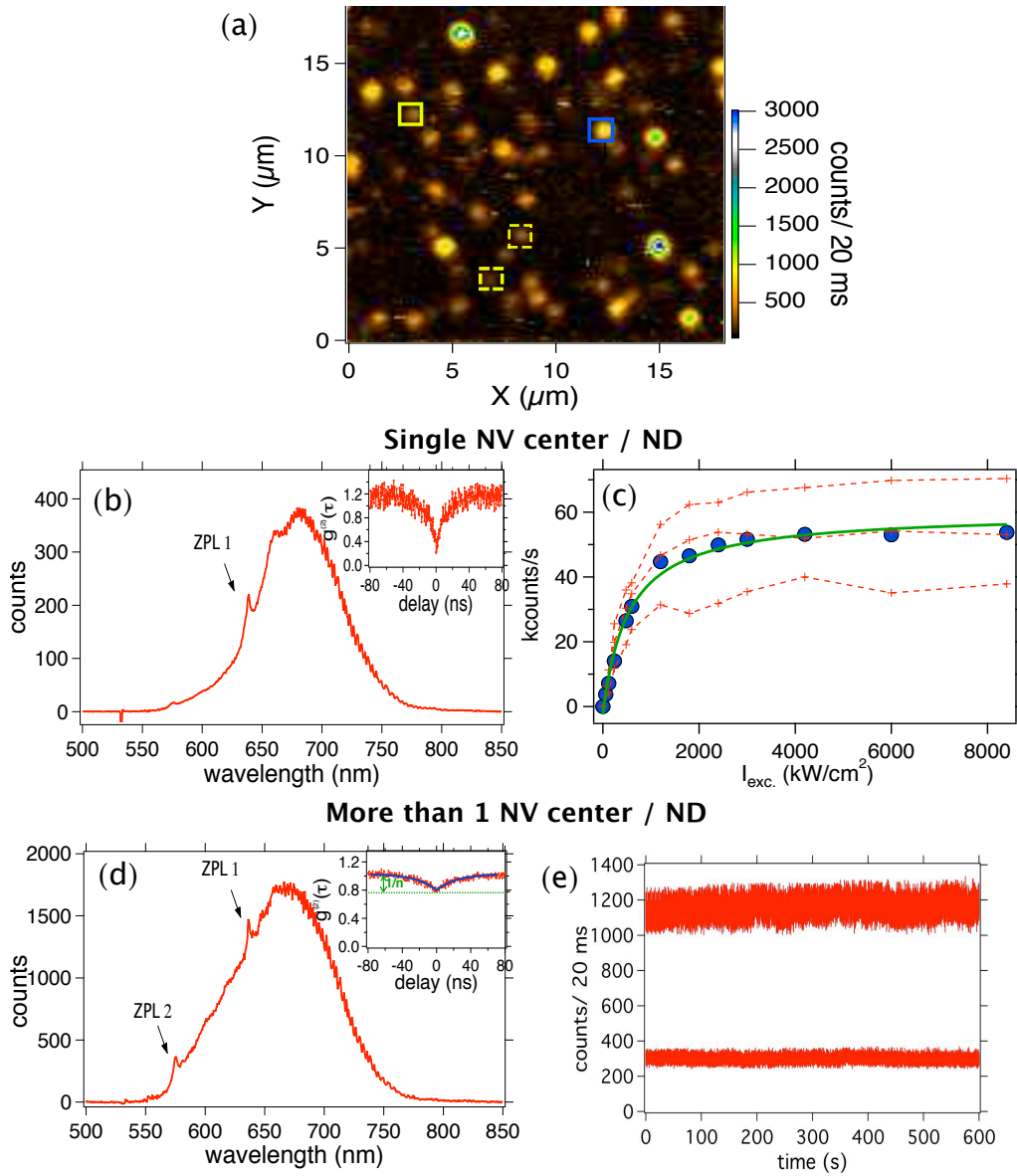


Figure 2.17: Photoluminescence study of NV centers in Np15 PNDs. (a) Confocal raster-scan of $Aq30\text{nm}-Np15$ solution deposited on a glass substrate by spin-coating. Excitation wavelength 532 nm, intensity $0.6 \text{ MW}/\text{cm}^2$ (power 1 mW), the image scale is saturated at 3000 counts/20 ms, in order to see easier the less intense spots. (b) Photoluminescence spectrum of the ND inside the plain yellow square of the confocal scan (a), characteristic Zero Phonon Line (ZPL) at 637 nm indicates that it is a NV^- center. Inset: intensity-time correlation function (Figure 2.16a) of the same PND, indicating $n = 1$. (c) Saturation curve (plain green) inferred from the fit of a two-level model of the average of the experimental saturation curves of 3 single NV centers (in yellow squares in (a)). (d) Photoluminescence spectrum of the ND in plain blue square of the confocal scan (a), containing both NV^- and NV^0 centers (ZPL1 and ZPL2 respectively). Inset: intensity-time correlation function of the same PND (Figure 2.16b) indicating $n = 4$ NV centers. (e) Time monitoring of the photoluminescence intensity of a single NV center and a ND containing 4 NV centers (of (b) and (d) respectively) over a period of 600 s, showing the perfect photostability (binning 20 ms). Excitation intensity $0.6 \text{ MW}/\text{cm}^2$.

constant over time (Figure 2.17e). Additionally, the signal of the PND with 4 NV centers is about 4 times larger than the one of the PND with a single emitter (1152 and 299 average counts/20 ms respectively). Note that for the single emitter the Signal-to-Noise Ratio (SNR) is about 15 (ratio of $\langle N \rangle = 299$ to its standard deviation $\sigma = 20$), while the shotnoise-limited SNR is by definition $\sqrt{N} = 17$. Thus the signal is almost shotnoise-limited.

2.3.2 Single dye molecules

Organic dye molecules are routinely used to label biomolecules [108]. We thus wanted to compare the photoluminescence properties of a single 30 nm ND containing a single NV center with the ones of a single dye molecule.

The dye is carbocyanine DiC₁₈(3) (Fluka, Spectrum Info, CAS No 41085-99-8) [109]. Cyanine dyes are often used in biology as biomolecule labels for a variety of applications such as DNA sequencing or to study single molecule dynamics [110–112].

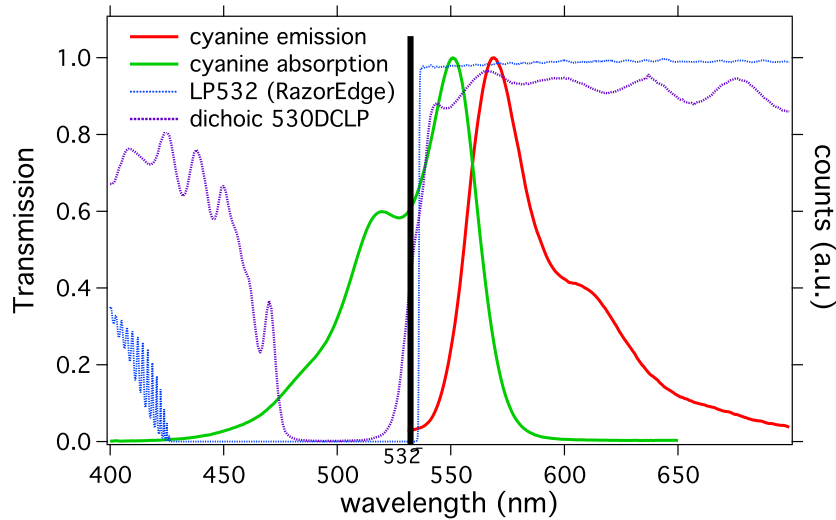


Figure 2.18: Absorption (in green) and emission (in red) spectra of carbocyanine DiC₁₈(3) molecules. The vertical black line shows the 532 nm excitation laser. In blue dashed is the long-pass (RazorEdge LP03-532RU-25) filter transmittance and in purple dashed the dichroic 530DCLP transmittance. Note that the choice of the filters is optimal for the carbocyanine fluorescence spectrum.

The photoluminescence emission peak of DiC₁₈(3) dye is centered on 580 nm, in the range of the NV center emission spectrum (Figure 2.18). To compare the dyes with PNDs photoluminescence, we measured the signal dependence with the laser excitation power. This task is not easy, because most dyes photobleach rapidly under laser beam exposure of a few kW/cm² excitation intensity. In addition, detection efficiency varies and depends on the environment and the molecule dipole orientation [113, 114], which are parameters that we cannot control.

Figure 2.19a displays a confocal raster scan of a sample of single molecules deposited on a microscope coverslip. We measured the counting rate versus the excitation laser intensity for 4 molecules and for up to ~ 14 kW/cm² excitation intensity before pho-

photobleaching (Figure 2.19b). The sudden decrease of the fluorescence intensity to the background level after some seconds of continuous excitation is the result of photobleaching and is a strong indication of the unicity of the examined dye molecule (Figure 2.19c). In order to fit the saturation curve (Figure 2.19b) we consider a three energy-level system model. For a slow intersystem crossing rate, such a model gives a fluorescence emission rate R :

$$R(I_{\text{pump}}) = \eta_Q \times \eta_{\text{det}} \frac{k_{21}}{(k_{21}/k_{12}) + (k_{23}/k_{31}) + 1} \quad (2.3)$$

where η_Q is the quantum yield of the molecule, η_{det} is the overall detection efficiency, and k_{ij} the corresponding transition rates between state i and j ($i, j = 1, 2$ or 3 , corresponding respectively to the ground, the excited, and the triplet states) [115, 116]. The absorption rate k_{12} is given by the relation $k_{12} = \sigma I_{\text{pump}}/h\nu_{\text{pump}}$, where σ is the absorption cross-section of the molecule ($\sigma \approx 4 \times 10^{-16} \text{ cm}^2$ for the cyanine dye [117]). To get a good agreement between the model and the data, we need to take into account a dependency of k_{31} on I_{pump} of the form $k_{31} = k_{31}^0(1 + \beta I_{\text{pump}})$, which is interpreted as the pumping of higher-energy triplet states from the lower triplet state. Our data are well fitted, with $\beta = 8 \times 10^{-5} \text{ W/cm}^2$, $\eta_Q \times \eta_{\text{det}} = 0.013$ and $k_{21} = 0.38 \times 10^9 \text{ ns}^{-1}$ [118].

If we consider excitation laser intensities values higher than the ones we used in the experiments where we are limited by photobleaching, and if we extend the fit of the data by equation 2.3 to these higher values, we obtain the saturation curve displayed in the inset of Figure 2.19b.

We then define a saturating counting rate $R^{\text{sat}} = \frac{1}{2} \times \lim_{I_{\text{exc}} \rightarrow \infty} R(I_{\text{exc}})$ which can be calculated from equation 2.3 with $\eta_Q \eta_{\text{det}} = 0.013$ and $k_{21} = 0.38 \text{ ns}^{-1}$, yielding $R^{\text{sat}}(\text{cy}) = 2475 \text{ kcounts/s}$. The corresponding saturation excitation intensity associated to this counting rate is $I_{\text{exc}}^{\text{sat}}(\text{cy}) = 1700 \text{ kW/cm}^2$. This counting rate at saturation value is relatively high, but it is never reached due to photobleaching. Just before photobleaching, the counting rate of a single molecule is $\sim 80 \text{ kcounts/s}$.

To study a system brighter than single organic molecules, we examined a sample of 20 nm beads doped with Nile Red (Invitrogen, USA), frequently used as labels. Figure 2.19d shows the time trace of the fluorescence intensity of one fluorescent bead under 532 nm cw excitation. We clearly see a stronger fluorescence signal than the one of a single DilC₁₈ molecule. However, after 20 seconds of illumination this signal almost vanishes due to photobleaching. The diminution of fluorescence occurs by steps, indicating the gradual photobleaching of the molecules one by one.

2.3.3 Individual commercial Quantum Dots

The most widely used inorganic probes as fluorescent labels in biology are the Quantum Dots (QDs) [12]. We thus studied the optical properties of commercial QDs.

The Quantum Dots used are Qdot-IgG conjugates (*lot N° 51017A*, Invitrogen, USA). They are CdSe core QDs, with a shell of ZnS. This specific QD reference was chosen because its photoluminescence emission peak is centered on 655 nm (Figure 2.20b), close to the NV color center emission spectrum maximum (Figure 2.20b).

Figure 2.20a shows a confocal raster scan of QDs deposited on a glass coverslip. Most of the isolated spots are well separated from each other except one aggregate in the center of the scan. The characteristic peak in the photoluminescence spectrum from a single

2.3 Optical properties of single photoluminescent nanodiamonds and comparison with single fluorescent bioprobes

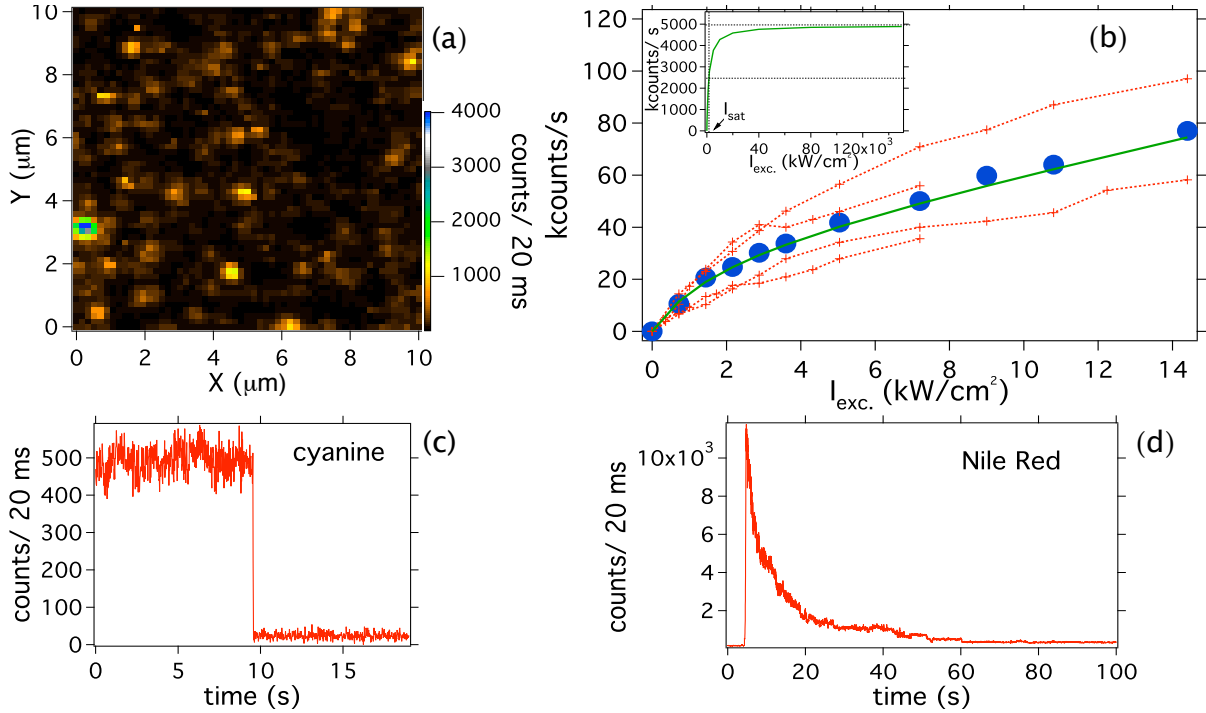


Figure 2.19: Photoluminescence of single dye molecules : (a) Confocal raster scan, cw excitation laser at 532 nm, intensity 12 kW/cm^2 (power $20 \mu\text{W}$). (b) Counting rate versus excitation intensity for 4 molecules (dashed colored), with plain green the fitting curve according to the three-level model expression of equation 2.3. Inset: the saturation curve for higher excitation intensity values. (c) A 20 s emission time trajectory of a single molecule (binning 20 ms) with the characteristic one-step bleaching, cw excitation laser at 532 nm, intensity 6 kW/cm^2 . (d) Time trace for a 20 nm Nile Red doped polystyrene bead, excitation 24 kW/cm^2 .

spot allows us to confirm that the emitting spot is a QD. The intensity time-correlation measurement of the light emitted from each isolated spot yields a photon antibunching corresponding to a single QD. To study the single-particle photoluminescence, we record the intensity during a “long” observation time period of 400 s. We clearly observe blinking in the photoluminescence, corresponding to the emitter switching randomly between an “on” and an “off” state (Figure 2.20d).

Considering the large fluctuations of the QDs photoluminescence intensity due to this blinking, defining a photoluminescent intensity is somewhat arbitrary (see Figure 2.20e, for example) and depends on whether we consider that the emission obeys a simple two states “on”-“off” model, or rather a three-state or even a continuous-state model [119, 120]. In most of the reported experiments, the methods that are used to quantify the photoluminescence intensity signal introduce a threshold level below which the QDs are considered to be in the “off” state. Despite the fact that more complicated techniques have recently been developed, like the changepoint method [121], we decided to use a threshold limit and set it at 50% of the maximum photoluminescence intensity observed on the time window of the measurement.

Figure 2.21a shows the photoluminescence intensity *vs* the laser excitation power for a single QD. Most of the studied QDs show a decrease of their photoluminescence in-

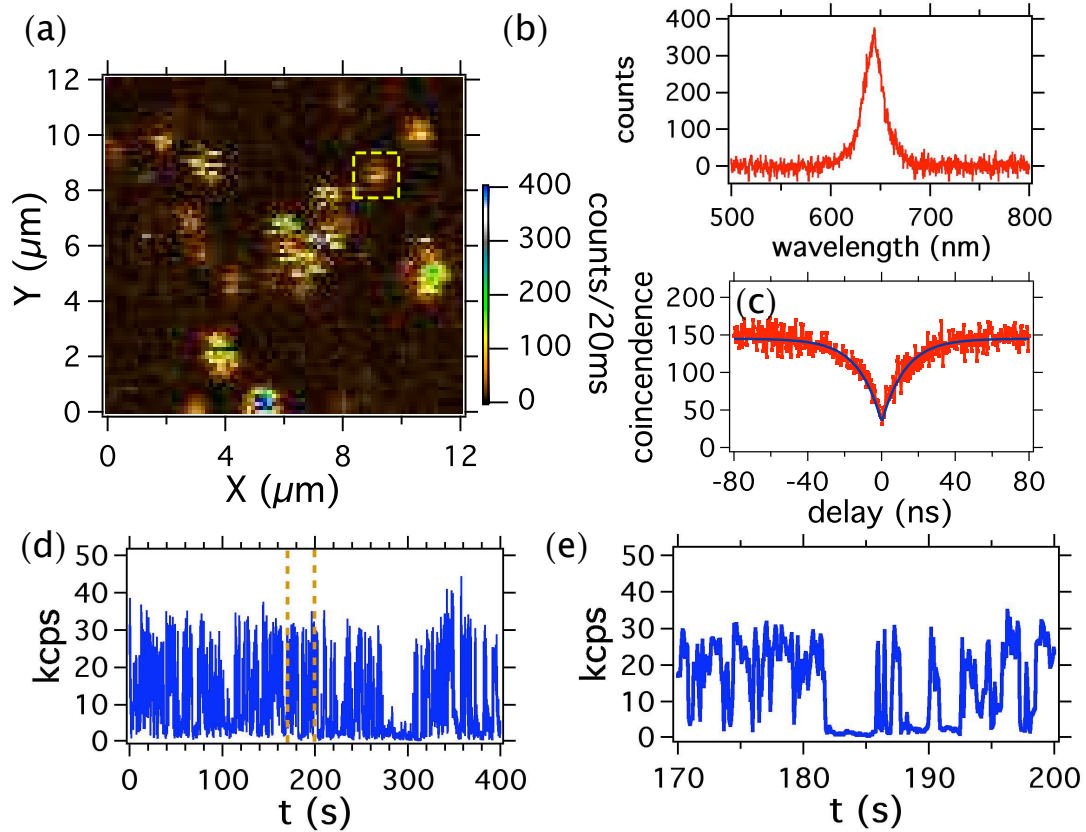


Figure 2.20: Photoluminescence intensity of single QDs showing photoblinking. (a) Confocal raster scan of a sample made of QDs spincoated on a glass coverslip, laser excitation intensity 3 kW/cm^2 (power $5 \mu\text{W}$); the blinking of QDs during the scan acquisition can be observed as dark lines interrupting bright spots. (b) Photoluminescence spectrum of the QD surrounded with a yellow square on the raster scan (a). (c) Intensity time correlation histogram of the same QD, showing antibunching at zero delay which proves that we address a single emitter. Excitation intensity 1.5 kW/cm^2 . (d) A 400 s long photoluminescence intensity trajectory of the same single QD (binning: 100 ms), laser excitation intensity: 3.6 kW/cm^2 . (e) zoom of the photoluminescence time-trace of (d). Cw excitation laser at 532 nm.

tensity at high excitation intensities, which almost vanishes at intensities higher than 60 kW/cm^2 (corresponding to $100 \mu\text{W}$ input power). We tentatively attribute this effect to photoinduced oxidation of the QDs surface. The photoluminescence saturation behavior is recorded for 5 single QDs from which an average curve is inferred (see Figure 2.21b).

In the following, in order to define a saturation intensity and compare it with the one of cyanine molecules and NV centers, we fit the experimental saturation curve with the two energy level model (same model as used for NV center). Because at high excitation intensities there is a decrease of the counting rate, we fit the data until the point where excitation intensity corresponds to the maximal value of the counting rate (i.e. $I_{\text{exc}}=18 \text{ kW/cm}^2$, in dashed blue on Figure 2.21b). We find $I_{\text{sat}} = 9 \pm 3 \text{ kW/cm}^2$ with the corresponding counting rate $R=148 \text{ kcounts/s}$.

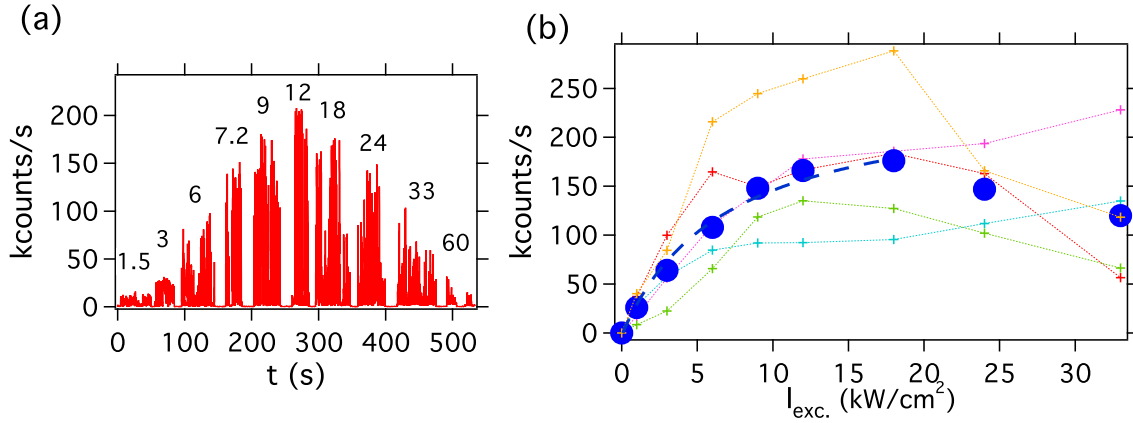


Figure 2.21: Photoluminescence intensity *vs* laser excitation intensity for QDs. (a) Single QD photoluminescence intensity dependence with excitation intensity, consecutive values equal to 1.5, 3, 6, 7.2, 9, 12, 18, 24, 33 and 60 kW/cm². Each time we changed the excitation laser power, we shut off the beam for a few seconds in order to measure exactly the power value; binning time: 50 ms. (b) Mean saturation curve (dashed blue) calculated from the average of 5 single QDs saturation curves (dashed colored).

2.3.4 Comparison of single photoluminescent nanodiamond, dye molecule and quantum dot photoluminescent properties

Single molecules - NV center in 30 nm PNDs

To compare the fluorescence properties of the molecular and NV color center system, we calculated the saturation intensity for a single molecule. The fit of equation 2.3 yields $I_{\text{exc}}^{\text{sat}} = 1700 \text{ kW/cm}^2$ and $R^{\text{sat}} = 2475 \text{ kcounts/s}$ (see Table 2.2).

The value of the saturation fluorescence counting rate is relatively high, but it is never reached due to photobleaching. Just before photobleaching, the counting rate of a single molecule is $\sim 80 \text{ kcounts/s}$, a value close to the one obtained from a single NV center.

The saturation excitation intensity for a single molecule is found ~ 3 times larger than the saturation excitation intensity required for a NV center. This result can be explained by the difference in the absorption cross section σ . The absorption cross-section for the cyanine molecules was inferred in the range $\sigma_{\text{cy}} \approx 4 - 6 \times 10^{-16} \text{ cm}^2$ at 532 nm excitation wavelength [117], while for the NV center $\sigma_{\text{NV}} \approx 3 \times 10^{-17} \text{ cm}^2$, according to Ref. [14].

Indeed, the excitation intensity at saturation ($I_{\text{exc}}^{\text{sat}}$) is roughly proportional to $(\sigma\tau)^{-1}$, τ being the emitter radiative lifetime. According to Table 2.2, one gets a value of :

$I_{\text{exc}}^{\text{sat}}(\text{cy})/I_{\text{exc}}^{\text{sat}}(\text{NV}) = 0.5$, which is 6 times smaller than the experimental value. This discrepancy can be explained due to the large error bar of the wide dispersion of the NV center radiative lifetime values in nanodiamonds and due to the low number of statistical data for the dye molecules (because of photobleaching the saturation values were calculated and not measured experimentally).

In contrast to single DilC₁₈ molecules or Nile Red-doped beads, we observe that the photoluminescence intensity of a single NV center is perfectly constant over time

(Figure 2.17). In the case of a PND containing 4 NV centers, the 4-5 fold increase of the photoluminescence intensity compared to the single NV center corresponds to a signal two times higher than the one of the single cyanine molecule just before photobleaching occurs.

	$\sigma \times 10^{-17} \text{ cm}^2$	τ_{rad} (ns)	$I_{\text{exc}}^{\text{sat}}$ (kW/cm ²)	R^{sat} (kcounts/ s)
single molecule	40-60 ^a	2.6 ^b	1700 ⁱ 14.5 ⁱⁱ	2475 ⁱ 74 ⁱⁱ
single QD	20-160 ^c	15-20 ^d	9 ± 3	148
single NV in PND	3 ^e	17 ± 15 ^f	529 ± 70	31

Table 2.2: Comparison of the photophysical properties of single molecules -single QDs - single NV centers in PNDs. Excitation laser at 532 nm. For single cyanine molecules, i) are the calculated values of the saturation curve fitting, after photobleaching occurs, ii) are the measured maximal values before photobleaching occurs. References: a: [117], b: [118], c: [122], d: [123], e: [14], f: [17]

QDs - NV center in 30 nm PNDs

According to our measurements carried out by the same experimental setup (i.e. same collection efficiency) and by the same excitation wavelength, a single QD yields an emission intensity at saturation 4.7 times larger than that of a single NV center. In addition the excitation laser saturation power for a single QD is $\times 60$ lower than the one required for a NV center. This result can be explained by the difference in the absorption cross section σ of the two types of emitters. In the case we consider the two emitters as two level systems (true for low excitation intensities) we expect $I_{\text{exc}}^{\text{sat}} \sim 1/\sigma\tau_{\text{rad}}$.

According to Table 2.2, one gets a maximal value (for $\sigma_{\text{QD:max}}$) of: $I_{\text{exc}}^{\text{sat}}(\text{NV})/I_{\text{exc}}^{\text{sat}}(\text{QD}) = 51.0$, which is slightly lower than the one observed experimentally. Similar to the carbocyanine - NV center comparison, this discrepancy may be due to the variations of the emitters decay lifetimes. In fact QDs have usually a multiexponential decay lifetime, for which we take a mean value of 16 ns (measured by time-intensity correlation on Figure 2.20c, similar values are reported in Ref. [123]). Moreover, NV centers in nanodiamonds have a broad distribution of τ_{rad} [17], this is the reason for a large error value (80%) found in the measurement.

It should be mentioned that the excitation was for both cases carried out with a cw laser at 532 nm. This excitation wavelength excites efficiently the NV center, but for the QDs the absorption cross section increases with the decrease of the excitation wavelength. Thus, for the QDs used in our experiment, excitation at 400 nm or at 300 nm is ~ 3 times and ~ 6 times more efficient than at 532 nm respectively¹⁰. However, for biological applications excitation at small wavelengths is often not appropriate (strong cell autofluorescence); an excitation at 532 nm is a good compromise.

Regarding the stability of the photoluminescence intensity in time, the QDs clearly show intermittent emission while the NV centers photoluminescence intensity is perfectly

¹⁰absorption and emission spectra of the QD-655 can be found at <http://www.invitrogen.com/site/us/en/home/support/Product-Technical-Resources/Product-Spectra.QD655SA.html>

stable. Recent studies show that the QD core-shell can be optimized to reduce the blinking [26, 27]. Despite the progress in suppressing the photoblinking, a significant fraction of the QDs nanocrystals still blinks. In our case we chose “regular” QDs and carbocyanine molecules, commercially available, because the aim of this comparison was to compare the PNDs photoluminescence to the one of widely used fluorescent probes and not with probes that are still under development.

Even though the photoluminescence saturation intensity from a single NV center is ~ 4.5 times smaller than the one from a QD, if we consider their perfect photostability they are still very interesting markers for applications in biology. In addition, as we will see in the following, by selecting nanodiamonds rich in nitrogen (nitrogen concentrations larger than 100 ppm) and by optimizing the conditions for the NV color center creation (irradiation and annealing process), one can obtain nanocrystals of about 30 nm nanodiamonds containing 7-8 NV centers (Figure 2.23), which display a photoluminescence intensity equivalent to the one of a single QD of similar size. Considering that the parameters of the NV creation can be further optimized to obtain PNDs even brighter, one can state that PNDs certainly hold a great potential as labels for biology.

2.4 Optimization of the photoluminescent nanodiamond fluorescence yield

The possibility to increase the concentration of NV centers in NDs will allow a better detection for labeling applications in biology. As already explained in section 1.1.2, active NV centers are created in nitrogen-rich ($[N] \sim 100$ ppm) type Ib diamond crystal by a two step procedure involving the generation of vacancies by electron or ion beams followed by thermal annealing of vacancy defects at temperature $> 600^\circ\text{C}$. At such temperatures the vacancies start migrating to the nearest substitutional nitrogen atoms [92, 124]. The conversion efficiency can however be limited due to competitive processes such as the formation of other defects and “vacancy-interstitial carbon” recombination.

A way to improve the photoluminescence properties is to increase the concentration of vacancies created in the diamond matrix by high energy beam irradiation. Here we study the improvement of the photoluminescence yield with the high energy electron irradiation dose and energy for diamond microcrystals (size 150-200 μm) and with the proton irradiation dose (at constant energy) for diamond 30 nm nanocrystals.

2.4.1 Diamond microcrystals

Figure 2.22a is a comparative study of type Ib diamond microcrystals irradiated under different electron doses, all annealed at 800°C for 2 h. We qualitatively observe an increase of the photoluminescence intensity with the increase of the irradiation dose, as expected due to the increase of the vacancy density with the increase of the irradiation dose (as long as the concentration of nitrogen is high enough in the lattice).

We recorded the spectra of microcrystals irradiated at two different doses or at two different energies (Ocean Optics spectrograph).

When we increase the irradiation dose 5 times, we observe an increase of the photoluminescence signal (Figure 2.22b). However, the values of the recorded photoluminescence signal depend strongly on the position of the focal point in the crystal, so a quantita-

tive study is difficult. The values that can be compared are the relative intensities of the $NV^-:NV^\circ$ Zero Phonon Lines (ZPL). For the low irradiation dose we find a ratio $NV^-:NV^\circ=2.77$, while for the high irradiation dose the ratio is 1.6. The increase of the NV° centers amount in diamond (1.7 fold in our case) with the irradiation dose can be explained by the increasing number of created vacancies, which (after annealing) are stabilized next to nitrogen atoms, leaving less nitrogen atoms free in the diamond lattice, thus fewer electron donors for a NV^- center.

When we increase the energy of the charged particles (electrons) we have a 1.4 fold increase of the $NV^-:NV^\circ$ ratio (Figure 2.22c). The reason of this increase is not evident and more investigations are necessary to understand the $NV^-:NV^\circ$ creation processes.

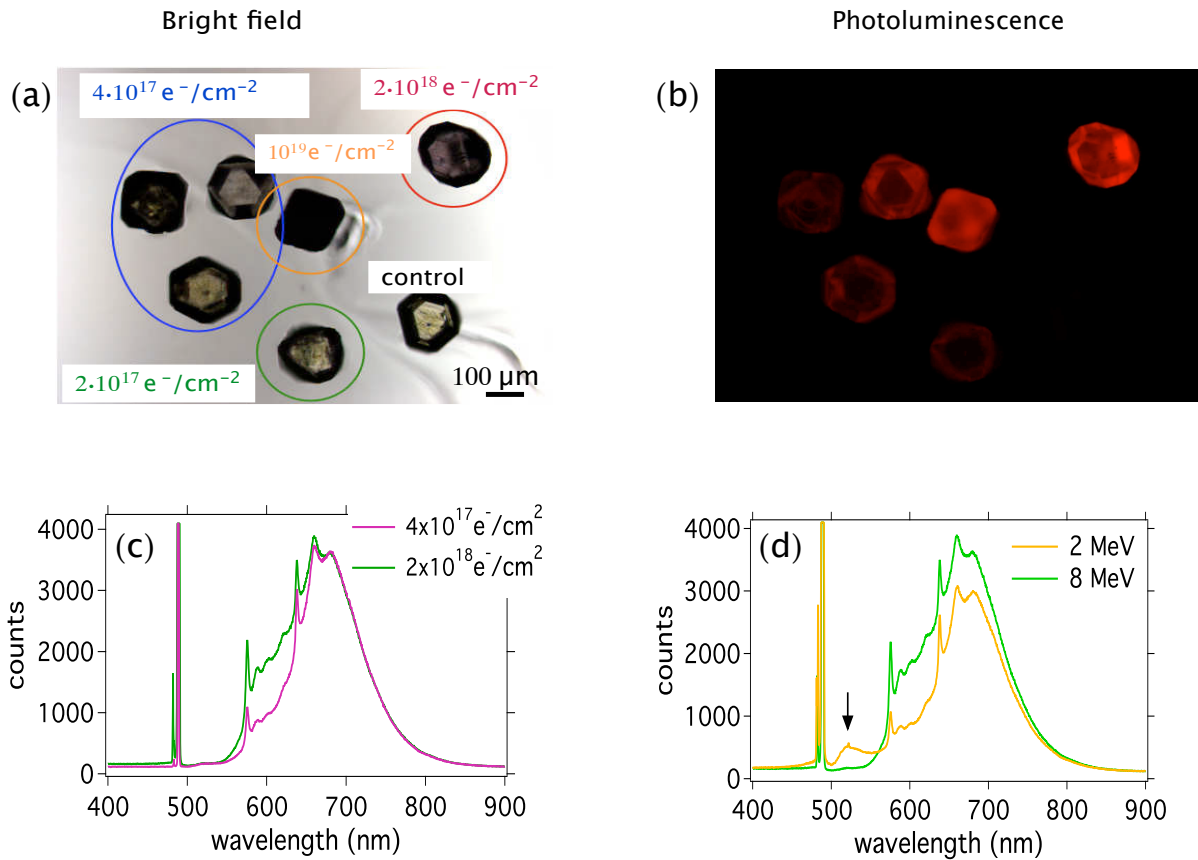


Figure 2.22: Photoluminescence comparison of diamond microcrystals under different irradiation conditions: (a,b) Comparison of the photoluminescence intensity of diamond microcrystals irradiated at different doses. Illumination at 500-550 nm (commercial fluorescence microscope). (c) Study on the irradiation dose, constant electron beam energy at 8 MeV, dose $4 \times 10^{17} e^-/cm^2$ in purple, dose $2 \times 10^{18} e^-/cm^2$ in green; (d) Study on the beam energy dependence, irradiation dose $2 \times 10^{18} e^-/cm^2$, beam energy at 2 MeV (in orange) and 8 MeV (in green). The characteristic Zero Phonon Line (ZPL) at 575 nm and 637 nm for the NV° and NV^- center respectively are well distinguished. On the spectrum of 8 MeV on (b), the peak at 510-520 nm (marked with an arrow) is due to H3 centers, analyzed in more detail in Appendix A. Excitation wavelength 488 nm (observed as a narrow line on the spectra), dichroic mirror used z488rcx, excitation power 0.5 mW, acquisition time 10 ms.

The previous studies of NV centers in microdiamonds have served as a guide for the studies in nanodiamonds. For biological applications, one has to use particles of nanometric size, thus we should be able to improve the photoluminescence properties in nanodiamonds. Type M PNDs were relatively dispersed in size, containing from 5-10 nm PNDs to 40-50 nm ones. We studied the influence of the irradiation dose in nanodiamonds for type N PNDs, with a more confined size dispersion about 30 nm.

2.4.2 Diamond nanocrystals

Here we varied the irradiation dose of H^+ ions applied to PNDs. Type Ib NDs were irradiated at doses of either $5 \times 10^{15} H^+/cm^2$ (sample Np15) or $5 \times 10^{16} H^+/cm^2$ (sample Np16) and then annealed at $800^\circ C$ for 2 h. It is worth noting that the latter dose is the highest proton irradiation dose used so far for this type of applications. The average size of PND suspensions was 30 nm in both cases (solutions *Aq30nm-Np15* and *Aq30nm-Np16*) (Figure 2.6). PNDs were deposited by spin coating on glass coverslips. Figure 2.23a,b shows two confocal scans, one for each irradiation dose. Next to each spot is indicated the measured number n of NV centers. For the low proton irradiation dose we infer a mean value of $n = 2.7 \pm 1.1$ NV centers/ PND, while for the 10 times higher dose the mean value is $n = 7.0 \pm 2.1$ NV centers/ PND. Figure 2.23c shows a comparison of the PND photoluminescence intensity distribution for the two irradiation doses. The statistical sampling is 75 and 100 nanoparticles respectively. We find a broad distribution in each case. For the low irradiation dose the median value is 315 kcounts/s while it is 986 kcounts/s for the one order of magnitude higher dose, indicating a 3 fold increase of the corresponding photoluminescence signal, in good agreement with the change in the number of color center content.

We infer from SRIM calculations that in this flat region the density of created vacancies is 8.17×10^{-6} vacancies/ $\text{\AA}/H^+$, i.e. 817 vacancies/cm/ H^+ (Figure 2.24). Considering that for proton irradiation the damage efficiency is about 10 vacancies per H^+ ion¹¹, the $5 \times 10^{15} H^+/cm^2$ dose produces per unit surface 5×10^{16} vacancies/cm² while the $5 \times 10^{16} H^+/cm^2$ dose produces 5×10^{17} vacancies/cm², according to Ref. [14, 91].

The irradiation dose of $5 \times 10^{16} H^+/cm^2$ is expected to produce in volume 4×10^{20} vacancies/cm³ resulting in ~ 5600 vacancies for a 30 nm diameter nanodiamond.

Taking into consideration the initial concentration of nitrogen in the type 1b diamond used (~ 100 ppm, equivalent to $1.76 \times 10^{19} N/cm^3$), we calculate that we have 480 N atoms in a 30 nm nanodiamond, indicating that a large proportion of the available nitrogen and vacancies in the nanodiamond matrix is not converted into NV centers. From intensity-time correlation measurements corresponding to NDs irradiated at this dose, the estimated ratio of the mean number of NV centers created (7) to the number of nitrogen atoms is about 7:480.

¹¹if the beam incident on the [111] direction, otherwise in case it is incident on the [100] direction it is 13 vacancies per proton [14]

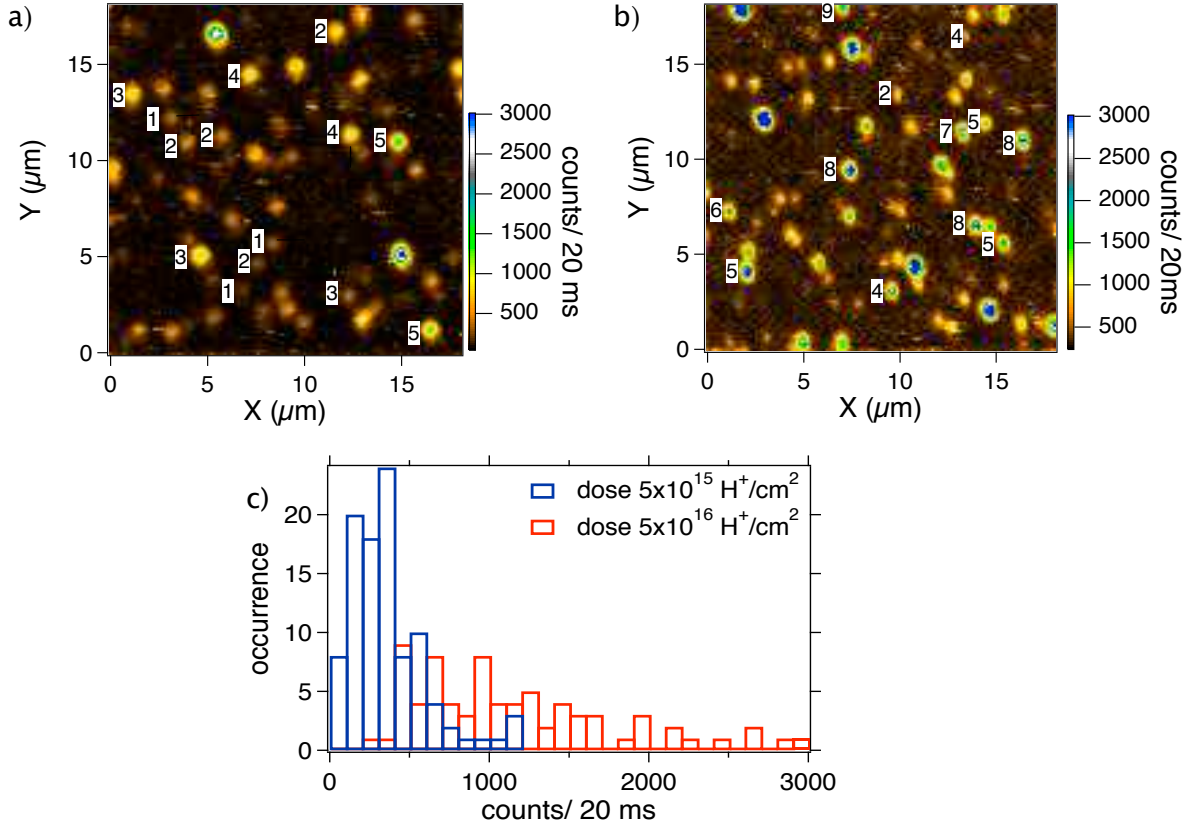


Figure 2.23: Photoluminescence comparison of 30 nm PNDs (*Aq30nm-Np xx* suspensions, with xx 15 or 16) spin-coated on glass coverslips, after H^+ irradiation and annealing. We measured the number of color centers in some of the well isolated spots - PNDs (indicated next to each spot). (a) Confocal scan of PNDs irradiated with $5 \times 10^{15} \text{ p}^+/\text{cm}^2$, mean value $n = 2.7 \pm 1.1$ NV centers/ PND ; (b) Confocal scan of PNDs irradiated with $5 \times 10^{16} \text{ p}^+/\text{cm}^2$, mean value $n = 7 \pm 2.1$ NV centers/ PND ; exc. wavelength 532 nm, exc. power 1 mW ; (c) Occurrence versus photoluminescence intensity for NDs irradiated with $5 \times 10^{15} \text{ H}^+/\text{cm}^2$ (in blue) and $5 \times 10^{16} \text{ H}^+/\text{cm}^2$ (in red) respectively.

2.4.3 Discussion

In this section we demonstrated that an increase of the irradiation dose results in an enhancement of the photoluminescence of diamond crystals, but this enhancement is less than the one theoretically expected. In our case, by using a high proton irradiation dose, SRIM calculations predict a high concentration of vacancies in nanodiamonds, which was not followed by a high increase of the NV center amount. A way to significantly increase the PND brightness once we reach the highest vacancy concentration would be to improve the conversion rate of non-complexed vacancies and nitrogen atoms to NV centers. Vacancies may not be trapped by nitrogen substitutional atoms during the anneal but recombine with interstitial carbon atoms or form other defects. The theoretical conversion percentage of 25 - 30% [91], confirmed experimentally in recent studies [14], is not yet achieved for NDs and gives a lot of margin for further improvement.

However, as mentioned in section 1.1.5, the probability of NV center creation in

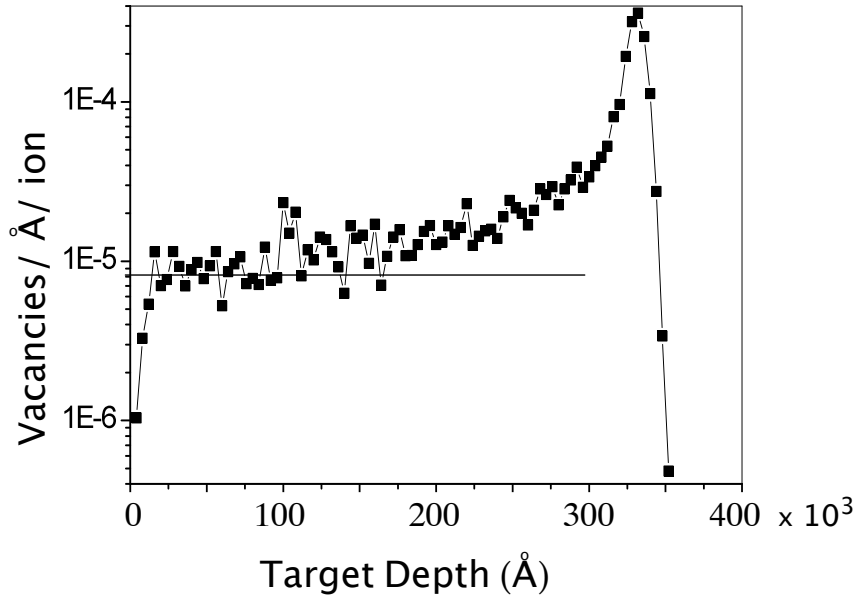


Figure 2.24: Spatial distribution of vacancies produced in diamond by ion beam irradiation as predicted by SRIM Monte Carlo simulations for 2.4 MeV proton irradiation. The number of damage events used in the simulations were 9999.

nanocrystals decreases with the square of the particle radius when the particles have sizes <10 nm [98, 125]. This is a consequence of the defects being stable only within the core region of the nanodiamonds, which has a reduced radius with respect to the total size of the particle. Additionally, vacancies can easily anneal to the surface, without forming NV centers.

In order to increase the number of NV centers in small size nanodiamonds, two ways (up to our knowledge) are possible. The first one consists of creating NV centers in diamond microcrystals, which can then be reduced in size by milling. This method was applied by Curmi et al. [90] and the first observations report that 12 nm NDs can contain up to 12 NV centers. The other method is by creating the NV centers in large size nanodiamonds (35-100 nm) and then reduce them in size by oxidative etching (in air at 500 °C for 1 – 2 h) [126]. A 7-fold increase of the photoluminescence signal was reported.

In our group we counted the NV centers per ND of the latter sample ¹², by carrying out confocal measurements, coupled with an AFM device. We observed that 10 nm PNDs created by the latter method contain in average 3 NV centers.

As inferred from the above, the creation of small and bright nanodiamonds is an area of open research activity. We showed that there is still margin for further improvement, either in terms of the proper adjustment of the irradiation and annealing temperature parameters, or in terms of the initial size of the NDs in which NV centers are created. The results indicate that in the near future the concentration of NV centers in small PNDs can be increased, a necessary requirement for bio-imaging applications.

¹²the initial size of the irradiated NDs, before etching, was 35 nm

2.5 Detonation nanodiamonds

One of the most impressive methods of producing small nanodiamonds is by the use of explosives (Figure 2.1). The final product is 5 nm primary size nanodiamonds. Particles of such size are ideal for biological applications. They have been used as drug delivery vehicles in cells [74, 75]. For biological labeling, fluorescence from naturally present NV centers in aggregates of detonation NDs was used for cell or biomolecule labeling or labeling to study membrane receptors [60, 127]. Very recently, proton irradiation of such nanoparticles enhanced the NV centers concentration and a stable photoluminescence signal was observed [98].

Here, we study the photoluminescence properties of “as produced” detonation nanodiamonds, neither irradiated nor annealed¹³. We first characterize their size and then study their photoluminescence.

2.5.1 Production and de-agglomeration of detonation nanodiamonds

Detonation nanodiamonds are the product of explosive materials containing carbon, a method developed in the former USSR in the 1960s. The explosive material is used as a precursor material; it typically consists of TNT (2-methyl-1,3,5-trinitrobenzene) and hexogen (in the proportion 60:40) composed of C, N, O and H, with a negative oxygen balance so that “excess” carbon is present in the system. The explosion takes place in a nonoxidizing medium of either gas or water (ice), which acts as a coolant.

The initial shock from a detonator compresses the highly-explosive material, which is heated and chemical decomposition occurs, thereby enormous amounts of energy in a fraction of a microsecond are released. As the detonation wave propagates through the material it generates high temperatures (3000-4000 K) and high pressures (20-30 GPa) which correspond to the region of thermodynamic stability for diamond.

The product of the explosion is a mixture of tiny particles of diamond (5-10 nm) with graphitic structures (35-45wt%) <20 nm and incombustible impurities [65]. The nanodiamonds consist of a diamond core of about 5 nm in size and a shell made up of sp²-coordinated carbon atoms [128]. Purification is performed by mechanical and chemical methods (Figure 2.25a). The mechanical methods consist of sieving while the chemical methods consist of strong acid treatments, which remove metal impurities and non-diamond carbon materials.

After the purification process, detonation nanodiamonds form clusters. To de-agglomerate them, the technique of attrition milling is widely used (Figure 2.25b) [129]. Zirconia beads of 30-50 μm are used and are stirred at high speeds with the diamond slurry in solution. The diamond suspension is circulated through the beads media, in which shear forces destroy the agglomerates. The resulting colloidal solutions contain primary size (5 nm) nanodiamonds, which can form stable suspensions in water. Another deagglomeration method recently introduced and used for the detonation NDs studied in our experiments is the bead-assisted sonic disintegration technique (BASD) [130]. It combines the use the shear force introduced by zirconia beads with a strong ultrasonication. This

¹³we actually irradiated detonation NDs, but we observed an intense graphitization. Thus we preferred to study their “natural” photoluminescence.

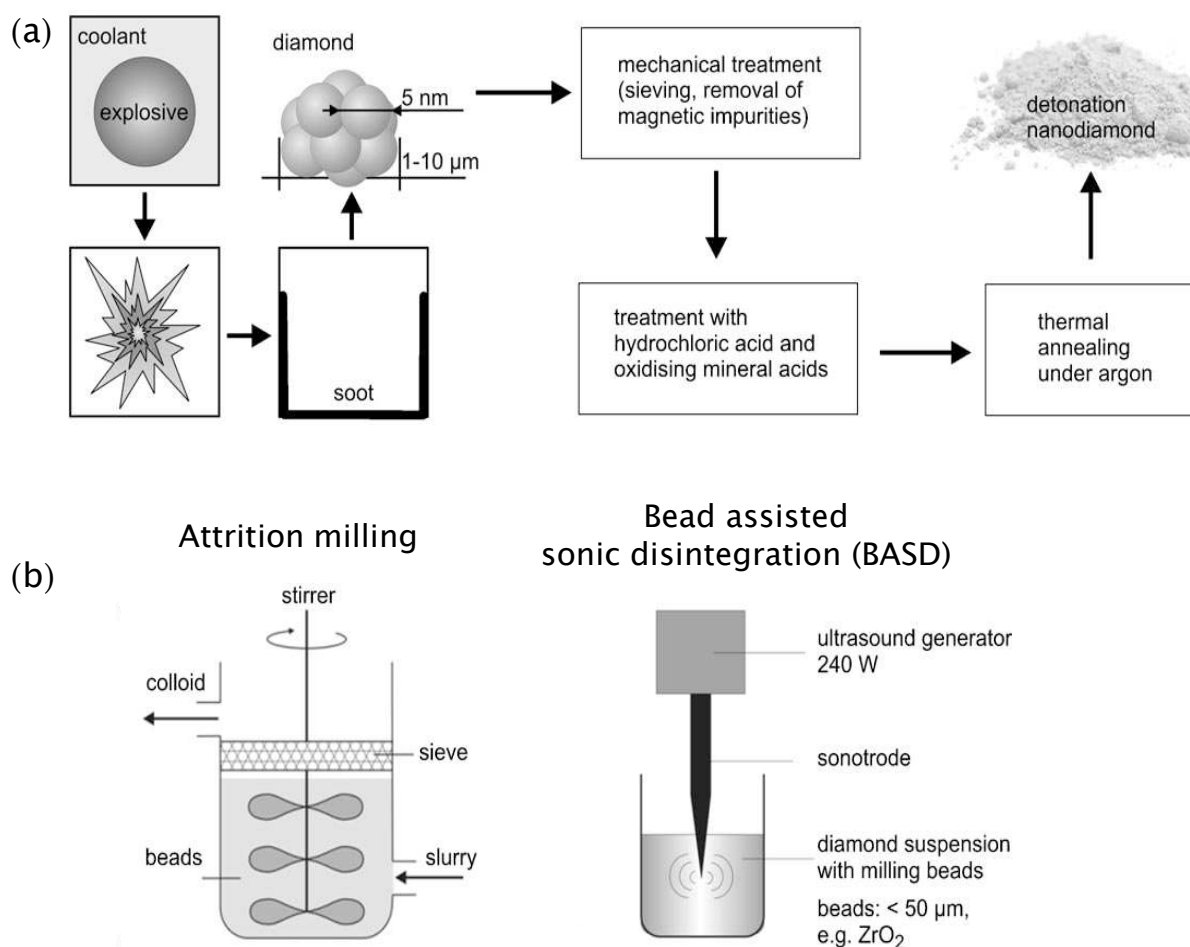


Figure 2.25: Production and de-agglomeration of detonation diamond. (a) Production of diamond after an explosion and mechanical and chemical purification of the detonation soot to extract the primary size NDs. (b) De-agglomeration of detonation diamond in primary size 5 nm nanoparticles by attrition milling and BASD method [73].

new method proved to be very efficient for the de-agglomeration of nanoparticles.

In our experiments we used detonation nanodiamonds provided by Anke Krüger. They formed stable suspensions in pure water. As demonstrated by AFM microscopy (AFM, apparatus: *Nanoscope IIIa*, Veeco Instruments Inc., USA), the solution contained primary size particles of 5-10 nm but also small aggregates of 20-40 nm (Figure 2.26a). DLS measurements (apparatus: *BI-200M*, Brookhaven Instruments Corp., USA) give a mean size of the solution at 29 nm (Figure 2.26b). We will call this solution *Aq29nm-Det*.

2.5.2 Optical properties

A drop of *Aq29nm-Det* solution was deposited on a glass substrate and spin-coated. We studied the photoluminescence of the sample with the home-built microscope. We focused our attention on a diffraction limited spot and recorded the photoluminescence spectrum (Figure 2.27a,b). We observe the NV⁰ color center emission, even though the

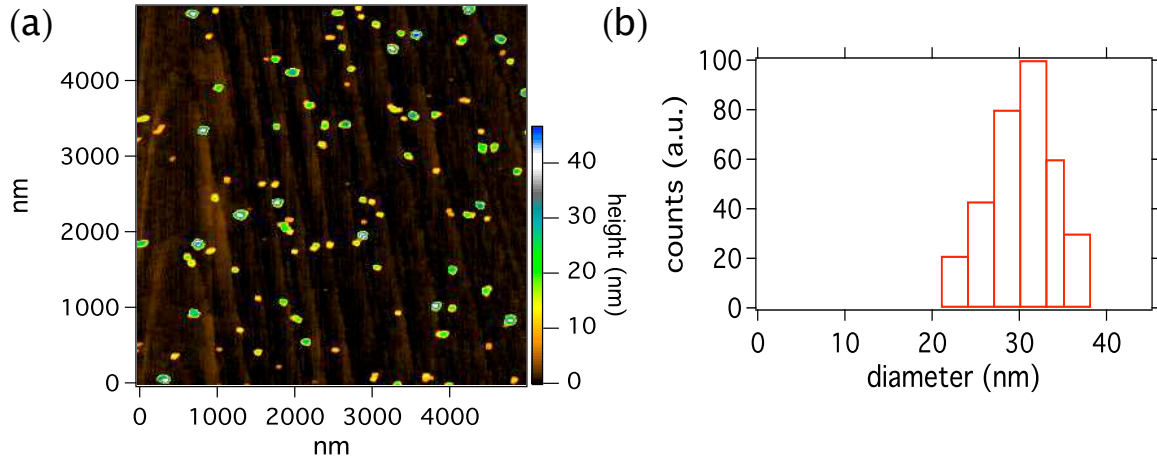


Figure 2.26: Size characterization of detonation nanodiamonds. (a) AFM scan of spin-coated NDs on a glass substrate, primary size 5-10 nm NDs are observed but also aggregates of 20-40 nm. (b) DLS measurement, mean size at 29 nm.

Zero Phonon Line at 575 nm is not well distinguished. The dichroic mirror used was the Q565LP (Chroma). Contrary to HPHT nanodiamonds of size < 50 nm, irradiated and annealed, the detonation nanodiamonds present here an unstable photoluminescence signal. Figure 2.27c depicts the photoluminescence intensity over a time period of 192 sec (recorded on one APD). We observed that the signal is not stable, but presents periods where it obtains very high values and other periods that is relatively constant, but remaining above the background level.

The counting rate for this ND is about $2000 \text{ counts}/50 \text{ ms} = 40 \text{ kcounts}/\text{s}$, corresponding to the counting rates recorded for single NV centers. This ND probably contains either one NV center (which like for the QDs presents “on“ and “off“ periods) or two NV centers. The latter case could explain the relatively constant signal at $1600 \text{ counts}/50 \text{ ms}$ (higher than the background level). No time-intensity correlation measurement was taken for this ND. To examine the generality of the “blinking” behavior, we recorded the signal from other nanodiamonds. We observe similar behaviors (Figure 2.27d).

2.5.3 Discussion

We have studied here the photoluminescence properties of pristine detonation nanodiamonds, neither irradiated nor annealed. The photoluminescence comes from NV° color centers. There was no NV^{-} characteristic spectrum in all the NDs studied (15 NDs). This is probably due to the lack of nitrogen donors in the diamond lattice, to form NV^{-} centers. The concentration of nitrogen atoms in detonation diamond has been recently studied and it was concluded that nitrogen atoms are mostly located in the diamond core, not in the graphitic shell [131]. The ratio of nitrogen to carbon atoms was found to be about 3%. This means that there is enough nitrogen in the diamond matrix to form NV centers.

However, nanodiamonds neither irradiated nor annealed may not have a large amount of vacancies, leading to a low probability of NV centers creation. This is the reason that

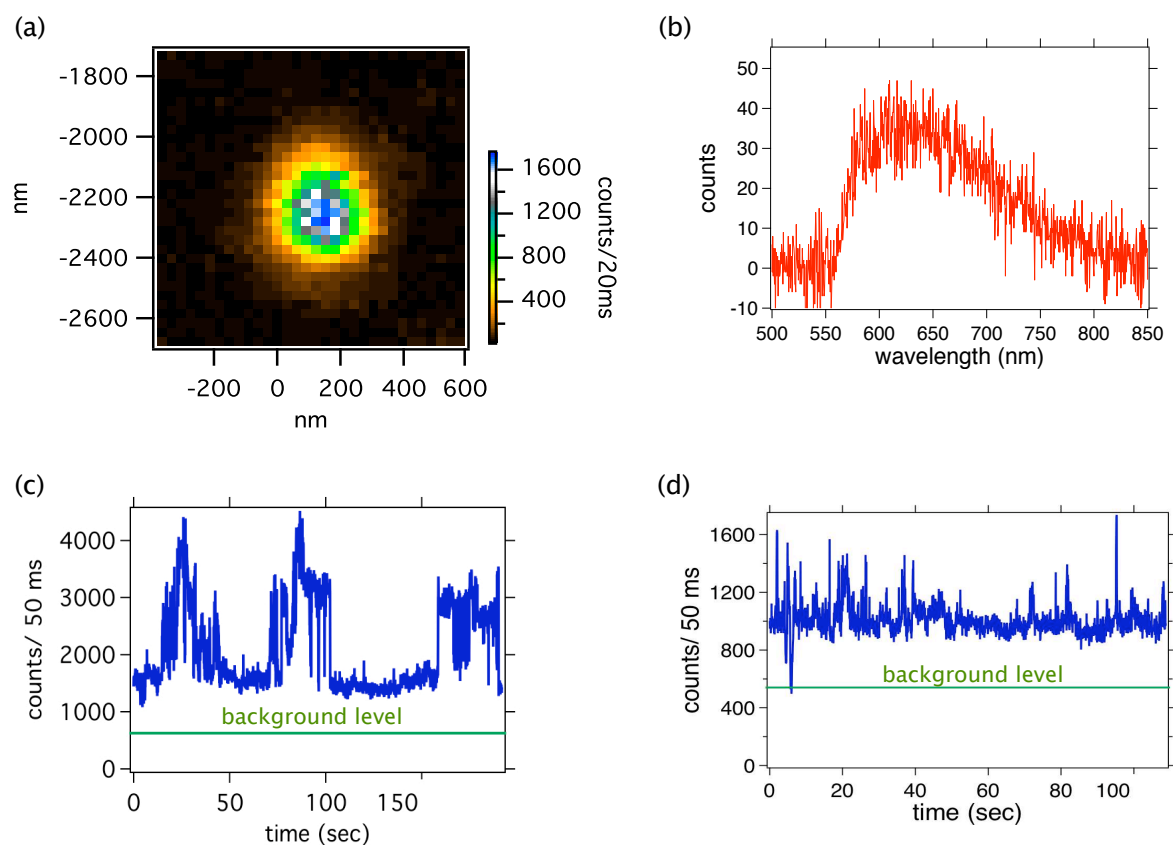


Figure 2.27: Photoluminescence properties of detonation nanodiamonds. (a) Confocal raster scan of the sample of Figure 2.26a, zoom in one nanodiamond (or small cluster of nanodiamonds); (b) Photoluminescence spectrum of (a), showing only NV° color center emission (the ZPL line is too weak to be well defined). (c) Photoluminescence intensity time trace sequence of the ND of (a), in green plain line the background level from the glass coverslip. (d) Photoluminescence intensity time trace of another nanodiamond of the same sample. Excitation cw laser at 488 nm, power 0.4 mW.

the photoluminescence signal recorded for our samples was relatively low. The instability of the signal is unusual for NV centers in HPHT NDs. For Quantum Dots of similar core size, the photoluminescence stability is characterized by a similar behavior (see section 2.3.3.). Size effects could play a crucial role for detonation nanodiamonds as well as the graphitic shell, which may act as a photoluminescence quencher.

Further investigations are necessary for the complete comprehension of this effect. Detonation nanodiamonds should be further irradiated and annealed, a process in progress in our team. Photoluminescent probes of this size have a great potential as labels and vectors of biomolecules in cells.

Chapter 3

Infrared pulsed excitation of NV centers in diamond micro- and nano-crystals

3.1 Two photon excitation of NV centers

3.1.1 Introduction

Two photon fluorescence microscopy (TPFM) is a technique widely used in biophotonics for the last two decades. The keypoint of this method for biology is that the wavelength of the excitation light lies in the infra-red, which is a low absorption spectral window for biological tissues and organs. Apart from endogenous fluorophores composing tissues, various organic molecules have been developed for efficient two photon excitation (TPEX). For a potential use of nanodiamonds as markers in biology, emission of NV color centers by 2-photon excitation could be of interest for *in vivo* imaging applications. We thus examined the TPEX efficiency of NV centers in bulk diamond and diamond nanocrystals and investigated the corresponding excitation spectra.

a Basic principles of two photon fluorescence microscopy

Two photon fluorescence microscopy belongs to the family of the non-linear microscopy techniques. In this family the rule is that:

$$(1 + \dots n) \text{ excitation photons} = 1 \text{ emission photon}$$

Maria Göppert-Mayer was the first, in 1931, to make the assumption that a fluorophore could simultaneously absorb two photons of low energy and emit one photon of higher energy [132]. After the first realization of a laser, by Ted Maiman in 1960, experimental verification of two photon absorption became possible [133]. Two years later Göppert-Mayer won the Nobel Prize in Physics. In 1982 two photon microscopy was used for spectroscopic studies of molecular excitation states [134]. Within a decade, Winfried Denk and Watt Webb developed the two-photon laser scanning microscopy for applications in neurobiology [135].

In two photon fluorescence, the simultaneous absorption of two photons is required. Two photons at pulsation ω having half the energy of the absorption transition ($E_{\text{abs}} =$

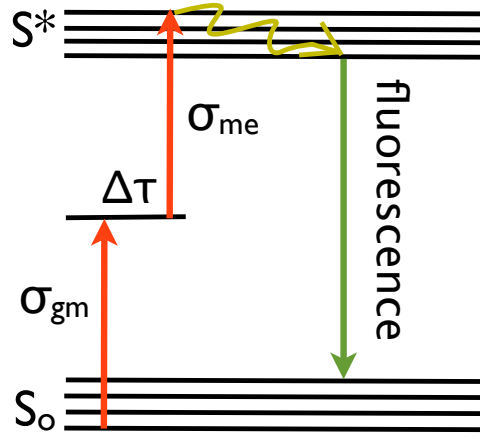


Figure 3.1: Simplified scheme of the energy transition occurring under Two Photon Excitation regime.

$2\hbar\omega_{1\text{phot}}$) of the absorption spectrum of the fluorophore are simultaneously absorbed. The probability of simultaneous absorption of two photons under natural light exposure is very small. According to a rough estimate, a molecule of rhodamine B, an excellent 1- or 2-photon absorber, absorbs one photon through a 1-photon process once a second, while it absorbs a photon pair by 2-photon absorption every 10^6 years [136].

From an experimental point of view, the probability for fluorescent emission from the fluorophores increases quadratically with the excitation intensity. As two photons need to be absorbed simultaneously, the use of pulsed lasers is much more appropriate to obtain high TPE yield.

The number n_a of absorbed photons per fluorophore per pulse can be expressed as:

$$n_a \approx \frac{\sigma_{2\text{ph}} P^2}{\tau_p f_p^2} \left(\frac{\text{NA}^2}{2\hbar c \lambda} \right)^2 \quad (3.1)$$

with P , f_p and τ_p the average power, repetition rate and pulse duration of the excitation laser respectively. $\sigma_{2\text{ph}}$ is the TPE cross section and NA the numerical aperture of the objective [135].

It is common to achieve the required high photon density by using pulsed lasers in the pico or femtosecond pulse duration regime, and high numerical aperture microscope objectives. Denk et al. used for the first time mode-locked lasers for TPE with pulse durations below 1 ps and fast repetition rates of about 100 MHz, to make two photon laser scanning microscopy adapted to biological applications [135].

Figure 3.1 illustrates the energy transitions occurring under 2-photon excitation. The time interval $\Delta\tau$ is the lifetime of the intermediate level m and is usually of the order of 10^{-15} s. The TPE cross subsection is defined as:

$\sigma_{2\text{ph}} \approx \sigma_{gm} \sigma_{me} \Delta\tau$, where σ_{gm} and σ_{me} are the single-photon cross-subsections for transition to and from an intermediate level m [137].

Usually the unit of Göppert-Mayer (GM) is used for the molecular cross section, where 1 GM is $10^{-50} \text{ cm}^4 \cdot \text{s} \cdot \text{photon}^{-1}$.

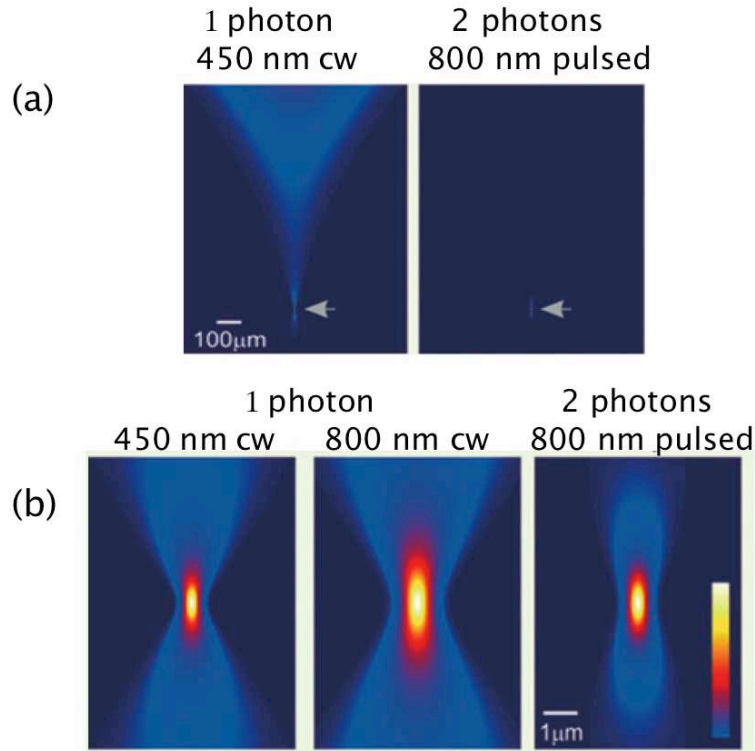


Figure 3.2: Advantages of TPFM, (a) intensity profile for one and two photon excitation along the penetration depth, note the point-shaped focus region of TPEx. (b) Two dimension images of the intensity profile in the $x-z$ or $y-z$ plane of a microscope, note the gain in the axial resolution for the TPEx. Numerical Aperture of the objective 0.5, abstract from [138].

The quadratic dependence of the absorption rate on the excitation power, gives TPFM its optical subsectioning properties because fluorescence is generated virtually only in the vicinity of the geometrical focus where the light intensity is high enough. While scanning the laser focus in both lateral x , y directions, fluorescence excitation is limited to the focal plane slice, and thus a confined image of a single subsection of the specimen is obtained [100, 137] (see Figure 3.2). Photodegradation of the surrounding medium is limited.

As a result, no detector pinhole is necessary, like in conventional (one photon) laser scanning confocal microscopy, since no fluorescence is generated outside the focal volume. The unique property of optical subsectioning as well as the long excitation wavelengths (for which the tissue absorption is low) allow deep penetration in tissues.

This technique is thus particularly well suited, e.g., for brain imaging, to record its functional signals, for instance from single dendritic spines [139–142].

TPFM is implemented in a very similar manner as laser scanning confocal fluorescence microscopy. This includes the acquisition of image stacks for subsequent 3-D reconstruction. Compared to confocal microscopy, TPFM provides a better imaging contrast, because the surrounding medium does not present TPEx properties.

The only crucial point for TPFM is that the molecules, tissues, etc that we want to examine must have a relatively high two photon absorption cross subsection [143],

otherwise the excitation power necessary to get a signal provokes photodamages to the biological sample.

b Two photon excitation of NV centers - state of the art

The first report on two photon luminescence of diamond nanoparticles was in 1999 by Mikov et al. [144]. They recorded the two photon excitation and luminescence spectra of detonation diamond nanoparticles with 4 nm average size. The observed TPEx luminescence bands, in the blue (400-500 nm) and ultraviolet (300-400 nm) were attributed to nitrogen-based defects (the N_2 and N_3 , different from NV centers [31]) by comparing the obtained spectra with the luminescence spectra in bulk diamond.

It was only in 2007 that Wee et al., in the team of H.-C. Chang, observed TPEx photoluminescence of NV centers in proton irradiated type Ib bulk diamond [14]. They excited diamond single millimeter-sized diamond crystals with a mode-locked Nd:YVO₄ picosecond laser at 1064 nm and recorded the two photon photoluminescence spectrum. In addition, they estimated that $\sigma_{2ph} = 0.45$ GM for the NV⁻ center, assuming that the fluorescence quantum yield is the same for both one photon and two photon processes. The obtained values for σ_{2ph} were further confronted to theoretical models [145]. These values are smaller in comparison with other two photon fluorescence probes (for CdSe/ZnS QDs, $\sigma_{2ph} = 50 \times 10^3$ GM [146]) but much higher than the ones of various molecules (like flavines, $\sigma_{2ph} = 0.05$ GM [147]).

The first report on two photon photoluminescence signal in nanodiamonds with NV centers came in 2008 [47]. They observed, under femtosecond laser illumination at 875 nm, the Two Photon Emission (TPEm) properties from NV centers embedded in 35 and 140 nm containing nanodiamonds deposited on substrates and in cells. They conclude that TPEm is a better method for filtering the intracellular medium background noise (Figure 3.3).

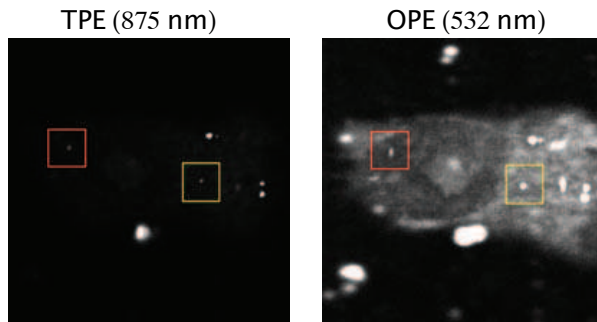


Figure 3.3: Two photon and one photon excited confocal photoluminescence scans of 140 nm PNDs in a fixed cell [47].

At the same time, in our team we were observing TPEm of nanodiamonds, with picosecond laser illumination at 1064 nm. Additionally, we studied the TPEx properties of NV centers in bulk diamond and in nanocrystals. With these results we determined the optimal excitation wavelength for TPEx.

3.1.2 Two Photon Excitation properties of NV centers in bulk diamond

Our objective was first to try to observe two-photon photoluminescence of the NV color center using a “home-built” picosecond pulsed laser and then to determine the optimal wavelength for TPE_x, using a tunable femtosecond laser.

a Experimental Setup

Mode-locked Nd:YVO₄ picosecond laser

The laser used was a “home-built” mode-locked Nd:YVO₄ picosecond laser. It was provided by P. Georges (Institut d’Optique, LCFIO, Palaiseau) and was built and aligned by F. Druon and D. Papadopoulos.

Figure 3.4a illustrates its basic components. It consists of a diode pump at 808 nm with a maximum output power of 30 W. The diode pumps a 10 mm long Nd:YVO₄ crystal. Light is guided in a multiple pass cavity (MPC) [148], where it makes round trips by 4 mirrors, reflects once on a Semiconductor Saturable Absorber Mirror (SESAM, $\lambda = 1064$ nm, saturable absorption 1.8%) [149], and goes the way back before leaving the cavity. The initial cavity length is about 2 m, and with the proper adjustment of the number of the round trips in the MPC the realized repetition rate is at 4.8 MHz (corresponding to a 32 m length in the MPC).

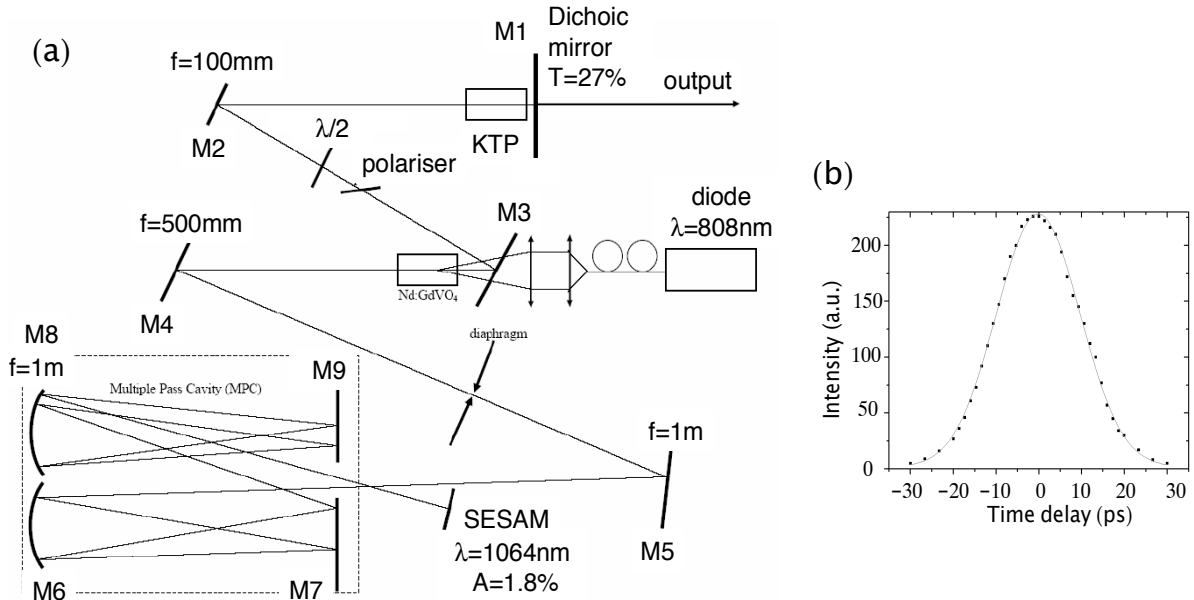


Figure 3.4: The setup of the “home-built” mode-locked Nd:YVO₄ picosecond laser. (a) Experimental setup of the laser cavity, abstract from [150]. (b) Intensity autocorrelation signal of a laser pulse. It has a Gaussian profile, with a pulse duration of 16 ps [148].

The system is mode-locked due to the SESAM. The output beam of the cavity re-passes through the Nd:YVO₄ crystal and a quadratic polarization switching (QPS) system defines the temporal characteristics of the ps pulses. It consists of a half-wave plate,

a polarizer, and a KTP crystal (length 8 mm) coupled with a plane output mirror ¹. The plane output mirror is the exit mirror of the laser system (Transmission 27% at 1064 nm).

Figure 3.5 shows the laser setup used in our experiments. The output mean power of the 1064 nm beam is 1.6 W. This is translated to a pulse energy of $E = P_{\text{average}}/f = 333 \text{ nJ}$ (f the repetition rate) and a peak power $P_{\text{peak}} = E/\Delta t = 21 \text{ kW}$, values sufficient for 2-photon excitation experiments. The low repetition rate (4.8 MHz) and the pulse duration (16 ps, Figure 3.4b) are values that allow us to measure the decay lifetime of the NV centers and perform time-gated imaging experiments (Annexe C).

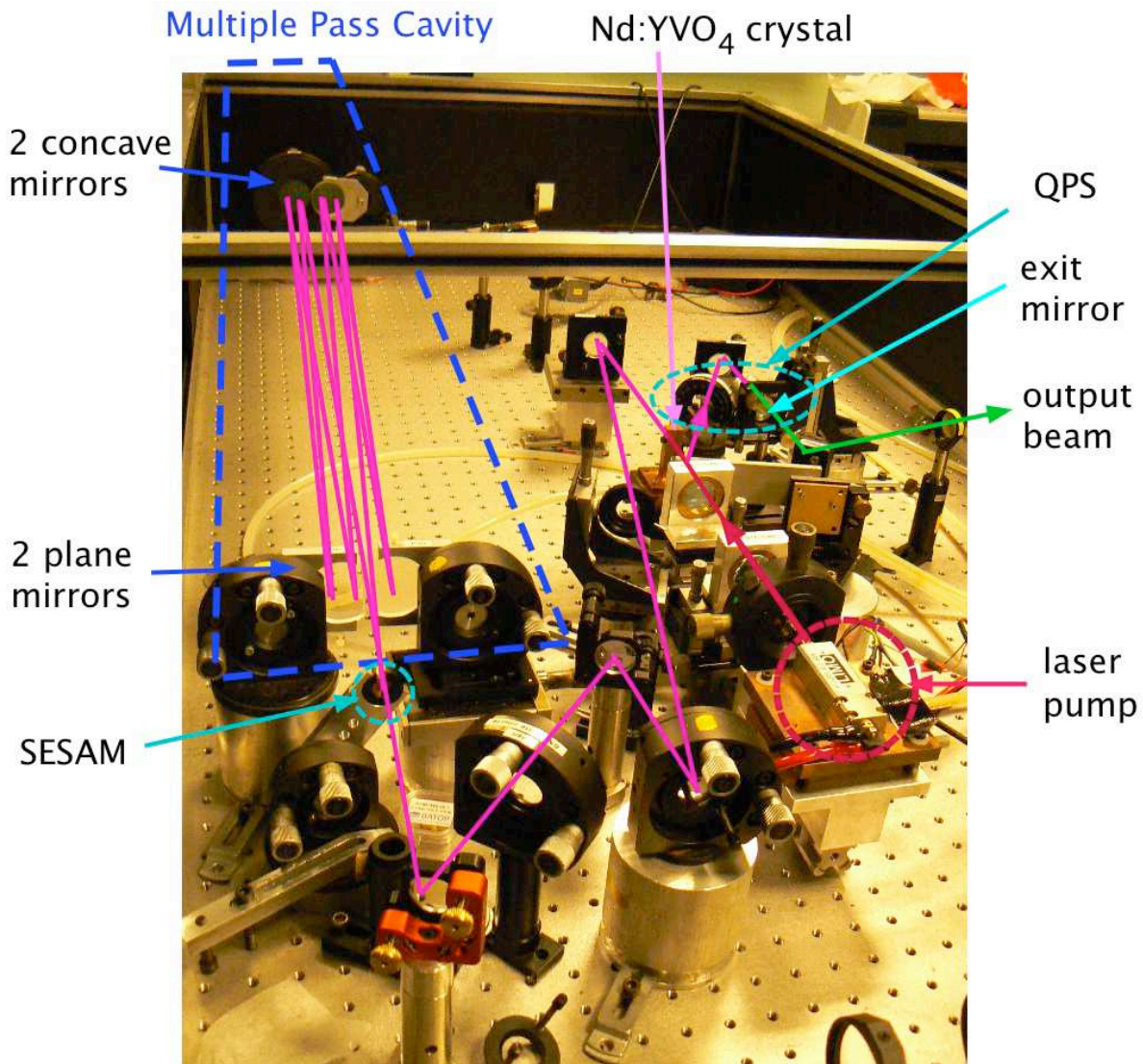


Figure 3.5: Photograph of the “home-built” mode-locked laser setup. In dashed blue the Multiple Pass Cavity (MPC), consisting of 2 concave mirrors ($f=1 \text{ m}$) and 2 plane mirrors. The output beam is represented in green, only to show the exact position of the KTP crystal of the QPS system, but it is the 1064 nm that is dominant in terms of mean power.

¹more details on QPS can be found in Ref. [150, 151]

Optical setup

TPEm of NV centers in diamond was firstly recorded by implementing the mode-locked picosecond laser on the home-built confocal microscope (described in chapter 2). We studied both diamond microcrystals and nanodiamonds. Figure 3.6 illustrates the optical setup for one and two photon excitation.

The picosecond laser operates at 1064 nm for TPEx and is subsequently doubled in frequency with a 1.5 cm long KTP crystal at 532 nm for one photon excitation (OPEx) experiments. After the KTP crystal a dichroic mirror reflects the green light and transmits the infra-red, resulting in a spatial separation of the two beams at the different wavelengths, which allows independent modifications of each beam. The green beam is collimated with a 500 mm focal length lens (L1), is spatially filtered by a 100 μm diameter pinhole (PH) and passes through a half-wave plate and a polarization beamsplitter (PBS), which enables us to control the green excitation power in the sample plane. A quarter-wave plate with the proper optical axis orientation transforms the polarization of the beam into a circular one, a necessary requirement to obtain a maximum signal from the sample (due to the the different emitting dipole orientations).

The infra-red beam is also collimated with a 500 mm focal length lens (L2) and passes through an equivalent system of a half-wave plate with a PBS. The beam is spatially filtered by a 100 μm diameter pinhole (PH). The green and infra-red beams are recombined through a broadband Beamsplitter (BS) (BSW14, Thorlabs).

For TPEx the green beam is blocked with a beam block while for one photon excitation the beam block is placed on the IR beam.

Both laser beams are reflected by a dichroic mirror (700dcsx, Chroma Technology Corp., USA) and focused by a microscope objective ($\times 60$, NA 1.4 oil immersion) onto the sample mounted on a piezoelectric scanning stage. The resulting one and two photon photoluminescence signal is collected using the same objective. The rest of the experimental setup is the same as the one described in chapter 2.

For this experiment we used only one photodiode (APD, SPCM-AQR14, Perkin-Elmer, Canada). In front of the photodiode a shortpass (SP) filter (Melles Griot 03SWP418) and a Schott KG4 shortpass filter cut the infra-red light and let pass the NV center fluorescence light. A Schott KG5 filter is put after the confocal pinhole to cut the remaining infra-red excitation light (it cuts selectively light above 750 nm). The residual 532 nm excitation laser light is removed with a long-pass filter (LPF, transmission of 97% at 539-1200 nm, *RazorEdge LP03-532RU-25*, Semrock, USA).

Tunable Femtosecond laser

The femtosecond laser used is a mode-locked Ti-sapphire laser (Mai-Tai from Spectra Physics) with a temporal pulse width of 80 fs and tunable wavelength in the 700-1020 nm range.

The optical setup is similar to the one of Figure 3.6, with the difference that no confocal pinhole is used.

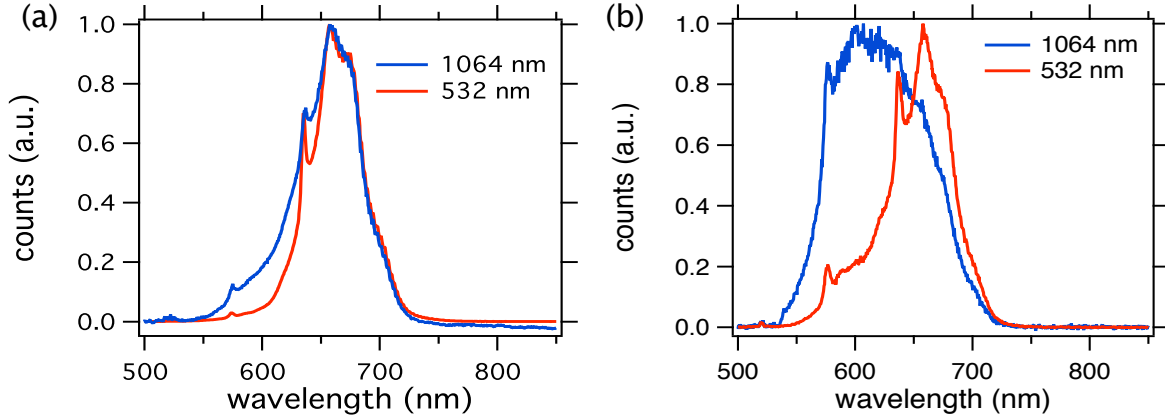


Figure 3.7: Comparison of one- and two-photon excited fluorescence spectra of a type Ib diamond microcrystal containing NV color centers. (a) “Low” excitation power regime $P_{\text{exc}}^{532} = 0.16$ mW and $P_{\text{exc}}^{1064} = 6.2$ mW. (b) “High” infra-red excitation power regime $P_{\text{exc}}^{532} = 0.24$ mW and $P_{\text{exc}}^{1064} = 186$ mW

c Two Photon Excitation spectra of NV centers in diamond microcrystals

The same crystals were examined under femtosecond laser excitation. The Ti:Sapphire laser with a tunable wavelength enables us to record the two photon excitation spectra of both NV center types. To spectrally select the NV° and NV^- center emission, we used the 10 nm bandpass filter 580/10 and HQ740 longpass filter respectively (Chroma Tehno. Corp., USA).

Figure 3.8 shows the two photon excitation spectra of NV° and NV^- centers recorded in the wavelength region of 750-1020 nm with 1 nm spectral resolution, at room temperature.

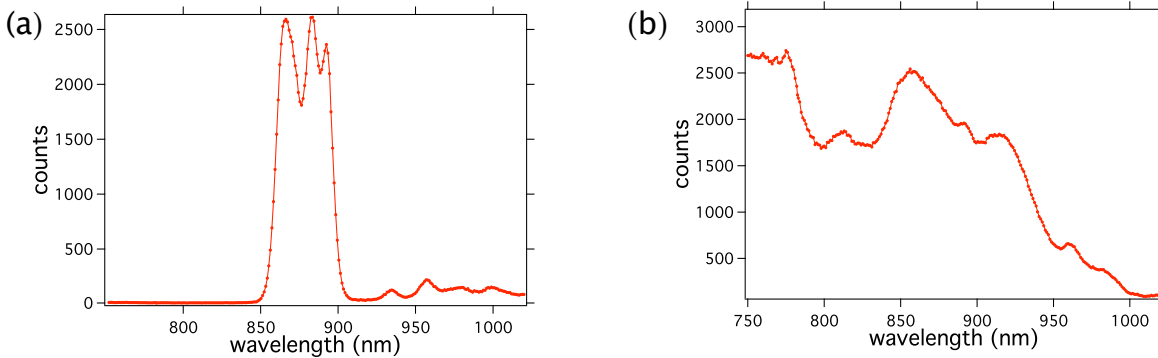


Figure 3.8: Two photon excitation spectra of NV center photoluminescence of (a) NV^- center and (b) NV° center. The spectrum was corrected for the wavelength dependence of the excitation power function of the Ti:Sapphire femtosecond laser with a 0.1 mW excitation power at 1064 nm.

The NV^- TPEX spectrum has a maximum in the region of 850-900 nm, has low intensity above 900 nm and vanishes below 850 nm. The latter observation is in agreement with previous reports of the one photon excitation spectrum of the NV^- center [13, 45].

As seen in chapter 2, Figure 1.4, below $850/2 = 425$ nm the excitation spectrum goes to zero, in perfect accordance with our measurements. However, if we look more carefully to the one photon excitation spectrum, we observe a maximum in the range of 500-600 nm, which should yield in the two photon excitation spectrum a maximum around 1000 nm. The recorded signal in this range (>1000 nm) is almost zero.

For the NV° center, we also observe almost no signal above 1000 nm, while the excitation spectrum is relatively broad and lies in the region of 750-900 nm. Similar blue shifts of the TPE spectra have been also reported for other fluorophores, like Rhodamine B and Fluorescein [152] and can be attributed to a higher probability for an excitation of higher excited energy states by TPE than by OPE.

d Corrections for the optical setup transmission

The above excitation spectra measurements have taken into account the corrections due to the optical components used. More specifically, the average excitation power of the laser was every time measured at the microscope entrance, i.e. before the dichroic mirror and the microscope objective. These elements present different transmission properties for the visible and infra-red light.

The conversion of excitation power from the input of the microscope to the sample plane was performed using the equation:

$$P_{\text{sample}} = \alpha \times P_{\text{measured}} \quad (3.2)$$

where α is a coefficient including the transmission of every optical component between the plane where the power is measured and the sample plane. In our case $\alpha = R_{DM} \times T_{\text{objective}}$, with R_{DM} being the reflectivity of the dichroic mirror and $T_{\text{objective}}$ the transmission of the objective.

Figure 3.9 illustrates the wavelength dependence of R_{DM} and of the Transmission of the microscope objective². The microscope objective reaches its maximum value of $T \approx 81\%$ for 520-570 nm. At 1064 nm the transmission becomes only 62%.

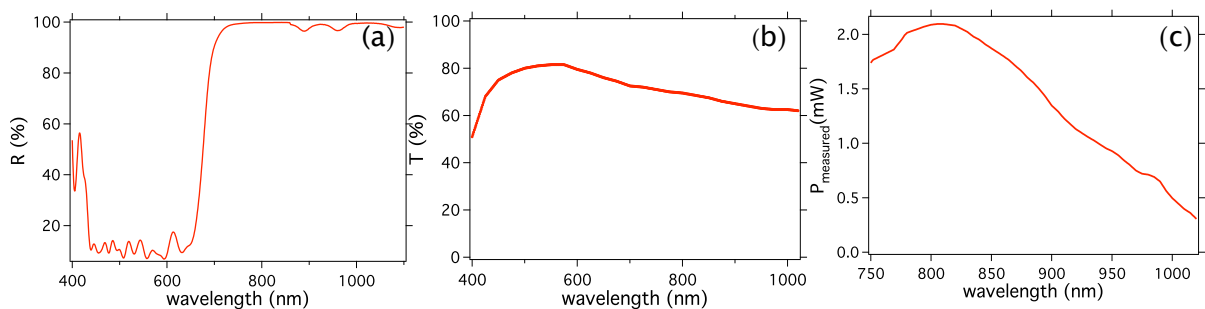


Figure 3.9: Power losses of the excitation beam before reaching the sample plane. (a) Wavelength dependence of the dichroic mirror reflectance. (b) Wavelength dependence of the objective transmission (provided by Nikon). (c) Incident power of the femtosecond laser versus its wavelength, measured just before the dichroic mirror.

²it is the Transmission curve of the Nikon $\times 100$, used on the femtosecond laser excitation setup. For the setup with the picosecond laser excitation we used a Nikon $\times 60$, see Appendix D.

For excitation with the Ti:sapphire laser and the TPE spectra, we took into account the output power dependence on the laser wavelength, which presents a maximum at 800 nm (Figure 3.9c).

3.1.3 Two Photon Excitation properties of NV centers in nanodiamonds

a Two Photon Excitation spectra of NV center photoluminescence in diamond nanocrystals

For biological applications one needs to use small and bright nanoparticles. To investigate the TPEx photoluminescence of nanodiamonds, we used type M nanodiamonds. We centrifuged at 25,000g for 20 min an aliquot of the *Aq164nm-Me18* solution and we obtained a solution of 100 nm PNDs (with a broad size distribution ± 42 nm, verified by DLS). We will call this sample *Aq100nm-Me18*. The PNDs solution was spin-coated on a glass coverslip. TPEx photoluminescence of nanodiamonds, displayed on Figure 3.10a, was recorded by using the femtosecond mode-locked Ti-sapphire laser.

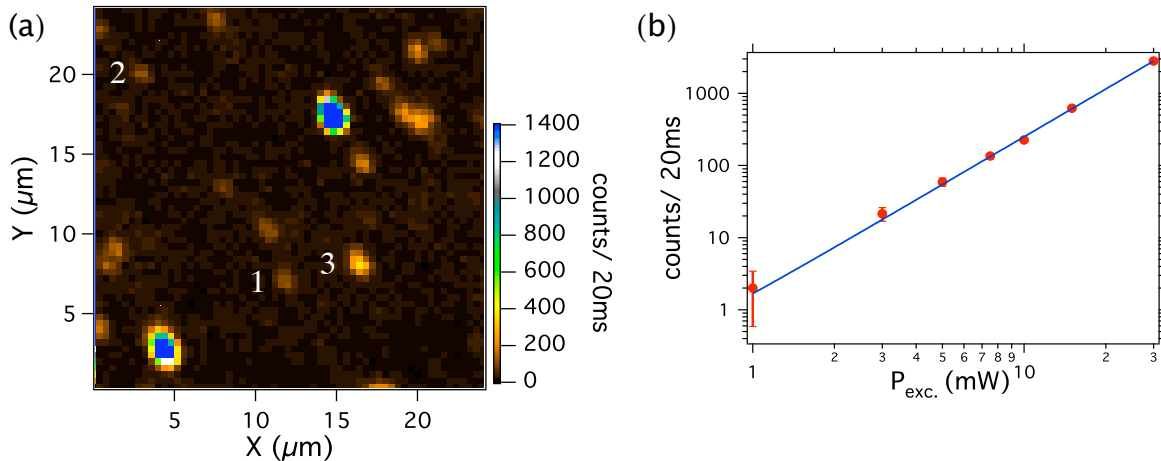


Figure 3.10: (a) Two photon excited photoluminescence raster-scan of PNDs deposited on a glass coverslip, excitation wavelength 820 nm, excitation power on the sample plane 9 mW. (b) Dependence of the photoluminescence intensity of a PND on the incident laser power in a log-log plot.

The two photon process is confirmed by the laser power dependence of the photoluminescence intensity. The fit, using a log-log plot, gives a slope of 2.09 ± 0.11 (Figure 3.10b).

Figure 3.11 shows the TPEx spectra of the three 3 nanodiamonds marked on the scan of Figure 3.10a. We observe that for PNDs containing only NV° centers (assessed from the emission spectrum characteristic zero-phonon line at 575 nm), the TPEx spectrum presents maximum values in the region of 750-800 nm. The nanodiamond of Figure 3.11c has a maximum excitation spectral region at 800-900 nm, but it contains both types of NV centers (Figure 3.11f). These measurements are in agreement with the excitation spectra recorded for diamond microcrystals. In both cases we observe for NV° center a maximum value region for 750-800 nm while for NV^{-} center this region lies in 850-900 nm.

Normally no differences between one- and two-photon fluorescence emission spectra should be observed, as for every two photon fluorophore there is usually substantial overlap between the TPEX and OPEX spectra when plotted at twice the wavelength [147]. Blue shifts are sometimes reported, for example for rhodamine and several ion-sensitive fluorophores.

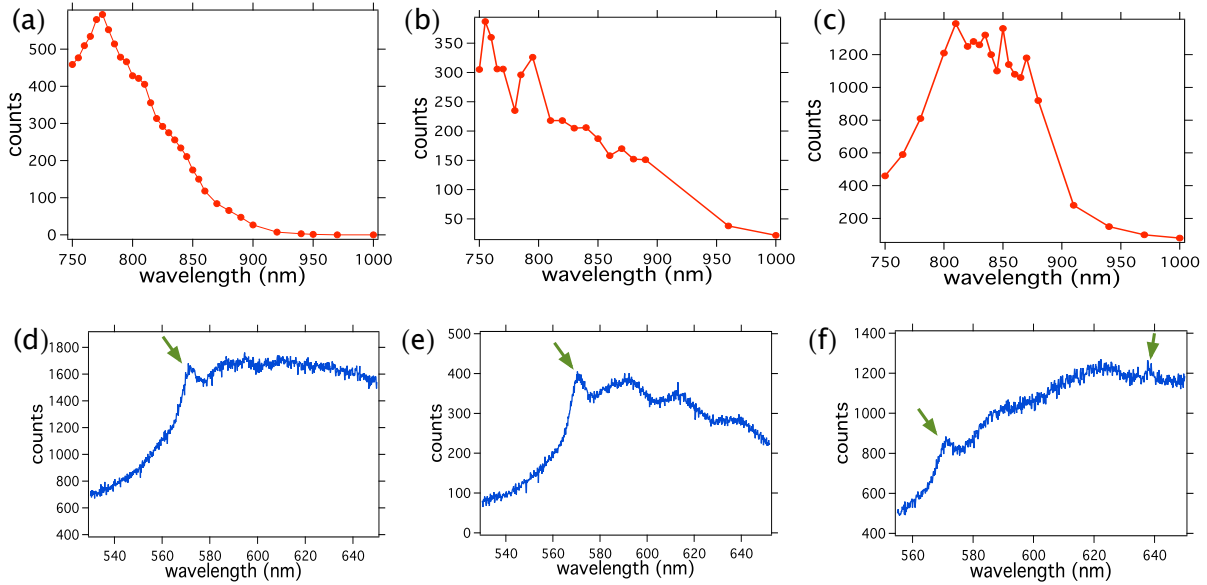


Figure 3.11: Two photon excitation spectra. (a-c) TPEX spectra of nanodiamonds 1, 2, 3 respectively of the scan of Figure 3.10, the excitation power was constant at 8 mW, the resolution step is 5-10 nm. (d-f) Two photon emission spectra of nanodiamonds 1, 2, 3 respectively, in green arrows the ZPL lines of NV° and NV^{-} centers.

However, in our case for both types of NV centers the expected signal above 1000 nm (two times the values of the OPEX spectrum maximum) does not exist. The TPEX spectrum becomes apparent for values below 900-950 nm. This indicates that in the region of 1000 nm another phenomenon is involved, which in a way quenches the TPEM of the NV center. This will be the object of study of the following section.

Note that the emission spectrum of Figure 3.11b presents some oscillations, which are due to the filter used; it was a shortpass Melles Griot 03SW416 while for the other spectra a shortpass Melles Griot 03SW418 was used and no oscillations were observed.

b Two Photon Excitation Photoluminescence properties of NV centers in nanodiamonds

TPEX with the picosecond laser at 1064 nm

As seen on the excitation spectra (Figure 3.11), TPEX photoluminescence signal is much stronger under an excitation wavelength of about ≈ 800 nm than at 1064 nm. Moreover, with our picosecond laser excitation the signal should be weaker than with a femtosecond excitation, as the repetition rate is lower (4.8 MHz versus 80 MHz for the femtosecond laser). Nevertheless, we tried to record a TPEX photoluminescence signal of NV centers in nanodiamonds by using the mode-locked picosecond laser at 1064 nm. Indeed, the

study under 1064 nm excitation has been done earlier than the one under 800 nm, since the picosecond laser was already available on the optical table, together with a cw 532 nm laser. Thus with these two lasers on the setup we could carry out comparative studies of the one and two photon excited photoluminescence spectra.

Figure 3.12 shows the corresponding raster scans for one and two photon excitation for 100 nm PNDs (*Aq100nm-Me18*), spin coated on a glass coverslip (the same sample as the one used for the TPEX spectra acquisition).

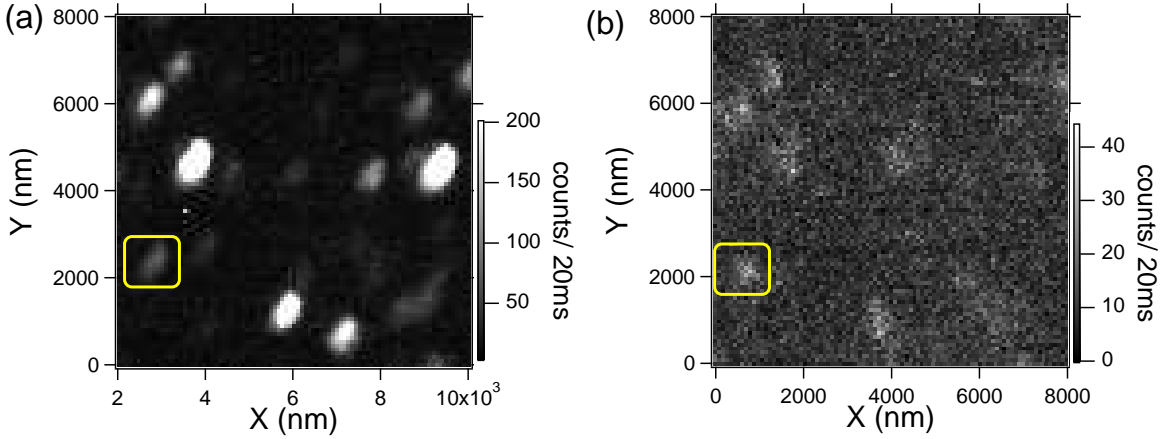


Figure 3.12: One and two photon excited photoluminescence of *Aq100nm-Me18* sample. (a) OPEX photoluminescence scan of 100 nm PNDs, excitation wavelength 532 nm, power 0.16 mW. (b) TPEX scan of the same region as in (a), excitation at 1064 nm, power 180 mW.

To confirm that the 1064 nm excited photoluminescence is indeed a two photon process, laser power dependence of the photoluminescence intensity was carefully measured. Figure 3.13a displays a logarithmic plot of the measured photoluminescence intensity versus the average laser power used for the excitation of the PND located in the yellow square on Figure 3.12. The slope of the linear fit is 1.79 ± 0.31 , indicating that we have a two photon process. Additionally, the TPEX photoluminescence signal is photostable over time.

The corresponding OPEM and TPEM spectra of the PNDs (*Aq100nm-Me18*) were also measured. The PNDs presented both NV° and NV^- centers, as we can distinctly see both types of zero-phonon lines on the OPEM spectrum (Figure 3.14a). Under TPEX the shape of the spectrum changes and only the NV° ZPL can be distinguished. The same ionization process as the one observed in bulk diamond occurs. By taking another OPEX spectrum, after two photon excitation with the 1064 nm laser, we interestingly observe that a fraction of the NV° centers was reconverted to NV^- . However, some centers were irreversibly converted to NV° centers. By calculating the intensity ratio of the corresponding ZPL lines, we conclude that for this nanodiamond 25% of the NV centers underwent an irreversible conversion in NV° .

This observation confirms earlier reports. Manson et al. and Dumeige et al. have previously reported a change of charge state of the NV center under a high excitation power [153, 154]. They identified a direct photo-ionization of the NV^- center, for a wide range of wavelengths (458 to 532 nm). More recently, Acosta et al. have carried

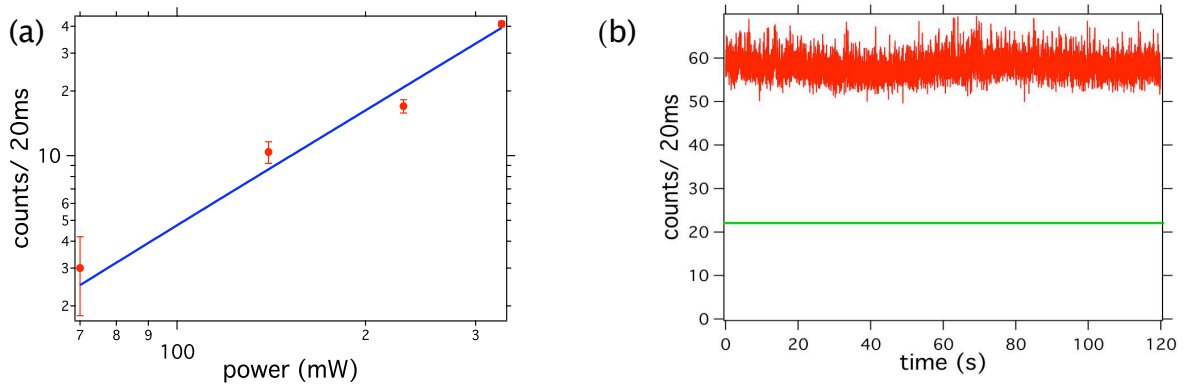


Figure 3.13: (a) Dependence of TPEm intensity on the incident laser power in a log-log plot of the PND in yellow square of Figure 3.12. (b) Photostability test of the same PND upon TPEx. In green, the background average level, excitation wavelength 1064 nm, power 180 mW.

out a systematic study, showing the $NV^{\circ}:NV^{-}$ ZPL intensity ratio dependence upon the pump laser power, for high and low nitrogen concentration diamond [155]. They found that for the high nitrogen concentration diamond the dependence is specifically strong (Figure 3.15).

In our case, the decrease of the photoluminescence intensity of the NV^{-} after illumination at 1064 nm (Figure 3.14c) is attributed either to a slight shift of the nanodiamond from its focus or to its partial surface graphitization, due to the high excitation power.

It is obvious that the excitation power needed for TPEx of nanodiamonds at 1064 nm is very high (average power >100 mW). It has to be mentioned that sometimes, due to the high excitation power, the TPEm signal of PNDs suddenly disappeared. Figure 3.16 shows a typical OPEx scan of a PND and the corresponding TPEx scan, with a characteristic “photobleaching”. One explanation is that the structure of the nanodiamond was altered due to the high excitation power. Graphitization and diamond “burning” effects were observed in our group for diamond crystals for this range of excitation powers.

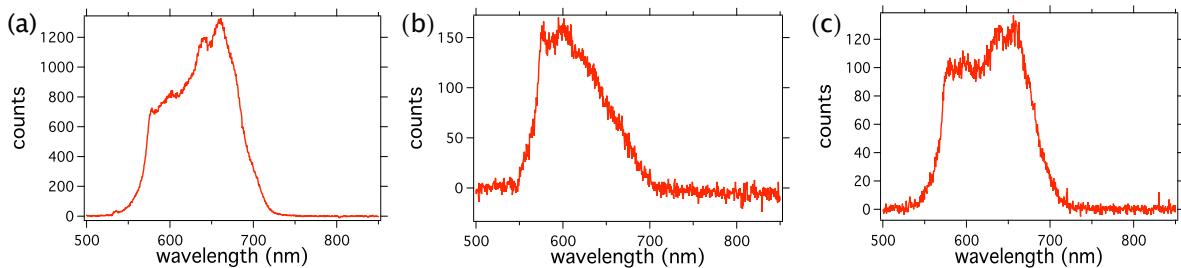


Figure 3.14: Comparison of photoluminescence spectra acquired with: (a) One photon excitation at 532-nm, excitation power 0.26 mW in sample plane, acquisition time 2×30 s. (b) Two photon excitation at 1064 nm, excitation power 200 mW, acquisition time 2×60 s. (c) One photon excitation after the TPEx, same parameters as in (a), the increase of the ZPL ratio in favor of the NV° ZPL indicates the conversion of NV^{-} in NV° center under the infra-red laser illumination.

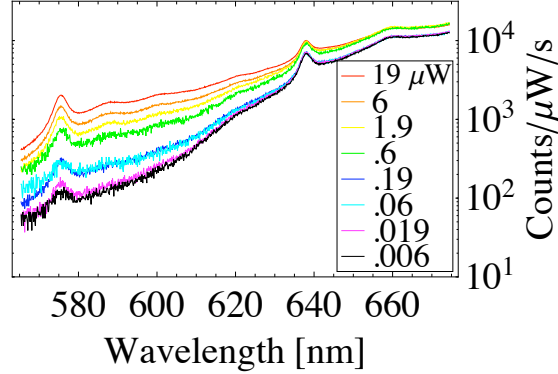


Figure 3.15: Photoionization of NV^- center according to Ref. [155]. The graph represents the $NV^\circ:NV^-$ ZPL intensity ratio as a function of the excitation power, for an electron irradiated bulk diamond sample.

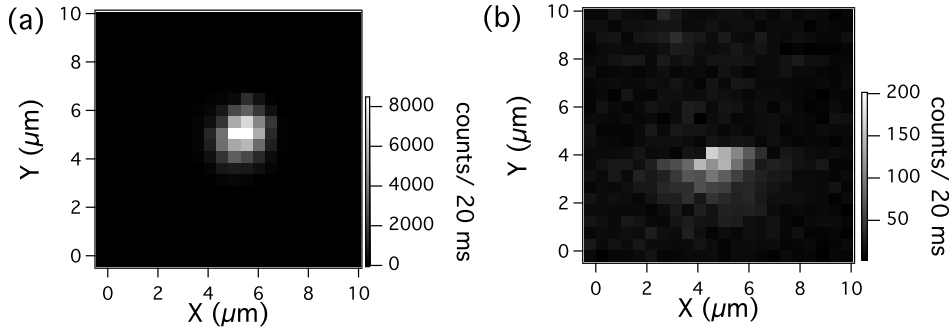


Figure 3.16: (a) OPEx photoluminescence scan of a PND, excitation power $80 \mu\text{W}$. (b) TPEx photoluminescence scan of the same PND, excitation power 250 mW . Photobleaching occurred during the scan.

3.1.4 Conclusion

In this section we studied the two photon excitation photoluminescence properties of NV centers in bulk diamond and in nanocrystals.

We observed that for bulk diamond, probably due to the high excitation power required for a two photon process, the NV centers undergo ionization. As a result, in the two photon emission spectra the characteristic features of the NV° center are always reinforced.

The two photon excitation spectra were also recorded, for both NV° and NV^- centers. We found that NV° and NV^- centers are better excited in the range of 750-800 nm and 850-900 nm, respectively. On the evidence of the one photon emission spectra, the NV^- center should be better excited for longer wavelengths. This criterion was fulfilled, but only up to a given value of wavelength. Above 950-1000 nm we recorded almost no two photon photoluminescence signal. We tentatively explain this phenomenon due to a quenching of the NV center photoluminescence, a phenomenon further addressed in the following subsection.

Finally, we recorded a two photon photoluminescence signal from nanodiamonds.

We observed similar effects of ionization of the NV center as in bulk diamond. The two photon excitation spectra were also similar to the ones obtained in diamond microcrystals. Although the two photon absorption cross section of NV⁻ center is relatively small [14] in comparison with other two photon fluorescence probes (quantum dots [146]), it is much higher than the one of various molecules responsible for endogenous fluorescence of tissues (like flavines [147]). We therefore believe that nanodiamonds with a larger number of NV centers can yield a high enough signal, to render nanodiamonds a promising two photon excitation probe for biological applications.

3.2 Quenching of the NV center photoluminescence and applications

3.2.1 State of the art

In regular confocal microscopy, image resolution is limited by diffraction, preventing to resolve complex small size structures which can be of great importance to understand biological processes. For life sciences, where the systems under study can have typical sizes in the nanometric scale, high resolution imaging is of fundamental importance. Special techniques allow the improvement of the resolution imaging allowing detailed studies of the conformations of biological complexes.

Different super-resolution techniques have been extensively developed over the past ten years (STED, GSD, PALM, STORM. . .) [156] among which the Stimulated Emission Depletion (STED) and Ground State Depletion (GSD) microscopies are the oldest ones. The STED technique is based on the depletion of the first excited state, while the principle of GSD is the ground state depletion.

Ground State Depletion microscopy

Ground state depletion (GSD) was first proposed by Stefan Hell in 1995 [157], but it was realized experimentally for the first time in 2007, because the appropriate fluorescence probes had to be developed (with optimal photophysical parameters, including a low photobleaching yield) [158].

In the case of an organic fluorophore, the physics principle lies on the selective switching of the molecule in an ON and OFF fluorescence state. The switching off of the fluorophore is obtained by transiently shelving the fluorophore down to its metastable dark triplet state T₁ via a non-radiative S₁ → T₁ crossing (Figure 3.17a). In this way, the transition from the S₀ ground state to the S₁ excited state is strongly saturated since the fluorophore is trapped in the T₁ OFF state.

Figure 3.17a illustrates the ON-OFF state mechanism. The molecule is excited from the ground state S₀ to the first excited electronic singlet state S₁ with an excitation rate $k_{\text{exc}} = \sigma \frac{\lambda}{hc} I$, with σ the absorption cross section, λ the excitation wavelength, c the speed of light and I the excitation intensity. The most probable relaxation from the S₁ state is the return to the ground state S₀ by internal conversion (with decay rate k_{Q}) or spontaneous emission of a photon (k_{fl}).

Another much less probable way for the molecule to return to the ground state is

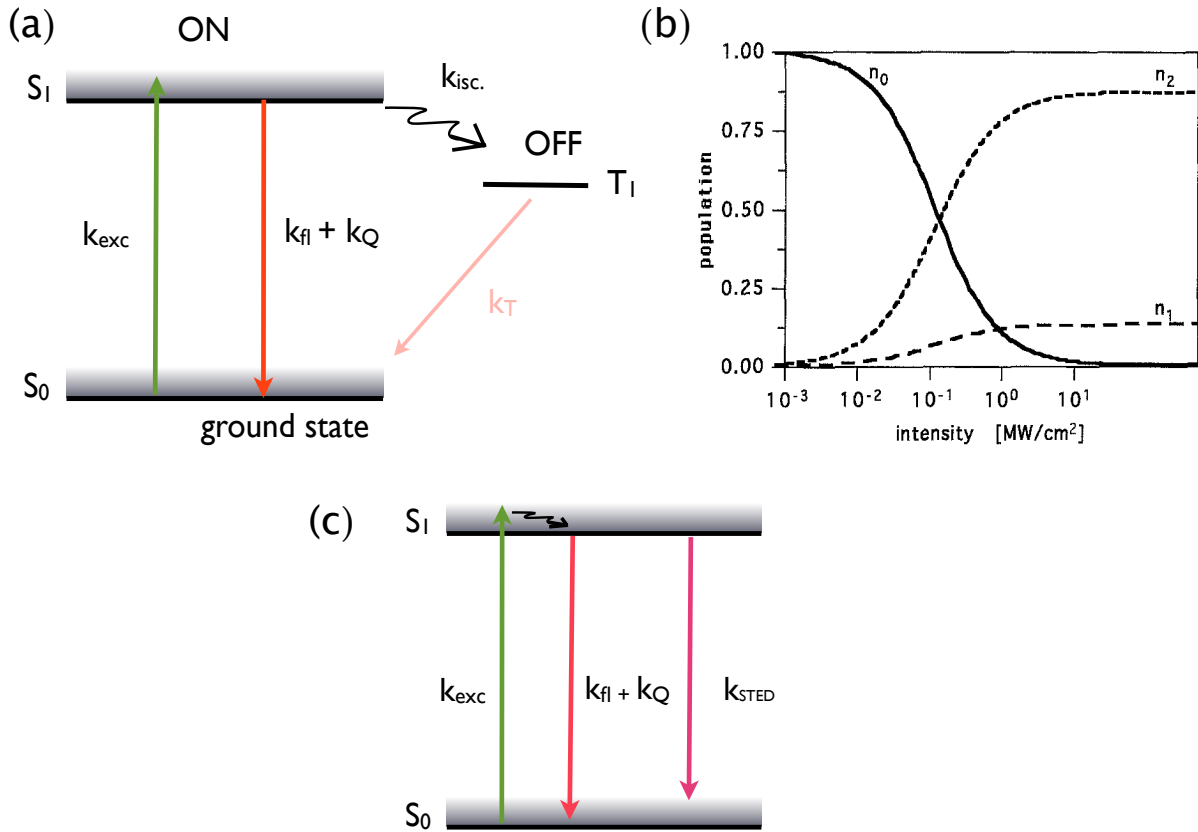


Figure 3.17: (a) Photophysical transition mechanism of bright and dark states for GSD. (b) Evolution as a function of the excitation intensity of the population probability of the ground state n_0 , the lowest energy excited singlet state n_1 , and the triplet state n_2 , for fluoresceine molecule [157]. (c) Photophysical transition mechanisms of fluorescence and stimulated emission. For an efficient quenching process one should achieve $k_{fl} \ll k_{STED}$.

that the molecule undergoes an intersystem crossing process (k_{isc}) from the S_1 state to the triplet state T_1 . From that intermediate state the molecule returns back to the S_0 state with a much slower rate k_T than for the $S_1 \rightarrow S_0$ transition. The decay rate of the triplet state is very low and this state is a dark state.

Under a strong laser illumination of the molecule (i.e. high excitation rate), it is possible to produce a nearly complete population of the triplet state (Figure 3.17b). The molecules are stocked in that state because of the state's long lifetime.

The population probabilities of Figure 3.17b were calculated by setting up a rate equation model for the three states, the 0, 1 and 2 for the ground, first excited and dark state respectively ³ [157, 159].

The population probability of the ground state at the equilibrium is found:

³The rate equation for the 3-level model:

$$\begin{aligned} \frac{dN_0}{dt} &= -k_{exc}N_0(t) + (k_{fl} + k_Q)N_1(t) + k_T N_2(t) \\ \frac{dN_1}{dt} &= k_{exc}N_0(t) - (k_{fl} + k_Q)N_1(t) - k_{isc}N_1(t) \\ \frac{dN_2}{dt} &= k_{isc}N_1(t) - k_T N_2(t), \text{ with } N_0 + N_1 + N_2 = 1 \end{aligned}$$

$$N_0 = 1 - \frac{k_{\text{exc}}k_{\text{isc}}}{D} \left(1 + \frac{k_{\text{T}}}{k_{\text{isc}}}\right) \quad (3.3)$$

with $D = k_{\text{T}}(k_{\text{exc}} + k_{\text{fl}} + k_{\text{Q}} + k_{\text{isc}}) + k_{\text{exc}}k_{\text{isc}}$

Equation 3.3 shows that the probability to have the fluorophore in the ON state reduces in a non linear way either by increasing the excitation intensity or by increasing the lifetime of the OFF state.

The observed fluorescence signal is proportional to $1 - n_2$ (where n_2 the probability for the system to be in the dark state). The normalized fluorescence signal (normalized to the initial signal without the depletion beam) can be expressed as :

$$\eta(I) = \frac{1}{1 + \frac{I}{I_s}} \quad (3.4)$$

with I_s the saturation excitation intensity.

The GSD principle has been used to improve the imaging resolution. By focusing on the fluorophore plane a doughnut-shaped beam (a beam featuring a central area with zero intensity, Figure 3.18) at the excitation wavelength, one achieves ground state depletion of the fluorophore, except in the case when it lies in the area located at the central part of the focused beam. A co-aligned beam focused on the doughnut center can read out the fluorophores of this area, that are not ground state depleted [160].

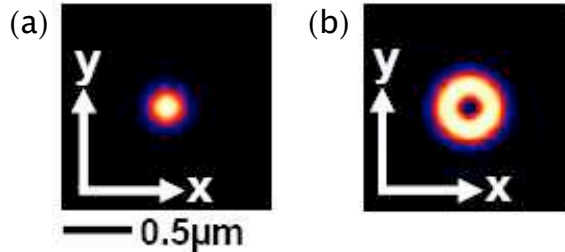


Figure 3.18: Excitation (a) and depletion beam PSF (b) in the lateral dimensions.

In the case of diamond and NV color center, ground state depletion is possible by using the excitation wavelength in the green region. The NV center is the ideal probe for this kind of technique, as no photobleaching occurs, even for high intensities, often necessary to completely deplete the ground state. As demonstrated by Rittweger et al. [161] by exciting the sample only by a doughnut shape beam (at 532 nm), depletion of the ground state occurs apart from the central area of the beam (i.e. of the probe) which shows up as a dark spot. With a high excitation power of the 532 nm beam one can provoke saturated absorption of the NV center, i.e. after transition on the excited state the system relaxes to the ground state but it returns directly and quickly on the excited state (this can be translated to a ground state depletion, but it should not be confused with the “traditional” GSD described above, where the system is shelved on a metastable state). Depending on the depletion doughnut shape beam excitation intensity, the central dark spot can be reduced in size, to achieve at the end a 10 nm lateral resolution for the NV center in bulk diamond (Figure 3.19).

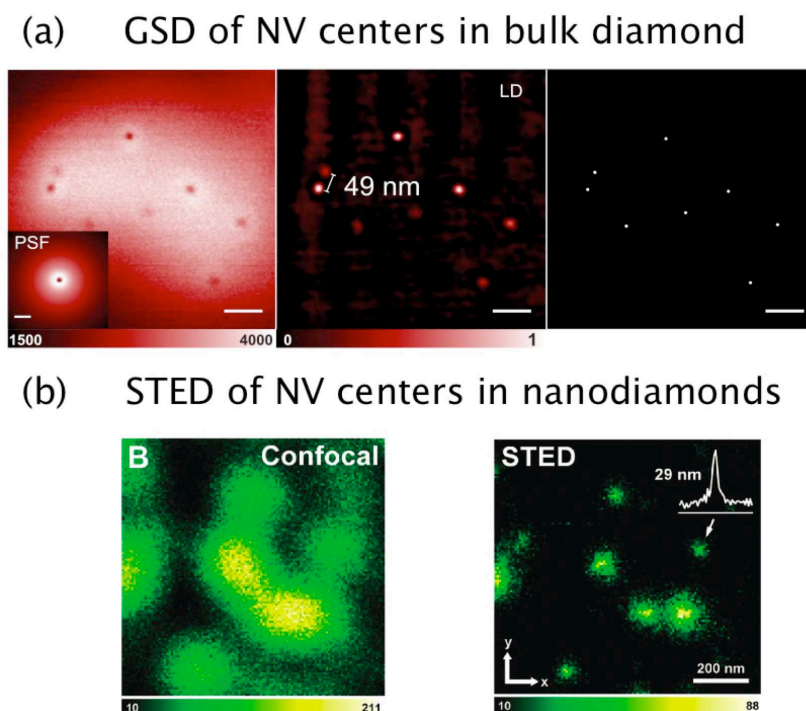


Figure 3.19: (a) GSD effect of NV color centers in type IIa bulk diamond sample, using only one excitation beam. The images exhibit the color centers as dark dips, with linear deconvolution with the calculated PSF (inset) one can render the image positive and determine the centroid position of each center [161]. (b) STED microscopy of 35 nm PNDs, a 29 nm spatial resolution is achieved [162].

Stimulated Emission Depletion microscopy

The other method of super-resolution imaging is the Stimulated Emission Depletion (STED) microscopy [156, 163]. Figure 3.19c shows the basic principle of the stimulated emission. An organic fluorophore is excited from the ground state to a higher vibronic state of the first excited state. After a fast non-radiative transition to the lowest energy level of the excited state, the molecule can relax to the ground state via the simple spontaneous emission, with emission of a red-shifted photon. However, it can also be directed to the ground state by stimulated emission. A second laser beam (the STED beam) is needed that matches the energy gap (between the first excited state and a higher vibrational level of the ground state) stimulating the molecule to relax to the ground state by emitting a photon with the same wavelength as the stimulation laser beam.

In contrast to GSD, here the normalized fluorescence signal follows an exponential dependence with the excitation intensity as follows:

$$\eta(I) \propto e^{-\frac{I}{I_s}} \quad (3.5)$$

For super-resolution imaging, the STED-beam is shaped to a doughnut form at the focus of the microscope objective so that upon the increase of its intensity, the emitter fluorescence intensity excited by the main laser of regular Gaussian shape, stays unaffected in the center of the doughnut spot, but decreases on its edges. The fluorescence spot size can decrease non-linearly with the increase of the STED beam intensity with only

practical limits the ones related to the realization of a true zero-intensity STED beam at the center and to the emitter photostability. The main limit in the case of a dye emitter is its photobleaching.

STED applied to the NV color centers overcomes completely this limit. Experiments on NV color centers embedded in bulk diamond and diamond nanocrystals have achieved a resolution down to 8 nm [164] and 29 nm for the 35 nm nanoparticles, respectively [162].

3.2.2 Quenching effect of NV center with green - infrared light

As illustrated previously, one way to achieve ground state depletion of NV centers is by exciting the probe with light in the green wavelength region. However, as we will demonstrate, this is also possible with a superposition of green light with an infra-red laser beam.

a Experimental setup

The experimental setup consists of three parts, the excitation laser part, the home-built confocal microscope and the detection setup. The ensemble is depicted on Figure 3.20.

The excitation laser is the mode-locked Nd:YVO₄ picosecond laser with a repetition rate of 4.8 MHz, used for the two photon excitation of NV centers. It operates at 1064 nm and is also frequency doubled with a 1.5 cm long KTP crystal.

The picosecond laser and the excitation setup are similar as the ones described for the TPEx experiment. The laser beams are reflected by a dichroic mirror (700dcsx, Chroma Tech. Corp.) and focused by a microscope objective ($\times 60$, NA 1.4 oil immersion or $\times 100$, NA 0.95, air, depending on the application) onto the sample.

Here we additionally use a Hanbury-Brown and Twiss time intensity correlator (section 2). In front of each photodiode a dielectric shortpass filter (Melles Griot 03SWP418) rejects the 830-1030 nm spectral region, to avoid optical cross-talk. A Schott KG5 filter is put after the confocal pinhole to cut the remaining infra-red excitation light.

The residual excitation light 532 nm is removed with the combination of both the long-pass filter (LP1) having a transmission of 97% between 539-1200 nm (RazorEdge LP03-532RU-25, Semrock, USA) and another long-pass filter (LP2) with transmission $>80\%$ in the range 580-750 nm (580EFLP, Omega Optical Inc., USA).

It has to be mentioned that the infra-red beam arrives after the green beam on the sample plane. In fact each infra-red pulse is on purpose delayed in comparison with the green one by a distance of $l = 2 \times \Delta x$ (with the time delay dt equal to : $dt = 2 \times \Delta x/c$, see Figure 3.20).

b Results

We first carried out experiments with single NV centers in single nanodiamonds. For this purpose we used nanodiamonds irradiated with a relatively low electron dose (DeBeers, Micron+MDA 0-0.5 μm , dose 3×10^{17} e⁻/cm², energy 1.5 MeV, 2 h annealing time at 850°C under vacuum) embedded in a polymer thin film. The mean size of the nanodiamonds is about 90 nm. The nanodiamonds were spin coated on a Bragg mirror substrate

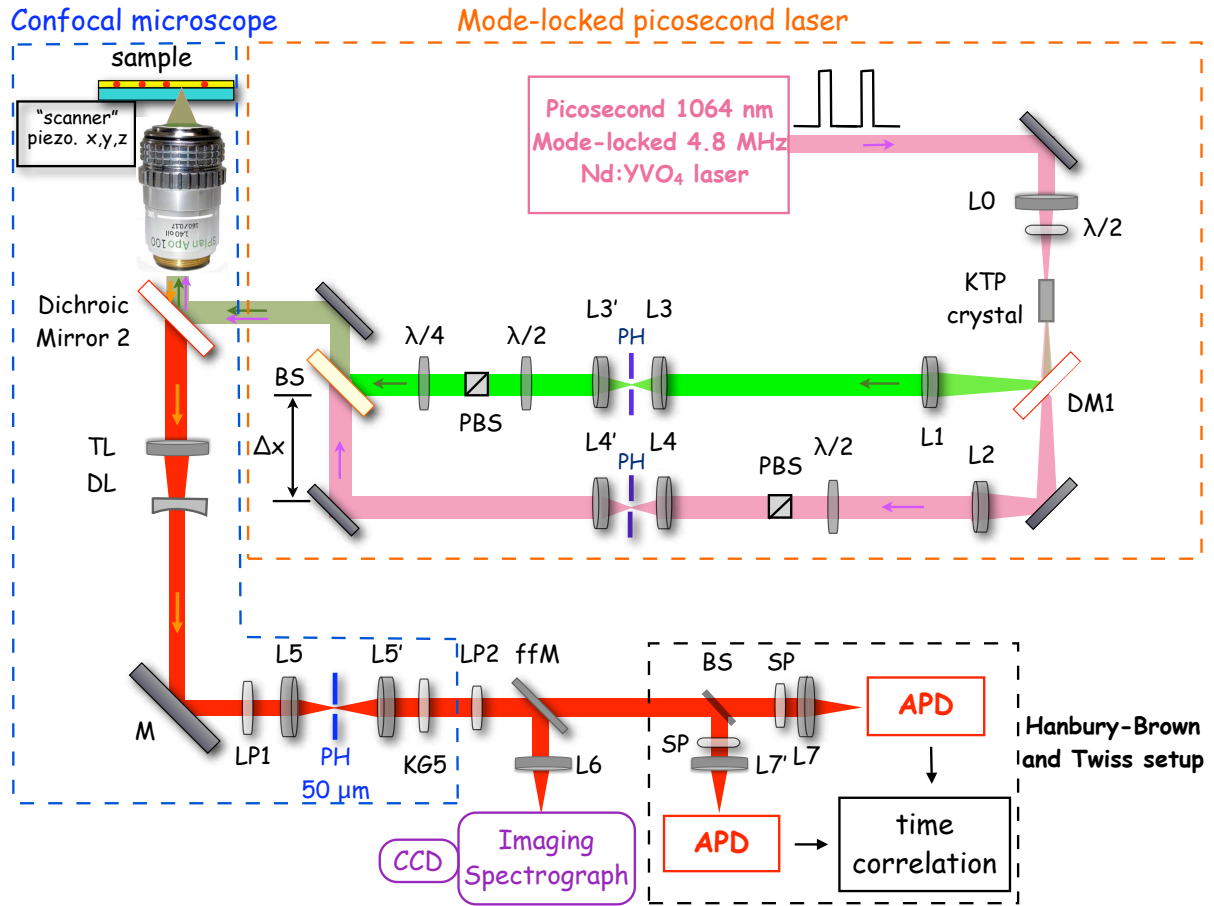


Figure 3.20: Optical setup used to excite the nanodiamonds simultaneously with a 532 nm and 1064 nm pulsed laser beams. Surrounded by i) the blue dashed-line box: the home-built confocal microscope; ii) the orange dashed-line box: the picosecond 532 and 1064 nm excitation laser optical setup; iii) the black dashed-line box: the Hanbury-Brown and Twiss time intensity correlation system.

(page 100, [32]). The mirror is made of alternating layers of silica and niobium oxide (Nb_2O_5) and has a 99% reflectance at 670 nm, corresponding to the NV^- color center emission maximum wavelength.

For this sample study the objective used was the metallographic one from Olympus working in air ($\times 100$, NA 0.95).

Figure 3.21a illustrates the surface plot of a typical confocal raster-scan of the sample, realized with a cw laser at 532 nm. We recorded a photon antibunching measurement showing a $g^{(2)}(\tau)$ dip at zero delay of ≈ 0.10 , which indicates that we have a single center. No bunching effects are observed, since the excitation power is low ($150 \mu\text{W}$). Therefore, by considering a simple two level model of the form: $g^{(2)}(\tau) = 1 - e^{-|\tau|/\tau}/N$, the fit of the data yields $N = 1$ NV center and $\tau = 19$ ns, which can be considered as the radiative decay lifetime of the NV center, since we are using very low excitation powers.

For the following, we excite the NV center with the picosecond pulsed laser system. We observe that when the infra-red beam is superimposed on its frequency-doubled green laser beam, the photoluminescence signal recorded from the NV center decreases.

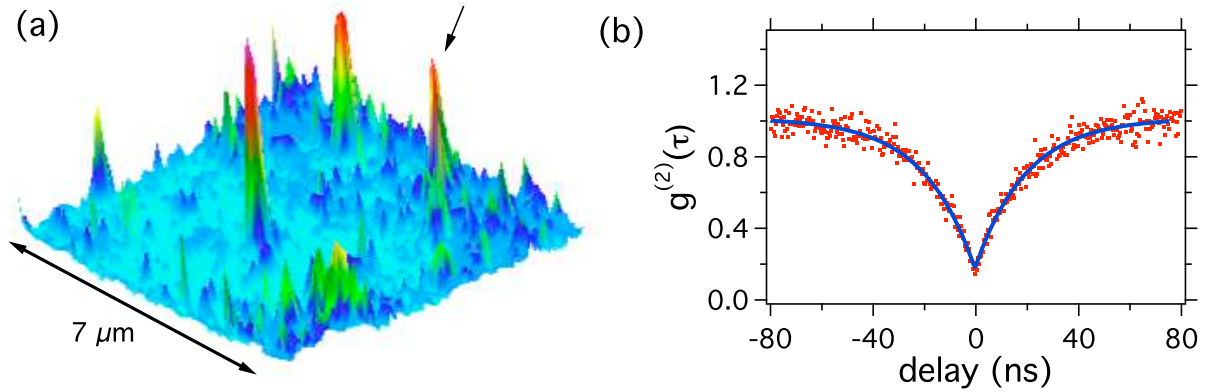


Figure 3.21: (a) Photoluminescence intensity surface plot of a typical confocal raster scan of PNDs spin-coated on a Bragg mirror substrate, excitation wavelength cw 532 nm, excitation power on the sample plane (after corrections due to the losses on the optical path) is $150 \mu\text{W}$. (b) Intensity correlation measurement of the PND in arrow on the scan, excitation power $150 \mu\text{W}$.

When the infra-red beam is blocked, the photoluminescence signal re-obtains its initial values.

Figure 3.22a depicts the phenomenon for the single NV center of Figure 3.21. We notice that background averaged value noise level is ≈ 50 counts/ 20 ms, almost half the value of the photoluminescence signal acquired when the two beams are superimposed. This specific center is a NV^- center. Note the reversibility of the ON-OFF switching phenomenon. It has to be mentioned that the infra-red beam for this experiment runs a distance of about $\Delta x = 20$ cm more than the green beam, before their recombination through the beam splitter. This corresponds to a time delay of 670 ps. If the beams excites the sample without any delay between them, the “quenching” effect does not occur.

To investigate further the photoluminescence decrease effect, we studied the spectra variations for PNDs containing more than one NV center. We used type M nanodiamonds, sample *Aq100nm-Me18*.

To determine for which kind of NV center the effect of the photoluminescence “quenching” occurs, we examined the emission spectra of PNDs under different excitation conditions. Figure 3.23a depicts the spectrum of PND #1 of the confocal scan on Figure 3.29a, corresponding to the emission of the NV° center (characteristic Zero Phonon Line (ZPL) at 575 nm).

When the 1064 nm beam is added to the 532 nm excitation, the photoluminescence signal decreases, as shown on the spectrum. The spectrum of PND #2 (Figure 3.29a), shows both NV° and NV^- centers. When we add the infra-red beam, we observe a decrease of the photoluminescence, stronger for the NV° center. This effect depends on the infrared laser power: at 3 mW the decrease of the NV° ZPL line is 46% and 26% for the NV^- center⁴. At IR excitation power of 42 mW, the NV° ZPL line totally disappears, while there is a 80% decrease for the NV^- center ZPL.

To investigate the relationship between the excitation power and the decrease of the

⁴decrease in comparison to the initial signal recorded by excitation with only the green beam

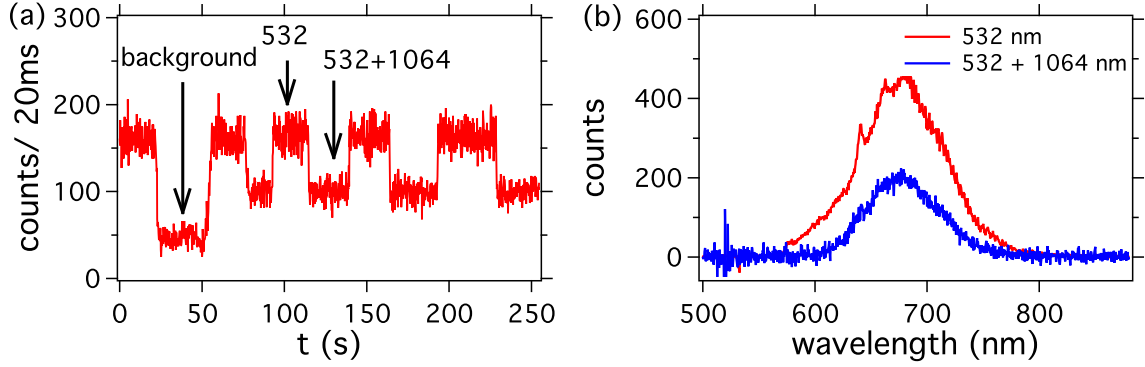


Figure 3.22: The photoluminescence “quenching” effect of a single NV-center. (a) With consecutive excitations with the green 532 nm beam or with the superimposed 532 nm and 1064 nm beams we achieve an ON-OFF state shift. The background was measured by slightly translating the piezo stage in the x direction, so the signal is recorded on a region next to the nanoparticle, excitation power for the green is $150 \mu\text{W}$, for the infrared beam 22 mW in the sample plane. (b) Photoluminescence spectra of the single NV center before and during the “quenching” process, excitation powers are the same as in (a), note the characteristic ZPL line at 637 nm , indicating that the center is NV^- .

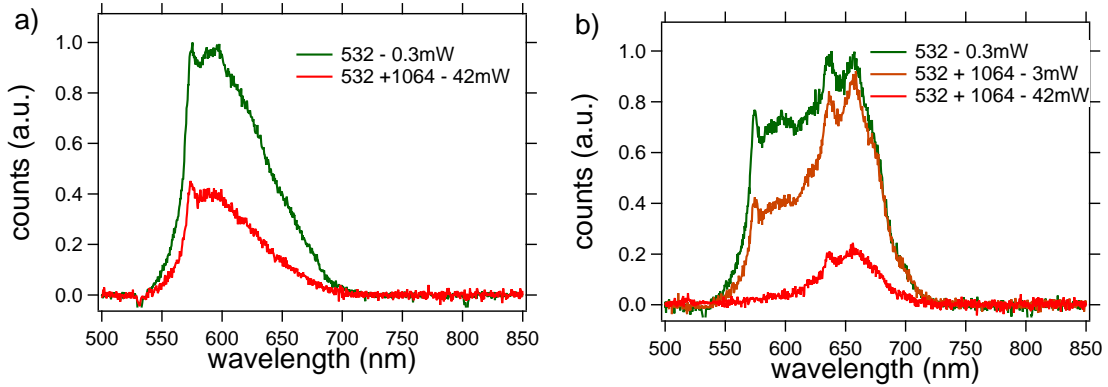


Figure 3.23: Investigation of the “quenching” effect for both charge states of NV centers: a,b) Photoluminescence spectra of PNDs #1 (NV° center only) and #2 (PND containing both NV° and NV^- color centers) respectively, for different IR excitation powers, the 532 nm excitation power was 0.3 mW in both cases. Due to the background subtraction during acquisition, a small dip can be distinguished at the excitation laser wavelength value, at 532 nm .

photoluminescence signal, we plotted the corresponding curve. For a single NV center the recorded photoluminescence signal was relatively low. We recorded the signal from a nanodiamond (*Aq100nm-Me18* sample) with more than one NV centers in it, for a better demonstration and study of the “quenching” effect.

Figure 3.24a shows the normalized photoluminescence signal $\eta(I)$ when we superimpose the 532+1064 nm beams as a function of the IR excitation power. A nonlinear relationship is indeed found in the experiment. An exponential fit of equation 3.5 fits adequately the data. For the nanodiamond of Figure 3.24a we find $P_s = 2.4 \text{ mW}$, which

is equivalent to an excitation intensity of 160 kW/cm^2 (considering an area of the infra-red beam on the focus plane of $S \approx 1.5 \text{ } \mu\text{m}^2$, measured with the CCD array)⁵ while for the nanodiamond of Figure 3.24c we find $P_s = 14.5 \text{ mW}$. It is thus difficult to extract an overall saturation excitation intensity value, as we observe that this value is significantly different for each nanoparticle (perhaps it is linked to the size and/or the surface cleanness-existence of graphite- of the particle). Note that the photoluminescence is reduced down to 10% and 35% of the initial value without IR excitation for each nanodiamond respectively (Figure 3.24a,c).

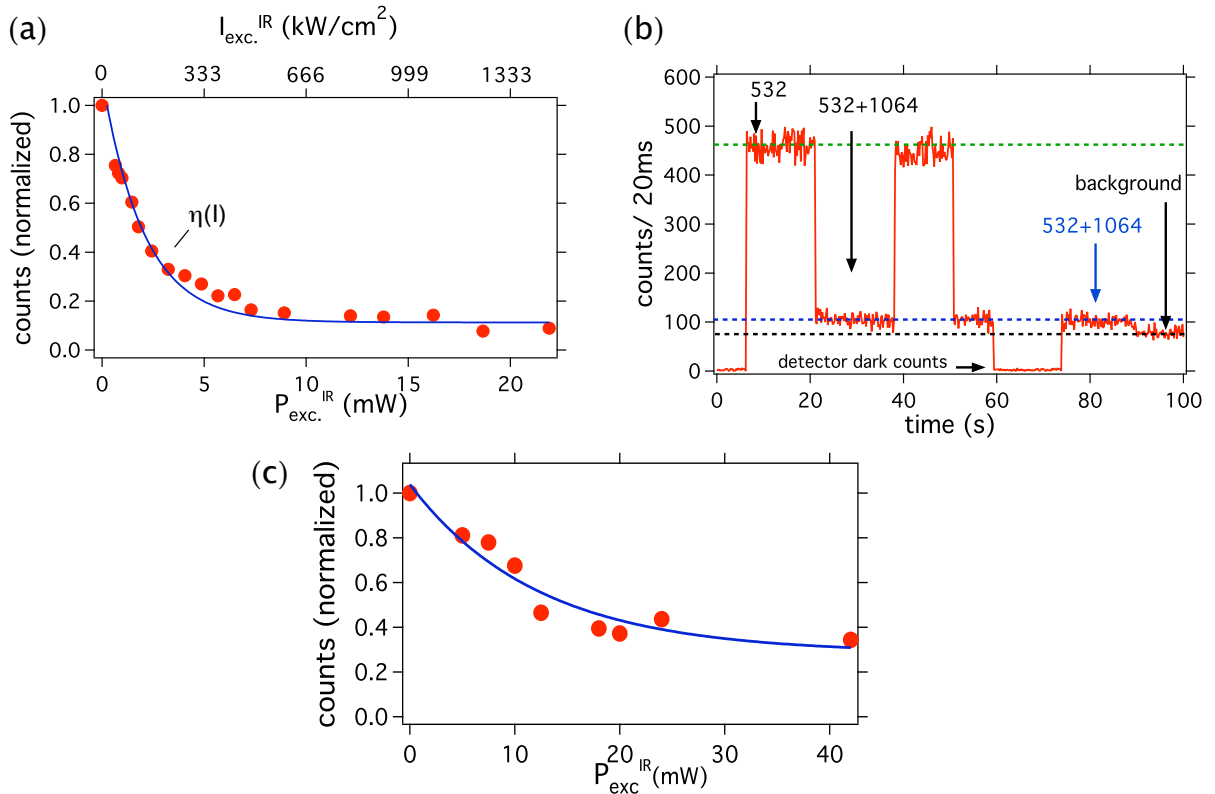


Figure 3.24: Quenching effect of the photoluminescence of a nanodiamond containing multiple NV centers. (a) Photoluminescence as a function of the 1064 nm laser excitation power, the green 532 nm excitation power is constant at 100 W/cm^2 (calculated in the sample plane), the blue plain line is the exponential fit of equation 3.5 for the experimental data. (b) Characteristic ON-OFF behavior of the photoluminescence when the 1064 nm beam (mean intensity 146 kW/cm^2) is superimposed on the 532 nm beam (100 W/cm^2). (c) Photoluminescence as a function of the 1064 nm laser excitation power for another nanodiamond (the blue line is the exponential fit of equation 3.5).

⁵The values of excitation powers or intensities for both wavelengths are corrected for the dichroic mirror and objective transmission coefficients for each wavelength region, to obtain the excitation power in the objective focal plane.

c Discussion

We have observed that the photoluminescence signal of the NV center decreases when 1064 nm pulsed light is superimposed to a 532 nm pulsed beam. A necessary condition for this effect to happen is that the infra-red beam pulse excites the sample with a temporal delay compared to the green pulse.

Our first suggestion was that the ground state is depleted, due to the trapping of the NV center into an OFF state. One hypothesis is that the system is trapped in the metastable 1A state (see Figure 1.3) and the IR pulse forces the system to do cycles in that state. Reports have demonstrated that this metastable state consists of two singlet states, with a non radiative transition to the lowest of these two states at 1046 nm, with a 10 nm spectral width [165]. However, in our case, the excitation with the 1064 nm pulse could difficulty force the system to stay blocked in that metastable state. The intersystem crossing lifetime of the first excited 3E state to the metastable 1A state is of the order of 33 ms [166].

Complementary measurements in our group realized during the redaction of this manuscript by Dingwei Zheng and Diep Lai showed that when one varies the time-delay between the green and the infra-red pulses, the depletion effect is strongly reduced for delays longer than about 10 ns (Figure 3.25a,b). An exponential fit of the experimental data of the signal decrease gives a characteristic time $\tau = 10.2$ ns, which is close to the decay lifetime of the NV center.

A realistic model to explain this effect involves the **depletion of the first excited state by non-radiative processes**. Experiments on the decay lifetime of NV centers in nanodiamonds showed that once the 1064 nm is superimposed to the 532 nm beam, the quenching occurs immediately, with a time-delay of 0.7 ns, which is of the order of the instrumental response time (Figure 3.25c).

Further experiments in bulk diamond showed the burning of the sample, due to the enormous infra-red excitation power. In the case of nanodiamonds, less energy is deposited on the area covered by the nanoparticle (in comparison to bulk diamond, which receives the total energy of the excitation pulse), so we observe no burning effects, apart from the case of extremely high excitation powers (Figure 3.16).

Thus, one possible explanation of the phenomenon is that it is a thermal effect, induced by the high power 1064 nm pulsed laser beam. Due to this thermal effect, the population of the excited state is depleted either directly towards the ground state, via non-radiative transitions, or towards firstly to other energy levels (e.g. metastable level) and then to the ground level, non-radiatively (Figure 3.25d). The thermal effect could have an impact on the position of the excited state and/or allow transitions that before could not take place.

Finally, there are two supplementary important key observations that support the thermal effect nature of the quenching effect. The first one is the independence of the quenching effect with the nature of the NV center. We showed on Figure 3.29 that the effect occurs for both NV° and NV^- center. One could test another type of color center in diamond (like the H3) to verify the validity of this assumption, but already the fact that the effect is independent to the neutral and negative NV center indicates that it is independent to their energy level positions.

The second key element is that the effect occurs only under laser pulsed excitation.

Experiments with cw laser excitation at 532 nm and pulsed (picosecond) excitation at 1064 nm showed that the quenching effect of the NV center does not occur, indicating the need of a first pulse at 532 nm (the first excited state is populated), and a following pulse at 1064 nm some ps later (to provoke the photoluminescence quenching by a population depletion of the first excited state).

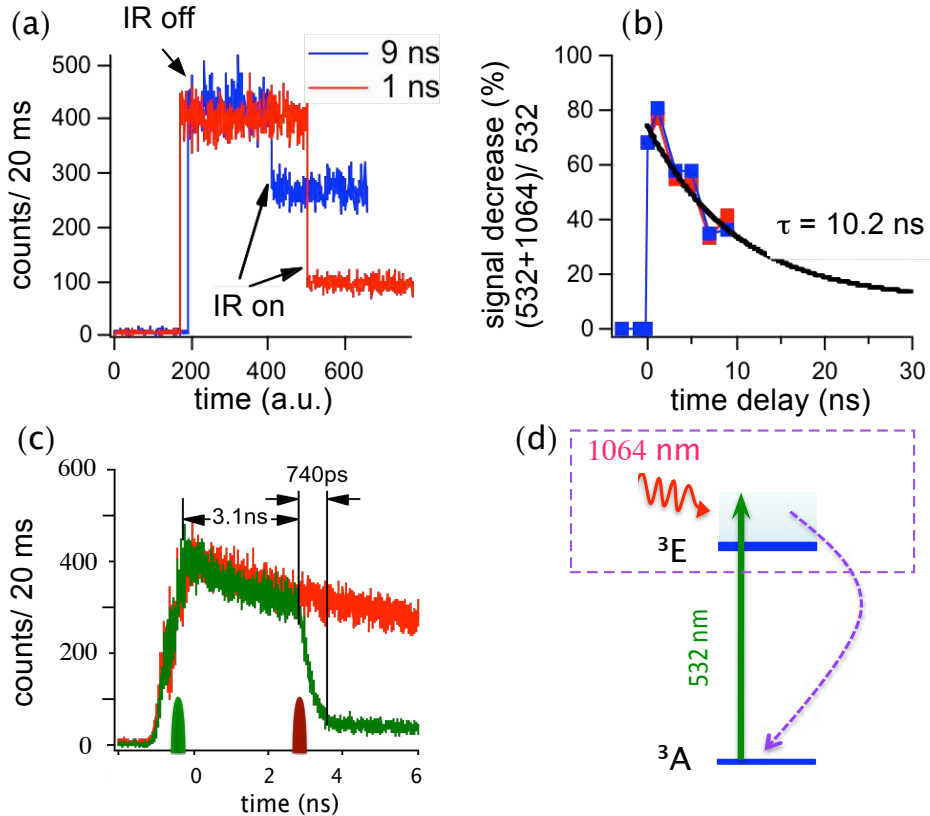


Figure 3.25: The photoluminescence “quenching” effect of a single nanodiamond with multiple NV centers. (a) Photoluminescence intensity over time for time delays 1 and 9 ns between the 532 and 1064 nm beam pulses. (b) Evolution of the photoluminescence intensity over variable time delays. In black the monoexponential fit, with lifetime 10.2 ns. (c) Decay lifetime of the NV center after excitation with the 532 nm beam. After 3.1 ns the 1064 nm beam is superimposed, provoking a sudden (0.74 ps) decrease of the photoluminescence signal. (d) Schematic illustration of the population depletion of the first excited state after excitation with the 1064 nm beam via a non-radiative transition to the ground state.

3.2.3 Super Resolution imaging of NV centers in nanodiamonds

As mentioned above, the super-resolution STED and GSD imaging techniques were recently applied to NV color centers in diamond [161, 162, 164]. NV center is an ideal probe for this kind of experiments, because it does not photobleach.

We saw previously that a 1064 nm pulsed beam superimposed on its frequency doubled 532 nm beam results in the “quenching” of the photoluminescence signal, probably due

to a ground state depletion mechanism. Here we examine the possibility to increase the resolution of NV centers in nanodiamonds using this depletion effect. The use of a 1064 nm excitation wavelength is better suited for biological tissues (lower absorption) than the green and near-IR wavelengths used so far for similar super-resolution imaging microscopies.

a Experimental validation of the resolution enhancement by simultaneous fundamental (1064 nm) and frequency-doubled beam illumination

The key point in increasing the optical resolution is that the beam that provokes the ground state depletion (or excited state depletion for STED) of the fluorophore has, in the focal plane, a shape with a local zero intensity point in the middle.

One way to achieve this local zero intensity is to use a phase mask. Resolution enhancement along one lateral dimension in the objective plane is achieved with a phase mask that retards a semi-circle of the back aperture of the objective by π (Figure 3.26a) [167]. The phase mask that introduces a helical phase retardation $0-2\pi$ to the beam creates a doughnut-shaped spot in the focus plane of the microscope objective and is used for uniform resolution enhancement in both lateral directions, but with no axial resolution improvement (Figure 3.26b). To enhance resolution in all axes, special masks are used, that retard an inner circle area of the back aperture of the objective by π (Figure 3.26c) [168]. This results in a strong reduction in the axial direction and a moderate reduction in the lateral directions.

In our case, we were mainly interested in resolution enhancement in the lateral directions. For that purpose we first used an alternative to phase masks, already available in our laboratory for the study of second-harmonic properties of KTP nanocrystals (led by Le Xuan Loc and Abdallah Slablab), a special Liquid Crystal - based polarization converter, provided by *ARCOptix* (Switzerland). This device is capable to convert a linear polarized light beam into a beam with perfectly radial or azimuthal polarization distribution, over a broad wavelength range (400-1700 nm). The intensity distribution of such kinds of polarized beams forms a doughnut shaped spot in the focal plane of a microscope objective [169].

Experimental setup

The **Liquid Crystal polarization converter** device (or θ cell) is constituted by nematic liquid crystal (LC) molecules.

The entrance and the exit plates of the cell are linearly and circularly rubbed respectively, the former determining the cell axis (Figure 3.27). The LC molecules have a local orientation that depends on their position and rotates as the beam propagates (for more details on the device look at Appendix C).

We placed the ARCOptix cell on the infra-red beam pathway, after the half-wave plate and the polarizer beamsplitter system (in the picosecond laser setup surrounded by the orange dashed-line box of Figure 3.20). The 1064 nm beam has at the output of the beamsplitter a horizontal linear polarization. The IR beam enters the ARCOptix cell, having its polarization perpendicular to the cell axis. By calibrating properly the cell the output beam obtains a radial polarization.

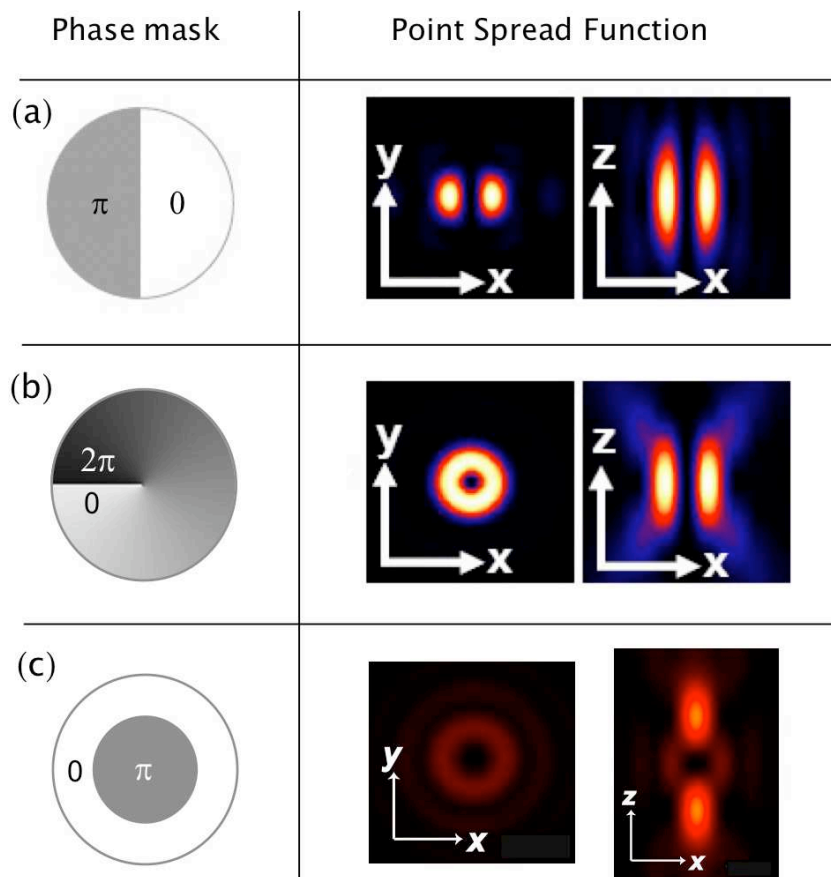


Figure 3.26: Phase masks and the corresponding PSF pattern of the depletion beam [159].

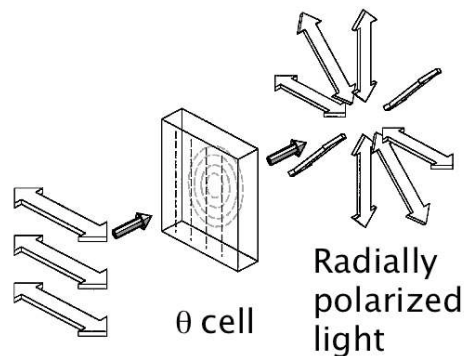


Figure 3.27: Generation of radially polarized light by the use of the θ cell [170].

We place a CCD array in the appropriate output port of the microscope in order to observe the beam shape.

Figure 3.28 shows the beam shapes recorded by the CCD array for the 532 nm and the 1064 nm beams. We observe that the shape of the infra-red beam is not that of a doughnut, as theoretically expected. This discrepancy is probably due to the dichroic mirror used (DM2 of Figure 3.20). At 1064 nm wavelength, the dichroic mirror reflects 99% of the incident light, but not in the same way for the vertical or horizontal polarization. Such a difference could be responsible for the two lobe pattern of a theoretically

doughnut-shaped beam on the objective focal plane [171, 172].

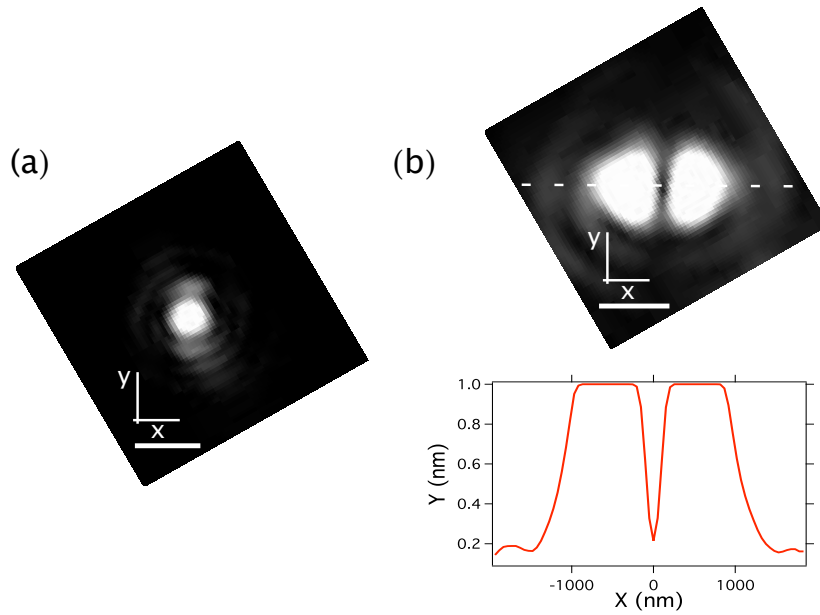


Figure 3.28: Experimental far field intensity distribution in the microscope objective focal plane of a beam which passed through the Arcoptix cell. (a) Case of the 532 nm beam. (b) Case of the 1064 nm radially polarized beam, the bar scale is 1 μm . Inset: the intensity profile of the infra-red beam for a power of 30 mW, the center of the beam approaches a zero intensity value.

b Sub-diffraction imaging limits with IR+green light excitation

Despite the fact that we did not manage to produce a doughnut shape beam at 1064 nm, we carried out a proof of principle experiment to show that we can obtain sub-diffraction imaging based on the IR+green ground state depletion effect. We used the *Aq100nm-Me18* sample. The choice of the size of NDs was a compromise, between a high photoluminescence signal and a nanoparticle size inferior to the resolution limit of the microscope.

Figure 3.29 shows the confocal scans (a) with the 532 nm beam alone and (b) with the superposition of the 532 and 1064 nm beams. In the latter case, when the infra-red beam passes through the Liquid Crystal polarization converter it yields a local zero intensity area at the microscope objective focus (Figure 3.28b).

We clearly see that the spot size is smaller with the addition of the IR beam, corresponding to an increased resolution. For example, on Figure 3.29a we observe a cluster of three particles, not well individually imaged with only the 532nm beam, but well separated after the addition of the IR beam.

To further verify that the resolution improvement is due to a “quenching” effect stimulated by the infra-red beam, we remove the Liquid Crystal polarization converter and record the photoluminescence signal for an isolated PND in the scan, as a function of the excitation power. We find a power dependence similar to the one displayed in Figure 3.24.

To quantify the lateral resolution improvement, we carried out a more detailed scan on PND #2. Figure 3.30a shows a typical confocal scan of PND #2, while Figure 3.30b is a confocal scan when both beams excite the sample, with a radially polarized infra-red beam. The resolution enhancement is more pronounced in the x direction. The resolution improvement is a direct consequence of the local zero intensity point of the infra-red beam in the objective focal plane (Figure 3.28). From the intensity profile of PND #2 on Figure 3.30c,d, we infer a resolution improvement of a factor of about 2.

An alternative method to create a doughnut-shaped beam in the objective focal plane is to use a $0-2\pi$ phase plate (Figure 3.26). Such a helix phase plate $0-2\pi$ was ordered by Silios Technologies (France) but arrived in the laboratory at the end of my PhD work. We will use it to replace the Arcoptix cell. Moreover, the microscope setup will be modified so that the phase-plate is put on the beam just before the microscope objective, without the use of a dichroic mirror. Doing so, the polarization artifact due to this mirror is suppressed.

The work of further resolution enhancement is in progress by Dingwei Zheng and Ngoc Diep Lai.

3.2.4 Conclusion

In this section we studied the quenching effect of the NV center photoluminescence when a 1064 nm beam is superimposed to a 532 nm one. The most up-to-date probable explanation is that the first excited state is depleted by the 1064 nm beam via non-radiative processes to the ground state, due to a thermal effect, provoked by the high energy infra-red pulse.

An application of the photoluminescence quenching is the resolution enhancement. By radially polarizing the 1064 nm beam, we manage to have in the objective focal plane a local zero intensity area. In this sub-diffraction size area the NV centers excited states are not depleted. A resolution improvement by a factor of 2 was achieved for 100 nm nanodiamonds. This technique is a promising alternative for super-resolution imaging of

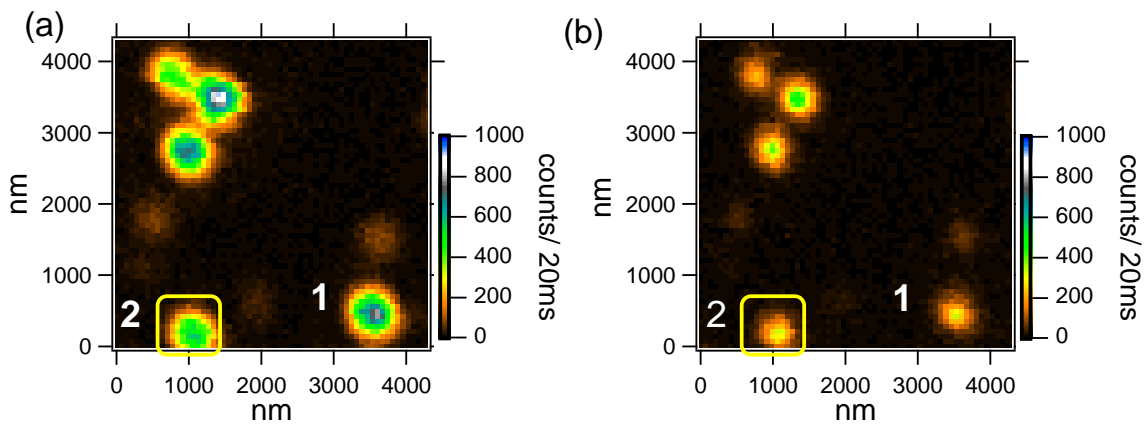


Figure 3.29: Confocal raster-scans of 100 nm PNDs. (a) Excitation with only the 532 nm pulsed laser, excitation power in the sample plane 0.15 mW. (b) Superposition of the 532 nm and 1064 nm radially polarized beams, IR beam excitation power 60 mW.

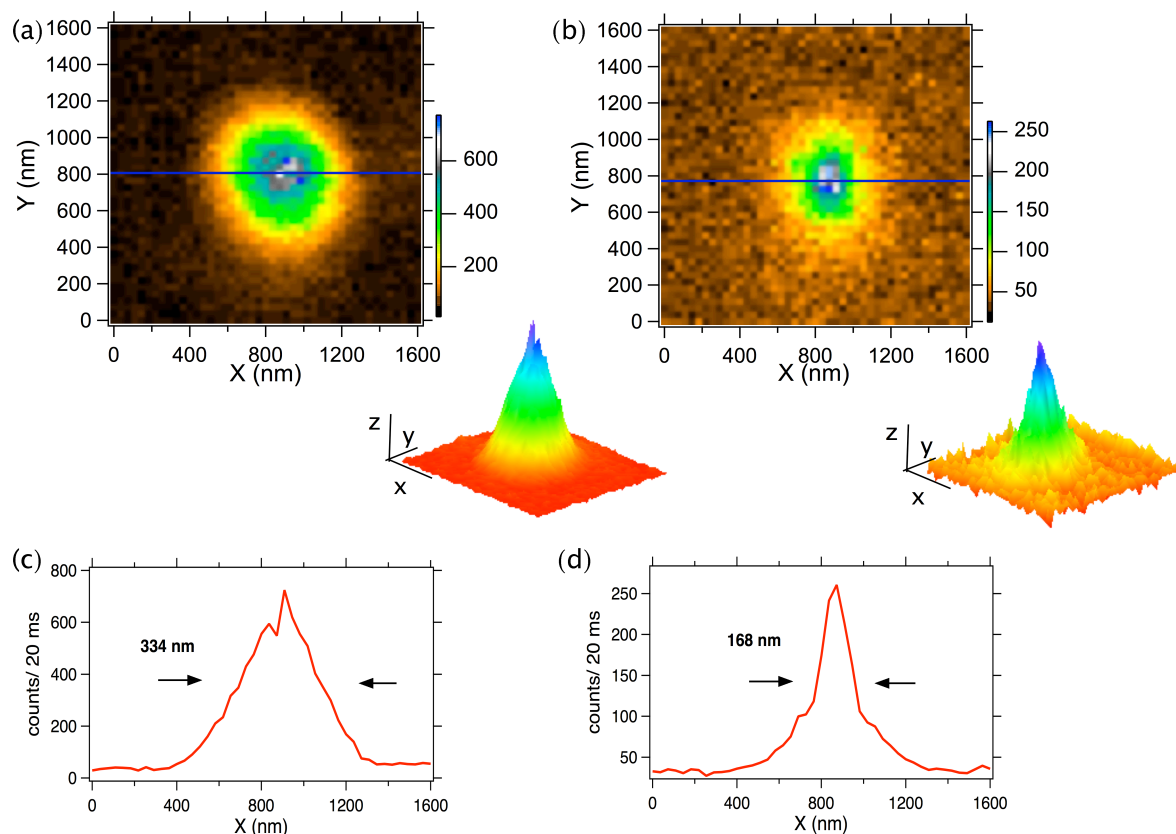


Figure 3.30: Sub-diffraction imaging of NV centers in nanodiamonds, a,b) confocal raster scan of PND #2 of Figure 3.29 with 532 nm excitation wavelength, excitation power 0.15 mW and with the 532+radially polarized 1064 nm beams respectively, excitation power of latter 60 mW; inset: photoluminescence intensity surface plots; c,d) Corresponding x -axis intensity profiles demonstrating ≈ 2 -fold reduction of the FWHM.

NV centers in nanodiamonds, for biological or quantum information applications.

Part II

Applications of photoluminescent nanodiamonds in Biology

Chapter 4

Internalization of photoluminescent nanodiamonds in cells

4.1 Introduction

The main application of PNDs in biology, envisaged in our research team, is in a first approach the cellular labeling and in a second approach the labeling of cellular compartments and the individual tracking of biomolecules. This needs multidisciplinary efforts to be achieved, like the appropriate functionalization of the NDs surface and the specific attachment to different biomolecules. A first step towards the use of PNDs in biology is the cell labeling and the comprehension of the cellular uptake mechanisms of PNDs in cells.

For intracellular tracking, a key challenge is the delivery of PNDs to the cytoplasm and organelles such as the nucleus and mitochondria. Traditional organic dyes used to label these organelles (DAPI, Mitotracker) are able to permeate cell membranes through passive diffusion. For the most widely used inorganic labels, the Quantum Dots (QDs), passive diffusion across the lipid bilayer is unlikely due to their size and surface properties. Nie et al. reported in 1998 that QDs-proteins bioconjugates are incorporated by living cells [22]¹. From then on many groups have reported the uptake of quantum dots by individual cells or by animal tissues [12, 173–175].

The cellular uptake of colloidal particles is an important area of biological research as it is related to a variety of applications, including drug, nucleic acid and gene delivery, or to the cell's communication with the outside world and the uptake of nutrients or even of viruses.

Regarding photoluminescent nanodiamonds, one of the main research topics of my PhD work was the detailed study of the spontaneous internalization of PNDs in cells. The first study of spontaneous internalization of PNDs in HeLa cells ² was reported in the group of H.-C. Chang [50]. In our group, in collaboration with the team of Patrick Curmi of Laboratoire Structure et Activité des Biomolécules Normales et Pathologiques of Université d'Evry-Val-d'Essonne, we equally studied the internalization of single PNDs

¹The uptake mechanism is receptor-mediated endocytosis for transferrin conjugated QDs, see chapter 5 for further details concerning this mechanism

²cancerous cells belonging to a strain continuously cultured since its isolation in 1951 from a patient (Henrietta Lacks - HeLa) suffering from uterine cervical carcinoma

in cells [48, 53, 176].

The cellular uptake can be observed by various microscopy methods; in this work we use confocal microscopy and wide-field illumination microscopy. While confocal microscopy uses a scanning stage system and the cells should be fixed, wide-field illumination microscopy allows the study of dynamic processes in living cells.

Wide-field illumination microscopy has made possible single particle tracking experiments (SPT). Although with traditional organic fluorophores one is able to probe individually biomolecule interactions and dynamics, the advent of QDs made SPT much easier, thanks to their remarkable photostability (in comparison with fluorophores). An example of SPT using QDs is the study of biomolecule dynamics, like the movement of neurotransmitters or glycine receptors [177, 178]. A high temporal and spatial resolution can be achieved thanks to the high signal to noise ratio [178, 179].

However due to QD blinking, the tracking of a single QD appears to be tedious and limits its use in such applications, especially if the trajectories are long or if the exact trajectory of the biomolecule has to be reconstructed in order to study its dynamics and interactions with time.

Other possible biomarkers suitable for long term wide-field observations are the gold nanoparticles. The team of B. Lounis has recently demonstrated the detection of 5 nm gold NPs using a photothermal tracking technique [180, 181]. The temperature rises when gold NPs are excited by a laser beam at the plasma resonance, leading to a local modification of the refractive index of the medium. This modification is detected with interference contrast with another laser beam. A recent application is the tracking of AMPA receptors marked with gold NPs in live cells. In the same work the team uses a procedure of triangulation for the exact prediction of the NPs position, with a high temporal resolution of 33 ms [182]. The drawback of the photothermal detection is the high excitation intensities required to observe the refractive index modification (400 kW cm^{-2} for 5 nm NPs and 200 kW cm^{-2} for 10 nm NPs).

Another promising biolabel, with a great potential of single particle tracking for long time-scales, is the lanthanide doped NPs. Synthesized directly in water, this kind of NPs presents remarkable photostability, with no emission intermittency. With the appropriate functionalisation, Beaurepaire et al. reported that they can act as artificial toxins and specifically target sodium channels, enabling their long-term tracking at the single molecule level [20].

In this work, we studied the free diffusion of PNDs in solution (water:glycerol mixture) and in cells using wide field laser illumination microscopy. We confirmed the free brownian motion in solution by calculating the diffusion coefficients of the PNDs trajectories and observed the confined motion of these particles inside cells [183].

4.2 Spontaneous internalization of photoluminescent nanodiamonds in HeLa cells

4.2.1 Experimental process

Cell culture preparation

To study the spontaneous internalization of PNDs, HeLa cells were grown in standard conditions on glass coverslips in Dulbecco Modified Eagle's Medium (DMEM) supplemented with 10% foetal calf serum (FCS) and 1% penicillin/streptomycin. Cells were seeded at a density of 2×10^5 cells/ 1.3 cm^2 and grown at 37°C in a humidified incubator under 5% CO_2 atmosphere. 24 h after seeding, the PND aqueous suspensions were added to the cell culture medium. After 2 h incubation, the excess of PNDs was removed by washing the cells with phosphate buffer saline (PBS). The cells were then fixed with 4% paraformaldehyde in PBS and mounted on microscope slides for phase contrast and confocal microscopy imaging.

Intracellular fluorescence observations

For intracellular visualization of PNDs, two types of microscope were used. The first one was a commercial confocal laser scanning microscope (Leica TCS SP2, Mannheim, Germany), with a $\times 63$, 1.4 numerical aperture oil immersion objective.

The second microscope was the home-built confocal setup described in chapter 2. It was used to visualize with high sensitivity the single NV centers of PNDs internalized in cells, thanks to the avalanche photodiode used in the single photon counting mode (in contrast to the Leica microscope where the detector is a photomultiplier). The excitation wavelength used in all cases was 488 nm.

4.2.2 Internalization of photoluminescent nanodiamonds in cells

To ensure that PNDs are internalized by cells, we performed vertical cross-section scans with the commercial confocal microscope. The NDs used are type M particles (*Aq46nm-Me18*). With excitation at 488 nm with an Ar ion laser and emission collected in the range of 600-750 nm (referred as *red channel*), a series of images of PNDs in different positions on the z-axis is plotted on Figure 4.1. Along the vertical direction the spacing of the optical sections is 632 nm, from the bottom to the top of the cell. We also recorded differential interference contrast (DIC) images of the cells, for a better contrast. We made a 3D reconstruction of the images, using the software *Imaris* (Bitplane, Switzerland). The internalized PNDs resided in the cytoplasm within perinuclear spaces. Similar observations have been reported in other studies [48, 51, 60].

To quantify the uptake kinetics, we estimated from the confocal raster scans the mean fluorescence intensity per cell in the red channel. For this purpose we used the *mean intensity* analysis/measure tool of *ImageJ* software (NIH, USA). About 40 cells were analyzed for each different incubation time.

We found an exponential behaviour in time, with a characteristic uptake half-life of 2.6 h (Figure 4.2). These measurements are in agreement with the 3 h uptake half-life

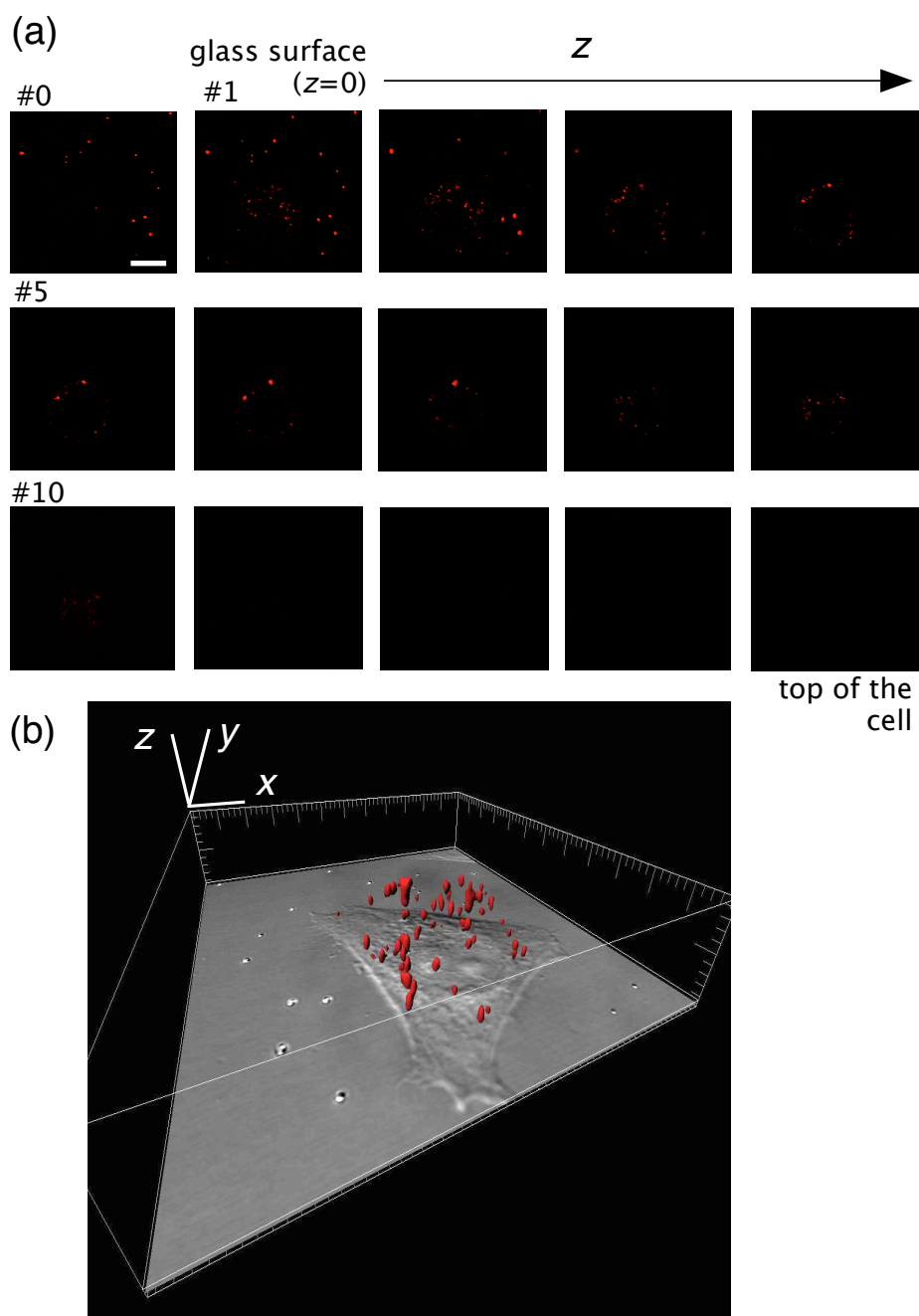


Figure 4.1: Three dimensional localization of PNDs in the HeLa cell. (a) Photoluminescence cross-sections of the cell done with the commercial confocal microscope, at increasing z focusing positions, from the coverglass mounting medium interface ($z = 0$, image #1) on which the cells are grown (upper left scan), to the top of the cell culture ($z \approx 8.9 \mu\text{m}$, bottom right scan). Vertical displacement steps between consecutive scans: 632 nm (image #0 is recorded at $z = -632 \text{ nm}$); white bar scale: $10 \mu\text{m}$. (b) 3-D reconstruction of PND spatial distribution. The DIC image of the cell is reproduced in the coverglass plane to localize the PNDs relative to the cell borders. The white bars indicating the 3-axis (x, y, z) orientations have a $10 \mu\text{m}$ length.

observed for 70 nm PNDs (examined by flow cytometry) [184] and the 1.9 h reported for 50 nm gold nanoparticles [185].

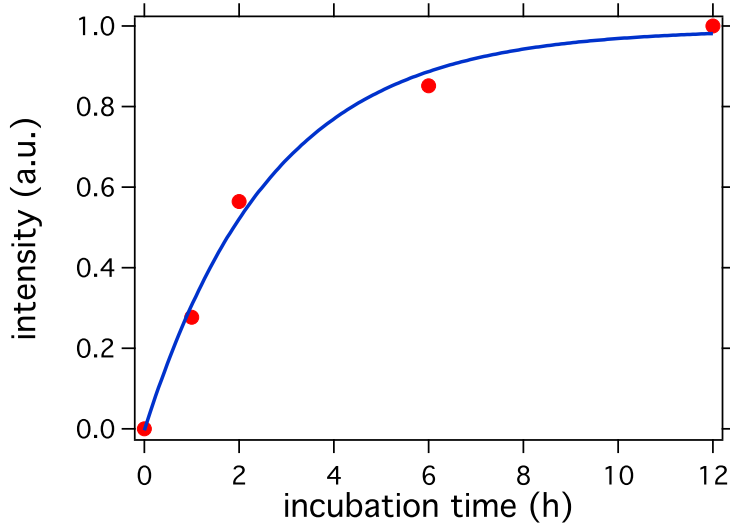


Figure 4.2: Dynamics of photoluminescent nanodiamond uptake by HeLa cells. The uptake efficiency is quantified by the mean photoluminescence intensity per cell, inferred from confocal imaging in the NV color-center emission spectrum region. This intensity is normalized to one at 12 hours incubation time. Blue solid curve is an exponential fit with a characteristic time of 2.6 hours.

4.2.3 Detection of individual photoluminescent nanodiamonds in cells

As far as internalization of PNDs in cells is demonstrated, the question whether these PNDs are found in clusters or individually arises. To answer that question we used the home-built confocal microscope setup, equipped with avalanche photodiodes, working in the single photon regime. We used the Nikon $\times 60$, NA 1.4, oil immersion objective, adapted for phase contrast observations. Cells were incubated with PNDs as previously. The PNDs used this time were type N NDs, the *Aq30nm-Np15* sample. Presence of internalized PNDs into the cells is checked from confocal scans obtained at different heights along the z -axis, using cw laser excitation at 488 nm.

Figure 4.3c is an optical scan zoomed in an intracellular region in the cytoplasm, at $z = 1500$ nm above the coverslip surface. We distinguish diffraction-limited spots that could be single PNDs but also larger ones, that are surely aggregates.

Photoluminescence spectrum from the PND in yellow square (Figure 4.3c) allows us to confirm that emission originates from NV color centers (NV $^{\circ}$ for this particle). Intensity time correlation measurement of the emitted light yields a photon antibunching dip of 0.55 at zero delay, indicating the presence of two emitters inside the diamond nanoparticle under study (Figure 4.3d).

In another study on the same sample, using near-field scanning optical microscopy, we have shown that about one third of the ND population contains 1 to 2 NV centers while the remaining population does not contain any NV center [16]. Independently, by

confocal observations of a large sampling (see chapter 2) we have found a mean density of 2.1 ± 1.1 NV/PND for this sample. In the present study, all the diffraction limited spots of PNDs under study (~ 20) that can be observed by photoluminescence inside the cell contain less than 4 emitters, which is a further indication that the nanoparticles detected are either two 30 nm particle agglomerates or more probably single (isolated and not agglomerated) nanoparticles. This observation is important for future applications such as drug delivery, which require individual PNDs with a high mobility inside the cell.

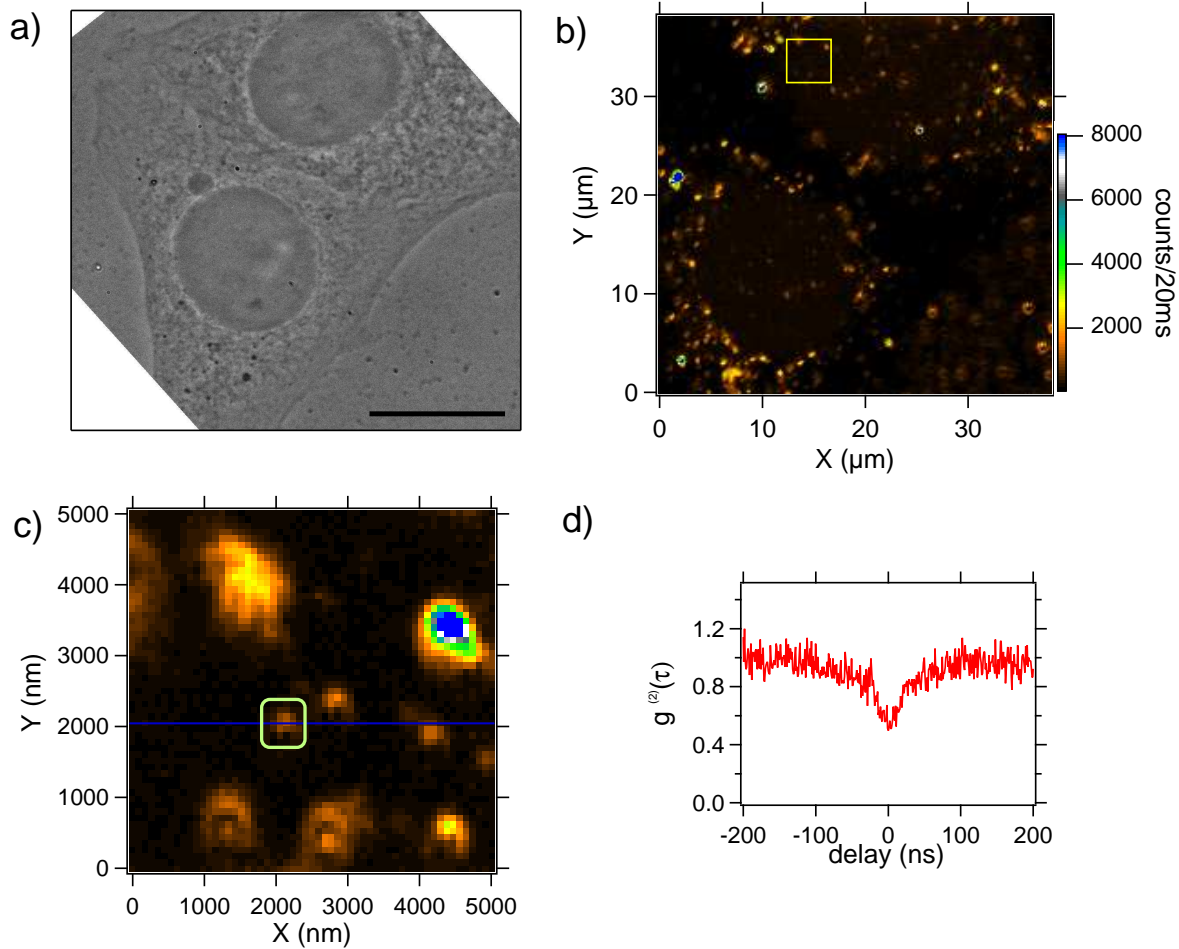


Figure 4.3: Photoluminescent nanodiamonds in HeLa cells : (a) Phase contrast image showing two cells, scale bar $15 \mu\text{m}$. (b) Confocal scan at $z = 1500 \text{ nm}$ above the coverslip surface, cw excitation laser at 488 nm , power 0.5 mW (i.e. $\sim 330 \text{ kW/cm}^2$). (c) Zoomed confocal scan of the yellow squared region from (b). (d) Normalized autocorrelation function of the PND of (c), with antibunching at zero delay associated to the emission of 2 NV color centers, excitation wavelength 488 nm , power 2 mW .

4.3 Tracking of single photoluminescent nanodiamonds in cells

4.3.1 Techniques of individual nanoparticle tracking

The technique of single particle tracking (SPT) allows the direct visualization of the trajectory of a biomolecule linked to a nanoparticle (NP), in contrary to other methods like Fluorescence Correlation Spectroscopy (FCS) or Fluorescence Recovery After Photobleaching (FRAP) that study the dynamics but not the single particle trajectories. The nanoparticle can be detected either by its fluorescence or by its scattered light. This technique gives the position of the NP with great precision, overcoming the diffraction limits. Normally for a nanoparticle, the resolution achieved by a microscope is of the order of the half of the light wavelength (Airy disk, for a numerical aperture close to unity). Let us consider that each nanoparticle forms an Airy pattern [186]. By adjusting the particle signal with a gaussian function the exact position can be found at the centroid of the Airy disk ³. The precision will depend on the number of photons collected from the nanoparticle, the number of pixels describing the Airy disk area and the noise level.

The first work on the tracking of single biomolecules coupled with an organic dye was realized by Webb [187]. Gold nanoparticles were later proposed as nanolabels of biomolecules by the team of Kusumi [188]. Gold nanoparticles of 40 nm were attached to biomolecules. The diffracted light was observed with a camera. The principal concepts proposed by Kusumi are nowadays widely used for SPT of various NPs, nanodiamonds in our case.

The Mean Square Displacements method

Depending on the trajectory followed by the complex NP-biomolecule recorded by SPT, one can infer the type of diffusion. A usual method to provide a diffusion coefficient is to calculate the mean square displacements (MSD) [188]. For each trajectory of a particle the two dimensional MSD is defined as:

$$MSD(\Delta t_n) = MSD_x(n\delta t) + MSD_y(n\delta t) = \quad (4.1)$$

$$\frac{1}{N-1-n} \sum_{j=1}^{N-1-n} \{[x(j\delta t + n\delta t) - x(j\delta t)]^2 + [y(j\delta t + n\delta t) - y(j\delta t)]^2\} \quad (4.2)$$

with $\Delta t_n = n\delta t$

where $[x(j\delta t + n\delta t)]$ and $[y(j\delta t + n\delta t)]$ describe the particle position following a time interval $\Delta t_n = n\delta t$, after starting at the position $[x(j\delta t), y(j\delta t)]$. N is the total number of frames in the video recording sequence, and n and j are positive integers, with n determining the time increment. The two-dimensional MSD is the sum of the MSDs in the x and y directions.

³because the differences between the two functions are minor, fitting a gaussian profile is easier in practice [179].

For each type of movement there is a corresponding MSD. Figure 4.4 adapted from Kusumi et al. article [188] shows the typical trajectories with the corresponding MSD for i) brownian diffusion, ii) directed diffusion and iii) restricted diffusion movement.

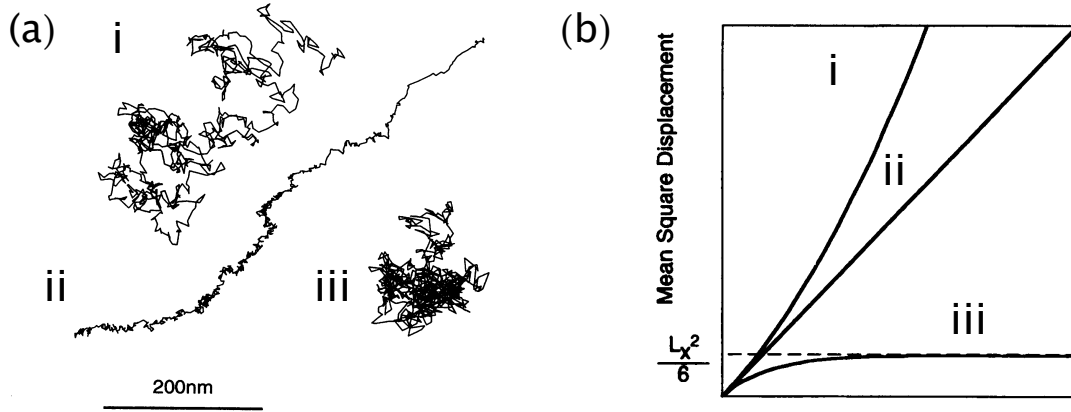


Figure 4.4: (a) Typical trajectories of gold particles attached to E-cadherin. (b) MSD plots as a function of Δt for the particles of (a), executing correspondingly: i) brownian diffusion, ii) directed diffusion and iii) restricted diffusion movement, where $L_x^2/6$ the explored length in the x direction.

For spherical particles executing a 2D free brownian motion, $MSD(t) = 4Dt$, where D is the diffusion coefficient and t the diffusion time. In the case where there are external forces (drifts) acting on the particles, the equation becomes $MSD(t) = 4Dt + v^2(t)$, where v represents the velocity of the directional movement. For confined motion the MSD takes a more complicated form, described explicitly in Kusumi's work [188].

Some other techniques for determining the NP motion exist apart from the MSD calculation, like the first-passage times method [189] or the method based on the radial particle density distribution [190].

The Inference method

Very recently a new technique was proposed by Masson et al. [191]. With an inference approach this method provides from the recorded trajectories the map of the local forces and potentials involved in confined motions; parameters not calculated by the MSD method. The detailed description of the inference method is out of the scope of this chapter. We will briefly describe its basic principles.

The particle is considered to execute Brownian motion under a force field. The motion of the particle is described by the Langevin equation:

$$m \frac{dv}{dt} = -\gamma v - \nabla V(r) + \sqrt{2D\gamma^2} \xi \quad (4.3)$$

where $v(t)$ the velocity of the particle, m the mass, γ and D the friction and diffusion coefficient, ξ the zero-average Gaussian noise. We see that the motion of the particle has three terms, one for the friction (described by γ), one for the forces acting on it (with $V(r)$ the potential) and one for the thermal noise (described by ξ).

The domain where the particle moves is divided in subdomains and the forces are supposed to be constant in these subdomains.

If we know F and D one can find the probability to go from (r_0, t_0) to (r, t) . By recording the particle trajectory, we know that the particle went from the point (r_0, t_0) to (r, t) and search F and D . With the inference method, one can calculate these values.

With F, D constants in each subdomain, for a trajectory starting at (r_0, t_0) , the probability of finding the particle at (r, t) can be expressed as :

$$P(r, t|r_0, t_0) = \frac{\exp[-\frac{(r-r_0-F\Delta t/\gamma)^2}{4D\Delta t}]}{4\pi D\Delta t} \quad (4.4)$$

with $\Delta t = t - t_0$.

For a trajectory T (with F, D constants) starting at (r_0, t_0) and ending at (r_N, t_N) , we obtain:

$$P(T|D, F) = P(r_N, t_N|r_{N-1}, t_{N-1}) \cdot \dots \cdot P(r_2, t_2|r_1, t_1) \cdot P(r_1, t_1|r_0, t_0) \quad (4.5)$$

To summarize, if we know the values of F and D , we can calculate the probability to go from the point (r_0, t_0) to the point (r, t) . In our case the inverse situation happens, i.e. we know that the particle executed the trajectory T from (r_0, t_0) to (r, t) and we search the probability of this transition for certain values of the parameters F and D .

By using the Bayes theorem [192] one can calculate the *posterior* probability of having the parameter values U given the observation of the trajectory T . According to that theorem:

$$P(U|T) = \frac{P(T|U) \times P_0(U)}{P(T)} \quad (4.6)$$

with T : trajectory of particle, U : parameters F and D , $P(T|U)$: the probability of observing the trajectory T given the parameter values U , $P_0(U)$: the *prior* probability, which is taken constant, $P(T)$: normalization constant.

Thus, it is possible, by knowing the trajectory of a particle, to calculate the constants F, D for each domain of the motion.

4.3.2 Experimental Setup

Wide-field illumination microscope

The experimental setup is the same as the one used for confocal imaging (chapter 2), except of two modifications. First, the excitation 532 nm laser beam was defocused before entering the objective of the microscope by a 300 mm converging lens (CL), making the beam converge onto the back focal plane of the objective. Second, the side output port of the microscope stand was used to image the focal plane onto a sensitive CCD array (*CoolSnap Monochrome*, Photometrics, USA). The acquisition time per frame for the video sequences was 50 ms. The total time per frame was 100 ms, because there is an additional 50 ms reading time of the CCD array. The excitation power was 30 mW at the microscope entrance, i.e. before the dichroic mirror and the microscope objective. This is translated to an intensity of ~ 1 kW/cm², as the illuminated surface in the sample plane

is around 25-30 μm . The dichroic mirror used is the *Q565LP* (Chroma). The residual excitation light is removed by the long-pass filter (LPF) with 97% transmission between 539-1200 nm (*RazorEdge LP03-532RU-25*, Semrock, USA).

Cell preparation

HeLa cells were grown in standard conditions on glass coverslips in DMEM as the culture medium, supplemented with 10% FCS. To study the internalization of PNDs, cells were seeded at a density of 10^5 cells/ 1.3 cm^2 and grown at 37°C in a humidified incubator under 5% CO_2 atmosphere. Twenty-four hours after the cell seeding, the PNDs aqueous suspensions were added to the cell medium. We performed the microscope observations after two hours incubation of the cells with the PNDs. No cell thermostatic incubator was used. The total observation time was one to two hours. After that time the cells started to get detached from their substrates, and cell death occurred.

4.3.3 Wide-field microscopy observations of freely diffusing nanodiamonds

In order to prove that PNDs are suitable for wide-field observations, we first examined the free brownian motion of PNDs in solution. We used PNDs of two different sizes, the *Aq30nm-Np16* and the *Aq164nm-Me18* sample.

Figure 4.5a shows an image of *Aq164nm-Me18* PNDs, freely diffusing in a 20% water - 80% glycerol solution. The PND diffusion in this solution is a free 3D-brownian motion, but the observations are restricted to the portion of this motion taking place in the focus plane. More precisely only PNDs which are moving within a slice of thickness equal to the depth of focus ($\approx 270\text{ nm}$) are observed. Therefore the recorded motion is a 2D-projection portions of the 3D trajectory contained in this slice. On the wide field images we distinguish the characteristic ring intensity patterns for the PNDs going out of focus.

To construct the particle trajectory from this record, we used the “ParticleTracker” plugin of NIH-*ImageJ* software, which implements the algorithm of Ref. [193]. The particles that are too far from the middle plane of the focusing slice appear as non diffraction-limited dimmer spots that are excluded by the software, using a filtering procedure. This procedure relies on a size restriction and intensity level cutoff. It selects the particle motions which take place in a slice thinner than the one limited by the optical depth of focus, so that the motion really taken into account for the trajectory construction is very close to a 2D one.

The “ParticleTracker” plugin also constructs a trajectory with a step resolution better than the real-space pixel size of $\approx 140\text{ nm}$. Tracking algorithms are characterized by two types of errors, the determinate and the indeterminate errors [194]. Determinate errors result from inaccuracies inherent to the algorithm (characterized by the bias b in the position with respect to the geometry of the system). Indeterminate errors cause the individual measurements to fluctuate randomly, and generally result from measurement fluctuations and imaging noise (characterized by the standard deviation σ between the measured and true positions). The former errors are also referred as *accuracy* and the latter as *precision*. A good tracking algorithm has to minimize both types of errors.

The critical signal-to-noise ratio ($\text{SNR} = \frac{S - B}{\sqrt{S}}$, with S the signal, B the background and \sqrt{S} the shot limited noise) for reaching an accuracy better than 0.1 pixel (for the maximum of the gaussian intensity distribution) is around 4.2 for the algorithm of “ParticleTracker”, while its precision is better than 1 pixel for all SNR larger than 1.3. For SNR better than 7.5, both accuracy and precision are below 0.1 pixel. These values are comparable to the ones of other tracking techniques, like the centroid or gaussian fit method [193].

For PNDs the SNR varies, depending on the number of NV centers embedded in the nanocrystals. For the image of Figure 4.5a the SNR of the corresponding particles is in the range between 1.3 and 12.

After the video processing and the trajectory reconstruction, the PNDs were mostly found to follow brownian trajectories with no directional force. By applying the MSD method we calculate the diffusion coefficients of PNDs following a brownian motion. For the PNDs of size 164 nm, we measured $D = 0.04 \mu\text{m}^2/\text{s}$ (Figure 4.5b,c). This is the mean value out of 6 particles, with lower and higher values at $D = 0.01 \mu\text{m}^2/\text{s}$ and $D = 0.05 \mu\text{m}^2/\text{s}$ respectively. A lower bound to the error bars results from the two extreme slopes of the $\text{MSD}(t)$. For 30 nm mean size PNDs (Figure 4.5d-e) the diffusion coefficient was found equal to $D = 0.20 \mu\text{m}^2/\text{s}$, which is 5 times bigger than the one of 164 nm PNDs. This measurement is the mean value over 5 particle trajectories, with extremes at $D = 0.05 \mu\text{m}^2/\text{s}$ and $D = 0.35 \mu\text{m}^2/\text{s}$ as lower and higher values respectively.

The above experimental values can be compared with the theoretical predictions given by the Stokes-Einstein equation $D = kT/(6\pi\eta a)$, a being the particle radius, η the dynamic viscosity of the medium (60 cP or 0.06 kg/m.s in SI), k the Boltzman constant, and T the temperature. The diffusion coefficients for 164 and 30 nm particles inferred from this equation are equal to $D = 0.04 \mu\text{m}^2/\text{s}$ and $D = 0.14 \mu\text{m}^2/\text{s}$ respectively. These values are in agreement with the experimental ones.

Note that the error bars on the measurement of the diffusion coefficients are large, which is an observation already reported in previous studies [188]. This broad distribution is mainly due to the fact that the trajectory analysis is done for a low number of steps. The precision on the measurement of the diffusion coefficient improves with the increase of the statistical sampling of the trajectory. However in a 2D study, it is not easy to record a continuous trajectory over a long observation time, since the particles, especially the small ones, are rapidly out of focus (depending on their size and the medium viscosity). In addition, the broad distribution of the diffusion coefficient is due to the particle size distribution, which is itself relatively broad.

4.3.4 Diffusion of photoluminescent nanodiamonds in living cells

The tracking of individual biomolecules in cells is of great importance in biology. In case the biomolecule is not photoluminescent, a photoluminescent marker can be attached to it in order to follow its motion. The first step for using PNDs as biomarkers is to verify that such a particle can enter the cell. What follows, is the recording of its trajectory in time. The spontaneous internalization of PNDs has been demonstrated in the previous section, here we will show that we are capable to follow the trajectories in cells. The

group of H.-C. Chang has managed to follow the three dimensional movement of single PNDs in cell [47]. In our group we did not develop the technique of 3D tracking, but followed the PNDs motion in two dimensions.

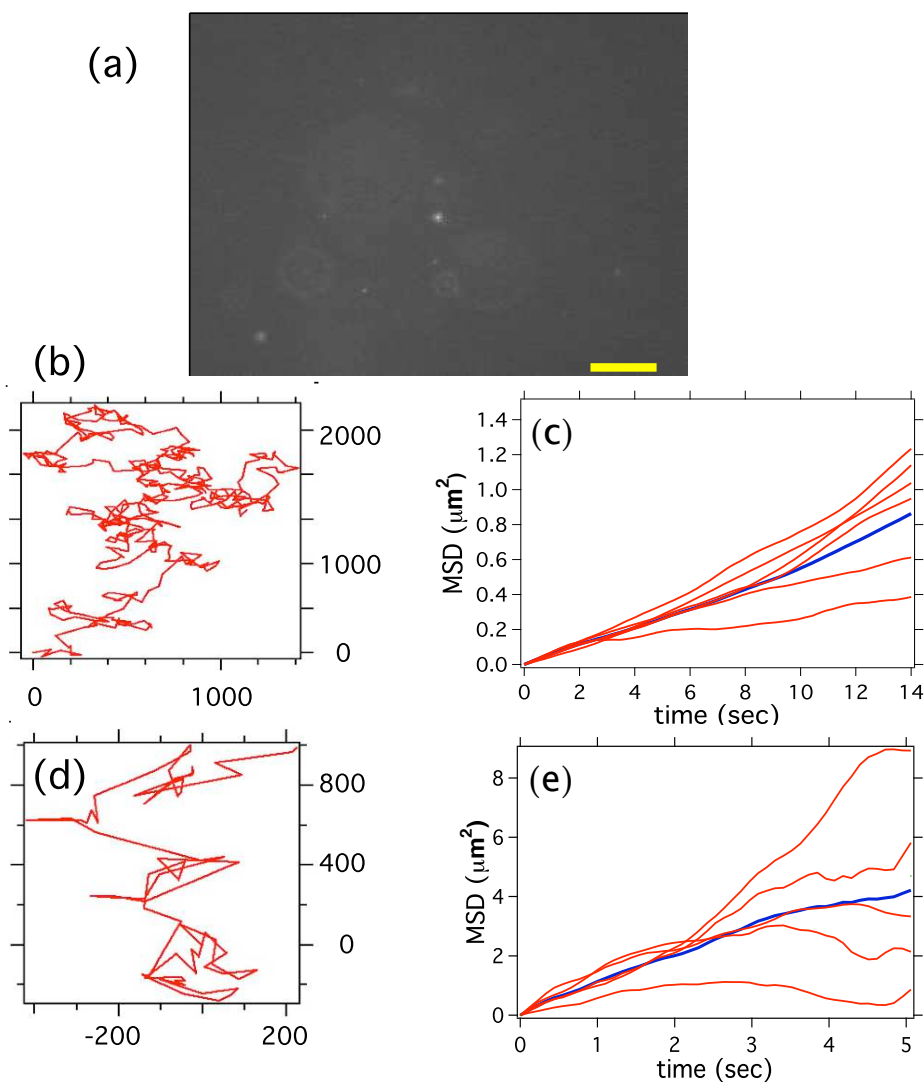


Figure 4.5: Free brownian diffusion of PNDs in a water:glycerol mixture : (a) One image frame of a sequence of 164 nm PNDs (*Aq164nm-Me18*) diffusing in a 20% water - 80% glycerol solution; exposure time per frame: 50 ms (+50 ms of reading time); this relatively long integration time is not a problem in our study as the water-glycerol proportion was deliberately chosen to induce slow nanodiamonds motions, allowing the resolution of individual steps in time; scale bar: 5 μm . (b) Trajectory of a single PND executing a free brownian motion. (c) Mean square displacements (MSD) for six different PNDs; the blue line is the mean value; (d-e) similar to (b-c) but for 30 nm mean size PNDs (*Aq30nm-Np16*).

Analysis of PND motion with the MSD method

Figure 4.6a shows the phase contrast image of a cell merged with the fluorescence image of PNDs (in red). In comparison with the video of a free PND in water:glycerol solution, it appears that here the motion is much more confined. We recorded video sequences with an acquisition time per frame of 50 ms (added to a reading time of 50 ms). By analyzing the MSD values at short times [195], where the experimental curve mainly follows its tangent at the origin equal to $4D$, we determine an equivalent “diffusion coefficient” $D = 0.006 \mu\text{m}^2/\text{s}$ (Figure 4.6b,c). Among all particle motions studied, the maximum diffusion coefficient found does not exceed the value of $0.010 \mu\text{m}^2/\text{s}$, in agreement with previous measurements for confined motions of nanodiamonds in cells [47].

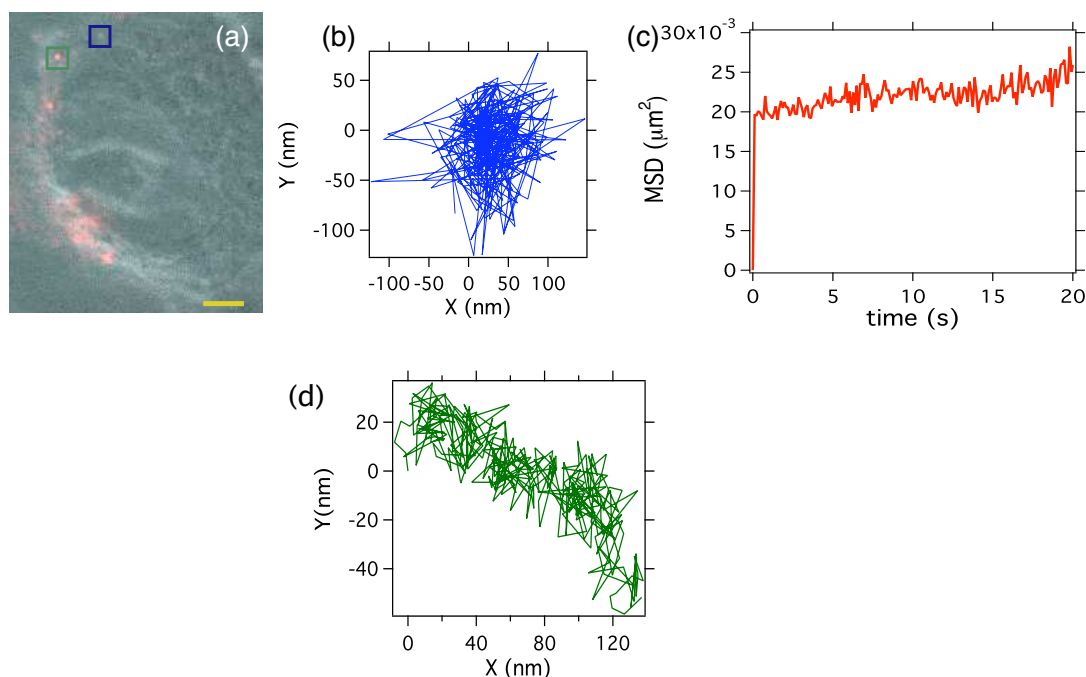


Figure 4.6: Intracellular trafficking of single 36 nm PNDs in a living HeLa cell: (a) Phase contrast image of the cell (centered on the cell nucleus) merged with photoluminescence image of PNDs (in red); bar scale: $3 \mu\text{m}$. (b) Trajectory of the PND located inside the blue square. (c) Mean square displacement of the PND of (b). (d) Trajectory of the PND surrounded by the green square.

Note that the confinement dimension is about 160 nm, higher than the local precision of the noise level ($\text{SNR} = 5.6$). This result proves that we observed a true -although very small- motion of the PND. Figure 4.6d shows a PND trajectory inside the same cell with a slightly directed motion on a short distance (before the particle goes out of focus) with a typical displacement of 15-20 nm (i.e. 0.1 pixel). The SNR for this PND is 6.9, so with the applied algorithm one should obtain a tracking error of the order of 0.1 pixel (i.e. 14 nm), in accordance with our measurements.

The values of the diffusion coefficients found are relatively low. The reason for the PNDs low mobility in cells is that the observed PNDs are probably captured in endosomal or lysosomal vesicles [48]. Due to the moderate sensitivity of the camera used, the smallest PNDs, with the most rapid movements and perhaps not trapped in endocellular vesicles,

are not observed. Our calculations of the diffusion coefficients are in good agreement with the reported diffusion of quantum dots confined within endosomes [196].

Analysis of PND motion with the inference method

Alternatively to the MSD method, we used the inference method to measure the forces applied on a PND in the cell executing a confined motion. We used an algorithm developed by Masson et al., based on Ref. [191], and provided to us by Silvan Türkcan and Antigoni Alexandrou (LOB, Ecole Polytechnique). As already mentioned, this algorithm infers the forces applied on the particle from the recorded trajectory data, calculating the diffusion coefficient as well. One should divide the area in which the particle moves in domains; in our case we divided the area in $8 \times 8 = 64$ domains.

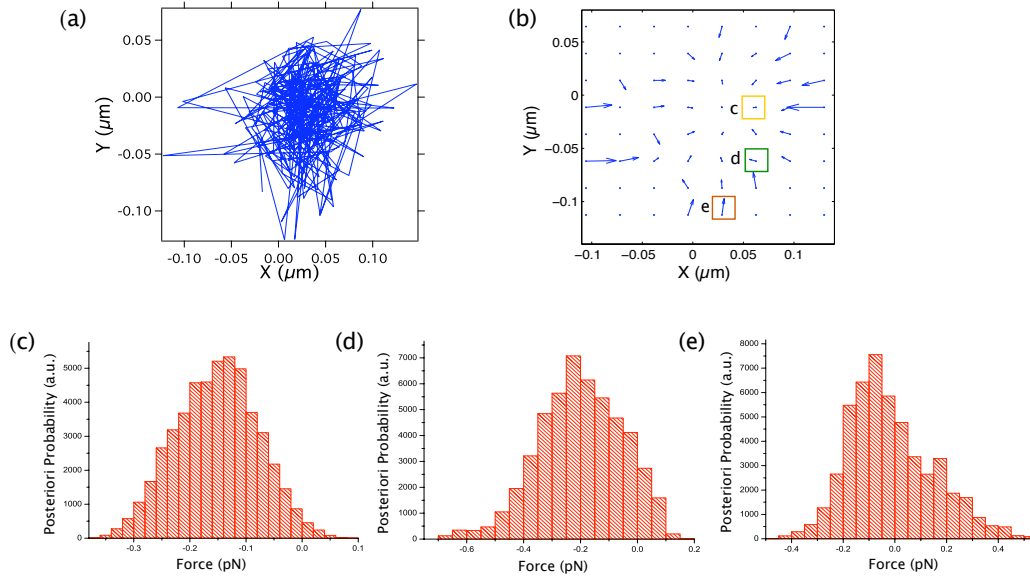


Figure 4.7: Force mapping of PNDs in cells using inferences method. (a) Trajectory of the PND located inside the blue square of Figure 4.6a. (b) Force field of PND of (a). (d-e) Posterior probability distributions of the horizontal component of the forces at the locations indicated with squares in (b).

We observe that the particle executes a confined motion, with all forces pointing towards the center (Figure 4.7b). The diffusion coefficient is found $(0.0059 \pm 0.0004) \mu\text{m}^2/\text{s}$ (Figure 4.7c). This value is in agreement with the one calculated by the MSD method.

One can also calculate the posteriori probability distribution of the forces for each domain, to verify the precision of the calculations. As shown on Figure 4.7c,d,e the probability force distributions of the selected domains are relatively broad, but not too broad, indicating the efficient force calculation by the inferences method.

We demonstrated that with this method one can map the forces applied on such a PND. Although in our case most probably no special interactions took place (Figure 4.7c-e), for further applications of PNDs as labels of biomolecules, the inference method could offer very important information on the dynamic evolution of the system and the involved forces.

4.4 Conclusion

In this chapter, we carried out tracking experiments on single PNDs. We observed that acid-cleaned PNDs can be spontaneously internalized by cells by using confocal microscopy. By wide-field illumination microscopy we recorded some confined motion of internalized PNDs, probably because these PNDs are trapped in intracellular vesicles. Because of the high viscosity of the cytosol, a 10 images/sec frame rate is sufficient to follow the intracellular motions of PNDs. Our results indicate that PNDs can be used for long-term single particle tracking, and are therefore promising candidates for bio-imaging.

Chapter 5

Elucidation of the cellular uptake mechanism and *in vitro* toxicity studies of PNDs

5.1 Introduction

The cellular uptake of nanoparticles is an important area of biological research. Because cells need to communicate with the outside world and because they need to take up nutrients they are equipped with natural transport pathways both for incorporating and for secreting materials. In general, these transport pathways are part of a whole network of cellular membrane traffic [197], which generally involves membrane-surrounded vesicles of aqueous content. Natural uptake into cells is called endocytosis [198–201], an energy-dependent uptake mechanism (in contrast to passive diffusion, which is energy independent). Depending on the size of endocytosed materials and on the detailed uptake mechanisms, various types of endocytosis exist: pinocytosis for small particles and dissolved macromolecules (diameters up to about 150 nm), phagocytosis for larger structures (such as whole cells, cell debris or bacteria).

Pinocytosis and endocytosis are often used as synonyms. Whether the dominant mechanism will be pinocytosis or phagocytosis depends on the nanoparticles size and the cell type under consideration. For example, macrophages (cells specialized in cleaning ‘large’ structures such as debris of dead cells or foreign intruders such as bacteria or colloidal nanoparticles) capture foreign substances by phagocytosis. The material to be incorporated is “engulfed” by invaginations that lead to the budding of an intracellular membrane-surrounded vesicle. According to the uptake mechanism and to the incorporated material, the fate of such vesicles differs. In pinocytosis these vesicles are called endosomes and lysosomes. They are responsible for the breakdown of ingested materials. These vesicles are equipped with specialized enzymes that degrade proteins and nucleic acids.

Depending on the cellular molecules involved in endocytosis, uptake of material can be specific or unspecific. In specific uptake, otherwise called receptor-mediated endocytosis (RME), a ligand binds to a cell surface receptor and is internalized as the membrane invaginates. The receptor transports the ligand into the cell, releases it and normally is recycled back to the cell membrane. Among the RME processes, the most studied

pathway is the clathrin mediated endocytosis. Clathrin is a protein cage that assembles around cell membrane invaginations during endocytosis, forming the so-called clathrin-coated pits (Figure 5.1) [202, 203]. Other main RME processes, which are clathrin-independent, occur mainly through the caveolae pathway. Caveolae are invaginated, flask-shaped plasma membrane domains, which are especially enriched in cholesterol. They are characterized by the presence of the integral membrane protein caveolin [204].

Another endocytosis mechanism, mediated by lipid rafts and clathrin-, caveolae-independent, is the macropinocytosis. This specific process involves the enclosing of actin-containing membrane extensions to form vesicles called macropinosomes. These vesicles are characterized by their big dimensions, which can often be greater than $1\ \mu\text{m}$ [205, 206].

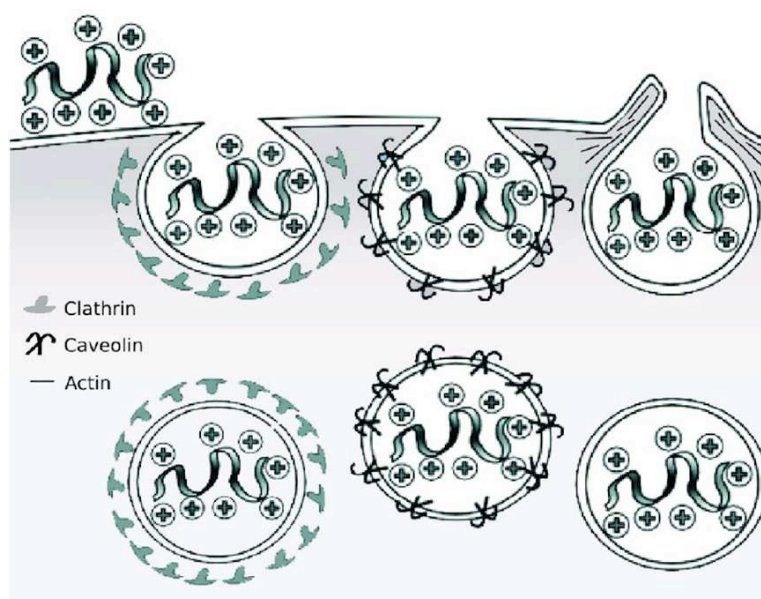


Figure 5.1: Endocytotic uptake mechanisms. From left to right: clathrin-mediated endocytosis, caveolin-mediated endocytosis, macropinocytosis [207].

Several groups have demonstrated the use of receptor-mediated endocytosis for intracellular delivery of nanoparticles. For QDs in particular, they have found that QDs entering cells by this pathway remain sequestered in endocytic vesicles, preventing the labeling of other intracellular structures [22, 174, 208]. Studies on latex fluorescent beads report a size dependent internalization mechanism, beads less than 200 nm in diameter are taken up through clathrin mediated pathway but as the size increases (up to 500 nm) the mode of uptake becomes increasingly caveolae-mediated [209]. Possible ways to have individual nanoparticles free in the cytosol, by passing through the endosomal route, is the proper surface functionalization of the nanoparticles. For example QDs or gold nanoparticles surface modification with a ligand shell of monohydroxy 1-mercaptopundec-11-yl tetraethylene glycol (PEG) and subsequent encapsulation in liposomes, leads to efficient endosomal uptake and release of the nanoparticles in the cytosol [173, 210]. More advanced techniques use the grafting of cell penetrating peptides (CPPs) on the nanoparticles surface, to facilitate the cell penetration [211, 212]. Indeed, sometimes it appears that nanoparticles coated with a combination of CPPs can escape from the inside of endo-

somes disrupting endosomal morphology and dissolving the endosomal membrane, once internalized in the cytoplasm [210]. Alternative, more invasive methods of nanoparticle internalization in cells exist, as microinjection, gene gun, sonication or the application of an osmotic or electric shock.

Regarding photoluminescent nanodiamonds, the determination of the uptake routes of PNDs in cells is a necessary requirement for further applications of PNDs beyond simple cell labeling, like for instance the intracellular biomolecule labeling or the use of PNDs as drug delivery devices.

To enlighten the internalization pathways, we blocked endocytosis with special cell treatments and with the use of specific drugs we inhibited the receptor mediated endocytotic procedures. The results show that the internalization of PNDs stems mainly from endocytosis, and we have strong indications that it is receptor-mediated endocytosis [176]. To check the endocytotic nature of the uptake and localize the internalized PNDs, we carried out immunofluorescence experiments, by labeling the endosomes and lysosomes of the cell, and complementary experiments with transmission electron microscopy [48, 176].

Additionally, for applications of diamond nanoparticles in biology, biocompatibility of the diamond material is of crucial importance. Since nanodiamonds are different from their respective bulk material due to their size, it is a natural question to ask for potential dangers arising from their tiny sizes [76]. Although the CVD diamond thin films are generally regarded as biologically inert, noninflammatory, and biocompatible [213], the question whether diamond nanoparticles are well tolerated by cells remains still open.

There are many ways by which nanoparticles introduced into an organism could interfere with its function and finally lead to its damage. The three most common ways are listed below.

1) Most evident, introduced nanoparticles can be composed of toxic materials. This is true, for example, for fluorescent CdSe/ZnS Quantum Dots as well as for magnetic Co particles. The coating of this kind of nanoparticles can be degraded with time and the toxic core can be released in the cell and provoke toxicity [29, 214, 215]. This is not true for diamond nanoparticles, as their composition consists of carbon atoms.

2) There might be a negative effect of particles in general on cells, regardless of the material of the particles. It is known that particles can stick to the surface of cell membranes [216] and particles are also known to be ingested by cells [208, 217]. Mantling of the cell membrane and storage of particles inside cells might have impairing effects, even for absolutely inert particles that do not decompose or react.

3) There might be an effect caused by the size and shape of the particles. It has been reported for example, that carbon nanotubes can pierce cells like needles [218, 219]. Nanoparticles of the same composition but of different shape induce different toxicity. For instance, carbon nanotubes that reach the mice lung are more toxic than carbon-black or graphite [219, 220].

Concerning nanodiamonds, according to previous studies, both detonation [76] and HPHT NDs appear to be biocompatible [50, 221], even more than carbon nanotubes [79]. As cytotoxicity depends on the size and shape of nanoparticles [30], we wanted to test the biocompatibility of all the NDs types used in our experiments with cells; the detonation and both types of HPHT NDs.

The first step towards understanding how a nanoparticle will react in the body often

involves cell-culture studies. Compared to animal studies, cellular testing is easier to control and to reproduce, and is less expensive as well. Here we limited our study to cell-cultures. Initially we examined the morphology of the cells, for different concentrations of nanodiamonds. Afterwards, we performed MTT cytotoxicity assays¹. We compared the cytotoxicity of the NDs with that of a common drug vector, the lipofectamine and found that NDs are biocompatible and not toxic for cells, at least for “low” concentrations [48, 176].

5.2 Determining the cellular uptake pathway of photoluminescent nanodiamonds

In chapter 4 we found that PNDs are spontaneously internalized by cells. The determination of the exact uptake mechanism is of crucial importance for future applications of PNDs apart from whole cell labeling, like drug delivery, intracellular trafficking or therapeutic applications.

5.2.1 Study of the endocytosis mechanism

To evaluate the contribution of endocytosis to PNDs internalization by HeLa cells, the cells were incubated with PNDs (type M, *Aq46nm-Me18*, concentration 20 $\mu\text{g}/\text{ml}$) under different conditions: (i) at 37°C (control), (ii) at 4°C and (iii) after pretreatment with NaN_3 . The latter treatment disturbs the production of ATP and blocks the endocytosis [226] since it is an energy-dependent process. Incubation of the cells at 4°C is also known to block the endocytosis.

Cells were treated as following:

- (i) *Incubation under normal conditions*: incubation of PNDs with cells was carried out as usual (look at chapter 4) with the solution kept at 37°C.
- (ii) *Low temperature incubation at 4°C*: incubation of PNDs with cells was carried out as usual with the solution kept at 4°C instead of 37°C.
- (iii) *Incubation of cells with PNDs under ATP depletion*: for the ATP depletion studies the cells were preincubated in PBS buffer solution and supplemented with 10 mM NaN_3 for 30 min at 37°C and then PNDs were added.

The large scale photoluminescence observations of PNDs in the cells were carried out with a commercial Leica TCS SP2 (Manheim, Germany) laser scanning confocal microscope, with a $\times 63$, 1.4 numerical aperture (NA) oil-immersion objective. Excitation comes from the cw argon ion laser line at 488 nm wavelength. We use one Airy Unit as the pinhole diameter, for all the acquisitions. For PNDs detection we spectrally selected light with wavelength in the range between 600-750 nm (we will address this range as the *red channel*).

Figure 5.2 shows that when endocytosis is hindered by low temperature or NaN_3 , the photoluminescence signal from PNDs strongly decreases (Figure 5.2b,c) compared to the control (Figure 5.2a).

¹MTT assay is a 3-[4,5 -thylthiazol- 2-yl]-2,5-diphenyl-tetrazolium bromide assay, a widely used toxicity test [222, 223] relying on mitochondrial activity measurement to assess cellular viability [224, 225].

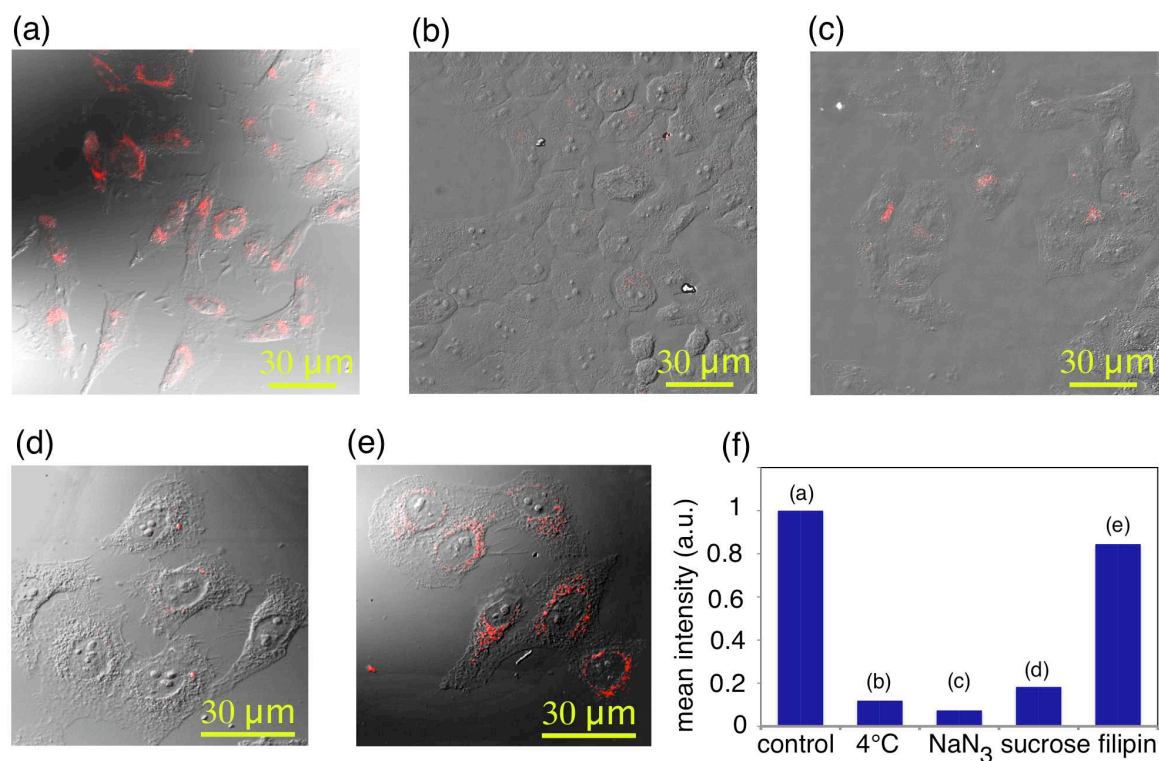


Figure 5.2: Nanodiamonds are uptaken by HeLa cells through endocytosis. Merged photoluminescence confocal raster scans (*red channel*) and DIC images of PNDs (concentration $20 \mu\text{g/ml}$) incubated for 2 hours with cells (a) at 37°C (control) and (b) at 4°C , or at 37°C but after pretreatment with either (c) NaN_3 (10 mM), or (d) sucrose (0.45 M), or (e) filipin ($5 \mu\text{g/ml}$). Confocal scans are acquired at $z = 1.5 \mu\text{m}$ above the coverglass surface, laser excitation power: 0.5 mW . (f) Mean photoluminescence intensity per cell (in the *red channel*) for the different cell treatments, normalized to the one of control cells and evaluated as described in chapter 4.

In order to check that low temperature blocks PNDs internalization even for the smallest particles that cannot be detected on the Leica TCS SP2 microscope, we used the home-built confocal microscope (described in chapter 2) able to detect the smallest PNDs, containing even a single NV center. The dichroic mirror used for these experiments was the 530dcxr. To ensure that the background noise is spectrally filtered and we collect only the NV center photoluminescence, we use an additional longpass filter, $\lambda > 580 \text{ nm}$ (*HQ580LP*, Chroma).

Figure 5.3 shows a series of confocal cross sections of one HeLa cell. The cells were first incubated with PNDs at 4°C and then fixed. We clearly see that almost no PNDs are present in the cytoplasm. The only ones observed are either on top of the cell, appearing as large aggregates (Figure 5.3d-f), or on the cell membrane as individual particles or small aggregates (Figure 5.3c).

These observations, together with the fact that the majority of the NDs composing the sample exhibit some photoluminescence (chapter 2), strongly suggest that very few NDs are internalized when endocytosis is blocked.

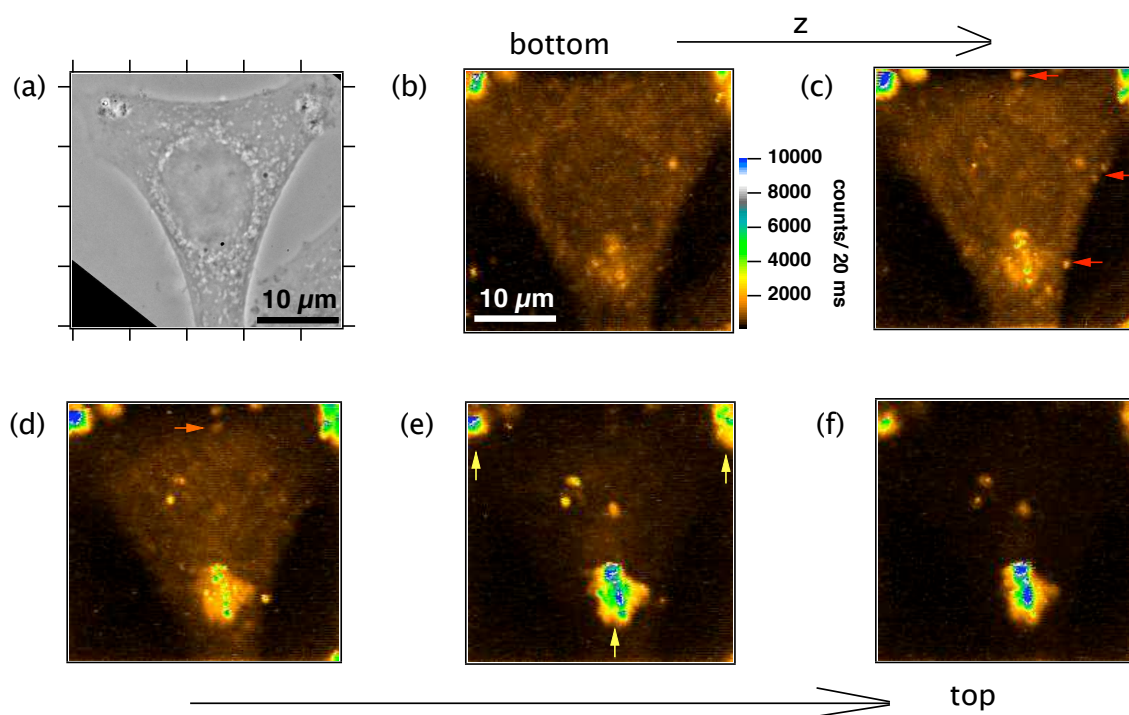


Figure 5.3: Photoluminescence confocal raster-scans of a HeLa cell incubated with PNDs at 4°C. (a) Phase contrast image of the cell under study. (b)-(f) A series of confocal raster scans done with the home-built microscope, at different focusing positions (1 μm displacement step between consecutive scans), from the bottom (coverglass plane, upper left) to the top of the cell (bottom right). Yellow arrows on scan (e) indicate PND-aggregates that are not internalized; red arrows on scan (c) show single PNDs that stay on the membrane; the orange arrow on scan (d) shows the only PND which is probably internalized.

5.2.2 Study of receptor-mediated uptake mechanisms

To further precise the endocytosis mechanism involved in nanodiamond cellular uptake, we investigated the receptor-mediated endocytosis (RME). Cells were incubated with PNDs under conditions that inhibit either the clathrin or the caveolae pathways. The conditions were the following:

- *Hypertonic treatment hindering the clathrin-mediated process*: the cells were preincubated for 30 min in PBS buffer solution and supplemented with 0.45 M sucrose followed by incubation with PNDs at 37°C.
- *Filipin treatment blocking caveolae pathway*: the cells were pretreated in PBS buffer solution and supplemented with filipin (5 $\mu\text{g}/\text{ml}$) for 30 min before exposure to PNDs at 37°C.

Interestingly, we observe on Figure 5.2d that pretreatment of cells with sucrose, a hypertonic treatment known to disrupt the formation of clathrin-coated vesicles [227, 228], reduces to a high degree the PNDs uptake (Figure 5.2d). To block the caveolae pathway, cells were pretreated with filipin which disrupts the formation of the cholesterol domains [228, 229]. In contrast to the clathrin-pathway blocking experiment, we observe on Figure 5.2e that pretreatment with filipin does not hinder the internalization of

PNDs, leading to the assumption that PNDs are mainly uptaken by the clathrin-mediated pathway.

For a more quantitative analysis, we evaluated the mean photoluminescence intensity per cell (in the *red channel*, corresponding to NV color center emission), in the same way as for PNDs cell internalization dynamic measurement. Figure 5.2f shows the change of this mean photoluminescence intensity per cell, normalized to the one of control cells. This graph summarizes quantitatively the effects of the different cell treatments, and supports the conclusion that the uptake mechanism of PNDs is endocytosis, with strong indications that it is clathrin mediated.

It should be mentioned that similar observations of clathrin mediated endocytosis were reported for other nanoparticles internalized by HeLa cells, like gold nanoparticles [185], single-walled carbon nanotubes noncovalently conjugated with DNA molecules [230] or very recently for 100 nm diamond nanoparticles [54].

5.2.3 Surface characterization of photoluminescent nanodiamonds in serum supplemented culture medium

The Foetal Calf Serum (FCS) was used to supplement DMEM (the cell culture medium) allowing normal cell growth. It contains a diverse set of proteins, like bovine serum albumin (BSA), transferrin, α - and β - globulin, etc... BSA is the dominant protein. We have strong indications that NDs uptake is receptor mediated. Such mechanism is usually influenced by the chemical functions present at the nanodiamond surface.

We therefore carried out Fourier Transport InfraRed (FT-IR) spectral analysis of the nanodiamonds after their interaction with the serum supplemented culture medium. This interaction changes the NDs surface functions, compared to their surface in aqueous suspension, due for example to nonspecific adsorption of serum proteins. Such binding could enhance the receptor-mediated endocytosis mechanism, as found recently for gold nanoparticles[185].

Zeta potential measurements

To check if the serum proteins can be adsorbed on PNDs surface, we measured the ζ -potential of nanodiamonds initially incubated with culture medium supplemented with foetal calf serum. Acid-treated type N PNDs (sample *Aq30nm-Np16*) were incubated with DMEM containing 10% FCS and sonicated for about 15 min. After two hours of incubation at room temperature and vortexing, the solution was washed by three successive centrifugations to eliminate the excess of proteins and then redispersed in pure water. The obtained PNDs aqueous suspensions exhibited a zeta potential $\zeta = -15,6$ mV (at pH=7), corresponding to a 2.5 fold decrease compared to pristine PNDs, which is a consequence of the change of its surface functions. This result agrees with previous studies, in which BSA was used as a stabilizer for Al_2O_3 or gold nanoparticles aqueous colloidal suspensions, where a similar change of the ζ -potential was observed [231, 232]. The suspension remained stable for many hours after the initial mixture. After a few days we observed the formation of some aggregates (confirmed by DLS measurements) which could be redispersed to the primary particles by sonication.

It is also worth to note that when PNDs are added to DMEM without serum they

strongly aggregate within one hour (to micron size aggregates), most probably due to the high ionic strength of DMEM leading to the screening of the NDs mutual electrostatic repulsion. On the contrary if one supplements DMEM with FCS, PNDs do not aggregate on a few hour timescale.

FT-IR spectroscopy measurements

To check the presence of adsorbed serum proteins on PNDs we performed FT-IR spectroscopy measurements. The PND-protein sample was mixed with KBr powder and pressed into pellets which were then placed in an IR cell. The FT-IR spectra of the KBr pellets were recorded with a FT-IR spectrometer (*Nicolet 8700 Research FT-IR*, Thermo Fisher Scientific Inc., USA) under a continuous flow of nitrogen gas to avoid water adsorption on the sample.

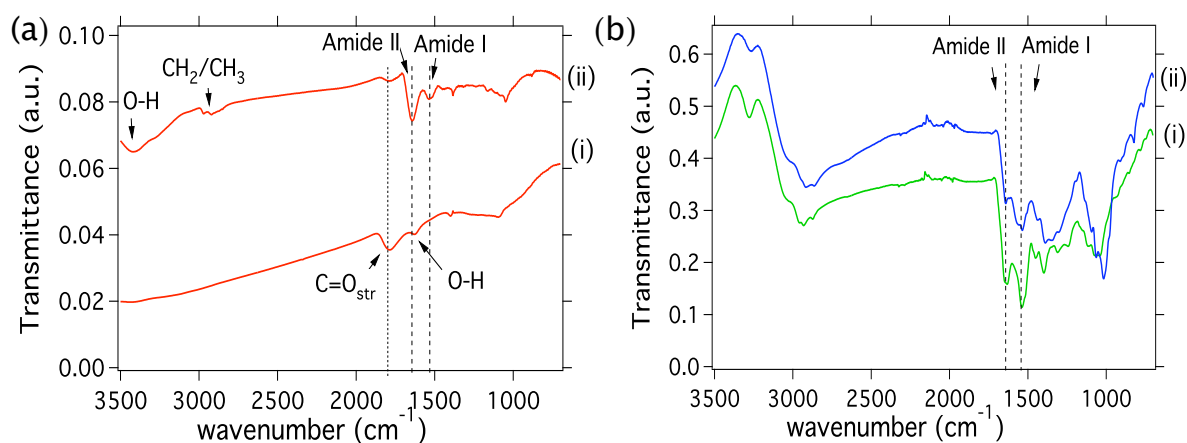


Figure 5.4: Infrared spectroscopic study of surface functions present on nanodiamonds after incubation with serum supplemented culture medium. (a) FT-IR spectra of nanodiamonds after incubation with foetal calf serum supplemented cell culture medium: (i) pristine PNDs; (ii) PNDs-serum proteins conjugates; (b) FT-IR spectra of serum proteins: (i) spectrum of DMEM medium containing 10% foetal calf serum (FCS); (ii) spectrum of pure FCS solution.

The transmission FT-IR spectrum of pristine PNDs (Figure 5.4a(i)) shows a band near 1775 cm^{-1} which can be attributed to the C=O stretching mode of the carboxylic acid groups, and a weak band near 1630 cm^{-1} that can be assigned to the O-H bending of the same groups on the ND surface [68, 70]. O-H bending band due to the remaining physically adsorbed water appears at 3400 cm^{-1} .

When nanodiamonds were incubated with serum proteins two new infrared bands appeared, one at 1640 cm^{-1} and the other at 1538 cm^{-1} (Figure 5.4a(ii)). These two bands are due to serum proteins according to the FT-IR spectrum of the serum proteins displayed on Figure 5.4b. The peak near 1640 cm^{-1} represents the amide II band and the peak at 1538 cm^{-1} corresponds to the amide I band [233, 234]. Moreover, on the pristine NDs spectrum, the 1775 cm^{-1} band is much weaker after ND interaction with serum proteins. This is due to the relative decrease of the carboxylic functions on the PND surface consecutive to the adsorption of serum proteins. This phenomenon probably

results from electrostatic attraction of positively charged amino groups of the proteins by the negatively charged nanodiamonds.

Finally, an additional proof of serum proteins adsorption on PNDs is the band at 2900 cm^{-1} , which can be attributed to the CH_2/CH_3 groups of the alkyl chain of the proteins [68].

5.3 Intracellular localization of photoluminescent nanodiamonds

5.3.1 Colocalization experiments of PNDs with endocytotic vesicles

After the endocytic uptake, the internalized compound is expected to be found in intracellular endosomal and lysosomal vesicles, before eventually being released in the cytosol or expelled from the cell. Endosomes are the vesicles involved in the transport of extracellular materials in the cell cytoplasm. After internalization, endosomes are either recycled towards the membrane and the material is released in the cytoplasm or they are fused with lysosomes [202]. In this work we stained the endocytotic vesicles with organic dyes and studied with confocal microscopy the colocalization with internalized PNDs. Moreover, we carried out complementary TEM experiments to visualize the PNDs in cells.

a Immunofluorescence experiments and optical setup

Endocytotic vesicles labeling

For the PNDs localization analysis in the cell we carried out immunofluorescence studies. The endosomes were labeled with FITC-conjugated Mouse Anti-human Early Endosome Antigen EEA1 (*Ref. 612006*, BD Transduction Laboratories, USA) after fixation. FITC dye has absorption/emission maxima at 490/520 nm respectively. The lysosomes were labeled with LysoTracker Green DND-26 dye (*L7526*, Invitrogen, USA), with absorption/emission maxima at 504/511 nm respectively. After two hours of incubation of PNDs at 37°C with the cells, the medium was replaced with prewarmed new medium containing the LysoTracker probe (75 nM), for one additional hour of incubation. The medium was then replaced with fresh medium just before cell fixation as described above.

Optical setup

The colocalization analysis was done with a commercial Leica TCS SP2 (Manheim, Germany) laser scanning confocal microscope, with a $\times 63$, 1.4 numerical aperture (NA) oil-immersion objective. Excitation comes from the cw argon ion laser line at 488 nm wavelength. The detection was done in two non-overlapping spectral channels: the *green channel* (500-530 nm) collecting the fluorescence from FITC and LysoTracker-green dye conjugates, and the *red channel* (600-750 nm) collecting NV photoluminescence (Figure 5.6a).

For the colocalization experiments, we checked that there is no crosstalk between the different fluorescence detection channels that could lead to artificial colocalization.

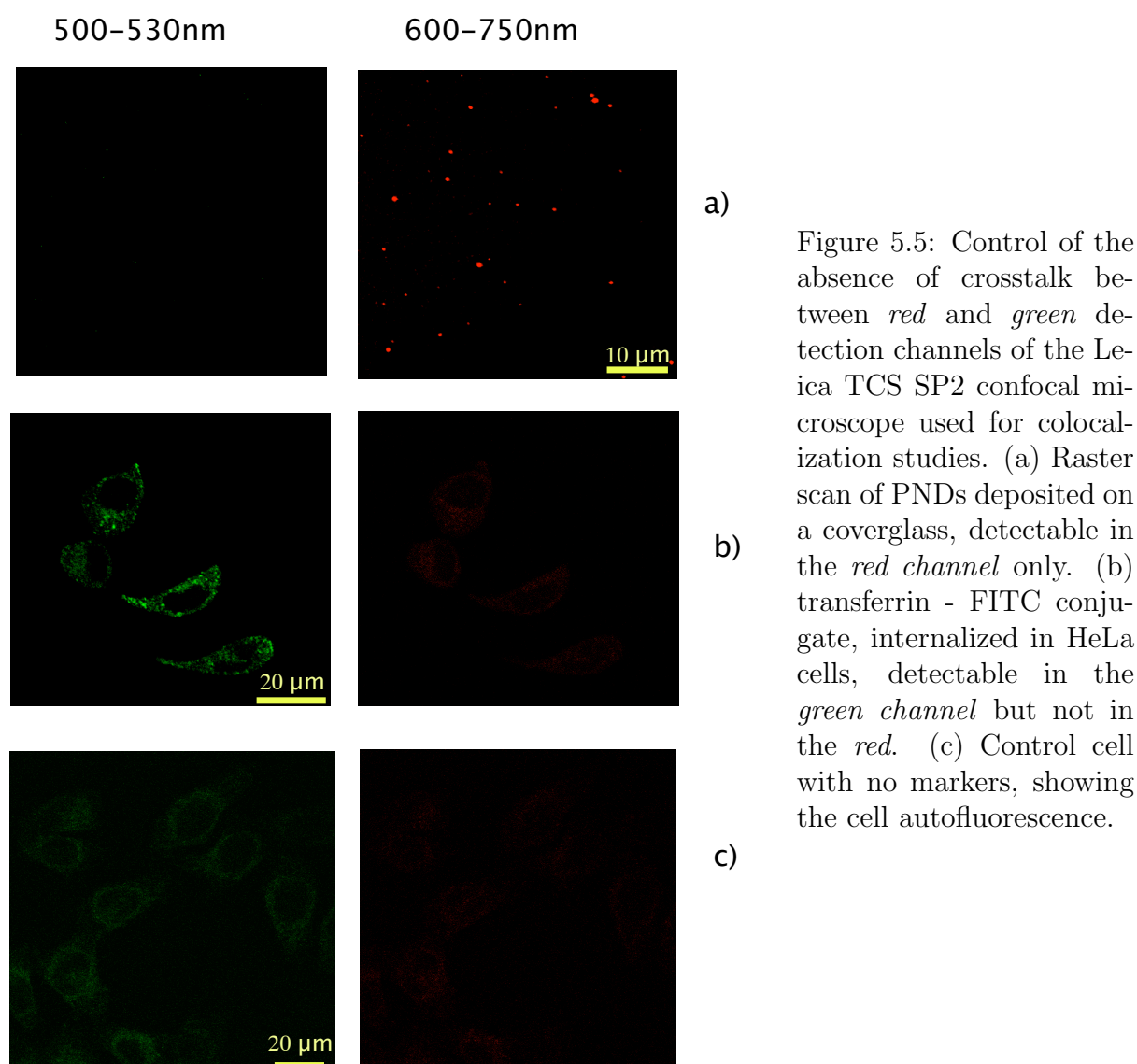


Figure 5.5: Control of the absence of crosstalk between *red* and *green* detection channels of the Leica TCS SP2 confocal microscope used for colocalization studies. (a) Raster scan of PNDs deposited on a coverglass, detectable in the *red channel* only. (b) transferrin - FITC conjugate, internalized in HeLa cells, detectable in the *green channel* but not in the *red*. (c) Control cell with no markers, showing the cell autofluorescence.

Figure 5.5 shows that there is no signal simultaneously detected in both channels for samples containing only PNDs or only FITC. Figure 5.5 also displays the autofluorescence signal of cells, detectable in the *green* but not in the *red channel*.

For more detailed studies of the internalized PNDs we used the home-built confocal microscope described in chapter 2. The dichroic mirror used was the Q530LP (Chroma Technology Corp., USA). An additional filter was added in colocalization studies to select either the fluorescence from FITC-labeled endosomes and Green LysoTracker lysosomes (500-550 nm bandpass filter *ET525-40m*, Chroma Technology Corp., USA), or from the NV color centers ($\lambda > 580$ nm longpass filter, *HQ580LP*, Chroma) (Figure 5.6b).

b Experimental results and discussion

Colocalization study with the commercial Leica confocal microscope

Scanning confocal imaging was carried out with the Leica TCS SP2 microscope. Figure 5.7 shows a high degree of colocalization of PNDs with both early endosomes and

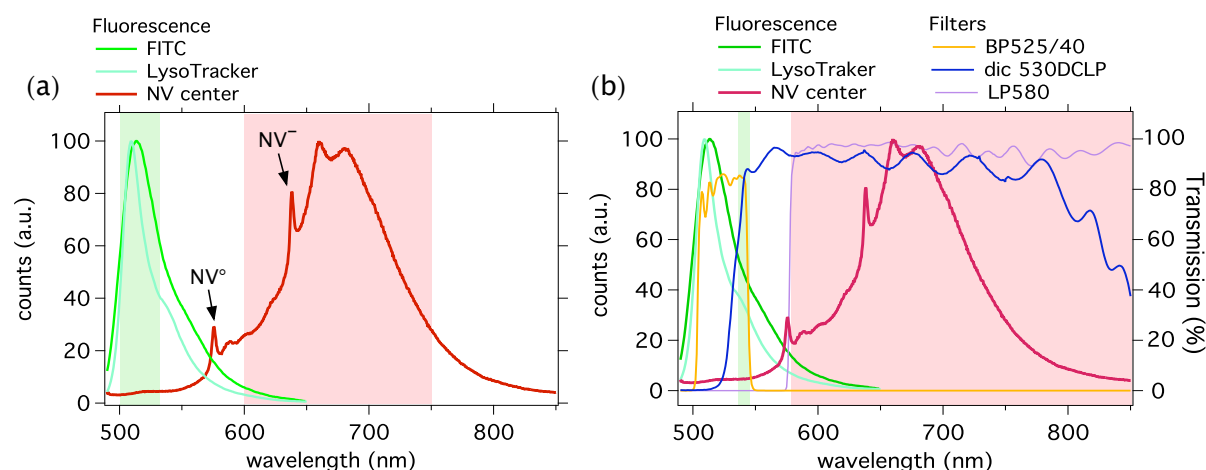


Figure 5.6: Comparative spectral selection of the fluorescence signal. (a) Spectral selection with the Leica commercial confocal microscope. The red/green rectangles behind NV and FITC/Green LysoTracker spectra respectively indicate the spectral range selected by the *red/green channels* filters of the microscope. The narrow lines pointed out by arrows at 575 nm and 637 nm indicate respectively the zero-phonon lines of the neutral NV° and negatively charged NV^{-} color centers, most often both presented in the PNDs of the sample. (b) Spectral selection with the home-built confocal microscope. In red rectangle the spectrum region recorded for the NV center detection, while in green rectangle the spectrum region recorded for the FITC/Green LysoTracker fluorescence signal. For the filters used their % Transmission is indicated on the right vertical axis.

lysosomes, which supports the fact that NDs follow the course of the endocytic cycle. This endosomal localization of PNDs also agrees with reports on other kinds of similar size nanoparticles, like QDs [174] or gold nanobeads [185, 210].

Colocalization study with the home-built confocal microscope

PND-endosome colocalization was studied at the single particle and single color-center sensitivity level, for both type M and N PNDs.

Figure 5.8 shows that 16 type M PNDs (*Aq46nm-Me18*) out of 65 internalized in the cell are colocalized with endosomes. Out of 20 cells and 256 internalized PNDs we find a $\sim 25\%$ colocalization [48]. For type N PNDs we find similar colocalization ratios.

A percentage of the PNDs considered as internalized for the calculation of the colocalization ratio is probably not really internalized, but attached on the cell membrane. Despite the careful washing of the remaining PNDs after the 2 hours of incubation with cells, it is possible that some PNDs remain attached on the cell membrane. We labeled the borders of the cell membrane, but this created a homogeneous background during the home-built confocal setup measurements, so we abandoned the membrane labeling. Although a probable percentage of PNDs considered as internalized in fact is on the membrane, there still remains a percentage of internalized PNDs not colocalized with endosomes.

The above results suggest that a proportion of internalized PNDs is not found in endocytotic vesicles in the cell, but has either not followed an endocytotic pathway or has

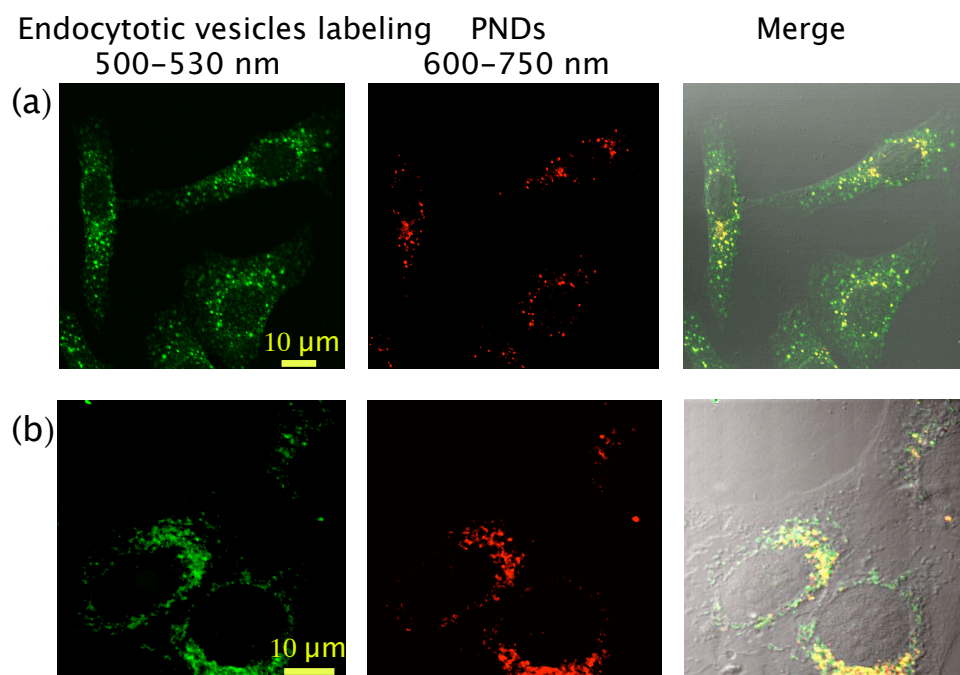


Figure 5.7: Localization of 46 nm photoluminescent nanodiamonds (*Aq46nm-Me18*) in HeLa cells. Confocal fluorescence raster-scan (Leica TCS SP2 microscope) of HeLa cell incubated with PNDs ($10 \mu\text{g/ml}$) in normal conditions, then fixed and marked with dye labeled endosomes or lysosomes. From left to right: raster-scan in the *green channel* (500-530 nm) showing the endocytic compartments; in the *red channel* (600-750 nm) showing the PNDs; the right images result from merging the green and red scans. (a) Colocalization study of PNDs with early endosomes marked with EEA1-FITC fluorescent conjugate. (b) Colocalization of PNDs with lysosomes marked with LysoTracker Green dye. PNDs colocalized with endosomes or lysosomes appear in yellow in the merged images.

escaped from endosomes after the internalization process. A supplementary colocalization study, of different incubation times is necessary, to determine the fate of the uptaken PNDs.

5.3.2 TEM Microscopy observations of PNDs in cells

In order to conclude on the partial colocalization of PNDs with endosomes and to investigate the fate of the smallest PNDs we also carried out Transmission Electron Microscopy (TEM) measurements.

The measurements were done with a High Resolution Transmission Electron Microscope (HR-TEM, Tecnai F20 operating at 200 keV). Cells were seeded for 24 h in standard conditions (the same as for fluorescence experiments). PNDs were added in cell solutions and incubated for 2 h at 37°C . Cells were then fixed in a solution of paraformaldehyde, glutaraldehyde and phosphate buffer for 45 min at room temperature. After dehydration with a graded series of ethanol, the cells were embedded in EPON resin. Ultrathin sections of the resin block were then cut (100 nm thickness) and stained with 2% uranyl acetate, for a higher contrast imaging under the HR-TEM microscope.

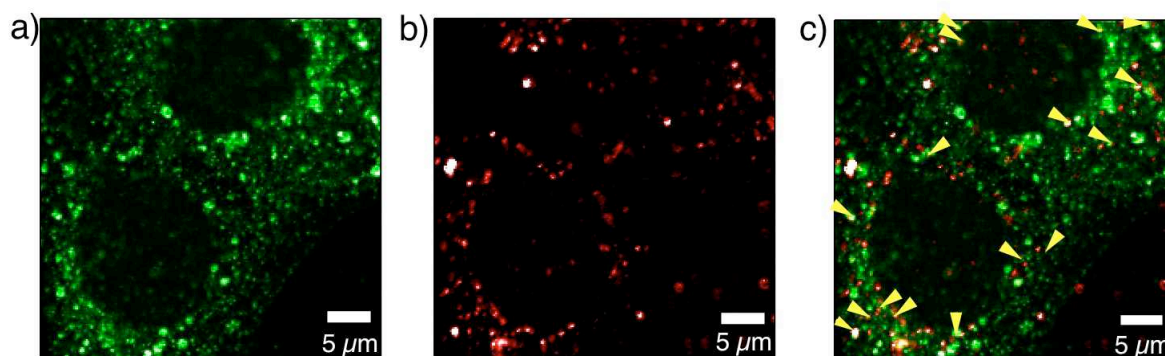


Figure 5.8: Colocalization of 30 nm PNDs (*Aq30nm-Np15*) with endosomes observed with the home-built confocal microscope. (a) Confocal raster-scan in the *green* detection channel (filter: bandpass 500-550 nm) showing early endosomes labeled by EEA1-FITC conjugate. (b) Photoluminescence raster scan in the *red channel* (filter: longpass $\lambda > 580$ nm), showing PNDs. (c) Merged image of (a) and (b) scans, with arrows showing 16 PNDs found to be colocalized with endosomes, out of the ~ 65 uptaken PNDs. Raster scans were recorded $1.5 \mu\text{m}$ above the coverglass surface, laser excitation wavelength 488 nm, power 0.4 mW.

As it can be seen on Figure 5.9a, PNDs are found in the cell cytoplasm after 2 h of incubation. PNDs particles appear as darker spots than cell organelles².

In the large scale TEM image (Figure 5.9a) of a part of a HeLa cell incubated with PNDs, one can observe the nanoparticles in the cytoplasm. They are either trapped in vesicles (Figure 5.9b,f), or free in the cytosol (Figure 5.9d). NDs trapped in vesicles form aggregates (Figure 5.9b), and represent the majority of the nanodiamonds observed by TEM inside the cell cytoplasm. This is in agreement with the confined motion of PNDs observed with wide-field microscopy of chapter 4 [47, 183]. Nanodiamonds which are free in the cytosol correspond to the smallest particles that can be observed at their primary size (5-10 nm) or as small aggregates of a few particles. These free nanoparticles have either been released from the endosomes or may have been directly internalized via passive transport (like facilitated diffusion) through the cell membrane. Interestingly, all internalized nanodiamonds, even of the smallest size (5 nm) are observed in perinuclear regions and none of them is present inside the nucleus.

5.4 Cell morphology after incubation with nanodiamonds

At the nanometer scale, due to the high surface-volume ratio, surface chemistry and size play an important role in the particle interaction with the surrounding medium [235]. As a consequence, changes in cytotoxicity may be observed for NDs of different types and sizes, like 5 nm detonation NDs and < 50 nm HPHT NDs.

²the diamond material nature is checked by carrying out a local area Fourier transform electron diffractogram on one of the TEM dark spots of size $\simeq 10$ nm (inset of Figure 5.9e).

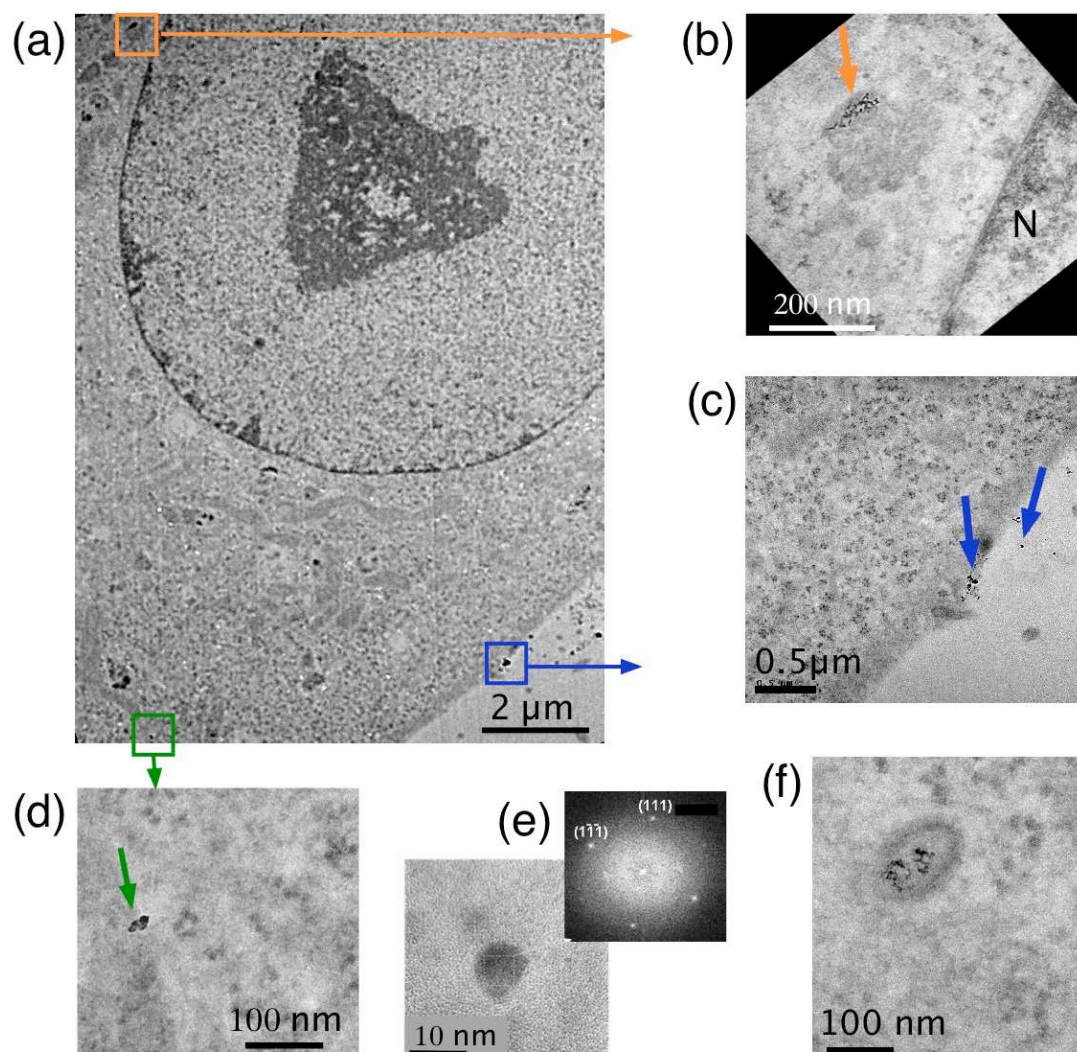


Figure 5.9: Transmission Electron Microscopy images of a HeLa cell initially incubated with PNDs for 2 hours. (a) Large scale image. (b) NDs trapped in endocellular vesicles, N indicates the position of cell nucleus. (c) NDs outside the cell and on the cell membrane (blue arrows), probably during the early stage of the internalization process, since the half-life uptake (2.6 hours) is longer than the incubation time. (d) Free NDs in the cytoplasm. (e) Zoom on one 10 nm ND, inset : local area Fourier transform diffractogram of this ND. (f) PNDs trapped in an endocellular vesicle of another cell from the same sample.

5.4.1 Experimental conditions

Type of nanodiamonds used

The NDs tested were detonation NDs on the one hand and HPHT photoluminescent NDs on the other hand (sample *Aq30nm-Np15*). The detonation NDs had primary size of 5 nm (see Figure 2.26, chapter 2 for size characterization). We observed that this type of NDs has the tendency to form clusters of ~ 30 nm in water. This aggregation can be reversed by tedious and strong sonication [130]. In cell culture medium buffer, these NDs also have the tendency to aggregate. Detonation NDs appropriately functionalized

to stay stable in cell culture media were made available by Anke Krüger [236], but at the time of the cytotoxicity tests we disposed only raw NDs.

Preparation of HeLa cells

HeLa cells were grown in standard conditions on glass coverslips in DMEM culture medium supplemented with 10% foetal calf serum (FCS). Cells were seeded at a density of 10^5 cells/ 1.3 cm^2 (1.3 cm^2 is the surface of the well dish bottom) and grown at 37° C in a humidified incubator under 5% CO_2 atmosphere. 24 hours after cell seeding, aqueous suspensions of NDs (after UV-sterilization) were added to the cell medium at different concentrations. The cells were grown under the same conditions for an additional period of time of 24 hours. After incubation, the excess of NDs was removed by washing cells with phosphate buffer saline (PBS) buffer. Cells were then fixed with 4% paraformaldehyde in PBS and mounted on microscope slides for microscope examination. The microscope used for cell morphology observations was a standard fluorescence microscope, used in bright field mode for detonation NDs and in Phase Contrast mode for HPHT NDs.

5.4.2 Results and Discussion

After 24 h of incubation with detonation NDs, cell morphology appeared similar to the one of the control cells with only some cells displaying an irregular shape (Figure 5.10a,b,c). NDs are agglomerated in the cell medium and observed as clusters on the cell membrane. Nevertheless the cells are still adherent to the substrate (the detachment of the cells from the dish bottom is a sign that cells are dead) even at high ND concentrations (up to $75\text{ }\mu\text{g/ml}$).

The results are similar for HPHT *Aq30nm-Np15* nanodiamonds (Figure 5.10d,e). When NDs are used in high concentrations ($100\text{ }\mu\text{g/ml}$), they tend to form aggregates, easily visible on the images. For the 24 hours incubation time used in our experiment, very few cells are found dead on the dish bottom .

5.5 Biocompatibility assessment

To further examine interactions between the cells and the nanoparticles, the changes in mitochondrial activity were examined by a standard toxicity test, the MTT assay.

5.5.1 Experimental conditions

Type of nanodiamonds used

We tested:

- detonation NDs (*Aq29nm-Det*, primary size 5 nm, mean size 30 nm, $\zeta = +38\text{ mV}$)
- type M NDs (*Aq46nm-Me18*, mean size 46 nm, polydispersed, round shape, $\zeta = -43.0\text{ mV}$)
- type N NDs (*Aq30nm-Np15*, mean size 30 nm, better monodispersed, angular shape, $\zeta = -41.3\text{ mV}$)

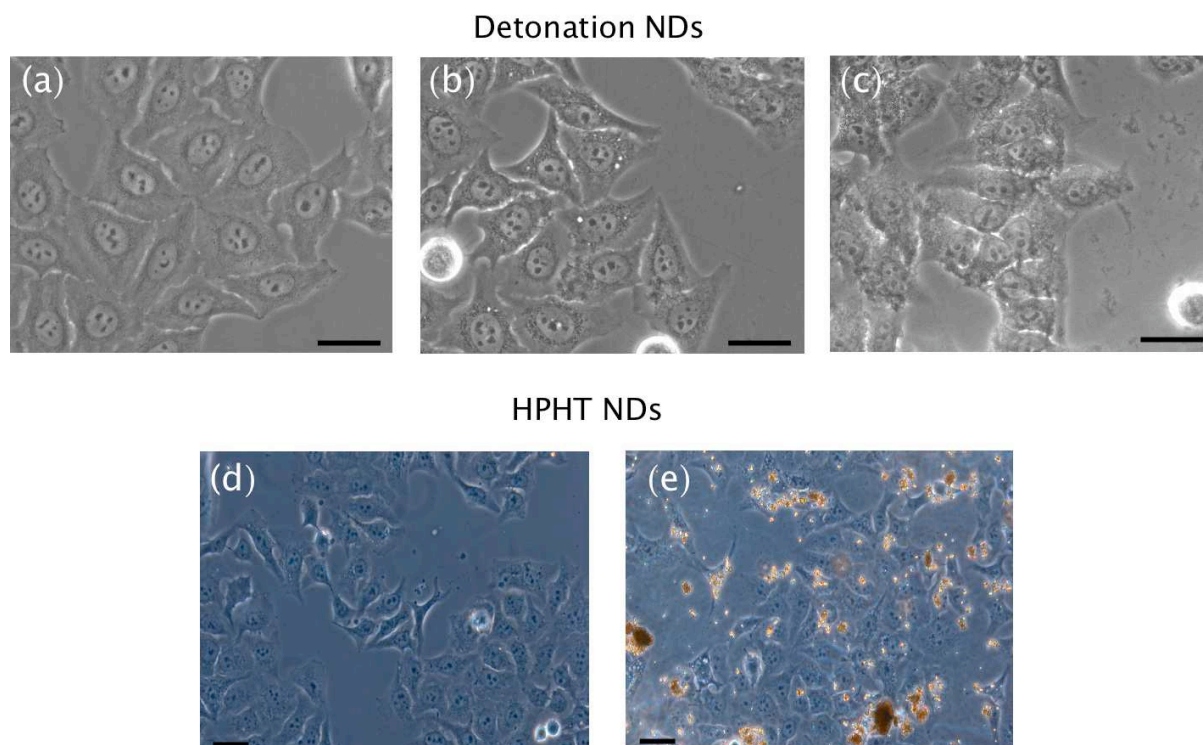


Figure 5.10: Morphological study of HeLa cells incubated for 24 h with pristine detonation NDs or HPHT NDs. Top: Bright field images of detonation NDs incubated with cells: (a) Control (no NDs) ; (b) NDs concentration $5 \mu\text{g/ml}$; (c) NDs concentration $75 \mu\text{g/ml}$. Scale bar $20 \mu\text{m}$. Bottom: Phase Contrast images of pristine HPHT *Aq30nm-Np15* NDs (mean size 30 nm) incubated with cells: (d) NDs concentration $5 \mu\text{g/ml}$; (e) NDs concentration $100 \mu\text{g/ml}$. Scale bar $40 \mu\text{m}$.

As a positive control we used Lipofectamine (Invitrogen, USA), which is widely used to facilitate cell transfection, but is toxic for long exposition times and high doses.

In order to determine if the culture medium composition and the aggregation state of NDs play a role in toxicity, we performed MTT assays for both HPHT types incubated in medium supplemented with or without foetal calf serum (FCS).

The cytotoxicity test

The cells were plated at a concentration of 2×10^5 cells/ 1.3 cm^2 for 24 hours and then treated with various concentrations of type M or type N PNDs for 24 h in Dulbecco Modified Eagle's Medium (DMEM) 10% FCS supplemented medium.

We then conducted the MTT assay [224, 225]. Mitochondrial dehydrogenase enzymes cleave the tetrazolium ring of MTT. Only active mitochondria contain these enzymes, thus this cleavage reaction can occur only in living cells. MTT is pale yellow in solution but produces a dark-blue formazan product within living cells, after 2h of incubation (indicating the cleavage of the tetrazolium salt by mitochondria in living cells). The purple formazan crystals are dissolved in acidified isopropanol and the absorbance of the solution is measured with a spectrophotometer (Uvikon XL, Secoman) at 570 nm. The absorbance of cells exposed to PNDs was compared to the one of control cells, not

exposed to NDs, which is associated to 100% absorbance. All measurements were made in duplicate.

5.5.2 Results and Discussion

Figure 5.11 shows the MTT assay results for detonation NDs. No or very low toxicity is observed for concentrations $< 100 \mu\text{g/ml}$.

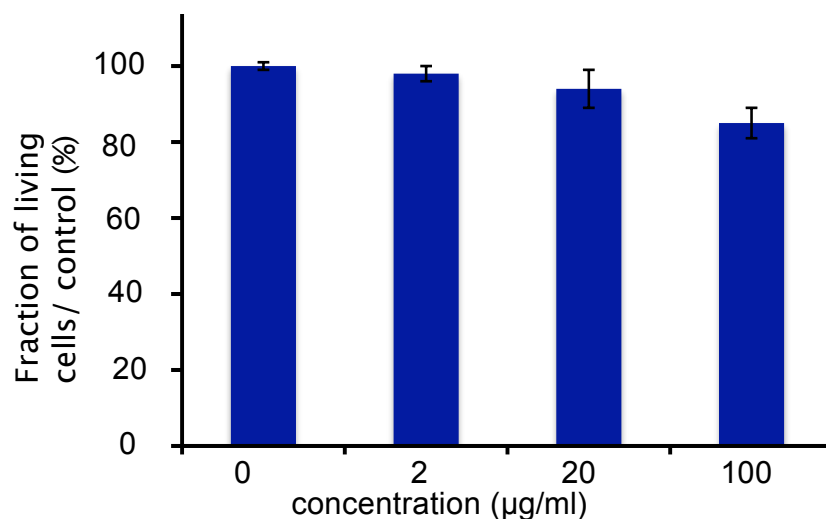


Figure 5.11: Cytotoxicity MTT assay results after 24 h of HeLa cell incubation with detonation NDs, for concentrations of 0, 2, 20 and $100 \mu\text{g/ml}$.

Figure 5.12a presents the survival rate as measured with MTT assay for both type M and type N HPHT NDs. We used lipofectamine as a comparative control (in blue color). The incubation time was 24 hours. We observe that both types of NDs do not significantly induce cell death, in contrast to lipofectamine.

Figure 5.12b shows the MTT assay results for nanodiamonds incubated in FCS free medium. In such culture conditions, one hour after incubation the NDs formed agglomerates (verified by DLS measurements). After one day, NDs formed larger aggregates, which precipitate at the bottom of the solution, visible to the naked eye. By comparing the results for NDs incubated with and without serum supplemented medium, we observe that cytotoxicity is higher (especially for high concentrations) for serum free cell culture medium. One explanation could be that NDs form aggregates, which may be more toxic for cells, an effect recently observed for carbon nanotubes [237].

5.6 Conclusion

In this chapter we demonstrated that the internalization of PNDs in HeLa cells occurs through endocytosis and we have indications that it is clathrin mediated. The efficient internalization of the negatively charged nanoparticles used in our experiments can be reinforced by the adsorption of serum proteins on the PNDs surface, a statement proved by FTIR experiments. We found that most of the nanodiamonds are localized in intracellular endocytotic vesicles in perinuclear regions, except a small portion and in particular

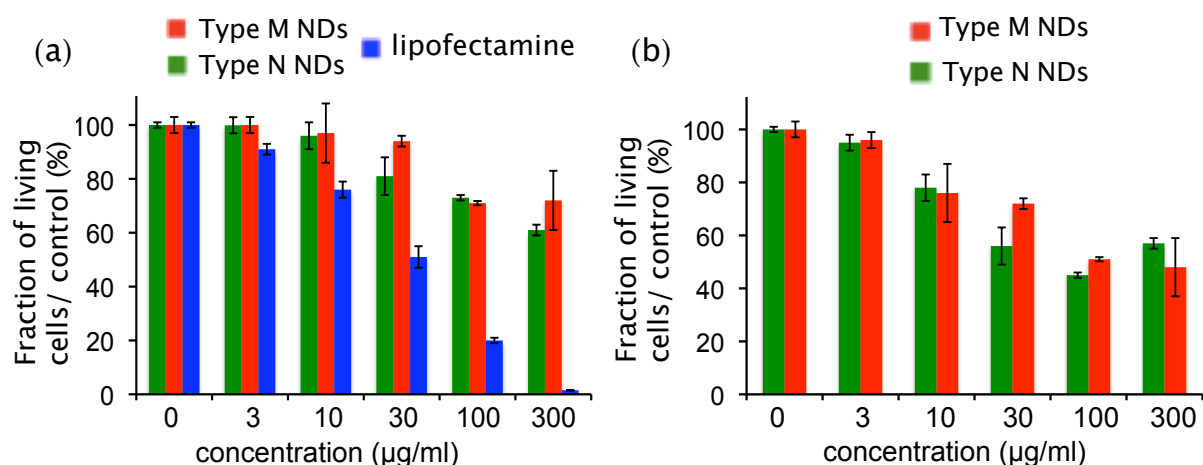


Figure 5.12: Cytotoxicity measurement of NDs after 24 h of incubation with HeLa cells in: (a) FCS supplemented medium. Both HPHT nanodiamond types and lipofectamine are tested. Similar trends in biocompatibility are observed for both types of PNDs, in contrast to the lipofectamine which appears to be toxic for concentrations $>10 \mu\text{g/ml}$; (b) Medium without FCS. Both ND types show a higher cytotoxicity in comparison with (a).

the smallest particles that remain free in the cytoplasm. Whether these nanoparticles have entered the cell by a mechanism different from endocytosis or have escaped from the endocytotic vesicles after internalization is a subject of further investigation. As cell is an inhomogeneous medium, a careful understanding of the distribution of nanoparticles into the cytoplasm and the reasons of the variability of their fate represents a critical step towards the use of diamond nanoparticles for targeted biomolecule delivery, with a long-term intracellular tracking possibility through its photoluminescence.

In addition, cytotoxicity experiments show that the NDs studied during my PhD thesis are not toxic for *in vitro* experiments with cells. As the nanoparticles size and shape determine cytotoxicity, it was essential to test the biocompatibility for each type of nanodiamond used. Examination of the cell morphology revealed no changes in cell shape, for not too high concentrations ($<100 \mu\text{g/ml}$). By using MTT assays and comparing the toxicity of NDs with lipofectamine, we observed that lipofectamine becomes toxic for high concentrations, in contrary to nanodiamonds, which appear biocompatible for 24-hour incubation with HeLa cells.

Very recently, *in vivo* cytotoxicity experiments with NDs have been reported, showing the accumulation of 50 nm NDs suspended in BSA solution in mouse liver, lung and spleen after 28 days [238]. Other teams however start reporting opposite results, with a low accumulation of NDs in mouse organs. The possible long-term pathologic effects of the internalized nanodiamonds require further long term toxicology experiments on animal models, a remaining task for future investigations.

Chapter 6

Conjugation of nanodiamonds with plasmid DNA

6.1 Introduction

Gene delivery is an area of research in biology which attracts a lot of interest, owing to its therapeutical applications.

Genetic materials (DNA, siRNA, oligonucleotides) are delivered to specific cell types either to inhibit non-desirable gene expression or express therapeutic proteins [240–242]. A common way to achieve genetic material transport is the viral gene delivery. Although gene delivery using modified viruses achieves high levels of gene expression, it has several drawbacks that make it problematic for human use. In particular, viral vectors can be immunogenic, or can induce inflammation that at the best render transgene expression only transient, or can even have oncogenic effects [243]. There is thus a high demand in the development of non-viral vectors.

As alternatives, synthetic nanoparticles bearing cationic groups, like Liposome - Polycation-DNA [244] complexes or other systems [240, 245, 246] have shown great promises. An example is the use of well-chosen ligands, like nanoliposomes carrying anticancer drugs. Nanoliposomes have been successfully used in cancer therapy, as their toxicity is very low [247–250]. By specific attachment on these particles with an organic dye [251], one can study their intracellular trafficking. However, dye photobleaching inhibits long observation times. Ideally, the nanocarrier should combine both drug delivery and bright and stable fluorescence properties.

Over the past few years, ultrafine silica nanoparticles, with surfaces functionalized by cationic-amino groups, have been shown to not only bind and protect plasmid DNA from enzymatic digestion but also transfect cultured cells and express encoded proteins [252–254]. Recently, fluorescent silica core-shell nanoparticles encapsulating dyes were implemented for vectorization and tracking of the biomolecules at the same time [255, 256]. The fluorescence of these particles still relies on dye emission, which fades over time.

For a carbon based vectorization system, carbon nanotubes are the most developed case. It has been demonstrated that peptide or plasmid DNA functionalized carbon nanotubes are capable of penetrating the mammalian plasma membrane [230] and translocating to the cell nucleus [257, 258]. These nanotubes are capable of eliciting an antigen-

specific neutralizing antibody response in vivo [259]. Bianco et al. reported the first case of carbon nanotube-mediated intracellular delivery of a biologically active molecule using ammonium-functionalized single-walled carbon nanotubes complexed to plasmid DNA [260]. A very recent and impressive achievement is the drug delivery in mice with carbon nanotubes conjugated to paclitaxel, a widely used chemotherapy drug, for in vivo cancer treatment [261].

However, systems that allow at the same time drug delivery and efficient intracellular trafficking of biomolecules are still missing. Using nanodiamonds for this purpose presents two major advantages: i) nanodiamonds are spontaneously internalized in cells and ii) they are perfectly photostable.

For this kind of applications, small nanodiamonds have to be used, in order not to hinder the trajectory of the carried biomolecule. Conjugation of non photoluminescent nanodiamonds to drugs for chemotherapeutic delivery has recently been demonstrated, by the conjugation with doxorubicin hydrochloride (DOX) drug [74]. Grafting of different peptides or lysozyme has also been reported for non photoluminescent nanodiamonds [70, 71]. The group of C.-L. Cheng has used the intrinsic photoluminescence of NDs to study the interaction between the growth hormone receptor of A549 human lung epithelial cells labelled with organic dyes with the growth hormone coupled with NDs [60].

In our group we studied the conjugation of NDs with DNA. Our goal was to demonstrate that NDs can form complexes with DNA, becoming eventually DNA carriers and improving the DNA transfection in cells. We used three different coatings for the negatively charged NDs, i) poly-L-lysine coating, ii) polyallylamine hydrochloride (PAH) coating, and iii) coating with Nickel divalent cations. Almost simultaneously with our experiments, the team of W. Fann demonstrated the efficient conjugation of DNA with poly-L-lysine coated PNDs [51].

6.2 DNA- Nanodiamond coupling

6.2.1 Nanodiamond size selection

For drug delivery experiments and for eventual tracking of the created complex in cells, the nanoparticle size has to be as small as possible. To achieve that, we selected the smallest nanodiamonds by a process of successive centrifugations, with a gradual increase of the angular speed. We ended up with controllable size distributed solutions containing small dimension particles, smaller than 10 nm.

The nanodiamonds used were type N HPHT nanodiamonds (not irradiated, SYP 005, with nominal size <50 nm). The centrifugation machine used is an Eppendorf Centrifuge 5810R, for centrifugation speeds up to 16,000 rpm and a Beckman Coulter Ultracentrifuge for speeds up to 110,000 rpm.

The centrifugation processes are listed in table 6.1.

When a centrifugation process was finished, two parts remained in the tube, the supernatant on the top and the pellet at the bottom. Every time the supernatant was collected and the centrifugation process went on.

For the accurate characterization of the size distribution of the particle solutions, we used an Atomic Force microscope (apparatus *Nanoscope IIIa*, Veeco Instruments Inc., USA). Usually (especially in the pellets) a portion of the particles was aggregated, so

centrifugation	speed (rpm)	acceleration (g)	duration (min)
1	200	8	15
2	500	50	15
3	1000	201	15
4	2000	805	15
5	4000	3220	15
6	8305	6400	15
7	16000	23755	15
8	30000	42300	15

Table 6.1: centrifugation process

they were strongly sonicated before the AFM measurements.

The supernatant of the solution 7 and the pellet of solution 8 had mean size of 5.6 ± 2.1 nm and 7.3 ± 3.2 nm respectively (median values out of about 100 nanoparticles) as measured by AFM scans. We preferred using the latter solution, containing a higher density of NDs.

The material of the surface was muscovite mica, “freshly” cleaved. This is a highly negatively charged surface. The crystal nature of mica allows it to be split into atomically flat sheets. In order to adsorb the negatively charged diamond nanoparticles on the surface, we treated the mica with divalent transition metal ions. These ions were strongly bound to the mica surface [262]. More precisely we used Nickel (Ni^{2+}) ions. This treatment decreases the net surface charge of the mica and forces the negatively charged diamond nanoparticles to be attached on the surface.

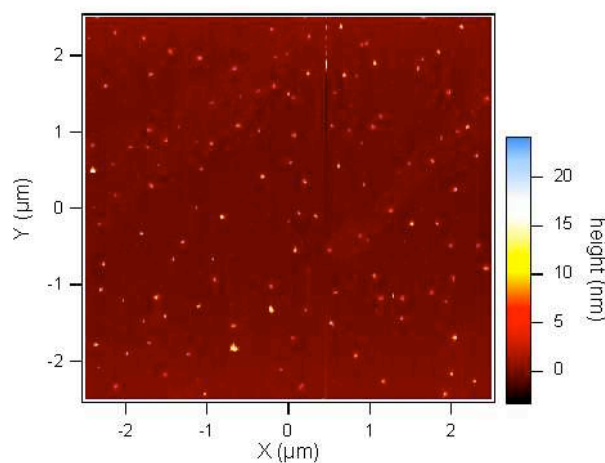


Figure 6.1: AFM scan of the ND solution (pellet of solution 8) used in the experiments.

6.2.2 Nanodiamond surface coating by polycations : poly-L-lysine

DNA has a negative surface charge, due to phosphate groups. The nanodiamonds we dispose have also a negatively charged surface, due to the carboxyl groups. To render

the NDs surface positive we coated them with poly-L-lysine ¹. It consists of the L-lysine amino-acid (n molecules of L-lysine, $(C_6H_{12}N_2O)_n$, Figure 6.2) and in water it is positively charged (positively charged amino $-NH_3^+$ group). Poly-L-lysine has a good affinity with DNA and is often used as DNA carrier itself [263]. Experiments report the immobilization of proteins on a poly-L-lysine layer coating NDs surface [67].

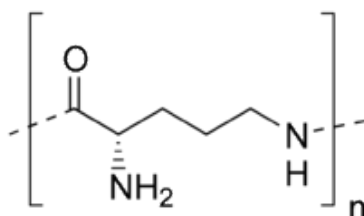


Figure 6.2: The polypeptide of poly-L-lysine.

We used a poly-L-lysine with a rather high molecular weight (70 kD). Poly-L-lysine and NDs were mixed together in 50 mM boric acid buffer (20 mM Na^+) at pH 8,5 for 30 min. The proportion of nanodiamonds to poly-L-lysine was 3:1. The mixture was washed 3 times, in 15 mM PBS buffer (pH 7.2) in order to remove the quantity of free poly-L-lysine. After the washing of the excess of poly-L-lysine (washing was carried out carefully, as poly-L-lysine may itself form complex with DNA) plasmid DNA was added.

a DNA - ND complex examination by Electrophoresis

One way to examine the DNA conjugation with nanoparticles is gel-electrophoresis. Gel-electrophoresis is a well known method used for the separation of nucleic acids and proteins according to their sizes and charges. The solutions are put in wells drilled in agarose gel. An electric field is applied and eventually the macromolecules (charged particles) migrate in the gel. The gel consists of a polymer, forming a porous lattice. As a result, the charged particles will migrate on a distance which depends on their size, their spatial conformation and their charge. In our case, the charged DNA, once complexed with the nanodiamonds, cannot migrate and stays blocked at the pores of the gel.

The initial ND-poly-L-lysine solution was separated in 5 solutions, in which DNA was added. The DNA used was plasmid, super-coiled. The quantity of DNA added was constant for every well at 0.2 μg and the concentration of nanodiamonds was the varying parameter. The first solution contained 8 μg of nanodiamonds, the second one 19 μg , the third 39 μg , the fourth 78 μg and the last one 136 μg . DNA was added to the solutions of poly-L-lysine coated nanoparticles and agitated for 2 hours. A pure DNA solution was used as a reference.

All the solutions were run on a 1% agarose gel, under 100 Volts for 20 min, prepared in TBE (Tris-Borate-EDTA) solution (pH 8) and subsequently stained with ethidium bromide, and documented by using an ultraviolet transilluminator in conjunction with an Olympus color camera with a UV filter.

Figure 6.3 represents the results of agarose gel electrophoresis of plasmid DNA, free and complexed with different ND concentrations.

¹in our case it is ϵ -poly-L-lysine. Epsilon refers to the linkage of the lysine amino acids, which are linked by the amino group at the epsilon position (called also epsilon amino group) and the carboxyl group (in contrast to the normal peptide bond where the linkage occurs at the alpha-carbon group).

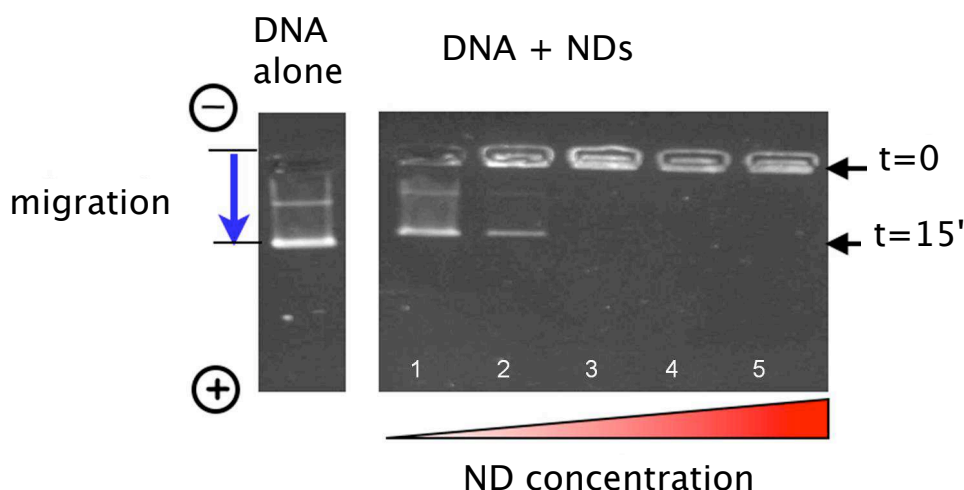


Figure 6.3: Image of agarose gel electrophoresis of DNA-poly-L-lysine-ND complex. In the well on the left DNA alone migrates and as the concentration of nanodiamonds increases we observe that the free DNA band disappears, all DNA is captured.

It can be clearly seen that as the concentration of nanodiamonds increases, the mobility of DNA gradually decreases. At the end, for high nanodiamond concentration there are no free molecules of DNA migrating (solutions in wells 3, 4, 5). The plasmid is no more able to move freely, because the resulting nanoparticle–DNA complex has restricted the mobility and forms complexes blocked in the pores of the polymer in the agarose gel.

b DNA - ND complex observation by AFM

An alternative method to observe the formation of DNA - ND complex is by Atomic Force Microscopy (AFM). The surface used was a mica surface, treated with nickel ions. The DNA - ND solution had to be diluted in a buffer solution of 10 mM Tris, pH 8, containing 10 mM MgCl_2 . Magnesium is necessary for a strong attachment of DNA on the mica surface [262]. In addition, just before the deposition of the 5 μl droplet of the solution on the mica surface, the sample is plunged in 0.02% diluted uranyl acetate solution, for a better fixation of the DNA on the surface.

Figure 6.4 shows the AFM scan of the different samples. We can clearly distinguish the free DNA, contained in the pure DNA solution. In the AFM scan of solution 2 of the electrophoresis experiment one can see free strands of DNA on the one hand, but also DNA complexed to NDs on the other hand. The maximal height for this scan is 11 nm, corresponding to the ND size of that solution, whereas for the scan of pure DNA, the maximal height observed is about 2 nm, equal to the height of a plasmid DNA molecule.

These results are in agreement with the electrophoresis results, where we observe that a part of DNA is captured and does not migrate in the well. Note that the ionic force of the solution is not high enough (around 20 mM of Na^+) to observe condensed forms of DNA on the mica surface. so this formation cannot be considered as a condensed molecule of DNA (it is confirmed that at high ionic forces, up to 200-300 mM of Na^+ , DNA molecules obtain a condensed form [262]).

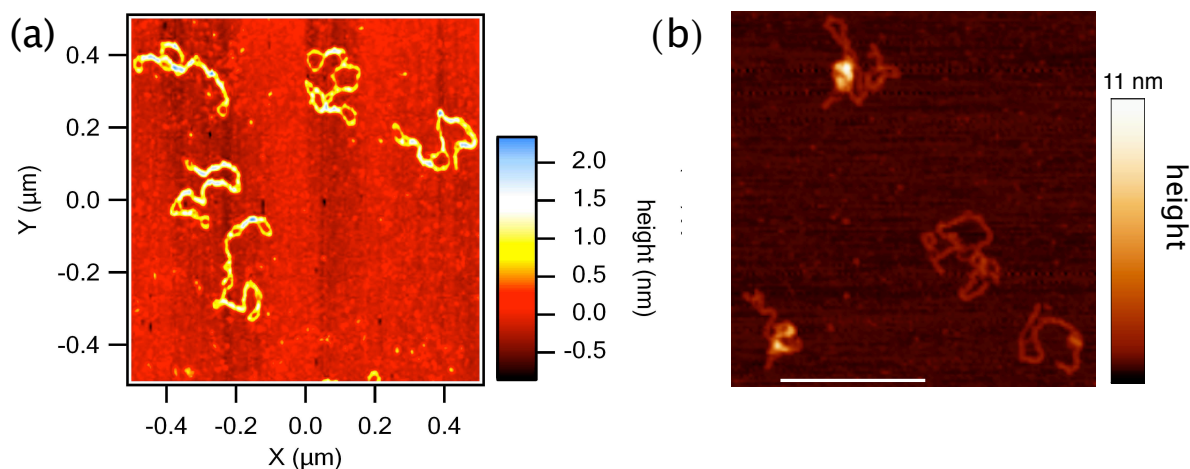


Figure 6.4: AFM scan of DNA-(poly-L-lysine coated)-ND complex deposited on mica surface. (a) Solution of DNA alone, (b) solution 2 of gel-electrophoresis, scale bar is 200 nm.

6.2.3 Nanodiamond surface coating by polycations: polyallylamine hydrochloride (PAH)

An alternative to poly-L-lysine is another positively charged polyelectrolyte, the polyallylamine hydrochloride (PAH). Similar to poly-L-lysine, we took advantage of the electrostatic interaction between the carboxylate functions of the NDs and the ammonium groups of PAH. The choice of PAH was made because PAH-coated NDs were used by the team of Solange Lavielle as vectors of peptides in cells [70].

The resulting solution was stable in HEPES buffer, was positively charged (+40 mV zeta potential) and had a concentration of 2 g/l.

The initial solution was separated in 4 solutions, in which DNA was added. The concentration of DNA was constant at $0.5 \mu\text{g}/\mu\text{l}$ and the quantity of nanodiamonds was 5, 10, 15 and 25 μl respectively. DNA was added to the solutions and agitated for 30 min. A pure DNA solution was used as a reference. The solutions were run on 1% agarose under 100 volts for 20 min, subsequently stained with ethidium bromide. Figure 6.5 shows the gel-electrophoresis results. We clearly see that DNA is captured with the increase of the NDs concentration.

6.2.4 Nanodiamond surface coating by divalent cations - Nickel

Nickel (Ni^{2+}) is widely used for mica surface pretreatment in DNA imaging by AFM, as it enhances the electrostatic force between the negatively charged surface and the also negative DNA molecules. For that reason we tried Nickel as the coating linker, instead of poly-L-lysine or PAH.

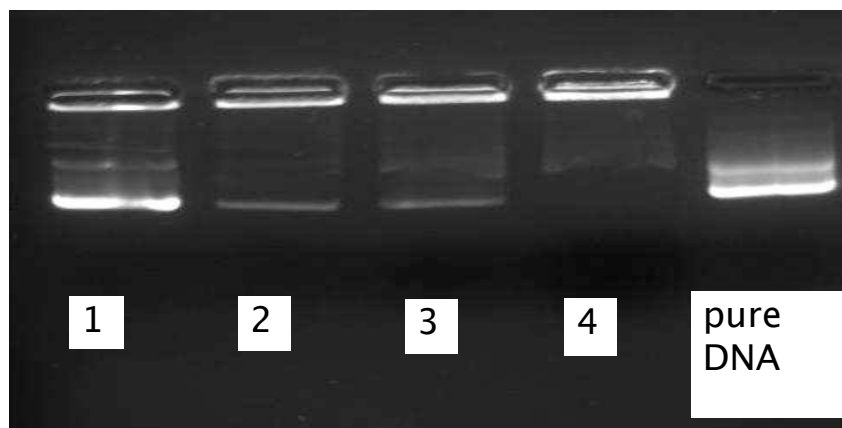


Figure 6.5: Image of agarose gel electrophoresis of DNA-PAH-ND complex. From left to right the concentration of nanodiamonds increases. The well on the right is taken as a reference, containing pure DNA solution.

a DNA - ND complex examination by Electrophoresis

The buffer contained 50 mM of Boric Acid and 20 mM of Na^+ , with a final pH 8.5. The washing of the excess quantity of Nickel was done with the same buffer, by three successive centrifugations, at 12,000 rpm for 10 min.

A final solution of 100 μl was obtained, containing 120 μg of nanodiamonds. This was divided in 4 parts of volumes 5, 10, 25, and 60 μl . A constant quantity of 0.2 μg of DNA was added in each solution, which was agitated for 2 hours. Figure 6.6 shows the gel-electrophoresis results.

It can be seen that as the ND concentration increases, the amount of the remaining free DNA decreases and finally becomes zero, indicating the complete capture of DNA by NDs.

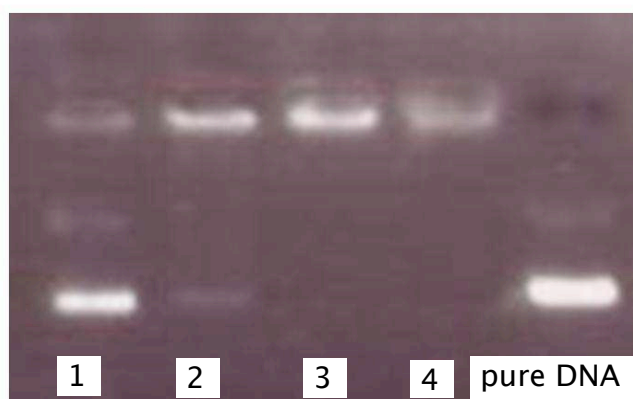


Figure 6.6: Image of agarose gel electrophoresis of DNA-Nickel-ND complex. From left to right the concentration of nanodiamonds increases. The well on the right is taken as a reference, containing pure DNA solution.

b DNA - ND complex observation by AFM

To visualize the DNA-ND complex formation we carried AFM scans of the different solutions. The surface preparation and the deposition process were the same as in the previous case of poly-L-lysine coating.

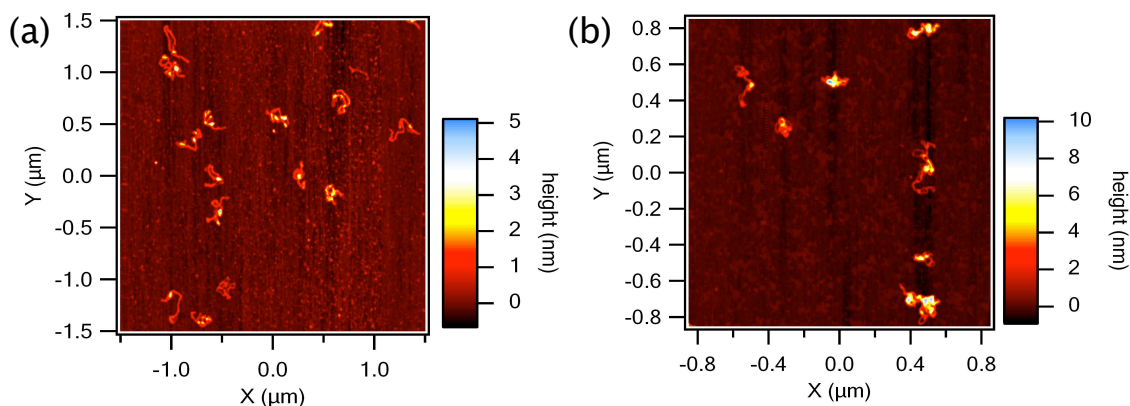


Figure 6.7: AFM scans of Nickel coated nanodiamond solutions, containing DNA. a) solution 1 of electrophoresis (some DNA captured); b) solution 2 of electrophoresis (very few free DNA).

Figure 6.7a shows the AFM image obtained from solution 1 of the gel. Most of the DNA molecules are free but some of them seem bound to some structures. Judging by the height of these formations, we suppose that they are the smallest diamond nanoparticles of the solution. As seen in the corresponding electrophoresis experiment for this solution, DNA is partially captured.

On the AFM scan of solution 2, only very few DNA molecules remain free. The others are bound to particles with slightly larger heights (Figure 6.7b). A single DNA plasmid seems to be complexed to several nanoparticles this time, which is expected, as the quantity of NDs has increased. Indeed the electrophoresis gel indicates that almost all DNA is captured.

In order to enhance the binding strength of the DNA-ND complex on the mica surface for AFM imaging, we tried pretreatment of the mica surface with poly-L-lysine which converts more efficiently the charge of the mica surface to positive, than the Nickel pretreatment. Instead of diluting the DNA-ND solution in $MgCl_2$ solution, we used glutaraldehyde to create a stronger interaction of the complexes with the substrate (glutaraldehyde is often used as a cross-linker in biological experiments). The results were similar to those obtained with Nickel treatment.

6.3 Transfection experiments of DNA - ND complex in HeLa cells

To confirm the prospect of using NDs as nonviral vectors, we performed transfection of the complex to cultured cells.

We used poly-L-lysine coated NDs. The complexes were added in a culture plate of HeLa cells and incubated for 48 h (37°C, 5% CO₂). After incubation, the transfected cells were rinsed with PBS, fresh culture medium was added, and cells were imaged immediately, with a commercial fluorescence microscope. The plasmid DNA included the gene of GFP, so if the DNA managed to enter the nucleus, then the GFP protein should be expressed and produced.

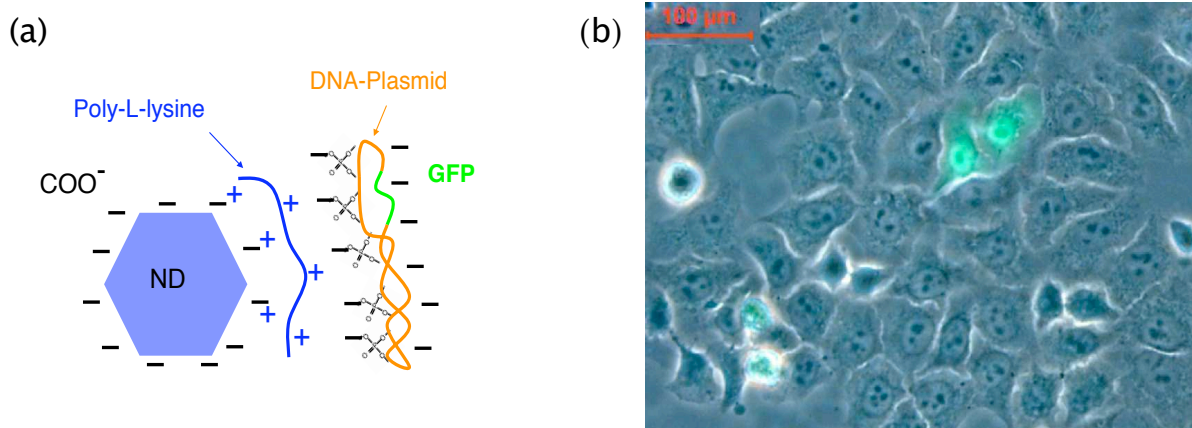


Figure 6.8: Transfection of DNA-ND complex. (a) representation of the formation of the complex DNA including GFP gene with NDs. (b) fluorescence image - combined Hoffman contrast of transfected HeLa cells.

Figure 6.8 shows combined fluorescence and Hoffman modulation contrast image, for DNA-ND concentration of the solution 3 of Figure 6.3. For the fluorescence, excitation was done with blue light. Cells appearing in green are the ones for which GFP was properly synthesized. However, this was observed only in one cell per about 50 for the acquired images, which is a low efficiency. In comparison to the control², we observed a transfection efficiency of the order of ~5%, which is much lower than the one achieved by transfection agents, like lipofectamine [264].

However, the fact that many cells are not fluorescent does not indicate that the DNA-ND complex has not entered the cell. Even if the complex enters the cell, DNA may be altered by enzymes (e.g. DNases) when it is released from the nanodiamonds.

A verification of the efficient ND-DNA complex formation in order DNA to be protected from enzymatic digestion, could be to treat the solutions used at the gel - electrophoresis experiments with the enzyme deoxyribonuclease I (DNase 1), which preferentially catalyzes the cleavage of phosphate ester linkages of “naked” plasmid DNAs. An additional gel-electrophoresis experiment of these solutions could reveal if there is some DNA digested by the enzymes. Normally the free plasmid should be completely digested whereas the plasmids bound to the polycation coated nanoparticles should be protected. Unfortunately this experiment was not carried out.

For the other concentrations of DNA-ND complexes the transfection results were similar to the one illustrated on Figure 6.8. For PAH coated or Nickel coated NDs, the transfection results were also not very different, the transfection efficiency was low.

²control is the incubation of plasmid DNA with cells, no NDs added. DNA alone cannot be internalized in cells.

A possible explanation could be that poly-L-lysine coated diamonds tend to aggregate (the electrostatic repulsion of nanoparticles can be decreased by the coating). As a result, DNA-ND complexes may be blocked in the pores of the gel and show retarded mobility due to their big size. A way to eliminate this kind of precipitations would be to use poly-L-lysine of lower molecular weight (for example 10 to 20 kD). In addition, the precipitations could be decreased by changing the ionic force of the solution.

Very recently, Zhang et al. reported the efficient transfection of plasmid DNA in the cell nucleus, using a polymer of low molecular weight (PEI, weight 0.8 kD) [239]. Thus the appropriate choice of the molecular weight of the polymer and the control of the polymer-nanoparticle attachment force are crucial parameters for an efficient transfection of genetic material in the cell nucleus.

An alternative and perhaps less difficult experiment showing that NDs can be used as vectors of biomolecules, is the vectorization of oligonucleotides or siRNA. In contrast to plasmid DNA, oligonucleotides or siRNA have smaller size and do not need to be in the nucleus to be translated. SiRNA delivery in cells for potential gene silencing has recently been demonstrated by the group of Hongjie Dai for carbon nanotubes [265, 266].

In collaboration with the team of Claude Malvy and Jean-Remi Bertrand, who traditionally work on siRNA and oligonucleotide delivery in cells [267–269], our aim is to use NDs as vectors of siRNA and visualize their intracellular trajectory. In particular, for siRNA delivery with polycationic coated NDs, the efficiency of the transport can be monitored through the inhibition of an oncogene due to the siRNA internalization. After release of siRNA from the endosomes into the cytosol, its interaction with the polycationic NDs will be confronted to the presence of anionic intracellular partners, including phosphatidylserine (PS) present on the internal leaflet of the plasma membrane. In this environment, siRNAs must be released from the polycationic NDs and bound to the specific messenger (mRNA) targets, leading to their degradation and thus inhibiting the expression of the corresponding protein, making possible the oncogene inhibition. This work is in progress.

6.4 Conclusion

In conclusion, we have managed to form DNA-ND complexes for different coatings of the nanodiamonds. Due to the lack of a positively charged surface of the nanodiamonds, we were obliged to use polycations or divalent cations to render the NDs positively charged, a necessary requirement for DNA binding. Gel-electrophoresis experiments allowed every time to examine the efficient binding. AFM scans of the complexes provided their better visualization and further confirmation of the complex formation.

We unfortunately concluded that transfection of plasmid DNA in cells due to NDs is not trivial, and further, more invasive methods, such as electroporation, gene gun or microinjections should be used for more outstanding results. An alternative idea is to use oligonucleotide (siRNA) as the cargo molecules. Nanodiamonds could serve as labels of the biomolecules at the same time, and various intracellular processes could be studied, like the exact uptake pathways of siRNA or its binding to the specific mRNA messenger. This is an ambitious project, which has just begun.

Chapter 7

Conclusion

In this thesis we studied the photoluminescence properties of NV color centers in diamond nanocrystals and showed some applications in bio-imaging.

We used this type of particles for cellular labeling. We observed by confocal microscopy that nanodiamonds can be spontaneously internalized in cells and we determined their localization in the cytoplasm by detecting the photoluminescence from individual nanoparticles. By wide-field illumination microscopy and a CCD array we were able to observe the motion of the internalized PNDs, which appeared to be mostly confined. Their perfect photostability could be used for long term bio-imaging applications. For example, small nanodiamonds could be used to label stem cells during their differentiation process, in week-scale experiments.

Moreover, we showed that the nanodiamonds studied in this work are not toxic for *in vitro* experiments with cells. Examination of the cell morphology revealed no changes in cell shape, and cytotoxicity tests demonstrated the low cytotoxicity of NDs, up to a time scale of 24 h. This is an encouraging result towards the use of photoluminescent nanodiamonds in life sciences. Further toxicology studies on animal models are necessary and are currently in progress.

A necessary condition to use PNDs for bio-imaging is that they can compete with traditional fluorescent labels. Indeed we showed that contrary to dye molecules or quantum dots, the emission of single NV centers in single nanodiamonds is perfectly stable in time, and found that nanodiamonds containing about 4-5 NV centers can have a photoluminescence signal equivalent or even higher to the one of commercial quantum dots, under higher excitation intensities.

For imaging applications of PNDs in cell medium, it is crucial to obtain a high S/B ratio. Thus we had to use and develop bright PNDs. In order to improve the NDs photoluminescence yield, we examined different proton beam irradiation doses to create high concentrations of vacancies in 30 nm nanodiamonds. We gained a factor of three regarding the photoluminescence intensity for a 10 fold increase of the irradiation dose. After calculations we conclude that there is still plenty of room to improve the conversion of the available vacancies and nitrogen atoms into NV color centers in the diamond lattice, by proper optimization of the sample preparation conditions.

Alternatively, nanodiamonds with a big number of NV centers, lacking photobleaching, and small in size could be used as donors in fluorescent resonance energy transfer (FRET) experiments. Due to the large Stokes shift of the NV centers, excitation only of

the NV center without excitation of the acceptor dye molecule is possible. The size of the nanoparticles plays a crucial role; a desirable nanoparticle size would be of the order of 5-10 nm. Measurements on the changes of the NV center radiative decay lifetime before and after interacting with a fluorophore (i.e. interaction between the protein labeled by the nanodiamond and a protein labeled by a fluorophore) can also indicate the FRET efficiency.

Another way to detect fluorescent probes with a high S/B ratio in cell medium is by two photon excitation microscopy, due to the low 2-photon background signal from cells. We showed that NV centers in nanodiamonds have low, but not negligible, 2-photon excitation photoluminescence, which is optimal at the excitation wavelength of 850 nm and almost zero at 1064 nm. We discovered that simultaneous pulsed excitation of NV centers at 1064 nm and the frequency doubled 532 nm beam depletes the first excited state.

A straight forward application of this effect is the super-resolution imaging of the NV center. We carried out a “proof of concept” experiment and achieved, on our setup, a resolution improvement by a factor of 2 for 100 nm bright (i.e. with many NV centers) nanodiamonds. This photoluminescence quenching technique, alternative to the usual methods like the STED one, is a very promising one. It is easy to implement, since it requires a single pulsed laser, instead of different laser systems, avoiding also the lasers temporal synchronization, necessary for the classical STED techniques. Moreover, for biology, the 1064 nm wavelength is a well adapted choice, due to the low absorption of the tissues at that wavelength. Some supplementary studies are necessary, to determine the excitation intensities required for resolution improvement down to some nanometers and to what extent the large wavelength used can be an obstacle to the resolution improvement.

The perfect photostability, the biocompatibility and the possibility to graft chemical moieties on the nanodiamond surface make this material a real “jewel” for biological applications. Due to their small size, NDs can serve as vectors of biomolecules in cells. Thus an understanding of their cellular uptake mechanism is necessary. After demonstrating that NDs can penetrate spontaneously in cells, the next step was to investigate their internalization pathways. We found that the dominant mechanism is endocytosis and we have indications that it is clathrin mediated.

We also found that the nanodiamonds in form of aggregates are localized in intracellular endocytotic vesicles in perinuclear regions, and a portion of individual PNDs, in particular the smallest particles, remain free in the cytoplasm. Whether these nanoparticles have entered cells by passive diffusion or have entered by endocytosis but have then escaped from the endocytotic vesicles is a subject of further investigation. For long-term intracellular tracking applications the high mobility of the markers is very important and most often the nanoparticles should stay free in the cytoplasm. An alternative method to fulfill this criterium is by electroporation, by which an electric pulse generates pore formation in the plasma membrane, facilitating internalization. This application will be used by our group in future experiments, where nanodiamonds will serve as delivery vehicles of biomolecules.

In that perspective, as a preliminary experiment we briefly investigated the possibility to use NDs as a plasmid DNA delivery vehicle. For that we coupled electrostatically nanodiamonds with DNA and examined the efficiency of DNA transport in the cell nucleus.

We observed a low transfection rate. Other experiments can be carried out to explore nanodiamond efficiency as vectors of genetic material in cell, overriding the necessary entrance in the cell nucleus. One possibility is the delivery of small oligonucleotides, like siRNA, which do not enter cells alone. Surface functionalization of the nanodiamonds with cationic groups, allows their conjugation with siRNA molecules. Efficient delivery of the ND-siRNA complex could lead to the binding of siRNA to specific messenger (mRNA) targets, leading to target *knockdown*, i.e. degradation and hence inhibition of the expression of a corresponding protein. This function could be used for oncogene inhibition, with therapeutic prospects.

In addition, photoluminescent nanodiamonds could be used not only as vectors of si-RNA or DNA in cells, but also as labels of the whole internalization and drug release process. Imaging, 3D-tracking and even super-resolution imaging of single nanodiamonds conjugated with biomolecules can unravel the intracellular dynamics of this complex and allow observations of how cells or organisms respond to the particle uptake over a time period of hours or even days.

Therefore, as demonstrated in this work, photoluminescent nanodiamonds, small in size and containing a large number of NV centers, are excellent and very promising probes for simultaneous bio-imaging and biomolecule delivery in cells.

Appendix A

H3 color center in diamond

A.1 Introduction

There are more than 500 optically active defects in diamond [15, 31]. Our main interest was focused on the NV color center, which is characterized by a well photostable photoluminescence in the red spectral range.

Here we will study another color center in diamond, the H3 center. It consists of one vacancy next to two substitutional nitrogen atoms (N-V-N). It is easier to obtain in type Ia diamond, which contains many A aggregates (two nearest-neighbor substitutional nitrogen atoms) [270].

A.2 H3 color center in micro-diamonds

The starting material was type Ib diamond synthetic micron size powder (Element Six, Netherlands) with a specified size of 150-200 μm . NV centers were created by electron irradiation. The electron beam energy was 8 MeV and the irradiation dose $2 \times 10^{18} \text{e}^- / \text{cm}^2$ (*Herotron Technologies GmbH*, Germany).

Annealing of the samples was carried out at 800°C under vacuum ($\sim 10^{-8}$ Torr) during 2 hours.

We observed the photoluminescence of the microdiamonds with light excitation in the range of 450-500 nm (filtered from a halogen high power white lamp, standard fluorescence microscope) and signal acquisition in the wavelength range 500-550 nm (used FITC filter).

An almost zero signal is recorded for non-irradiated diamond crystals, while with irradiation the photoluminescence intensity increases drastically (the CCD array is saturated). After a 2 h annealing, the photoluminescence intensity decreases (Figure A.1)

For biological applications, fluorescent probes should be photostable. We tested the photostability of the crystals, before and after the annealing process. We observe that before and after annealing the crystals are perfectly photostable under more than six hours of illumination (Figure A.2).

To better examine the green photoluminescence of the diamond crystals, we recorded the spectra of untreated microcrystals, irradiated and annealed with our home-built confocal setup (Ocean Optics spectrograph). Figure A.3 shows that untreated crystals present

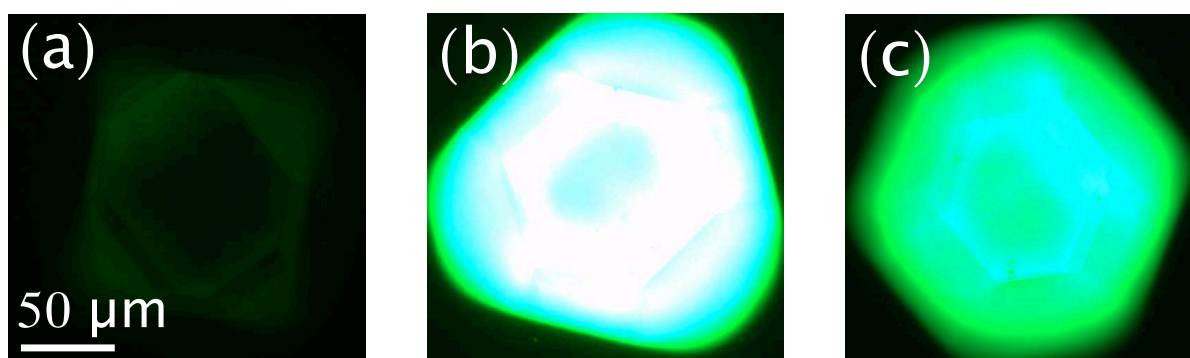


Figure A.1: Photoluminescence images of (a) untreated (non-irradiated) crystal; (b) electron irradiated crystal at a dose $2 \times 10^{18} \text{e}^-/\text{cm}^2$ at 8 MeV; (c) crystal annealed for 2 h at 800°C after the electron irradiation. Excitation and collection wavelengths for the photoluminescence image are respectively 450-500 and 500-550 nm. CCD exposure time is 1.5 s.

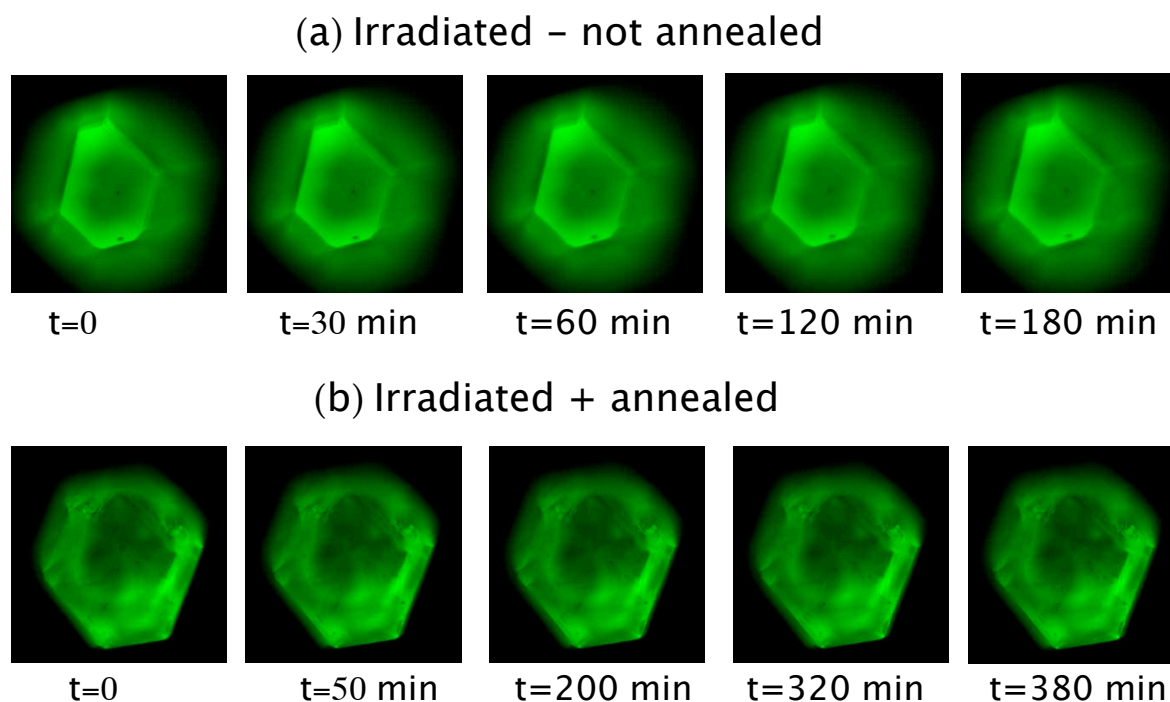


Figure A.2: Photoluminescence intensity over time for a diamond microcrystal. (a) The crystal was irradiated but not annealed ($2 \times 10^{18} \text{e}^-/\text{cm}^2$, energy 8 MeV). Exposure time 50 ms. (b) The crystal was irradiated and annealed (2 h at 800°C). Exposure time 100 ms. In both cases, the crystal presents a perfect photostability. Excitation wavelength 450-500 nm, collection at 500-550 nm.

a band with a Zero Phonon Line (ZPL) about 525 nm, corresponding to H3 color centers [270]. When the crystal is irradiated the intensity of this band is enhanced, while after an annealing process it decreases. It should be mentioned however that this observation was crystal-sensitive. For some microcrystals we observed no green photoluminescence.

This probably indicates that the nitrogen concentration is not homogeneous for the used microcrystals.

On the other hand, the NV color center (both NV° and NV^-) presents a very weak photoluminescence signal in untreated and non annealed crystals, while in annealed crystals the signal increases drastically.

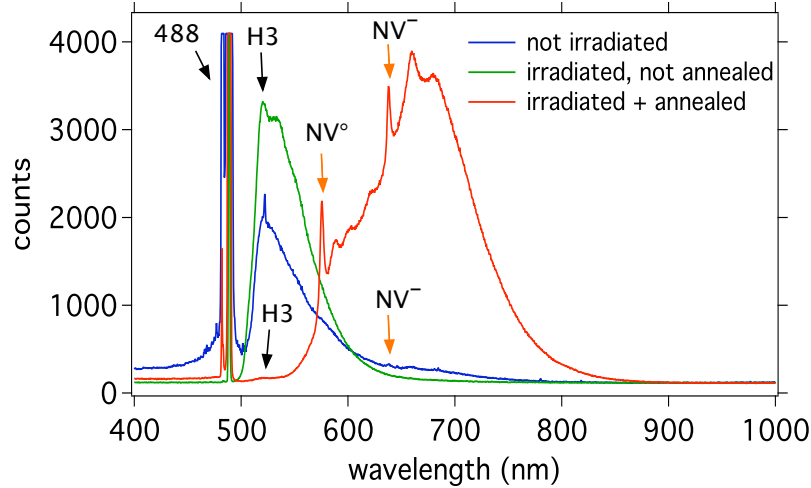


Figure A.3: Study of the H3 photoluminescence spectrum. Photoluminescence spectra of diamond microcrystals not treated (in blue), electron irradiated at $2 \times 10^{18} \text{ e}^-/\text{cm}^2$ with a beam energy 8 MeV (in green) and annealed after irradiation (in red). The characteristic Zero Phonon Line (ZPL) at 522 nm of the H3 is well distinguished for the non irradiated and irradiated crystals, while it decreases after an annealing process. The ZPL at 575 nm and 637 nm for the NV° and NV^- center respectively are well distinguished after annealing, while they are very low in untreated crystals. Excitation wavelength at 488 nm (observed as a narrow line on the spectra), dichroic mirror used z488rcx, excitation power 0.5 mW.

A.3 Conclusion

To conclude, we observed the H3 color center in diamond Ib microcrystals. We observed that the photoluminescence signal is perfectly stable and is maximal after an irradiation process, but before annealing. The reason why after irradiation the H3 signal is maximum is not evident. It has been reported that under very high temperatures nitrogen aggregates (symbolized by A) are decomposed to form single nitrogen atoms ($A \rightarrow N+N$). However this temperature is relative high (2000°C [271]) and is not achieved here.

It should be mentioned that not all microcrystals presented a high photoluminescence signal in the green region, indicating that not all crystals had a high amount of A nitrogen aggregates (which comes as a consequence of the Ib diamond type used).

Previous reports on H3 center creation are focused on type Ia diamond, rich in A aggregates [272]. Recently, nanodiamonds of type Ia diamond with a strong H3 photoluminescence signal were produced (after an irradiation and annealing process), were internalized in cells and detected with fluorescence microscopy and flow cytometry [184].

Further investigation is needed, to understand and control the creation process of H3 centers, in order to introduce them in nanodiamonds rich in NV centers, and achieve two-color labeling, often necessary for bio-imaging experiments.

Appendix B

Time Gated Imaging of photoluminescent nanodiamonds in cells

B.1 Introduction

Individual imaging of fluorescent nanoparticles in cells is often hindered by the high cell autofluorescence. Even with confocal microscopy, where a great part of the light coming from the surrounding region of interest (confocal volume) is spatially filtered by the pinhole, cell autofluorescence is still present and reduces the contrast.

A method to enhance the signal-to-background ratio and selectively filter the cell autofluorescence is the time-gated imaging. It has been already used for other photoluminescent nanoparticles, like quantum dots [123], oxide nanoparticles [20] or silica encapsulated europium nanoparticles [273]. If the photoluminescence decay time is longer than the one of the cell autofluorescence lifetime, it is possible to build an image showing the photoluminescent nanoparticles, only with photons collected after the excitation laser pulse time reference for times longer than the autofluorescence lifetime.

Thanks to the NV color center long, but not too long, decay lifetime (10-30 ns), we managed to increase the image contrast and improve the nanodiamonds intracellular imaging. Before exposing the details of the time-gated imaging experiment for nanodiamonds, we briefly present the lifetime measurements for NV centers, in bulk diamond and nanocrystals.

B.2 NV color center radiative decay lifetime

B.2.1 Experimental setup

To detect the signal coming from the NV centers we used the standard home-built scanning stage confocal setup. Laser excitation of PNDs was carried out by the home-built picosecond pulse laser relying on a diode pumped Nd:YVO₄ passively mode-locked laser emitting at 1064 nm, subsequently doubled in frequency to get 532 nm excitation (see chapter 3). The excitation beam is focused onto the sample with the $\times 60$ oil immersion

Nikon objective, 1.4 numerical aperture. The photoluminescence is collected from the sample by the same objective (dichroic mirror 700dcsx, Chroma), is spectrally and spatially filtered by a long-pass filter (RazorEdge LP03-532RU-25) and a confocal pinhole and is detected by an APD (see chapter 2 for setup details).

To measure the photoluminescence lifetime of the NV centers we used the TAC (Time-to-Amplitude Converter) and the Multi-Channel Analyzer (MCA). The excitation laser pulse was synchronized with the Start of the TAC and the APD with the Stop. Once the laser pulse arrives at the Start, it launches a voltage ramp, which stops when a photon from the APD arrives at the Stop. The amplitude reached by the ramp is directly proportional to the Start-Stop delay. A PC plug-in multi-channel analyzer board acquires the signal from the TAC and produces histograms of photon arrival times for each pixel in the raster scan. The time acquisition window of the TAC for the following experiments was fixed at 100 or 200 ns. The instrumental response function has a characteristic time of ~ 500 ps.

B.2.2 Measurement of NV decay lifetime in bulk diamond

A thorough study of the lifetime of the NV^- center has been undertaken by Alexios Beveratos [32, 274]. In his work he calculates the decay lifetime of NV^- center with two methods, by the “traditional methods” using a pulsed laser or by fitting the antibunching curve with a $g^{(2)}(\tau)$ function associated to a three level model. In our case we measure the lifetime of both NV° and NV^- centers by pulsed laser excitation. We were interested in verifying that for both types of NV emitters in diamond the decay lifetime remains higher than the cell autofluorescence corresponding lifetime.

The bulk diamond used were microdiamonds, electron irradiated (2×10^{18} e⁻/cm², energy 8 MeV) and annealed at 800°C for 2 hours (see chapter 2). They were deposited on a glass substrate and the photoluminescence signal was observed by the confocal home-built setup. The mean excitation power of the pulsed laser was measured 0.8 mW.

The dominant centers that we observed in this kind of microdiamonds were the NV^- , but there was also a small portion of neutral NV° centers (Figure B.1). To measure the lifetimes separately for each type of NV center, we separated spectrally the two centers, by using a BP 580/10 and HQ740 LP filter (Chroma) for selecting the NV° and NV^- respectively. The signal of NV^- center becomes visible for wavelengths greater than 600 nm and the signal of NV° vanishes for wavelengths >700 nm.

The excitation light was focused on the same spot in the microcrystal and we measured the corresponding lifetimes. Figure B.2a shows the photoluminescence lifetime of the microcrystal, without using any additional filters to select each type of NV center. The best adapted fit function is a biexponential one:

$$f(t) = A_1 e^{-t/\tau_1} + A_2 e^{-t/\tau_2} \quad (\text{B.1})$$

with $\tau_1 = (10.5 \pm 0.7)$ ns, $\tau_2 = (18.1 \pm 4.5)$ ns and $A_1/A_2 = 3.3$. We see that the fast time (attributed later to the NV^- center) is the dominant one but there is also a longer time, at 18.7 ns.

If we spectrally select only the NV° signal, we obtain a monoexponential fit (Figure B.2b in blue), with $\tau = (17.6 \pm 0.1)$ ns, which is in agreement with the longer

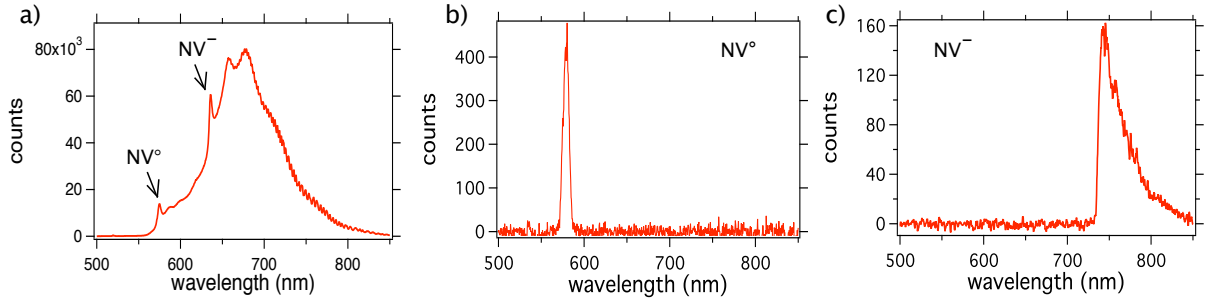


Figure B.1: Spectral selection of NV centers in microdiamond with pulsed laser excitation of mean power 0.8 mW at 532 nm: (a) the complete photoluminescence spectrum of microdiamond; (b) photoluminescence spectrum with BP 580/10 filter selecting NV° signal; (c) photoluminescence spectrum with the HQ740 LP filter selecting NV⁻ signal.

lifetime value measured without any filter. When we spectrally select the photoluminescence of the NV⁻ center, a biexponential fit is more appropriate with $\tau_1 = (4.9 \pm 0.7)$ ns , $\tau_2 = (11.8 \pm 1.7)$ ns and $A_1/A_2 = 0.3$. Our latter result is in accordance to previous measurements of NV⁻ lifetime in synthetic Ib type bulk diamond, found equal to 11.6 ns [275]. For the lifetime of the NV° center there are not yet any reports in the bibliography.

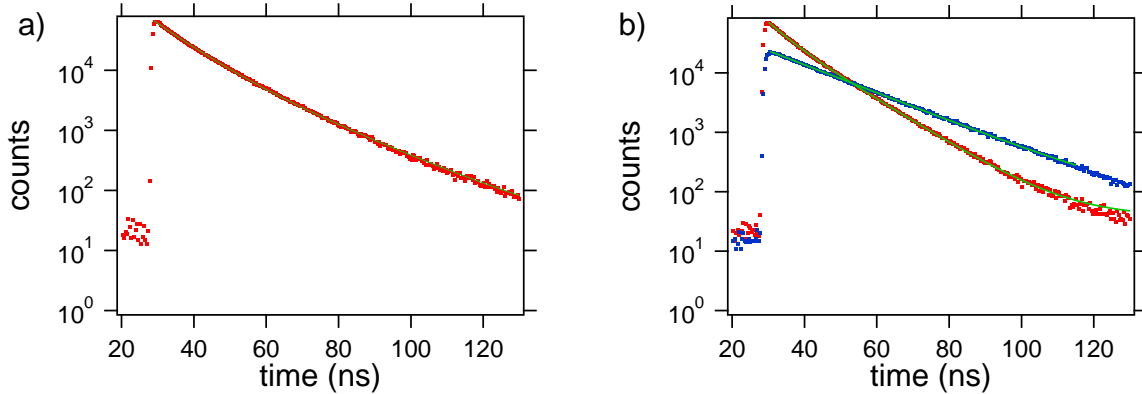


Figure B.2: Microdiamond photoluminescence decay lifetime: (a) without any filtering of the microdiamond with spectrum of Figure B.1a, in green is the biexponential fit; (b) spectrally selected NV° center decay lifetime in blue and NV⁻ lifetime in red respectively; in green is the corresponding monoexponential fit.

B.2.3 NV decay lifetime in nanodiamonds

a Influence of the emitters environment on the decay lifetime

The fluorescence decay time is the characteristic time that a fluorophore remains in the excited state after excitation, and it is defined as : $\tau = \frac{1}{k_r + k_{nr}}$, where k_r is the radiative rate constant, and k_{nr} the non-radiative rate constant.

The fluorescence decay time depends on the intrinsic characteristics of the fluorophore itself, but it also depends in a measurable way upon the local environment and the dipole orientation [113]. The dependency is in the radiative constant k_r . Experiments performed on europium atom layers using metallic mirrors showed the modification of the fluorescence decay rate [114, 276, 277]. The dependence of k_r upon the environment was also demonstrated for other nanoprobe systems [278, 279]. Single molecule experiments in far field microscopy also demonstrated the expected orientational dependence of k_r [280].

For an emitter in an unbound dielectric medium with a refractive index n , the Fermi golden rule indicates that the radiative decay k_r is enhanced by a factor of n compared to its value in vacuum k_r^{vac} : $k_r = nk_r^{vac}$ [32].

b Measurement of the decay lifetime of nanodiamonds

The nanodiamonds used for these measurements were of type 2, with size smaller than 50 nm (initial powder SYP 0-0.05, irradiated under a 2.4 MeV proton beam, with a dose of 5×10^{16} H⁺/cm²). An aqueous solution of these PNDs was deposited on glass substrates by spin coating (no polymer used). Most of the NDs had both types of centers. Figure B.3a shows the photoluminescence spectrum of one PND. The antibunching dip of 0.65 corresponds to 2 NV centers, one negative NV⁻ and one neutral NV^o center. It should be mentioned that for the intensity-time correlation measurement, the sample was excited with a cw 532 nm laser, introduced to the microscope setup with the use of a flip-flop mirror.

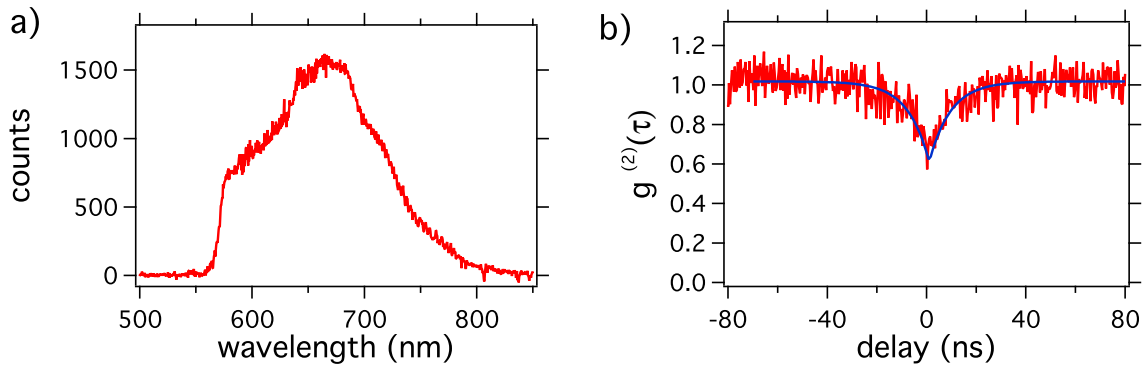


Figure B.3: Photoluminescence spectrum and quantification of NV centers in one PND. (a) Photoluminescence spectrum of one PND, the sudden decrease to zero level at ~ 565 nm is due to the dichroic mirror (Q565LP, Chroma) used for this measurement; (b) intensity autocorrelation measurement of the same nanodiamond, showing that it contains two color centers (fit curve of a symmetric exponential function in blue), cw laser excitation power 0.3 mW at 532 nm.

The recorded photoluminescence decay signal was corrected from the residual excitation laser background. The latter was recorded separately and follows a monoexponential decay with $\tau = 0.5$ ns, associated to the instrumental response function (IRF) characteristic time. A second characteristic time component at 14 ns is also present at the IRF, making a biexponential fit possible, but with the coefficients ratio equal to 50 in favor to

the short time values; in consequence the long time contribution is not taken into account (Figure B.4a).

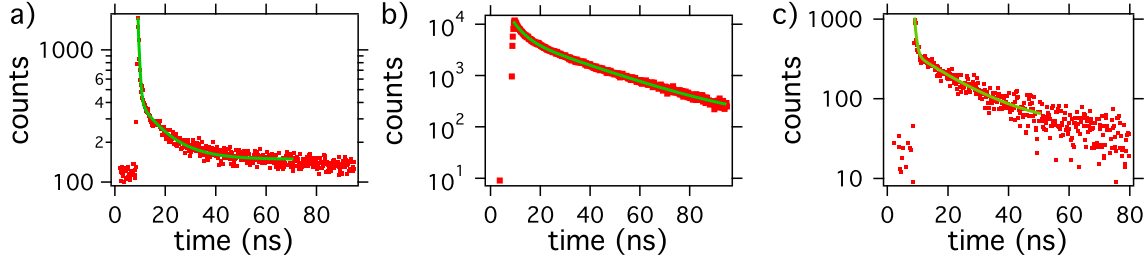


Figure B.4: Nanodiamonds photoluminescence decay lifetime: (a) decay lifetime of one laser picosecond pulse; b) photoluminescence decay lifetime of PND of Figure ?? (with green color the triexponential fit); (c) spectrally selected decay lifetime of NV° center (with green color the biexponential fit).

When we record the total signal coming from the ND, the best function that fits the measured data is a triexponential one, with $\tau_1 = (1.4 \pm 0.1)$ ns , $\tau_2 = (10 \pm 0.4)$ ns , $\tau_3 = (26.7 \pm 0.8)$ ns and coefficients $A_1 = A_2 \simeq 0.7A_3$.

In order to define the origins of each time τ component, we measure the decay lifetime of the same ND by adding a BP filter 580/10 in front of the APD detector, selecting only the signal coming from the NV° center. The signal is relatively weak compared to the laser background, but with the appropriate background subtraction we can infer the decay lifetime curve. This can be fitted by a biexponential decay function, with $\tau_1 = (1.6 \pm 0.3)$ ns , $\tau_2 = (15.7 \pm 1.2)$ ns and $A_1/A_2 = 2$. We consider that the short time is a residual from the excitation laser background. It is not easy to completely eliminate this background signal just by recording the decay curve at a position next to the nanocrystal.

The decay lifetime of the NV^{-} center was measured by finding a single NV^{-} emitter in a single PND (Figure B.5). The decay lifetime is found 27.3 ± 1.4 ns, following a monoexponential decay. Out of a large number of nanodiamonds studied (>30), the decay lifetimes of the NV^{-} center had a wide dispersion in the range of 10-30 ns, in agreement with other reports [17, 274]. According to a recent publication of Tisler et al. [17], they observed a decay lifetime dispersion in the range of 7-40 ns, for 5-20 nm nanodiamonds. The starting material was Van Moppes, SYP 0-0.02, the same like the one used here (Van Moppes, SYP 0-0.05), only the size distribution was slightly lower.

B.2.4 Discussion

From the previous measurements both types of NV center have lifetimes longer than 10 ns in nanodiamonds. For biological applications and time-gated imaging this is convenient, as one can select only the “late” photons, with arrival time on the detector longer than the ones coming from the cell autofluorescence.

However, NV center photoluminescence decay often consists of two lifetimes, one for NV° and another for the NV^{-} center.

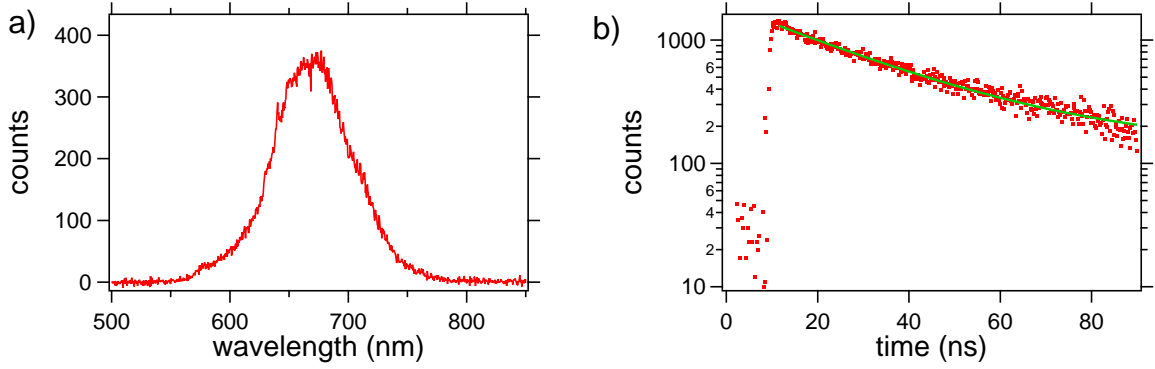


Figure B.5: Study of the decay lifetime of the NV⁻ center. (a) Photoluminescence spectrum of a nanodiamond containing a single NV⁻ center; (b) decay lifetime of the color center in the same nanodiamond (with green color the monoexponential fit).

NV⁻ center

As we mentioned, the environment of the emitter can modify its decay lifetime. The difference is obvious for the measurements of the NV⁻ center in bulk diamond (τ_b) and in a 20-40 nm crystal (τ_{nc}). We obtain $\tau_b = 11.8 \pm 1.7$ ns and $\tau_{nc} = 27.3 \pm 1.4$ ns respectively. The ratio between the two spontaneous emission rates is equal to $k_b/k_{nc} = 2.3 \simeq n_{\text{diamond}} = 2.4$.

The small deviation from the theoretical ratio of 2.4 can be attributed to the dispersion of the decay lifetime values among different PNDs. We considered that the air is the immediate interface to the NDs. However a small percentage of their surface forms an interface with the glass substrate, which has a different refraction index than the one of the air. The proportion of air/glass interface with the PND can alter slightly the observed decay lifetime. In addition the dipole orientation regarding the air/glass substrate interface induces a dispersion at the lifetimes values [281, 282]. Additionally, the lifetime dispersion could be attributed to the presence of quenchers, for example the graphite atoms on the nanoparticle surface. Normally, most of the graphite is removed by the surface treatment.¹

Diamond type	τ_{NV° (ns)	τ_{NV^-} (ns)	τ both centers (no filter used) (ns)	A fit coefficient
bulk	17.6 ± 0.1	11.8 ± 1.7	18.1 ± 4.5 and 10.5 ± 0.7	$A_1/A_2 = 3.3$
$ND_{\text{both centers}}$	15.7 ± 1.2	-	$1.4 \pm 0.1, 10 \pm 0.4, 26.7 \pm 0.8$	$A_1 = A_2 \simeq 0.7A_3$
$ND_{NV^- \text{ only}}$	-	27.3 ± 1.4	-	
$ND_{NV^\circ \text{ only}}$	11-16	-	-	

Table B.1: Measured lifetimes for bulk diamond and nanodiamonds

¹Batalov et al. reported that there is a slow lifetime at 7 ns, associated to the spin state $m_s = \pm 1$ [283]. In our case we did not clearly observed this decay time, as probably the excitation laser pumped rapidly the system in the $m_s = 0$ state.

NV^o center

For the NV^o center there were no previous published data about its exact lifetime value. Our measurements can throw light to the understanding of its photophysical properties, but further work has to be done.

For the bulk diamond we find $\tau_b = 17.6 \pm 0.1$ ns and for NDs $\tau_{nc} = 15.7 \pm 1.6$. These values do not fulfill the theoretical relation of $k_b/k_{nc} = 2.4$. For nanodiamonds containing only NV^o centers we observed that τ_{NV^o} is always between 11 - 16 ns. For bulk diamond, we tested two more samples, to verify the credibility of our measurements. We tested microcrystals that were electron irradiated at a dose of 2×10^{17} e⁻/cm², energy 2 MeV and annealed at 800°C for 1 hour and another sample with a $\times 10$ times increase of the dose (at Gent facilities, Belgium). The measurements of the NV^o lifetime are always between 11 - 18 ns. The complete understanding of the NV^o photophysical mechanism is out of the scope of our work. For further investigations, low temperature and dipole orientation dependence measurements are needed.

It has to be mentioned that in the lifetime measurements we often observe a short time component, in the range of 1.5 - 5 ns (Figure B.2a or Figure B.4a). This short time can be attributed to the non perfect subtraction of the laser noise signal, but as its value is higher than 1 ns, the explanation can also be different. Values of short decay lifetimes have once been referred previously by Hanzawa [13]. Hanzawa found by picosecond laser excitation two exponential components in bulk synthetic Ib diamond, of 2 and 8 ns at room temperature. The explanation of this short time remains a mystery, as no other teams have mentioned it afterwards.

B.3 Time-gated imaging of photoluminescent nanodiamonds internalized by cells

B.3.1 Cell preparation and PNDs uptake

HeLa cells were grown in standard conditions on glass coverslips in DMEM culture medium supplemented with 10% FCS. To study internalization of PNDs, cells were seeded at a density of 10^5 cells/1.3 cm² and grown at 37°C in a humidified incubator under 5% CO₂ atmosphere. 24 h after cell seeding, PNDs diluted in aqueous suspensions were added to the cell medium. The cells were grown under the same conditions for an additional period of 2 hours. After incubation, the excess of PNDs was removed by washing cells with PBS. Cells were then fixed with 4% paraformaldehyde in PBS and mounted on microscope slides for confocal examination.

B.3.2 Improving intracellular PNDs image contrast

We took advantage of the “long” fluorescence lifetime of NV centers in PNDs to enhance image contrast and sensitivity of PNDs detection. Despite the fact that the fluorescence lifetime of NV centers in PNDs presents an important dispersion due to the different crystalline environments, we demonstrated that most of the NV centers in NDs have a lifetime longer than 10 ns. Time selection of “late” photons arriving at the detector with a delay much higher than the autofluorescence lifetime ensures that the image is

dominated by the NV color center emission.

Figure B.6 shows time-resolved confocal images of a HeLa cell after incubation with PNDs. Selection of “late” photons reduces dramatically the noise from the autofluorescence of the cell and in turn enhances the PNDs signal-to-background ratio by an order of magnitude (Figure B.6b) [48]. The high contrast and sensitivity combined with the perfect photostability allow a precise localization of the nanoparticles inside the cell.

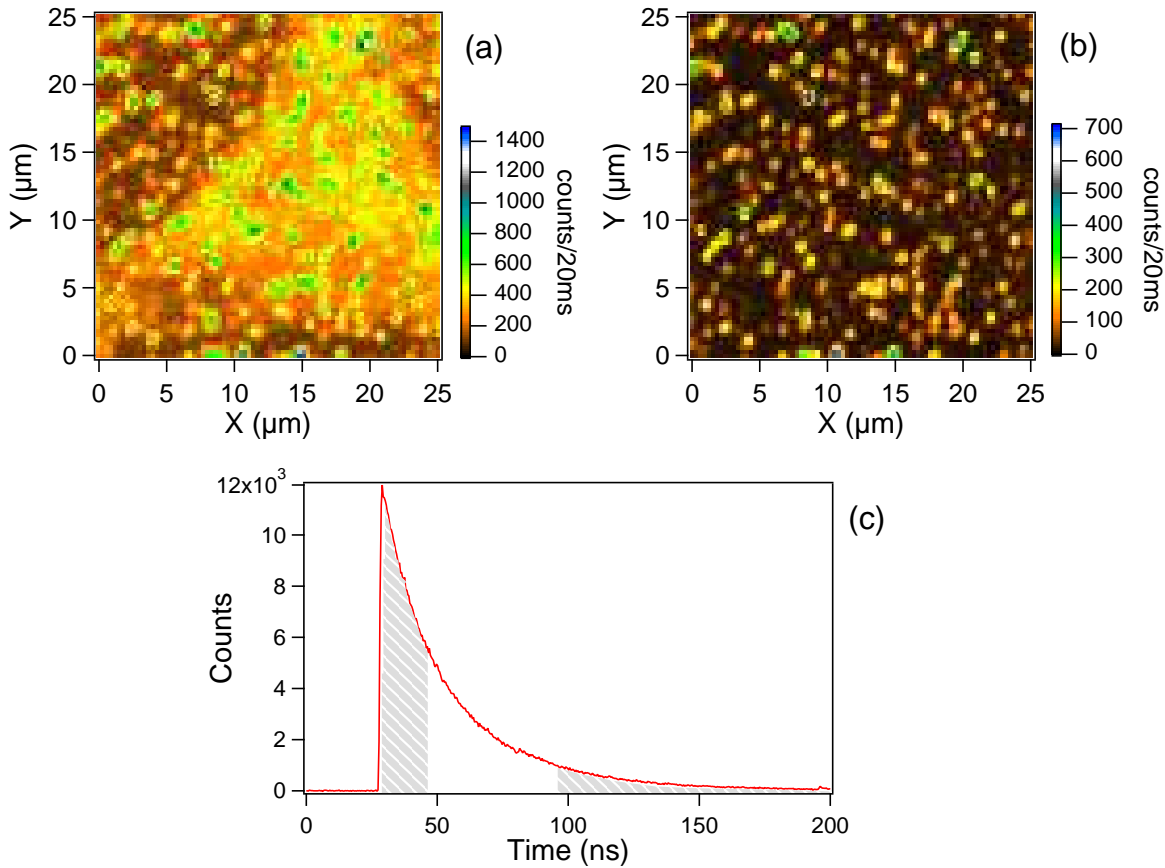


Figure B.6: Time-resolved confocal rasterscans of a fixed HeLa cell containing PNDs: (a) rasterscan obtained from all detected photons, displaying PNDs together with autofluorescence from the cell; (b) Time-gated rasterscan constructed from photons detected between 15 and 53 ns after the laser excitation pulse. Scan area is $25 \times 25 \mu\text{m}$. The mean laser power is $700 \mu\text{W}$ at 532 nm; integration time is 20 ms/pixel; (c) Characteristic fluorescence lifetime of a PND showing the time selection (non-grayed portion of the curve)

Time-gated imaging is not the only way to improve the contrast. In confocal microscopy, the pinhole diameter plays a crucial role for the contrast of the images, as its diameter is related to the dimension of the explored sample region. We decided to replace the $50 \mu\text{m}$ diameter pinhole by a $30 \mu\text{m}$ diameter one. By that, we can reduce the background signal but on the same time we collect less signal from the nanoparticles. Figure B.7a,b shows a cell image with internalized PNDs without and with time-gated imaging. We observe an improvement of the contrast, but it is not as high as with the $50 \mu\text{m}$ diameter pinhole. If we focus on a PND (in green square) we find a value of

signal-to-background ratio of 6 when we collect all photons while with time-gated imaging we obtain a ratio of 19. The 3.2 improvement of contrast is 3 times lower than the one achieved when a $50\ \mu\text{m}$ pinhole was used; nevertheless there is a gain in the contrast.

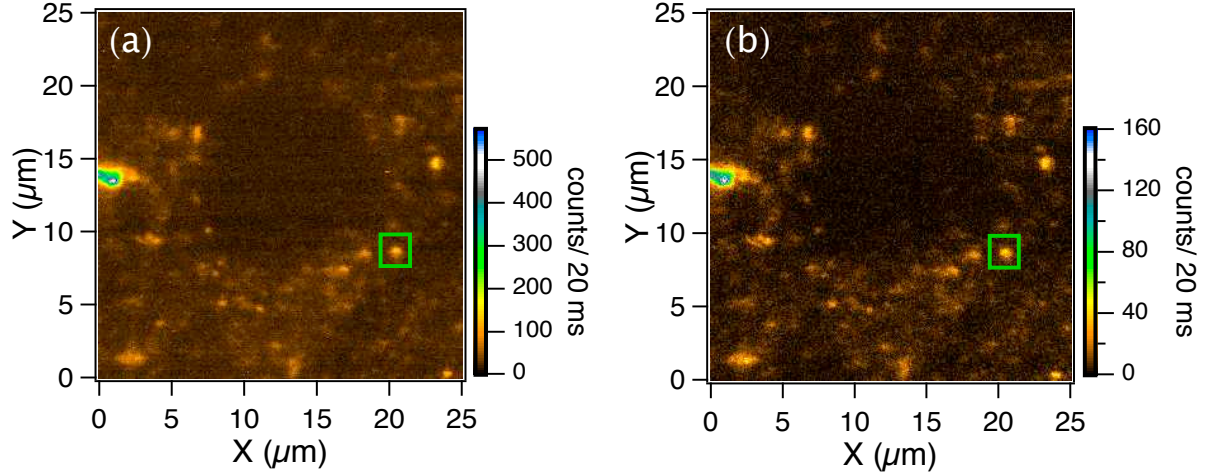


Figure B.7: Time-resolved confocal rasterscans of a fixed HeLa cell containing PNDs. The scans were taken using a $30\ \mu\text{m}$ diameter confocal pinhole. (a) Raster-scan obtained from all detected photons, displaying PNDs together with autofluorescence from the cell; (b) Time-gated rasterscan constructed from photons detected between 15 and 53 ns after the laser excitation pulse. The mean laser power is $700\ \mu\text{W}$ at 532 nm; integration time is 20 ms/pixel; in green square we focus on a single FND and observe a 3 times contrast gain.

B.4 Conclusion

In conclusion we showed that PNDs are easily detected at the single particle level over the cell autofluorescence background by time-gated imaging. The NV center photoluminescence decay lifetime was measured for each type of center in nanodiamonds and compared to the values found in bulk diamond. For NV^- center the difference is in agreement with the theoretical expected refractive index dependence and to the values reported in literature. For the NV° center the values of the lifetime for nanodiamonds and bulk diamond are quite similar, something that cannot be explained in a simple way. Given the fact that no investigation has still been carried out regarding the photophysics mechanism of this type of NV center, further measurements are necessary.

Meanwhile, in both cases the lifetimes for both NV centers in nanodiamonds are found higher than 10 ns. By selectively filtering the “early” photons coming from the cell autofluorescence we managed to collect only the photons coming from the NV centers and improve by a factor of 10 the image contrast.

Appendix C

Optical elements for doughnut-shaped intensity pattern in the microscope objective focal plane

C.1 Liquid Crystal Polarization Converter

The Liquid Crystal Polarization Converter is produced by *ArcOptix* (Switzerland)¹. It consists of nematic liquid crystal (LC) molecules.

Each molecule is characterized by a twist angle (the angle between the orientation of the molecules at the entrance and at the exit plates) and the LC converter device (or θ -cell) has a cell axis.

A linearly polarized beam incident on the entrance plate, with electric field vector parallel or perpendicular to the cell axis, experiences a rotation of its linear incident polarization direction by the LC molecule twist angle [170]. Azimuthally polarized light is achieved for light incident with a linear polarization parallel to the cell axis, while radially polarized light is achieved for light incident perpendicular to the cell axis.

Apart from the radial Liquid Crystal based polarization converter, the system includes a polarization rotator and a variable phase shifter(Figure C.2).

The variable phase shifter is a transparent cell providing a tunable phase delay between the two half planes (top and down on Figure C.1a, separated by the defect line). This delay compensates the phase step of π , introduced by the LC molecules between the two parts of the θ -cell, due to the fact that the LC molecules have an opposite rotation on both sides of the defect.

The phase shifter contains liquid crystals giving a maximum retardation optical path difference of 1260 nm at room temperature. If a voltage is applied to the phase shifter LC, the retardation can be adjusted continuously. One half of the cell is equipped with an electrode (black line in Figure C.2a) that permits to change the twisting angle of the LC molecules.

¹look at <http://www.arcoptix.com/Application%20Notes%20for%20The%20Polarization%20Converter.pdf> for a detailed description of the device.

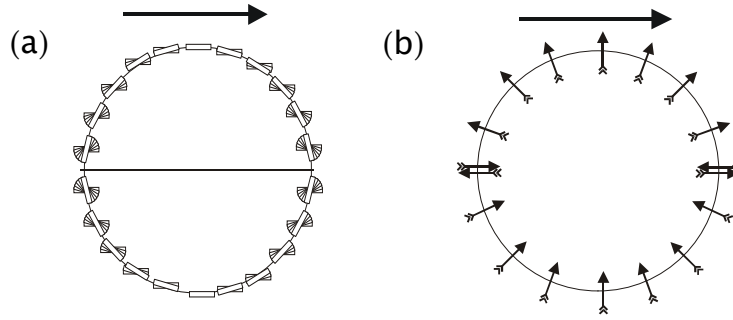


Figure C.1: (a) Orientation of the LC molecules in a θ -cell viewed from top, the line in the center represents a defect line (parallel to the cell axis) which is present because of difference in the upper and lower parts. The arrow represents the entrance polarization. (b) Radially polarized light at the output of the cell, when the incident beam is linearly polarized along the cell axis (arrow on top of the graph).

The polarization rotator is a twisted nematic cell capable to rotate the entrance polarization by 90° , permitting to switch between azimuthal and radial polarization.

The θ -cell can be rotated and translated with respect to the polarization rotator and the phase shifter with the rotation lever and the $x - y$ adjustment screws (Figure C.2b). Moreover, to get the radial polarization required for the Ground State Depletion beam, an AC power supply producing a square wave signal with change of polarity has to be provided to the polarization rotator and the phase shifter. For the twisted nematic cell (polarization rotator), a bias of 5 V rms is applied at 1 kHz, providing at the output of the whole system a radial polarization distribution. If the bias on the polarization rotator is switched off, the output yields an azimuthal polarization. For the phase shifter, the bias allows to adjust the phase shift between the upper and lower part. For 1064 nm light, the bias required to compensate the π phase step is about 2.1 V rms.

C.2 Helical $0-2\pi$ phase mask

A phase mask that introduces a helical phase retardation ($0-2\pi$) to the incident creates a doughnut-shaped spot in the focus plane of the microscope objective.

Such a helix phase plate $0-2\pi$ was produced by Silios Technologies (France) and was tested in our laboratory.

The substrate is fused silica, on which is etched a multilevel phase profile. In our case the phase profile is divided in 8 phase regions, of $\pi/4$ phase difference each (Figure C.3).

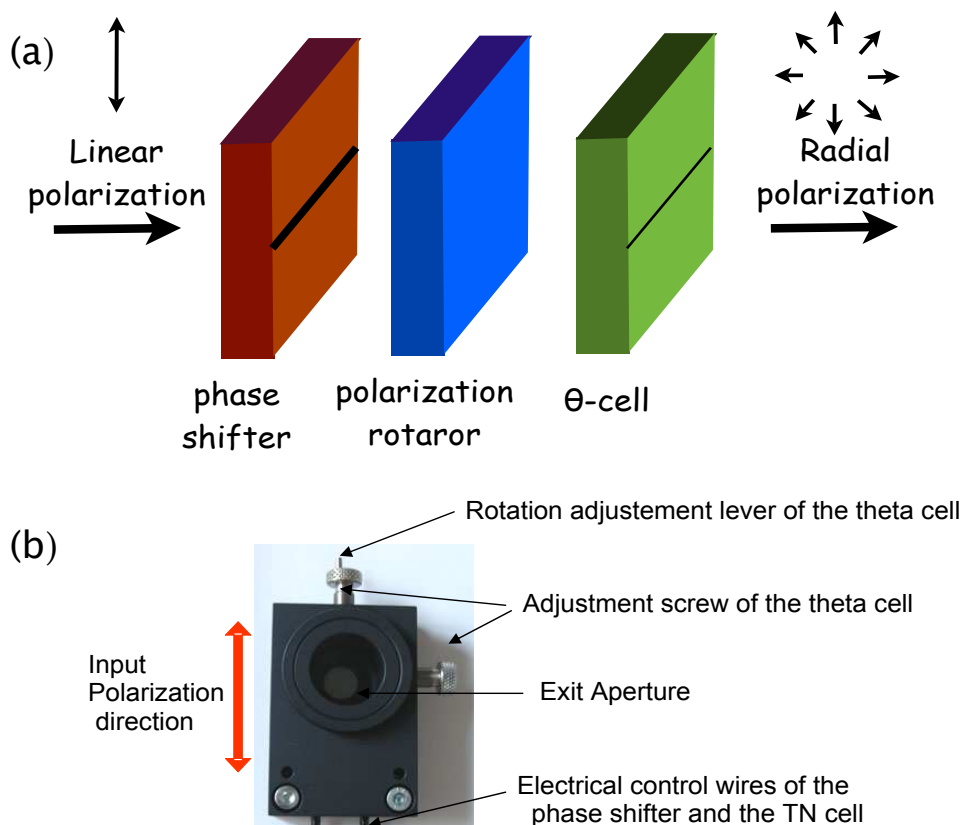


Figure C.2: (a) Liquid crystal alignment in the polarization converter for the ArcOptix cell. The line in the center represents a defect line present because of different twist direction of the upper and lower part. The arrow represents the entrance linear polarization orientation. (b) Picture of the whole ArcOptix cell device, the aperture is 10 mm.

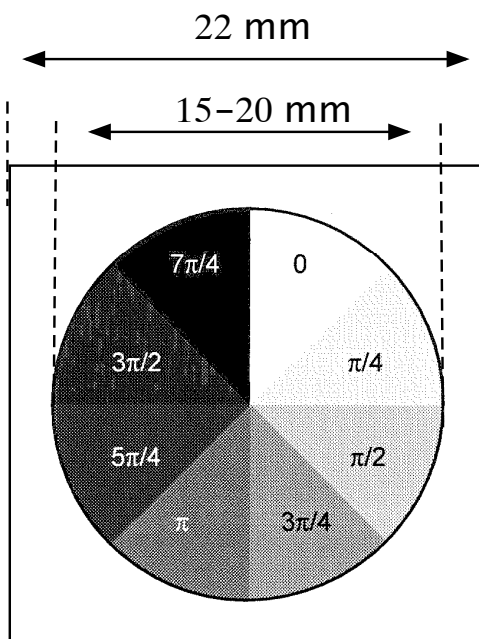


Figure C.3: Helical $0-2\pi$ phase mask.

Appendix D

Collection efficiency and transmission spectra of optical elements

D.1 Collection efficiency

For NV centers in bulk diamond the collection efficiency of the photoluminescence signal is limited by the high refractive index of diamond ($n = 2.4$). Most of the emitted light is trapped by total reflection on the diamond-air interface in the diamond lattice. However, to avoid this difficulty, NV centers embedded in diamond particles, of sub-wavelength size, are used. The collection efficiency is limited by the following factors:

- The collection efficiency of the microscope objective.

For an objective with numerical aperture NA , we have: $NA = n \sin\theta$, where θ the collection angle and n the refractive index of the medium. The refractive index between the sample and the objective is the same to the one of the medium (PNDs are embedded in polymer thin films of index ~ 1.3). For $NA = 1.4$ and $\theta_{\max} = 68^\circ$, we calculate that the collection efficiency of the objective is equal to $\eta_c = 0.43$ [32].

- The transmission of the microscope objective.

For NV centers and about 650 nm fluorescence light, the transmission of the Nikon objective is $\sim 85\%$ ($\eta_o = 0.85$) (Figure D.1b).

- The transmission of the dichroic mirror.

For 532 nm excitation light, the dichroic mirror used is Q565LP (Chroma) with transmission for the emitted fluorescence signal of the NV center of $\sim 90\%$, so $\eta_d = 0.9$. For excitation with 488 nm we use a 530DCLP or z488RDX (Chroma) dichroic mirror, with similar transmission values.

- The transmission through the various optical elements.

The use of lens and filters decreases the signal intensity recorded on the photodiodes. Here, the efficiency is a parameter difficult to calculate. It depends on the number of optical elements used and their quality. For a high precision, one has to measure their

transmission, a measurement not done. Additionally, the objective introduces some spherical aberrations, which lead to a not perfect focalization of light on the confocal pinhole.

- The sensitivity of the avalanche photodiodes.

The efficiency of the silicon avalanche photodiodes working on a single photon counting mode, for the spectral region of the NV center, is in the range of $\eta_{\text{APD}} = 0.60 - 0.65$ (Figure D.1c).

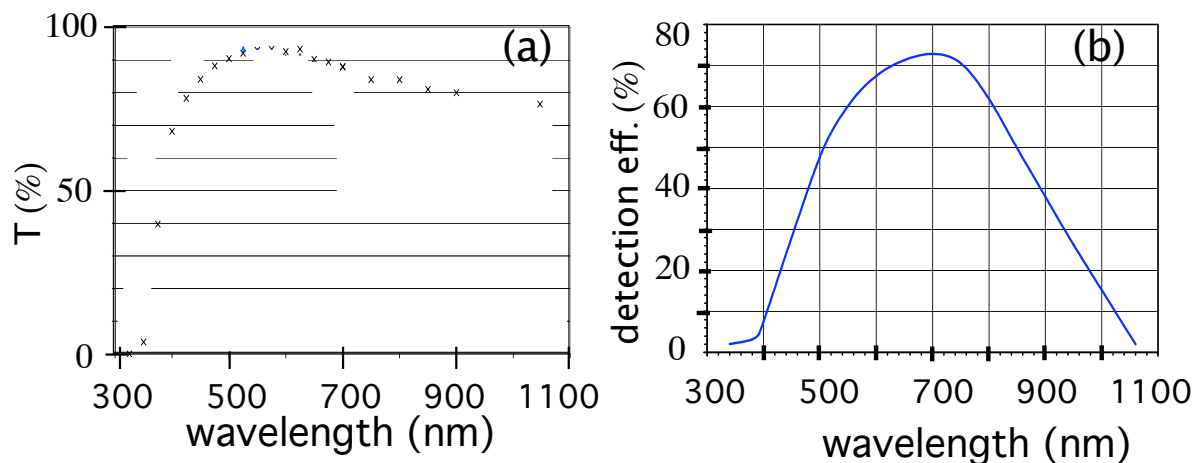


Figure D.1: Experimental response of various optical components. (a) Wavelength dependence of the microscope objective (Nikon Apo) transmission. (b) Detection efficiency of the silicon avalanche photodiode (SPCM-AQR14, Perkin-Elmer).

D.2 Transmission spectra of optical elements

Here we present the transmission spectra of the various optical elements used in this work.

D.2.1 Dichroic mirrors

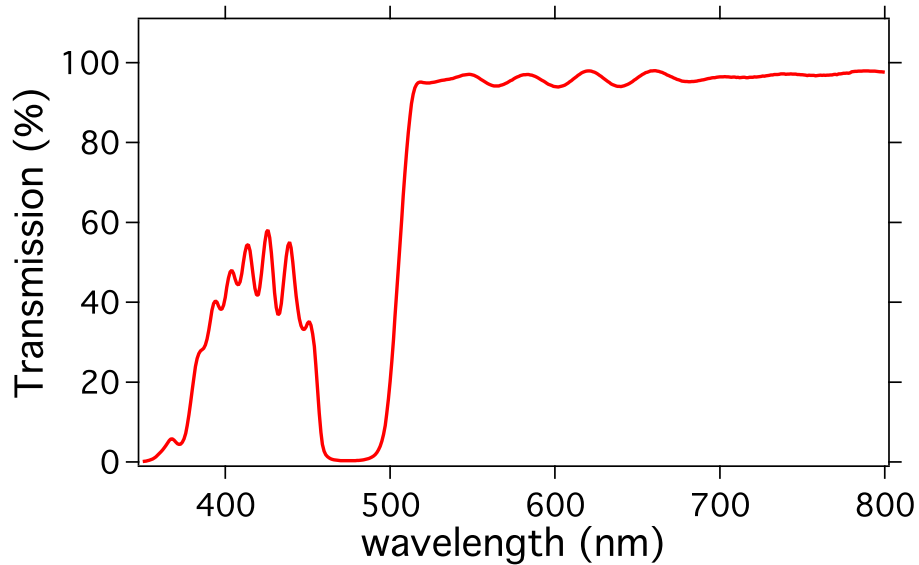


Figure D.2: Dichroic mirror z488RDX (Chroma, USA).

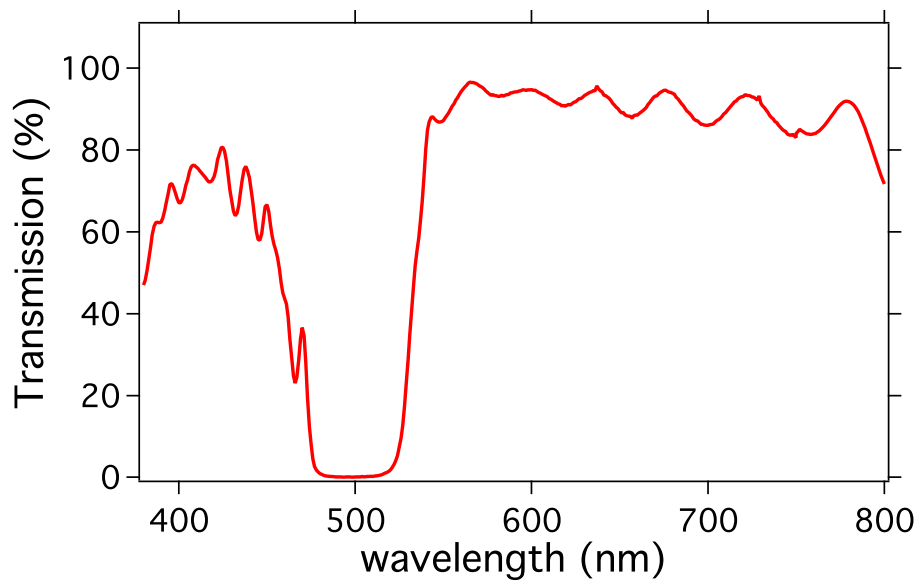


Figure D.3: Dichroic mirror 530DCLP (Chroma).

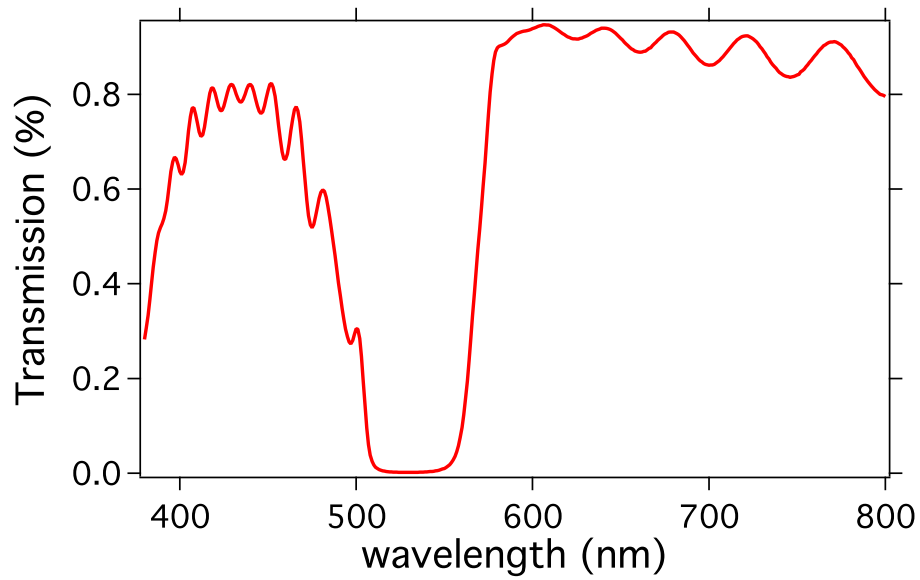


Figure D.4: Dichroic mirror Q565LP (Chroma).

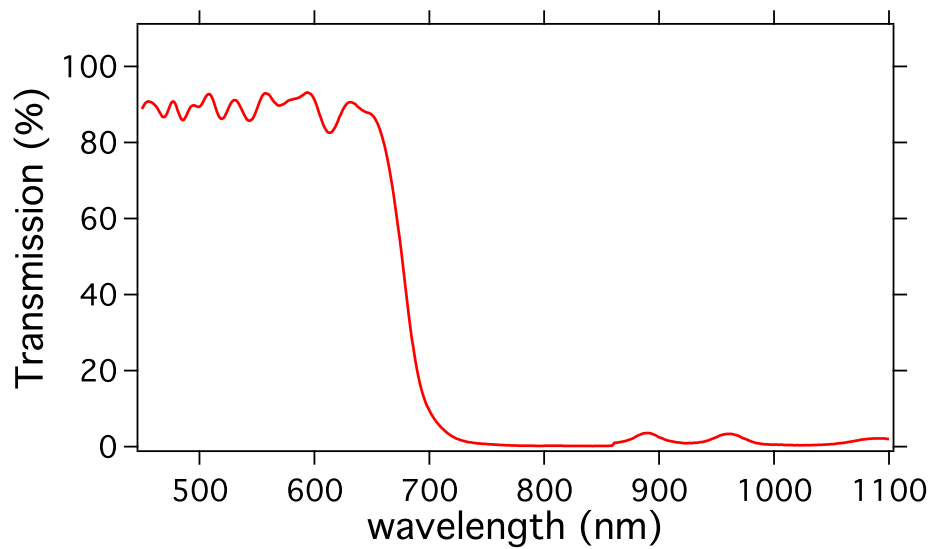


Figure D.5: Dichroic mirror 700DCSX (Chroma).

D.2.2 Long-pass filters

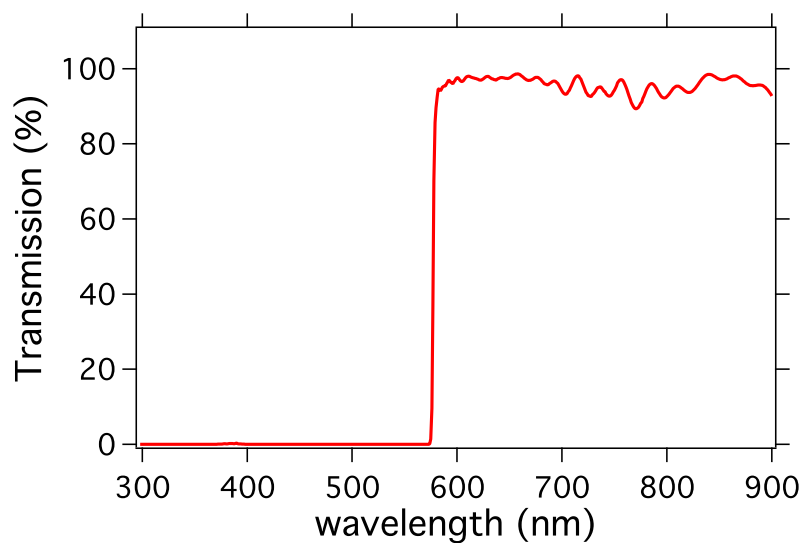


Figure D.6: Long-pass 580EFLP filter (Omega Optical Inc., USA).

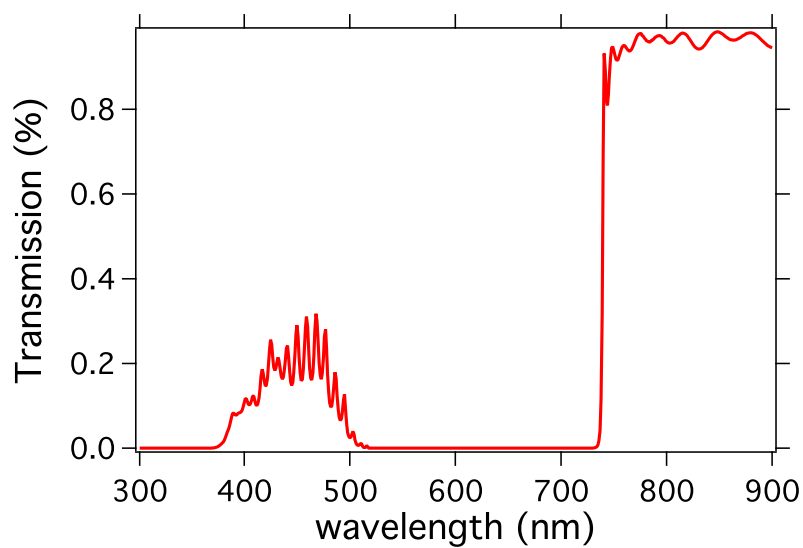


Figure D.7: Long-pass HQ740 filter (Chroma). Used to record only the photoluminescence signal coming from the NV^- center.

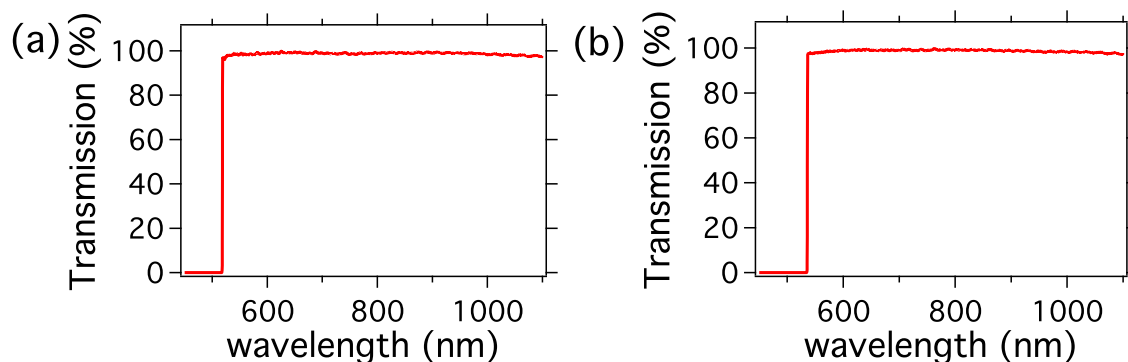


Figure D.8: (a) Long-pass filter RazorEdgeLP02-514RU-25 (Semrock, USA), with 97% transmission in the range of 521-1160 nm. Used to filter the 488 nm excitation laser. (b) Long-pass RazorEdgeLP03-532RU-25 (Semrock), with 97% transmission in the range of 538-1200 nm. Used to filter the 532 nm excitation laser.

D.2.3 Band-pass filters

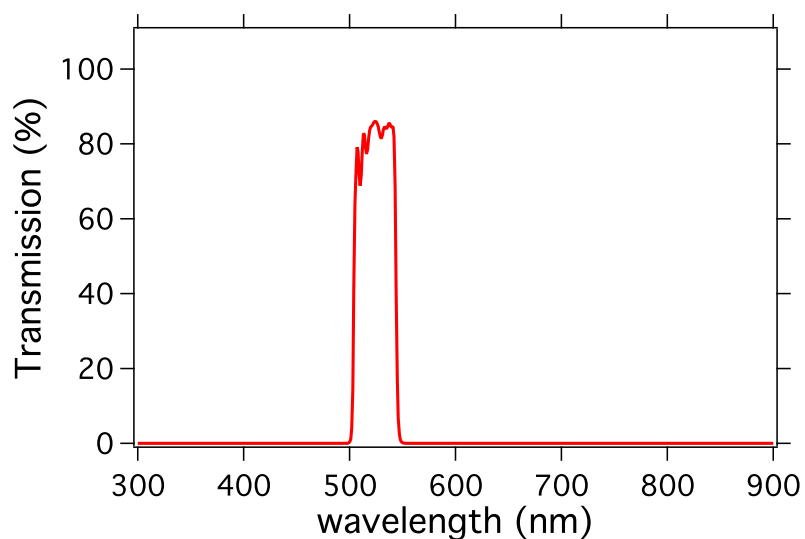


Figure D.9: Band-pass 525/40 filter (Chroma). Used to record only the FITC fluorescence signal.

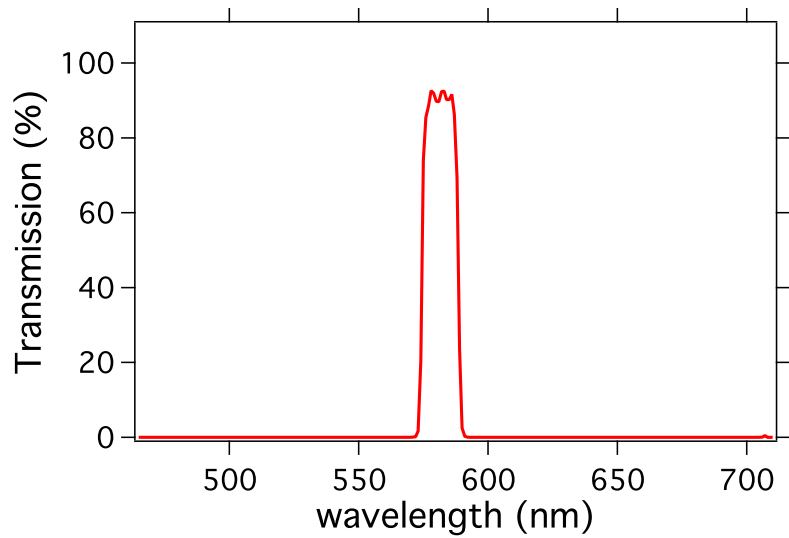


Figure D.10: Band-pass 580/10 filter (Chroma). Used to record only the NV⁰ photoluminescence signal.

D.2.4 Short-pass filters

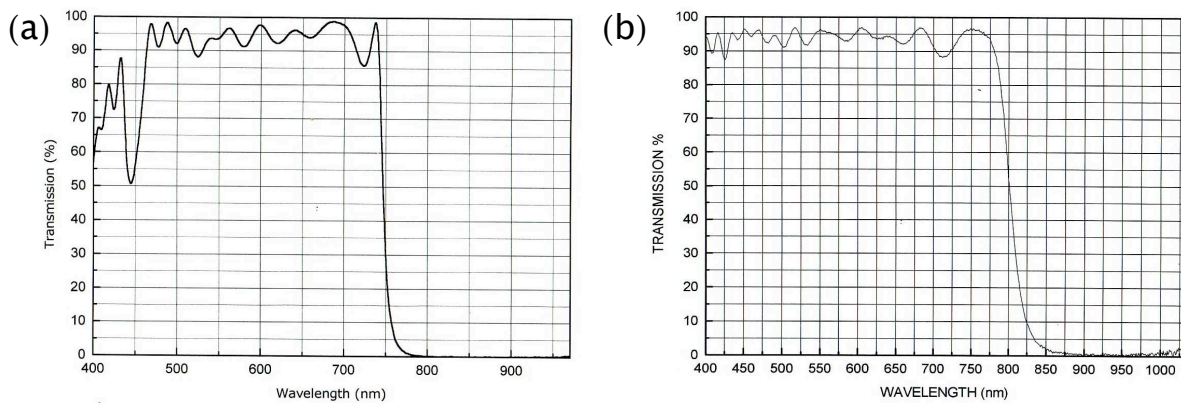


Figure D.11: Short-pass filter (a) 03SWP416 and (b) 03SWP418 (Melles Griot). Used to filter the cross-talk signal of the APDs and/or to filter the 1064 nm excitation laser of the 2-photon excitation experiments.

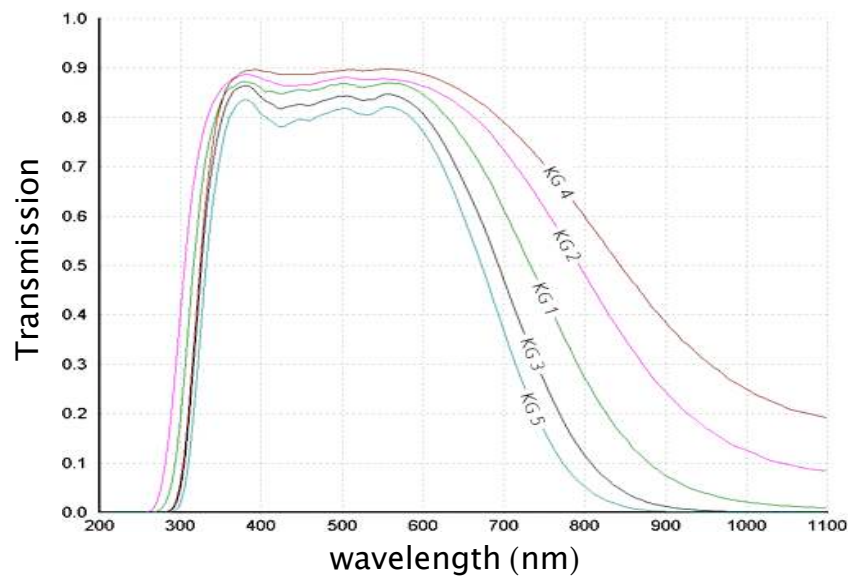


Figure D.12: Short-pass KG filters.

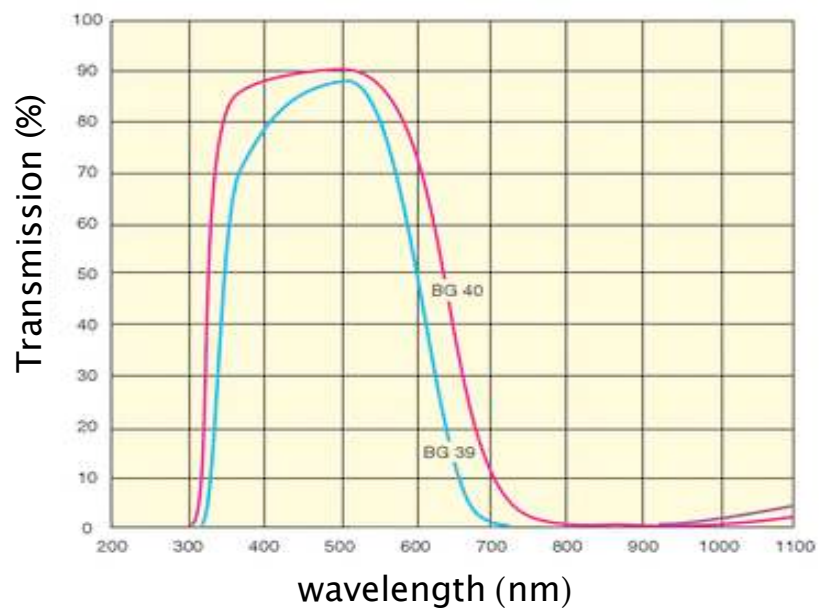


Figure D.13: Short-pass BG filters.

Bibliography

- [1] J.R. Lakowicz. *Principles of Fluorescence Spectroscopy*. Kluwer Academic, 1999.
- [2] W.T. Mason. *Fluorescent and luminescent probes for biological activity*. Academic Press, London, 2nd edn edition, 1999.
- [3] A.H. Coons, H.J. Creech, and R.N. Jones. Immunological properties of an antibody containing a fluorescent group. *Proc Soc Exp Biol Med*, 47:2000, 1941.
- [4] A.H. Coons and M.H. Kaplan. Localization of antigen in tissue cells: Improvements in a method for the detection of antigen by means of fluorescent antibody. *J Exp Medicine*, 91:1–13, 1950.
- [5] A.P. Alivisatos. The use of nanocrystals in biological detection. *Nature Biotech.*, 22:47–52, 2004.
- [6] Shimomura O., F. Johnson, and Y. Saiga. Extraction, purification and properties of aequorin, a bioluminescent protein from the luminous hydromedusan, aequorea. *J Cell Comp Physiol*, 59:223–239, 1962.
- [7] D. Prasher, V. Eckenrode, W. Ward, F. Prendergast, and M. Cormier. Primary structure of the aequorea victoria green-fluorescent protein. *Gene*, 111:229–233, 1992.
- [8] M. Ormö, A. Cubitt, K. Kallio, L. Gross, R. Tsien, and S. Remington. Crystal structure of the aequorea victoria green fluorescent protein. *Science*, 273(5280):1392–1395, 1996.
- [9] J. Zhang, R.E. Campbell, A.Y. Ting, and R.Y. Tsien. Creating new fluorescent probes for cell biology. *Nat. Reviews*, 3:906–918, 2002.
- [10] N.C. Shaner, P.A. Steinbach, and R.Y. Tsien. A guide to choosing fluorescent proteins. *Nat. Methods*, 2:905–909, 2005.
- [11] U. Resch-Genger, M. Grabolle, S. Cavaliere-Jaricot, R. Nitschke, and T. Nann. Quantum dots versus organic dyes as fluorescent labels. *Nat. Methods*, 9:763–775, 2008.
- [12] X. Michalet, F. Pinaud, L. Bentolila, J. Tsay, S. Doose, J.J. Li, G. Sundaresan, A.M. Wu, S. Gambhir, and S. Weiss. Quantum Dots for Live Cells, in Vivo Imaging, and Diagnostics. *Science*, 307:538–544, 2005.
- [13] H. Hanzawa, Y. Nisida, and T. Kato. Measurement of decay time for the NV centre in Ib diamond with a picosecond laser pulse. *Diamond Relat. Mater.*, 6:1595–1598, 1997.
- [14] T.-S. Wee, Y.-K. Tzeng, C.-C. Han, H.-C. Chang, W. Fann, J.-H. Hsu, K.-M. Chen, and Y.-C. Yu. Two-photon Excited Fluorescence of Nitrogen-Vacancy Centers in Proton-Irradiated Type Ib Diamond. *J. Phys. Chem. A*, 111:9379–9386, 2007.
- [15] G. Davies. *Properties and growth of diamond*. INSPEC, The Institution of Electrical Engineers, EMIS Data Review Series, London, 1994.
- [16] Y. Sonnefraud, A. CuChe, O. Faklaris, J.-P. Boudou, T. Sauvage, J.-F. Roch, F. Treussart, and S. Huant. Diamond nanocrystals hosting single NV color centers sorted by photon-correlation near-field microscopy. *Opt. Lett.*, 33:611, 2008.

- [17] J. Tisler, G. Balasubramanian, B. Naydenov, R. Kolesov, B. Grotz, R. Reuter, J.-P. Boudou, P. A. Curmi, M. Sennour, A. Thorel, M. Boersch, K. Aulenbacher, R. Erdmann, P.R. Hemmer, F. Jelezko, and J. Wrachtrup. Fluorescence and Spin Properties of Defects in Single Digit Nanodiamonds. *ACS Nano*, 3:1959–1965, 2009.
- [18] J.H. Warner, A. Hoshino, K. Yamamoto, and R.D. Tilley. Water-soluble photoluminescent silicon quantum dots. *Angew. Chem. Int. Ed.*, 44:4550 – 4554, 2005.
- [19] H. Ow, D. Larson, M. Srivastava, B. Baird, W. Webb, and U. Wiesner. Bright and Stable Core-Shell Fluorescent Silica Nanoparticles. *Nano Letters*, 5:113–117, 2005.
- [20] E. Beaupaire, V. Buissette, M.-P. Sauviat, D. Giaume, K. Lahlil, A. Mercuri, D. Casanova, A. Huignard, J.-L. Martin, T. Gacoin, J.-P. Boilot, and A. Alexandrou. Functionalized Fluorescent Oxide Nanoparticles: Artificial Toxins for Sodium Channel Targeting and Imaging at the Single-Molecule Level. *Nano Lett.*, 4:2079–2083, 2004.
- [21] A.P. Alivisatos. Semiconductor Clusters, Nanocrystals, and Quantum Dots. *Science*, 271(5251):933 – 937, 1996.
- [22] W.C.W. Chan and S. Nie. Quantum Dot Bioconjugates for Ultrasensitive Nonisotopic Detection. *Science*, 281:2016–2018, 1998.
- [23] M. Bruchez, M. Moronne, P. Gin, S. Weiss, and A.P. Alivisatos. Semiconductor nanocrystals as fluorescent biological labels. *Science*, 281:2013 – 2016, 1998.
- [24] D. Larson, W.R. Zipfel, R.M. Williams, S/W/ Clark, M.P. Bruchez, F.W. Wise, and W.W. Webb. Water-soluble quantum dots for multiphoton fluorescence imaging in vivo. *Science*, 300:1434–1436, 2003.
- [25] M. Nirmal, B. Dabbousi, M.G. Bawendi, J.J. Macklin, J.K. Trautman, T.D. Harris, and L.E. Brus. Fluorescence intermittency in single cadmium selenide nanocrystal. *Nature*, 383:802–804, 1996.
- [26] B. Mahler, P. Spinicelli, S. Buil, X. Quelin, J.P. Hermier, and B. Dubertret. Towards non-blinking colloidal quantum dots. *Nature Nanotech.*, 7:659–664, 2008.
- [27] Y. Chen, J. Vela, H. Htoon, J.L. Casson, D.J. Werder, D.A. Bussian, V.I. Klimov, and J.A. Hollingsworth. Giant multishell cdse nanocrystal quantum dots in suppressed blinking. *J. Am. Chem. Soc.*, 130:5026–5027, 2008.
- [28] X. Wang, X. Ren, K. Kahen, M.A. Hahn, M. Rajeswaran, S. Maccagnano-Zacher, J. Silcox, G.E. Cragg, A.L. Efros, and T.D. Krauss. Non-blinking semiconductor nanocrystals. *Nature*, 459(7247):686–689, 06 2009.
- [29] C. Kirchner, T. Liedl, S. Kudera, T. Pellegrino, A. Javier, H. Gaub, S. Stoelze, N. Fertig, and W.J. Parak. Cytotoxicity of Colloidal CdSe and CdSe/ZnS Nanoparticles. *Nano Lett.*, 5:331, 2005.
- [30] N. Lewinski, V. Colvin, and R. Drezek. Cytotoxicity of Nanoparticles. *Small*, 4:26 – 49, 2008.
- [31] A.M. Zaitsev. *Optical Properties of Diamond. A Data Handbook*. Springer-Verlag, Berlin, 2001.
- [32] A. Beveratos. *Réalisation expérimentale d’une source de photons uniques par fluorescence de centres colorés du diamant; application à la cryptographie quantique*. PhD thesis, Université Paris 11 (Orsay), 2002.
- [33] A. Gruber, A. Dräbenstedt, C. Tietz, L. Fleury, J. Wrachtrup, and C. Von Borczyskowsky. Scanning confocal optical microscopy and magnetic resonance on single defect centers. *Science*, 276:2012, 1997.
- [34] A. Beveratos, R. Brouri, T. Gacoin, A. Villing, J.-P. Poizat, and P. Grangier. Single photon quantum cryptography. *Phys. Rev. Lett.*, 89:187901, 2002.
- [35] N. R. S. Reddy, N. B. Manson, and E. R. Krausz. Two-laser spectral hole burning in a colour centre in diamond. *J. Luminesc.*, 38:46–47, 1987.

- [36] P. Neumann, R. Kolesov, V. Jacques, J. Beck, J. Tisler, A. Batalov, L. Rogers, N.B. Manson, G. Balasubramanian, F. Jelezko, and J. Wrachtrup. Excited-state spectroscopy of single NV defects in diamond using optically detected magnetic resonance. *New J. Phys.*, 11(1):013017, 2009.
- [37] F. Jelezko, T. Gaebel, I. Popa, M. Dohman, A. Gruber, and J. Wrachtrup. Observation of coherent oscillations of a single nuclear spin and realization of a two-qubit conditional quantum gate. *Phys. Rev. Lett.*, 93:130501, 2004.
- [38] T. Gaebel, M. Domhan, I. Popa, C. Wittmann, P. Neumann, F. Jelezko, J.R. Rabeau, N. Stavrias, A.D. Greentree, S. Prawer, J. Meijer, J. Twamley, P.R. Hemmer, and J. Wrachtrup. Room-temperature coherent coupling of single spins in diamond. *Nat. Physics*, 2:408–413, 2006.
- [39] G. Balasubramanian, I.Y. Chan, R. Kolesov, M. Al-Hmoud, J. Tisler, C. Shin, C. Kim, A. Wojcik, P.R. Hemmer, A. Krueger, T. Hanke, A. Leitenstorfer, R. Bratschitsch, F. Jelezko, and J. Wrachtrup. Nanoscale imaging magnetometry with diamond spins under ambient conditions. *Nature*, 455:648–651, 2008.
- [40] S. Schietinger, M. Barth, T. Aichele, and O. Benson. Plasmon-enhanced single photon emission from a nanoassembled metal-diamond hybrid structure at room temperature. *Nano Lett.*, 9:1694–1698, 2009.
- [41] A. Cuche, A. Drezet, Y. Sonnefraud, O. Faklaris, F. Treussart, J.F. Roch, and S. Huant. Near field optical microscopy with a nanodiamond-based single-photon tip. *Optics Express*, 17:19969, 2009.
- [42] R. Koselov, B. Grotz, G. Balasubramanian, R.J. Stohr, A.A.L. Nicolet, R.P. Hemmer, F. Jelezko, and J. Wrachtrup. Wave-particle duality of single surface plasmon polaritons. *Nature Phys.*, 5:470–474, 2009.
- [43] C.L. Degen. Scanning magnetic field microscope with a diamond single-spin sensor. *Appl. Phys. Lett.*, 92:243111, 2008.
- [44] J.R. Maze, P.L. Stanwix, J.S. Hodges, S. Hong, J.M. Taylor, P. Cappellaro, L. Jiang, M.V. Gurudev Dutt, E. Togan, A.S. Zibrov, A. Yacoby, R.L. Walsworth, and M.D. Lukin. Nanoscale magnetic sensing with an individual electronic spin in diamond. *Nature*, 455:644–647, 2008.
- [45] Y. Mita. Change of absorption spectra in type-Ib diamond with heavy neutron irradiation. *Phys. Rev. B*, 53:11360, 1996.
- [46] F. Treussart, V. Jacques, E. Wu, T. Gacoin, P. Grangier, and J.-F. Roch. Photoluminescence of single colour defects in 50 nm diamond nanocrystals. *Physica B*, 376–377:926–929, 2006.
- [47] Y.-R. Chang, H.-Y. Lee, K. Chen, C.-C. Chang, D.-S. Tsai, C.-C. Fu, T.-S. Lim, Y.-K. Tzeng, C.-Y. Fanf, C.-C. Han, H.-C. Chang, and W. Fann. Mass production and dynamic imaging of fluorescent nanodiamonds. *Nature Nanotech.*, 3:284–288, 2008.
- [48] O. Faklaris, D. Garrot, V. Joshi, F. Druon, J.P. Boudou, T. Sauvage, P. Georges, P.A. Curmi, and F. Treussart. Detection of single photoluminescent diamond nanoparticles in cells and study of their internalization pathway. *Small*, 4:2236–2239, 2008.
- [49] Y.T. Lim, S. Kim, and A. Nakayama. Selection of quantum dot wavelengths for biomedical assays and imaging. *Mol. Imaging*, 2:50–64, 2003.
- [50] S.-J. Yu, M.-W. Kang, H.-C. Chang, K.-M. Chen, and Y.-C. Yu. Bright Fluorescent Nanodiamonds: No Photobleaching and Low Cytotoxicity. *J. Am. Chem. Soc.*, 127:17604–17605, 2005.
- [51] C.-C. Fu, H.-Y. Lee, K. Chen, T.-S. Lim, H.-Y. Wu, P.-K. Lin, P.-K. Wei, P.-H. Tsao, H.-C. Chang, and W. Fann. Characterization and applications of single fluorescent nanodiamonds as cellular biomarkers. *Proc. Nat. Acad. Sc. USA*, 104:727, 2007.
- [52] F. Neugart, A. Zappe, F. Jelezko, C. Tietz, J.-P. Boudou, A. Krueger, and J. Wrachtrup. Dynamics of Diamond Nanoparticles in Solution and Cells. *Nano Lett.*, 7:3588–3591, 2007.

- [53] O. Faklaris, Y. Sonnefraud, A. Cuche, T. Sauvage, V. Joshi, J. P. Boudou, P. A. Curmi, J. F. Roch, S. Huant, and F. Treussart. Diamond nanoparticles as photoluminescent nanoprobos. *Ann. de Physique*, 32(2-3):155–158, 2007.
- [54] K.-K. Liu, C.-C. Wang, C.-L. Cheng, and J.-I. Chao. Endocytic carboxylated nanodiamond for the labeling and tracking of cell division and differentiation in cancer and stem cells. *Biomaterials*, 30:4249–4259, 2009.
- [55] M. Mkandawire, A. Pohl, T. Gubarevich, V. Lapina, D. Appelhans, G. Rödel, W. Pompe, J. Schreiber, and J. Opitz. Selective targeting of green fluorescent nanodiamond conjugates to mitochondria in HeLa cells. *J. Biophot.*, 2:596–606, 2009.
- [56] Y. Colpin, A. Swan, A.V. Zvyagin, and T. Plakhotnik. Imaging and sizing of diamond nanoparticles. *Opt. Lett.*, 31:625, 2006.
- [57] B.-R. Smith, M. Niebert, T. Plakhotnik, and A.-V. Zvyagin. Transfection and imaging of diamond nanocrystals as scattering optical labels. *J. Luminesc.*, 127:260, 2007.
- [58] S. Praver, K.W. Nugent, J.D.N. Jamieson, O. Orwa, L.A. Bursill, and J.L. Peng. The Raman spectrum of nanocrystalline diamond. *Chem. Phys. Lett.*, 332:93–97, 2000.
- [59] P.-H. Chung, E. Perevedentseva, and C.-L. Cheng. The particle size-dependent photoluminescence of nanodiamonds. *Surface Science*, 601:3866–3870, 2007.
- [60] J.-I. Chao, E. Perevedentseva, P.-H. Chung, K.-K. Liu, C.-Y. Cheng, C.-C. Chang, and C.-L. Cheng. Nanometer-sized diamond particle as a probe for biolabeling. *Biophys. J.*, 93:2199, 2007.
- [61] A. Krüger. Diamond Nanoparticles: Jewels for Chemistry and Physics. *Adv. Mater.*, 20:2445–2449, 2008.
- [62] C. E. Nebel, B. Rezek, D. Shin, H. Uetsuka, and N. Yang. Diamond for bio-sensor applications. *J. Phys. D: Appl. Phys.*, 40:6443–6466, 2007.
- [63] D. Ballutaud, F. Jomard, B. Theys, C. Mer, D. Tromson, and P. Bergonzo. Hydrogen diffusion and stability in polycrystalline CVD undoped diamond. *Diamond Relat. Mater.*, 10:405–410, 2001.
- [64] K.B. Holt, B. Ziegler, D.J. Caruana, J. Zang, E.J. Millan-Barrios, J. Hu, and J.S. Foord. Redox properties of undoped 5 nm diamond nanoparticles. *Phys. Chem. Chem. Phys.*, 10:303–310, 2008.
- [65] Y. Gogotsi. *Nanomaterials Handbook*. Taylor and Francis Group, 2006.
- [66] A. Krüger, Y. Liang, G. Jarre, and J. Stegk. Surface functionalisation of detonation diamond suitable for biological applications. *J. Mater. Chem.*, 16:2322–2328, 2006.
- [67] L.C. Huang and H.C. Chang. Adsorption and immobilization of cytochrome c on nanodiamonds. *Langmuir*, 20(14):5879–5884, 2004.
- [68] P.-H. Chung, E. Perevedentseva, J.-S. Tu, C.-C. Chang, and C.-L. Cheng. Spectroscopic study of bio-functionalized nanodiamonds. *Diamond Relat. Mater.*, 15:622, 2005.
- [69] S. Osswald, G. Yushin, V. Mochalin, S.O. Kucheyev, and Y. Gogotsi. Control of sp²/sp³ carbon ratio and surface chemistry of nanodiamond powders by selective oxidation in air. *J. Am. Chem. Soc.*, 128:11635–11642, 2006.
- [70] S. Vial, C. Mansuy, S. Sagan, T. Irinopoulou, F. Burlina, J.P. Boudou, G. Chassaing, and S. Lavielle. Peptide-grafted nanodiamonds: preparation, cytotoxicity and uptake in cells. *Chem-BioChem*, 9:2113–2119, 2008.
- [71] T.-T. Nguyen, H.-C. Chang, and V.-W. Wu. Adsorption and hydrolytic activity of lysozyme on diamond nanocrystallites. *Diamond Relat. Mater.*, 16:872, 2007.
- [72] A. Krüger, J. Stegk, Y. Liang, L. Lu, and G. Jarre. Functionalised nanodiamond: Biotinylation of detonation diamond. *Langmuir*, 24:4200–4204, 2008.

- [73] A. Krüger. Diamond nanoparticles for biological applications. *J. Chem. Eur.*, 14:1382, 2008.
- [74] H. Huang, E. Pierstorff, E. Osawa, and D. Ho. Active Nanodiamond Hydrogels for Chemotherapeutic Delivery. *Nano Lett.*, 7:3305–3314, 2007.
- [75] M. Chen, E.K. Pierstorff, R. Lam, S.-Y. Li, H. Huang, E. Osawa, and D. Ho. Nanodiamond-Mediated Delivery of Water-Insoluble Therapeutics. *ACS Nano*, 3:2016–2022, 2009.
- [76] A. M. Schrand, H. Huang, C. Carlson, J. Schlager, E. Osawa, S.M. Hussain, and L. Dai. Are diamond nanoparticles cytotoxic? *J. Phys. Chem. B*, 111(1):2–7, 2007.
- [77] ASTM International. Terminology for Nanotechnology. *ASTM E*, pages 2456–06, 2006.
- [78] G. Jia, H. Wang, L. Yan, X. Wang, R. Pei, T. Yan, Y. Zhao, and X. Guo. Cytotoxicity of carbon nanomaterials: Single-wall nanotube, multi-wall nanotube, and fullerenes. *Environ. Sci. Technol.*, 39:1378, 2005.
- [79] A.M. Schrand, L. Dai, J.J. Schlager, S.M. Hussain, and E. Osawa. Differential biocompatibility of carbon nanotubes and nanodiamonds. *Diamond Relat. Mater.*, 16:2118–2123, 2007.
- [80] K.K. Liu, C.L. Cheng, and C.C. Chang. Biocompatible and detectable carboxylated nanodiamond on human cell. *Nanotechnology*, 18:325102, 2007.
- [81] M. Nunez-Regueiro, P. Monceau, and J.L. Hodeau. Crushing C60 to diamond at room temperature. *Nature*, 355:237–239, 1992.
- [82] L.M. Cao, C.X. Gao, H.P. Sun, G.T. Zou, Z. Zhang, X.Y. Zhang, M. He, M. Zhang, Y.C. Li, J. Zhang, D.Y. Dai, L.L. Sun, and W.K. Wang. Synthesis of diamond from carbon nanotubes under high pressure and high temperature. *Carbon*, 39:311, 2001.
- [83] F. Banhart and P.M. Ajayan. Carbon onion as nanoscopic pressure cell for diamond formation. *Nature*, 382:433, 1996.
- [84] P. Wesolowski, Y. Lyutovich, F. Banhart, H.D. Carstanjen, and H. Kronmuller. Formation of diamond in carbon onions under MeV ion irradiation. *Appl. Phys. Lett.*, 71:1948, 1997.
- [85] D.V. Fedoseev, V.L. Bukhovets, I.G. Varshavskaya, A.V. Lavrentev, and B.V. Derjaguin. Transition of graphite into diamond in a solid state under the atmospheric pressure. *Carbon*, 21:237, 1983.
- [86] Wei. B., J. Zhang, J. Liang, and D. Wu. The mechanism of phase transformation from carbon nanotube to diamond. *Carbon*, 36:997, 1998.
- [87] S. Hu, F. Tian, P. Bai, S. Cao, J. Sun, and J. Yang. Synthesis and luminescence of nanodiamonds from carbon black. *Mater. Sc. and Engin. B*, 157:11–14, 2009.
- [88] B. Dischler and C. Wild. *Low pressure synthetic diamond: manufacturing and applications*. Springer, 1998.
- [89] F.C. Waldermann, P. Olivero, J. Nunn, K. Surmacz, Z.Y. Wang, D. Jaksch, R.A. Taylor, I.A. Walmsley, M. Draganski, Reichart P., A.D. Greentree, D.N. Jamieson, and S. Praver. Creating diamond color centers for quantum optical applications. *Diamond Rel. Mat.*, 16:1887 – 1895, 2007.
- [90] J.P. Boudou, P.A. Curmi, F. Jelezko, J. Wrachtrup, P. Aubert, M. Sennour, G. Balasubramanian, R. Reuter, A. Thorel, and E. Gaffet. High yield fabrication of fluorescent nanodiamonds. *Nanotechnology*, 20:235602, 2009.
- [91] S.C. Lawson, D. Fisher, D. Hunt, and M. Newton. On the existence of positively charged single-substitutional nitrogen in diamond. *J. Phys. Condens. Mater.*, 10:6171 6180, 1998.
- [92] N.B. Iakoubovskii and G.J. Adrianenssens. Trapping of vacancies by defects in diamond. *J. Phys. C*, 13:6015–6018, 2001.

- [93] L.-C. L. Huang and H.-C. Chang. Adsorption and immobilization of cytochrome c on nanodiamonds. *Langmuir*, 20:5879 – 5884, 2004.
- [94] D. Maurice and H Courtney. The physics of mechanical alloying: a first report. *Metall. Mater. Trans. A*, 21:289–303, 1990.
- [95] P.P. Chattopadhyay, I. Manna, S. Talapatra, and S.K. Pabi. A mathematical analysis of milling mechanics in a planetary ball mill. *Mater. Chem. Phys.*, 68:85–94, 2001.
- [96] Y.G. Gogotsi, A. Kailer, and K.G. Nickel. Materials: transformation of diamond to graphite. *Nature*, 401:663–664, 1999.
- [97] E. Gaffet, F. Bernard, J.C. Niepce, F. Charlot, C. Gras, G.L. Caër, J.L. Guichard, P. Delcroix, A. Mocellin, and O. Tillement. Some recent developments in mechanical activation and mechanosynthesis. *J. Mater. Chem.*, 9:305–314, 1999.
- [98] A. V. Zvyagin, D. Gruber, C. J. Noble, R. Vogel, E. Sawa, and T. Plakhotnik. Five-Nanometer Diamond with Luminescent Nitrogen-Vacancy Defect Centers. *Small*, 14:1591–1595, 2009.
- [99] M. Minsky. Memoir on inventing the confocal microscope. *Scanning*, 10:128–138, 1988.
- [100] Pawley JB, editor. *Handbook of biological confocal microscopy*. New York: Plenum Press, 1995.
- [101] F. Zernike. Phase-contrast, a new method for microscopic observation of transparent objects. *Physica*, 9:974–986, 1942.
- [102] F. Zernike. How I discovered phase contrast. *Science*, 121:345–349, 1955.
- [103] L. Mandel and E. Wolf. *Optical coherence and quantum optics*. Cambridge University press, 1995.
- [104] H. Kimble, M. Dagenais, and L. Mandel. Photon antibunching in resonance fluorescence. *Phys. Rev. Lett.*, 39:691, 1977.
- [105] R.H. Brown and R. Twiss. Correlation between photons in two coherent beams of light. *Nature*, 177:22, 1956.
- [106] C. Kurtsiefer, P. Zarda, S. Mayer, and H. Weinfurter. The breakdown flash of silicon avalanche photodiodes - back door for eavesdropper attacks ? *Mod. Opt.*, 48:2039, 2001.
- [107] G. Greenstein and A.G. Zajonc. *The Quantum Challenge*. Jones and Bartlett, 2nd ed. edition, 2005.
- [108] S. Weiss. Fluorescence spectroscopy of single biomolecules. *Science*, 283:1676, 1999.
- [109] F. Treussart, R. Alléaume, V. Le Floc’h, L.T. Xiao, J.-M. Courty, and J.-F. Roch. Direct measurement of the photon statistics of a triggered single photon source. *Phys. Rev. Lett.*, 89:093601, 2002.
- [110] R.Y. Tsien. Fluorescent probes of cell signaling. *An. Rev. Neuroscience*, 12:227–253, 1989.
- [111] S.C. Blanchard, H.D. Kim, R.L. Gonzalez, J.D. Puglisi, and S. Chu. tRNA dynamics on the ribosome during translation. *Proc. Natl. Acad. Sci. USA*, 101:12893–12898, 2004.
- [112] L.S. Churchman, Z. Okten, R.S. Rock, J.F. Dawson, and J.A. Spudich. Single molecule high-resolution colocalization of Cy3 and Cy5 attached to macromolecules measures intramolecular distances through time. *Proc. Natl. Acad. Sci. USA*, 102:1419–1423, 2005.
- [113] E.M. Parcell. Spontaneous emission probabilities at radio frequencies. *Phys. Rev. B*, 69:681, 1946.
- [114] K. H. Tews, O. Inacker, and H. Kuhn. Variation of the Luminescence Lifetime of a Molecule Near an Interface Between Different Polarizable Dielectrics - Erratum. *Nature*, 228:791, 1970.
- [115] F. Treussart, A. Clouqueur, C. Grossman, and J.-F. Roch. Photon antibunching in the fluorescence of a single dye molecule embedded in a thin polymer film. *Opt. Lett.*, 26:1504, 2001.

- [116] T. Basche, W.E. Moerner, M. Orrit, and U.P. Wild. *Single-Molecule Optical Detection, Imaging and Spectroscopy*. VCH, Weinheim, Germany, 1st edition, 1997.
- [117] H. Gruber, C. Hahn, G. Kada, C. Riener, G. Harms, W. Ahner, T. Dax, and H.G. Knaus. Anomalous Fluorescence Enhancement of Cy3 and Cy3.5 versus Anomalous Fluorescence Loss of Cy5 and Cy7 upon Covalent Linking to IgG and Noncovalent Binding to Avidin. *Bioconj. Chem.*, 5:696–704, 2000.
- [118] F. Treussart, R. Alléaume, V. Le Floch, and J.F. Roch. Single photon emission from a single molecule. *C. R. Physique*, 3:501–508, 2002.
- [119] R. Verberk, A.M. van Oijen, and M. Orrit. Simple model for the power-law blinking of single semiconductor nanocrystals. *Phys. Rev. B*, 66:233202, 2002.
- [120] K. Zhang, H. Chang, A. Fu, A.P. Alivisatos, and H. Yang. Continuous distribution of emission states from single CdSe/ZnS Quantum Dots. *Nano Lett.*, 6:843–847, 2006.
- [121] L.P. Watkins and H. Yang. Detection of intensity change points in time-resolved Single-Molecule measurement. *J. Phys. Chem. B*, 109:617–628, 2004.
- [122] B. Lounis, H.A. Bechtel, D. Gerion, A.P. Alivisatos, and W.E. Moerner. Photon antibunching in single CdSe/ZnS quantum dot fluorescence. *Chem. Phys. Lett.*, 329:399–404, 2000.
- [123] M. Dahan, T. Laurence, F. Pinaud, D.S. Chemla, A.P. Alivisatos, M. Sauer, and S. Weiss. Time-gated biological imaging by use of colloidal quantum dots. *Opt. Lett.*, 26:825, 2001.
- [124] L. Allers, A.T. Collins, and J. Hiscock. The annealing of interstitial-related optical centres in type II natural and CVD diamond. *Diamond Relat. Mater.*, 7:228–232, 1998.
- [125] C. Bradac, T. Gaebel, N. Naidoo, J.R. Rabeau, and A.S. Barnard. Prediction and measurement of the size-dependent stability of fluorescence in diamond over the entire nanoscale. *Nano Lett.*, page DOI:10.1021/nl9017379, 2009.
- [126] N. Mohan, Y.-K. Tzeng, L. Yang, Y.-Y. Chen, Y.Y. Hui, C.-Y. Fang, and H.-C. Chang. Sub-20-nm fluorescent nanodiamonds as photostable biolabels and fluorescence resonance energy transfer donors. *Adv. Mater.*, 10.1002/adma.200901596, 2009.
- [127] C.-Y. Cheng, E. Perevedentseva, J.-S. Tu, P.-H. Chung, C.-L. Cheng, K.-K. Liu, J.-I. Chao, P.-H. Chen, and C.-C. Chang. Direct and in vitro observation of growth hormone receptor molecules in A549 human lung epithelial cells by nanodiamond labeling. *Appl. Phys. Lett.*, 90:163903, 2007.
- [128] A.E. Aleksenskii, M.V. Baidakova, A.Y. Vul, and V.I. Siklitskii. The structure of diamond nanoclusters. *Phys. Solid State*, 41:668–671, 1999.
- [129] A. Krüger, M. Ozawa, F. Kataoka, T. Fujino, Y. Suzuki, A.E. Aleksenskii, A. Y. Vul, and E. Osawa. Unusually Tight Aggregation in Detonation Nanodiamond: Identification and Disintegration. *Carbon*, 43:1722 – 1730, 2005.
- [130] M. Ozawa, M. Inakuma, M. Takahashi, F. Kataoka, A. Krueger, and E. Osawa. Preparation and Behaviour of Brownish Clear Nanodiamond Colloids. *Adv. Mater.*, 19:1201 – 1206, 2007.
- [131] S. Turner, O.I. Lebedev, O. Shenderova, I.I. Vlasov, J. Verbeeck, and G. Van Tendeloo. Determination of size, morphology, and nitrogen impurity location in treated detonation nanodiamond by transmission electron microscopy. *Adv. Funct. Mater.*, 19:2116–2124, 2009.
- [132] M. Göppert-Mayer. Über Elementarakte mit zwei Quantensprungen. *Ann Phys*, 9:273–294, 1931.
- [133] W. Kaiser and C.B.G. Garrett. Two-photon excitation in $CaF : Eu_2$. *Physiol. Rev. Lett.*, 7:229–231, 1961.
- [134] D.M. Friedrich. Two-photon molecular spectroscopy. *J. Chem. Educ.*, 59:472–481, 1982.

- [135] W. Denk, J. Strickler, and W. Webb. Two-photon laser scanning fluorescence microscopy. *Science*, 248:73–76, 1990.
- [136] W. Denk and K. Svoboda. Photon Upmanship: Techreview Why Multiphoton Imaging Is More than a Gimmick. *Neuron*, 18:351–357, 1997.
- [137] Diaspro A. *Confocal and two-photon microscopy: foundations, applications, and advances*. New York: Wiley-Liss., 2001.
- [138] P. Dufour, S. Dufour, A. Castonguay, N. McCarthy, and Y. De Koninck. Microscopie à deux photons pour l'imagerie cellulaire fonctionnelle : avantages et enjeux. *Médecine/ Sciences*, 22:837–44, 2006.
- [139] R. Yuste and W. Denk. Dendritic spines as basic functional units of neuronal integration. *Nature*, 375:682–684, 1995.
- [140] M. Oheim, E. Beaurepaire, E. Chaigneau, J. Mertz, and S. Charpak. Two-photon microscopy in brain tissue: parameters influencing the imaging depth. *J. Neurosc. Meth.*, 112:205, 2001.
- [141] J.-W. Wang, A.-M. Wong, J. Flores, L.-B. Vosshall, and R. Axel. Two-Photon Calcium Imaging Reveals an Odor-Evoked Map of Activity in the Fly Brain. *Cell*, 112:271–282, 2003.
- [142] F. Helmchen and W. Denk. Deep tissue two-photon microscopy. *Nat. Methods*, 2:932 – 940, 2005.
- [143] M. Albota, D. Beljonne, J.-L. Brédas, J. Ehrlich, J. Fu, A. Heikal, S. Hess, T. Kogej, M. Levin, S. Marder, D. McCord-Maughon, J. Perry, H. Röckel, M. Rumi, G. Subramaniam, W.-W. Webb, X. Wu, and C. Xu. Design of Organic Molecules with Large Two-Photon Absorption Cross Sections. *Science*, 281:1653–1656, 1998.
- [144] S. Mikov, A. Igo, and V. Gorelik. Two-photon-excited luminescence spectra in diamond nanocrystals. *Phys. Sol. State*, 41:1012–1014, 1999.
- [145] C.-K. Lin, Y.-H. Wang, H.-C. Chang, M. Hayashi, and S.-H. Lin. One- and two-photon absorption properties of diamond nitrogen-vacancy defect centers: A theoretical study. *J. Chem. Phys.*, 129:124714, 2008.
- [146] D.R. Larson, W.R. Zipfel, R.M. Williams, S.W. Clark, M.P. Bruchez, F.W. Wise, and W.W. Webb. Water-Soluble Quantum Dots for Multiphoton Fluorescence Imaging in Vivo. *Science*, 300:1434–1436, 2003.
- [147] S. Huang, A.A. Heikal, and W.W. Webb. Two-Photon Fluorescence Spectroscopy and Microscopy of NAD(P)H and Flavoprotein. *Biophys. J.*, 82:2811–2825, 2002.
- [148] D.N. Papadopoulos, S. Forget, M. Delaigue, F. Druon, F. Balembois, and P. Georges. Passively mode-locked diode-pumped Nd:YVO₄ oscillator operating at an ultralow repetition rate. *Opt. Lett.*, 28(19):1838–1840, 2003.
- [149] U. Keller, D.A.B. Miller, G.D. Boyd, T.H. Chiu, J. Ferguson, and M.T. Asom. Solid-state low-loss intracavity saturable absorber for Nd:YLF lasers: an antiresonant semiconductor Fabry–Perot saturable absorber. *Opt. Lett.*, 17:505–507, 1992.
- [150] C. Gerhard, F. Druon, and P. Georges. Stable mode-locked operation of a low repetition rate diode-pumped Nd:GdVO₄ laser by combining quadratic polarisation switching and a semiconductor saturable absorber mirror. *Opt. Express*, 14(16):7093–7098, 2006.
- [151] V. Couderc, F. Louradour, and A. Barthélémy. 2.8 ps pulses from a mode-locked diode pumped Nd:YVO₄ laser using quadratic polarization switching. *Opt. Communications*, 166:103–111, 1999.
- [152] C. Xu and W.W. Webb. Measurement of two-photon excitation cross sections of molecular fluorophores with data from 690 to 1050 nm. *J. Opt. Soc. Am. B*, 13:481, 1996.
- [153] N.B. Manson and J.P. Harrison. Photo-ionization of the nitrogen-vacancy center in diamond. *Diamond Rel. Mat.*, 14:1705 – 1710, 2005.

BIBLIOGRAPHY

- [154] Y. Dumeige, F. Treussart, R.A. Alléaume, T. Gacoin, J.F. Roch, and P. Grangier. Photo-induced creation of nitrogen-related color centers in diamond nanocrystals under femtosecond illumination. *J. Luminesc.*, 109:61–67, 2000.
- [155] V. M. Acosta, E. Bauch, M.P. Ledbetter, C. Santori, K.-M. C. Fu, P.E. Barclay, R.G. Beausoleil, H. Linget, J.F. Roch, F. Treussart, S. Chemerisov, W. Gawlik, and D. Budker. High nitrogen-vacancy density diamond for magnetometry applications. *Phys. Rev. B*, 80:115202, 2009.
- [156] S.W. Hell. Far-Field Optical Nanoscopy. *Science*, 316:1153–1158, 2007.
- [157] S.W. Hell and M. Kroug. Ground-state-depletion fluorescence microscopy: a concept for breaking the diffraction resolution limit. *Appl. Phys. B*, 60:495–497, 1995.
- [158] S. Bretschneider, C. Eggeling, and S.W. Hell. Breaking the Diffraction Barrier in Fluorescence Microscopy by Optical Shelving. *Phys. Rev. Lett.*, 98:218103, 2007.
- [159] S. Bretschneider. *Ground-State-Depletion Fluorescence Microscopy*. PhD thesis, Georg-August Göttingen University, 2008.
- [160] J. Foelling, M. Boss, H. Bock, R. Medda, C.A. Wurm, B. Hein, S. Jakobs, C. Eggeling, and S.W. Hell. Fluorescence nanoscopy by ground-state depletion and single-molecule return. *Nat. Methods*, 5:943–945, 2007.
- [161] E. Rittweger, D. Wildanger, and S.W. Hell. Far-field fluorescence nanoscopy of diamond color centers by ground state depletion. *Eur. Phys. Lett.*, 86:14001, 2009.
- [162] K.Y. Han, K.I. Willig, E. Rittweger, F. Jelezko, C. Eggeling, and S.W. Hell. Three-Dimensional Stimulated Emission Depletion Microscopy of Nitrogen-Vacancy Centers in Diamond Using Continuous-Wave Light. *Nano Lett.*, in press doi/abs/10.1021/nl901597v, 2009.
- [163] S.W. Hell and J. Wichmann. Breaking the diffraction resolution limit by stimulated emission: stimulated-emission-depletion fluorescence microscopy. *Opt. Lett.*, 19:780–782, 1994.
- [164] E. Rittweger, K.Y. Han, S.E. Irvine, C. Eggeling, and S.W. Hell. STED microscopy reveals crystal colour centres with nanometric resolution. *Nat. Photonics*, 3:144, 2009.
- [165] L.J. Rogers, S. Armstrong, M.J. Sellars, and N.B. Manson. Infrared emission of the nv centre in diamond: Zeeman and uniaxial stress studies. *New J. Phys.*, 10:103024, 2008.
- [166] N. B. Manson, J. P. Harrison, and Sellars M. J. Nitrogen-vacancy center in diamond: model of the electronic structure and associated dynamics. *Phys. Rev. B*, 74:104303, 2006.
- [167] T.A. Klar, E. Engel, and S.W. Hell. Breaking Abbe’s diffraction resolution limit in fluorescence microscopy with stimulated emission depletion beams of various shapes. *Phys. Rev. E*, 64(066613):1–9, 2001.
- [168] B. Harke, J. Keller, C.K. Ullal, V. Westphal, A. Schoenle, and S.W. Hell. Resolution scaling in STED microscopy. *Opt. Express*, 16:4154–4162, 2008.
- [169] K.S. Youngworth and T.G. Brown. Focusing of high numerical aperture cylindrical- vector beams. *Opt. Express*, 7(2):77–87, 2000.
- [170] M. Stalder and M. Schadt. Linearly polarized light with axial symmetry generated by liquid-crystal polarization converters. *Opt. Lett.*, 21:1948–1950, 1996.
- [171] G. Machavariani, Y. Lumer, I. Moshe, A. Meir, S. Jackel, and N. Davidson. Birefringence-induced bifocusing for selection of radially or azimuthally polarized laser modes. *Appl. Optics*, 46:3304–3310, 2007.
- [172] G. Machavariani, Y. Lumer, I. Moshe, A. Meir, and S. Jackel. Efficient extracavity generation of radially and azimuthally polarized beams. *Opt. Express*, 32:1468–1470, 2007.

- [173] A. Derfus, W.-C. Chan, and S. Bhatia. Intracellular delivery of Quantum Dots for Live Cell Labelling and Organelle Tracking. *Adv. Mater.*, 16(12), 2004.
- [174] J.-K. Jaiswai, H. Mattoussi, J. Mauro, and S.-M. Simon. Long-term multiple color imaging of live cells usings quantum dot bioconjugates. *Nature Biotech.*, 21:47, 2002.
- [175] I.L. Medintz, H.T. Uyeda, E.R. Goldman, and H. Mattoussi. Quantum dot bioconjugates for imaging, labelling and sensing. *Nat. Materials*, 4:435, 2005.
- [176] O. Faklaris, V. Joshi, T. Irinopoulou, P. Tauc, H. Girard, C. Gesset, M. Sennour, A. Thorel, J.C. Arnault, J.P. Boudou, P.A. Curmi, and F. Treussart. Photoluminescent nanodiamonds for cell labeling: study of their uptake mechanism in mammalian cells . *ACS Nano*, DOI: 10.1021/nm901014j, 2009.
- [177] L. Groc, M. Lafourcade, M. Heine, M. Renner, V. Racine, J.B. Sibarita, B. Lounis, D. Choquet, and L. Cognet. Surface trafficking of neurotransmitter receptor: comparison between single-molecule/quantum dot strategies. *J. Neurosci.*, 27:12433, 2007.
- [178] M. Dahan, S. Lévi, C. Luccardini, P. Rostaing, B. Riveau, and A. Triller. Diffusion Dynamics of Glycine Receptors Revealed by Single-Quantum Dot Tracking. *Science*, 302:442–445, 2003.
- [179] R.E. Thomson, D.E. Larson, and W.W. Webb. Precise Nanometer Localization Analysis for Individual Precise Nanometer Localization Analysis for Individual Fluorescent Probes. *Biophys. J.*, 82:2775, 2002.
- [180] D. Boyer, P. Tamarat, A. Maali, B. Lounis, and M. Orrit. Photothermal Imaging of Nanometer-Sized Metal Particles Among Scatterers. *Science*, 297:1160, 2002.
- [181] L. Cognet, C. Tardin, D. Boyer, D. Choquet, P. Tamarat, and B. Lounis. Single metallic nanoparticle imaging for protein detection in cells. *Proc. Natl. Acad. Sci. USA*, 100:11350–11355, 2003.
- [182] D. Lasne, G.A. Blab, S. Berciaud, M. Heine, L. Groc, D. Choquet, L. Cognet, and B. Lounis. Single Nanoparticle Photothermal Tracking (SNaPT) of 5-nm Gold Beads in Live Cells. *Biophys. J.*, 91:4598–4604, 2006.
- [183] O. Faklaris, D. Garrot, V. Joshi, J.P. Boudou, T. Sauvage, P.A. Curmi, and F. Treussart. Comparison of the photoluminescence properties of semiconductor quantum dots and non-blinking diamond nanoparticles and observation of the diffusion of diamond nanoparticles in living cells. *J. Europ. Opt. Soc. Rap. Public.*, 4:09035, 2009.
- [184] T.-L. Wee, Y.-W. Mau, C.-Y. Fang, H.-L. Hsu, C.-C. Han, and H.-C. Chang. Preparation and characterization of green fluorescent nanodiamonds for biological applications. *Diamond Relat. Mater.*, 18:567–573, 2009.
- [185] B.D. Chithrani, A.A. Ghazani, and W.-C. Chan. Determining the Size and Shape Dependence of Gold Nanoparticle Uptake into Mammalian Cells. *Nano Lett*, 6:662–668, 2006.
- [186] M. Saxton and K. Jakobson. Single particle tracking: applications to membrane dynamics. *An. Rev. Biophys. Biomol. Struct.*, 26:373, 1997.
- [187] L.S. Barak and W.W. Webb. Fluorescent low density lipoprotein for observation of dynamics of individual receptor complexes on cultured human fibroblasts. *J. Cell Biol.*, 90(595-604), 1981.
- [188] A. Kusumi, Y. Sako, and M. Yamamoto. Confined lateral diffusion of membrane receptors as studied by single particle tracking. *Biophys. J.*, 65:2021, 1993.
- [189] S. Condamin, V. Tejedor, R. Voituriez, O. Bénichou, and J. Klafter. Probing microscopic origins of confined subdiffusion by first-passage observables. *Proc. Natl. Acad. Sci. USA*, 105:5675–5680, 2008.

BIBLIOGRAPHY

- [190] S. Jin, P.M. Haggi, and A.S. Verkman. Single-Particle Tracking of Membrane Protein Diffusion in a Potential: Simulation, Detection, and Application to Confined Diffusion of CFTR Cl₂ Channels. *Biophys. J.*, 93:1079–1088, 2007.
- [191] J.B. Masson, D. Casanova, S. Turkcan, G. Voisinne, M.R. Popoff, M. Vergassola, and A. Alexandrou. Inferring Maps of Forces inside Cell Membrane Microdomains. *Phys. Rev. Lett.*, 102:048103, 2009.
- [192] D.J. McKay. *Information Theory, Inference, and Learning Algorithms*. Cambridge University Press, 2003.
- [193] I.F. Sbalzarini and P. Koumoutsakos. Feature point tracking and trajectory analysis for video imaging in cell biology. *J. Struct. Biol.*, 151:182–195, 2005.
- [194] M.K. Cheezum, W.F. Walker, and G.H. Guilford. Quantitative Comparison of Algorithms for Tracking Single Fluorescent Particles. *Biophys. J.*, 81:2378–2388, 2001.
- [195] C. Dietrich, B. Yang, T. Fujiwara, A. Kusumi, and K. Jakobson. Relationship of lipid rafts to transient confinement zones detected by single particles tracking. *Biophys. J.*, 82:274, 2002.
- [196] L. Holtzer, T. Meckel, and T. Schmidt. Nanometric three-dimensional tracking of individual quantum dots in cells. *Appl. Phys. Lett.*, 90:053902, 2007.
- [197] S. Munro. Organelle identity and the organization of membrane traffic. *Nat. Cell Biol.*, 6:469–72, 2004.
- [198] L. Pelkmans and A. Helenius. Insider information: what viruses tell us about endocytosis. *Curr. Opin. Cell Biol.*, 15:414–422, 2003.
- [199] M. Marsh and H.T. McMahon. Cell biology - the structural era of endocytosis. *Science*, 285:215, 1999.
- [200] E.D. Gundelfinger, M.M. Kessels, and B. Qualmann. Temporal and spatial coordination of exocytosis and endocytosis. *Nature Rev. Mol. Cell Biol.*, 2:127–139, 2003.
- [201] S. Murkherjee, R.N. Ghosh, and F.R. Maxfield. Endocytosis. *Physiol. Rev.*, 77:759–803, 1997.
- [202] R. Steinman, I. Mellman, W. Muller, and Z. Cohn. Endocytosis and the Recycling of Plasma Membrane. *J. Cell Biol.*, 96:1–27, 1983.
- [203] S.A. Mousavi, L. Malerod, T. Berg, and R. Kjekken. Clathrin-dependent endocytosis. *Biochem. J.*, 377:1–16, 2004.
- [204] L. Pelkmans, T. Bürli, M. Zerial, and A. Helenius. Caveolin-Stabilized Membrane Domains as Multifunctional Transport and Sorting Devices in Endocytic Membrane Traffic. *Cell*, 118:767–780, 2004.
- [205] J.P. Richard, K. Melikov, H. Brooks, P. Prevot, B. Lebleu, and L.V. Chernomordik. Cellular uptake of unconjugated TAT peptide involves clathrin-dependent endocytosis and heparan sulfate receptors. *J. Biol. Chem.*, 280:15300–15306, 2005.
- [206] B.J. Nichols and J. Lippincott-Schwartz. Endocytosis without clathrin coats. *Trends Cell Biol.*, 11:406–412, 2001.
- [207] P. Wender, W.C. Galliher, E.A. Goun, L.R. Jones, and T.H. Pillow. The design of guanidinium-rich transporters and their internalization mechanisms. *Adv. Drug Deliv. Rev.*, 60:452–472, 2008.
- [208] W.J. Parak, R. Boudreau, M. Le Gros, D. Gerion, D. Zanchet, C.M. Micheel, S.C. Williams, A.P. Alivisatos, and C.A. Larabell. Cell Motility and Metastatic Potential Studies Based on Quantum Dot Imaging of Phagokinetic Tracks. *Adv. Mater.*, 14:882, 2002.
- [209] J. Rejman, V. Oberle, I.S. Zuhorl, and D. Hoekstra. Size-dependent internalization of particles via the pathways of clathrin- and caveolae-mediated endocytosis. *Biochem. J.*, 377:159–169, 2004.

- [210] P. Nativo, I.A. Prior, and M. Brust. Uptake and Intracellular Fate of Surface-Modified Gold Nanoparticles. *ACS Nano*, 2:1639–1644, 2008.
- [211] M. Stroh, J.P. Zimmer, D.G. Duda, T.S. Levchenko, K.S. Cohen, E.B. Brown, D.T. Scadden, V.P. Torchilin, M.G. Bawendi, D. Fukumura, and R.K. Jain. Quantum dots spectrally distinguish multiple species within the tumor milieu in vivo. *Nat. Medicine*, 11:678–682, 2005.
- [212] A. Tkachenko, H. Xie, D. Coleman, W. Glomm, J. Ryan, M.F. Anderson, S. Franzen, and D. Feldheim. Multifunctional Gold Nanoparticle-Peptide Complexes for Nuclear Targeting. *J. Am. Chem. Soc.*, 125:4700–4701, 2003.
- [213] L. Tang, C. Tsai, W.W. Gerberich, L. Kruckebergshort, and D.R. Kania. Biocompatibility of chemical-vapour-deposited diamond. *Biomaterials*, 16:483–488, 1995.
- [214] R. Hardman. A Toxicologic Review of Quantum Dots: Toxicity Depends on Physicochemical and Environmental Factors. *Envir. Health Perspectives*, 114(2), 2006.
- [215] S.J. Cho, D. Maysinger, M. Jain, B. Roder, S. Hackbarth, and F.M. Winnik. Long-Term Exposure to CdTe Quantum Dots Causes Functional Impairments in Live Cells. *Langmuir*, 23:1974–1980, 2007.
- [216] L. Ghitescu and A. Fixman. Surface charge distribution on the endothelial cell of liver sinusoids. *J. Cell Biol.*, 99:639–647, 1984.
- [217] C. Wilhelma, C. Billoteya, J. Rogerc, J.N. Ponsc, J.C. Bacria, and F. Gazeau. Intracellular uptake of anionic superparamagnetic nanoparticles as a function of their surface coating. *Biomaterials*, 24:1001–1011, 2003.
- [218] K. Kostarelos, L. Lacerda, G. Pastorin, W. Wu, S. Wieckowski, J. Luangsivilay, S. Godefroy, D. Pantarotto, J.P. Briand, S. Muller, M. Prato, and A. Bianco. Cellular uptake of functionalized carbon nanotubes is independent of functional group and cell type. *Nature Nanotech.*, 2:108, 2007.
- [219] C.-W. Lam, J.T. James, R. McCluskey, and R.L. Hunter. Pulmonary Toxicity of Single-Wall Carbon Nanotubes in Mice 7 and 90 Days After Intratracheal Instillation. *Toxicol. Sci.*, 77:126–134, 2004.
- [220] D.B. Warheit, B.R. Laurence, K.L. Reed, D.H. Roach, M. Reynolds, and T.R. Webb. Comparative Pulmonary Toxicity Assessment of Single-wall Carbon Nanotubes in Rats. *Toxicol. Sci.*, 77:117–125, 2004.
- [221] V. Vijayanthimala, Y.-K. Tzeng, H.-C. Chang, and C.-L. Li. The biocompatibility of fluorescent nanodiamonds and their mechanism of cellular uptake. *Nanotechnology*, 20:425103, 2009.
- [222] E. Connor, J. Mwamuka, A. Gole, C. Murphy, and M. Wyatt. Gold Nanoparticles Are Taken Up by Human Cells but Do Not Cause Acute Cytotoxicity. *Small*, 1:325–327, 2005.
- [223] R. Shukla, V. Bansal, M. Chaudhary, A. Basu, R.R. Bhone, and M. Sastry. Biocompatibility of Gold Nanoparticles and Their Endocytotic Fate Inside the Cellular Compartment: A Microscopic Overview. *Langmuir*, 21:10644–10654, 2005.
- [224] T. Mosmann. Rapid colorimetric assay for cellular growth and survival: application to proliferation and cytotoxicity assays. *J. Immunol. Methods*, 65:55–63, 1983.
- [225] J. Carmichael, W.D. DeGraff, A.F. Gazdar, J.B. Minna, and J. Mitchell. Evaluation of a tetrazolium-based semiautomated colorimetric assay: Assessment of chemosensitivity testing. *Cancer Res.*, 47:936–942, 1987.
- [226] S.L. Schmid and L.L. Carter. ATP is Required for Receptor-mediated Endocytosis in Intact Cells. *J. Cell Biol.*, 111:2307–2318, 1990.
- [227] J. Heuser and R.G. Anderson. Hypertonic media inhibit receptor-mediated endocytosis by blocking clathrin-coated pit formation. *J. Cell Biol.*, 108:389–400, 1989.

BIBLIOGRAPHY

- [228] M. Qaddoumi, H. Gukasyan, J. Davda, V. Labhasetwar, K.J. Kim, and V. Lee. Clathrin and caveolin-1 expression in primary pigmented rabbit conjunctival epithelial cells: Role in PLGA nanoparticle endocytosis. *Molec. Vis.*, 9:559–568, 2003.
- [229] H.S. Kruth and M. Vaughan. Quantification of low density lipoprotein binding and cholesterol accumulation by single human fibroblasts using fluorescence microscopy. *J Lipid Res*, 21:123–130, 1980.
- [230] N.W.S. Kam, Z. Liu, and D. Dai. Carbon Nanotubes as Intracellular Transporters for Proteins and DNA : An Investigation of the Uptake Mechanism and Pathway. *Angew. Chem. Int. Ed.*, 45:577–581, 2006.
- [231] K. Rezwan, L.P. Meier, M. Rezwan, J. Voros, M. Textor, and L.J. Gauckler. Bovine Serum Albumin Adsorption onto Colloidal Al₂O₃ Particles: A New Model Based on Zeta Potential and UV-Vis Measurements. *Langmuir*, 20:10055–10061, 2004.
- [232] S. H. Brewer, W.R. Glomm, M.C. Johnson, M.K. Knag, and S. Franzen. Probing BSA Binding to Citrate-Coated Gold Nanoparticles and Surfaces. *Langmuir*, 21:9303–9307, 2005.
- [233] V. Militello, C. Casarino, A. Emanuele, A. Giostra, F. Pullara, and M. Leone. Aggregation kinetics of bovine serum albumin studied by FTIR spectroscopy and light scattering. *Bioph. Chem.*, 107:175187, 2004.
- [234] K. Murayama and M. Tomida. Heat-Induced Secondary Structure and Conformation Change of Bovine Serum Albumin Investigated by Fourier Transform Infrared Spectroscopy. *Biochem.*, 43:11526–11532, 2004.
- [235] L. Dai. *Carbon Nanotechnology: Recent Developments in Chemistry, Physics, Materials Science and Device Applications*. Elsevier: Amsterdam, 2006.
- [236] A. Krueger. New Carbon Materials: Biological Applications of Functionalized Nanodiamond Materials. *Chem. Eur. J.*, 14:1382–1390, 2008.
- [237] P. Wicka, P. Mansera, L.K. Limbachd, U. Dettlaff-Weglikowskab, F. Krumeichc, S. Rothb, W.J. Starkd, and A. Bruininka. The degree and kind of agglomeration affect carbon nanotube cytotoxicity. *Toxicol. Lett.*, 168:121–131, 2007.
- [238] Y. Yuan, Y. Chen, J.-H. Liu, H. Wang, and Y. Liu. Biodistribution and fate of nanodiamonds in vivo. *Diamond Relat. Mater.*, 18:95100, 2009.
- [239] X.Q. Zhang, M. Chen, R. Lam, X. Xu, E. Osawa, and D. Ho. Polymer-Functionalized Nanodiamond Platforms as Vehicles for Gene Delivery. *ACS Nano*, 3:2609 – 2616, 2009.
- [240] S. Davis. Biomedical applications of nanotechnology — implications for drug targeting and gene therapy. *Trends Biotechnol.*, 15:217–224, 1997.
- [241] W.F. Anderson. Human gene therapy. *Nature*, 392:25–30, 1998.
- [242] T. Taguchi, M. Shimura, Y. Osawa, Y. Suzuki, Y. Mizoguchi, L. Niino, F. Takaku, and Y. Ishizaka. Nuclear trafficking of macromolecules by an oligopeptide derived from Vpr of human immunodeficiency virus type-1. *Biochem. Biophys. Res. Communic.*, 320:18–26, 2004.
- [243] C.E. Thomas, A. Ehrhardt, and M.A. Kay. Progress and problems with the use of viral vectors for gene therapy. *Nature Rev. Genetics*, 4:346–358, 2003.
- [244] S.D. Li and L. Huang. Surface-modified LPD nanoparticles for tumor targeting. *Ann NY Acad Sci*, 1082:1–8, 2006.
- [245] I. Roy, S. Mitra, A. Maitra, and S. Mozumdar. Calcium phosphate nanoparticles as novel non-viral vectors for targeted gene delivery. *Intern. J. Pharmaceutics*, 250:25–33, 2003.

- [246] K. McAllister, P. Sazani, M. Adam, M.J. Cho, M. Rubinstein, R.J. Samulski, and D.J. DeSimone. Polymeric Nanogels Produced via Inverse Microemulsion Polymerization as Potential Gene and Antisense Delivery Agents. *J. Am. Chem. Soc.*, 154:15198–15207, 2002.
- [247] O.C. Farokhzad, J. Cheng, B.A. Teply, I. Sherifi, S. Jon, P.W. Kantoff, J.P. Richie, and R. Langer. Targeted nanoparticle-aptamer bioconjugates for cancer chemotherapy in vivo. *Proc. Natl. Acad. Sci. USA*, 103:6315–6320, 2006.
- [248] N.V. Koshkina, J.C. Waldrep, and V. Knight. Camptothecins and Lung Cancer: Improved Delivery Systems by Aerosol. *Curr. Cancer Drug Targets*, 3:251–264, 2003.
- [249] C.O. Noble, M.T. Krauze, D.C. Drummond, Y. Yamashita, R. Saito, M.S. Berger, D.B. Kirpotin, K.S. Bankiewicz, and J.W. Park. Novel Nanoliposomal CPT-11 Infused by Convection-Enhanced Delivery in Intracranial Tumors: Pharmacology and Efficacy. *Cancer Res.*, 66:2801–2806, 2006.
- [250] H.H. Chou, K.L. Wang, C.A. Chen, L.A. Wei, C.H. Lai, C.Y. Hsieh, Y.C. Yang, N.F. Twu, T.C. Chang, and M.S. Yen. Pegylated liposomal doxorubicin (Lipo-Dox®) for platinum-resistant or refractory epithelial ovarian carcinoma: A Taiwanese gynecologic oncology group study with long-term follow-up. *Gynecol. Oncol.*, 101:423–428, 2006.
- [251] J.R. Lakowicz. *Principles of Fluorescence Microscopy*. Springer, New York, 2006.
- [252] C. Kneuer, M. Sameti, A.G. Haltner, T. Schiestel, H. Schirrab, H. Schmidt, and C.M. Lehr. Silica nanoparticles modified with aminosilanes as carriers for plasmid DNA. *Intern. J. Pharmaceutics*, 196:257–261, 2000.
- [253] C. Kneuer, M. Sameti, U. Bakowsky, T. Schiestel, H. Schirra, H. Schmidt, and C.-M. Lehr. A Nonviral DNA Delivery System Based on Surface Modified Silica-Nanoparticles Can Efficiently Transfect Cells in Vitro. *Bioconj. Chem.*, 11(6):926–932, 2000.
- [254] X. He, K. Wang, W. Tan, B. Liu, X. Lin, C. He, D. Li, S. Huang, and J. Li. Bioconjugated Nanoparticles for DNA Protection from Cleavage. *J. Am. Chem. Soc.*, 125(24):7168–7169, 2003.
- [255] I. Roy, T.Y. Ohulchanskyy, D.J. Bharali, H.E. Pudavar, R.A. Mistretta, N. Kaur, and P.N. Prasad. Optical tracking of organically modified silica nanoparticles as DNA carriers: A non-viral, nanomedicine approach for gene delivery. *Proc. Nat. Acad. Sc. USA*, 102:279–284, 2005.
- [256] J.E. Fuller, G.T. Zugates, L.S. Ferreira, H.S. Ow, N.N. Nguyen, U.B. Wiesner, and R.S. Langer. Intracellular delivery of core-shell fluorescent silica nanoparticles. *Biomaterials*, 29:1526–1532, 2008.
- [257] D. Pantarotto, J.P. Briand, M. Prato, and A. Bianco. Translocation of bioactive peptides across cell membranes by carbon nanotubes. *Chem. Commun.*, 1:16 – 17, 2004.
- [258] R. Singh, D. Pantarotto, D. McCarthy, O. Chaloin, J. Hoebeke, C. Partidos, J.P. Briand, M. Prato, A. Bianco, and K. Kostarelos. Binding and Condensation of Plasmid DNA onto Functionalized Carbon Nanotubes: Toward the Construction of Nanotube-Based Gene Delivery Vectors. *J. Am. Chem. Soc.*, 127:4388–4396, 2005.
- [259] D. Pantarotto, C.D. Partidos, J. Hoebeke, F. Brown, E. Kramer, J.P. Briand, S. Muller, M. Prato, and A. Bianco. Immunization with Peptide-Functionalized Carbon Nanotubes Enhances Virus-Specific Neutralizing Antibody Responses. *Chem. Biol.*, 10:961–966, 2003.
- [260] D. Pantarotto, R. Singh, D. McCarthy, M. Erhardt, J.P. Brinad, M. Prato, K. Kostarelos, and A. Bianco. Functionalized carbon nanotubes for plasmid DNA gene delivery. *Angew. Ch.*, 43:5242–5246, 2004.
- [261] Z. Liu, K. Chen, C. Davis, S. Sherlock, Q. Cao, X. Chen, and H. Dai. Drug Delivery with Carbon Nanotubes for In vivo Cancer Treatment. *Cancer Res*, 68(16):6652–6660, 2008.

BIBLIOGRAPHY

- [262] D. Pastré, O. Piétrement, S. Fusil, F. Landousy, J. Jeusset, M.O. David, L. Hamon, E. Le Cam, and A. Zozime. Adsorption of DNA to Mica Mediated by Divalent Counterions : A Theoretical and Experimental Study. *Biophys. J.*, 85:2507–2518, 2003.
- [263] G. Liu. Biological Properties of Poly-L-lysine-DNA Complexes generated by Cooperative Binding of the Polycation. *J. Biol. Chem.*, 276:34379–34387, 2001.
- [264] P. Felgner, T. Gadek, M. Holm, R. Roman, H. Chan, M. Wenz, J. Northrop, N. Ringold, and M. Danielsen. Lipofection: A highly efficient, lipid-mediated DNA-transfection procedure. *Proc. Nat. Acad. Sc. USA*, 84:7413–7417, 1987.
- [265] N. Wong, S. Kam, Z. Liu, and H. Dai. Functionalization of Carbon Nanotubes via Cleavable Disulfide Bonds for Efficient Intracellular Delivery of siRNA and Potent Gene Silencing. *J. Am. Chem. Soc.*, 127(36):12492–12493, 2005.
- [266] Z. Liu, M. Winters, M. Holodniy, and H. Dai. siRNA Delivery into Human T Cells and Primary Cells with Carbon- Nanotube Transporters. *Angew. Chem. Int. Ed.*, 46:2023 –2027, 2007.
- [267] A. Maksimenko, V. Polard, M. Villemeur, H. Elhames, P. Couvreur, J.R. Bertrand, M. Aboubakar, M. Gottikh, and C. Malvy. In vivo potentialities of EWS-Fli-1 targeted antisense oligonucleotides-nanospheres complexes. *Ann N Y Acad Sci.*, 1058:52–61, 2005.
- [268] J.Y. Pille, E. Blot, J-R. Bertrand, A. Maksimenko, P. Opolon, L. Protchard, H. Lu, J.P. Vannier, J. Soria, C. Malvy, H. Li, and C. Soria. Intravenous delivery of anti-RhoA siRNA loaded in nanoparticles of chitosan in mice: safety and efficacy in xenografted breast cancer. *Human Gene Therapy*, 17:1019–1026, 2006.
- [269] H. de Martimprey, J-R. Bertrand, A. Fusco, M. Santoro, P. Couvreur, C. Vauthier, and Malvy. siRNA nanoformulation against the ret/PTC1 junction oncogene is efficient in an in vivo model of papillary thyroid carcinoma. *Nucleic Acids Res.*, 36(1):1–13, 2008.
- [270] Davies G., S.C. Lawson, A.I. Collins, A. Mainwood, and S.J. Sharp. Vacancy- related centers in diamond. *Phys. Rev. B*, 46:13157–13170, 1992.
- [271] M. R. Brozel, T. Evans, and R.F. Stephenson. Partial Dissociation of Nitrogen Aggregates in Diamond by High Temperature-High Pressure Treatments. *Proc. R. Soc. Lond. A*, 361:109–127, 1978.
- [272] G. Davies. The effect of nitrogen impurity on the annealing of radiation damage in diamond. *J. Phys. C*, 5:2534–2542, 1972.
- [273] J. Wu, G. Wang, D. Jin, J. Yuan, Y. Guan, and J. Piper. Luminescent europium nanoparticles with a wide excitation range from UV to visible light for biolabeling and time-gated luminescence bioimaging. *Chem. Commun.*, pages 365 – 367, 2008.
- [274] A. Beveratos, R. Brouri, T. Gacoin, J.-Ph. Poizat, and Ph. Grangier. Nonclassical radiation from diamond nanocrystals. *Phys. Rev. A*, 64:061802, 2001.
- [275] A. Collins. Excitation and decay of H4 luminescence in diamond. *J. Phys.: Condens. Matter*, 16:6691, 1983.
- [276] K. H. Drexhage. Influence of a dielectric interface on fluorescence decay time. *J. Luminesc.*, 1:693, 1970.
- [277] R.E. Kunz and W. Lukosz. Changes in Fluorescence lifetimes induced by variable optical environments. *Phys. Rev. B*, 21(10):4814–4828, 1980.
- [278] G. Bourdon, I. Robert, R. Adams, K. Nelep, I. Sagnes, J.M. Moison, and I. Abram. Room temperature enhancement and inhibition of spontaneous emission in semiconductor microcavities. *Appl. Phys. Lett.*, 77:1345, 2000.

- [279] M. Bayer, T.L. Reinecke, F. Weidner, A. Larionov, A. McDonald, and F. Forchel. Inhibition and Enhancement of the Spontaneous Emission of Quantum Dots in Structured Microresonators. *Phys. Rev. Lett.*, 86:3168, 2001.
- [280] J. J. Macklin. Imaging and Time-Resolved Spectroscopy of Single Molecules at an Interface. *Science*, 272:255, 1996.
- [281] W. Lukosz. Light emission by magnetic and electric dipoles close to a plane dielectric interface. ill. radiation patterns of dipoles with arbitrary orientation. *J. Opt. Soc. Am.*, 69:1495, 1979.
- [282] W. Lukosz and M. Meier. Lifetimes and radiation patterns of luminescent centers close to a thin metal film. *Opt. Lett.*, 6(5):251–253, 1981.
- [283] A. Batalov, C. Zierl, T. Gaebel, P. Neumann, G. Chan, I.-Y. Balasubramanian, P.R. Hemmer, F. Jelezko, and J. Wrachtrup. Temporal Coherence of Photons Emitted by Single Nitrogen-Vacancy Defect Centers in Diamond Using Optical Rabi-Oscillations. *Phys. Rev. Lett.*, 100:077401, 2008.

Résumé

Ce travail de thèse porte sur l'utilisation des NanoDiamants Photoluminescents (NDPs) pour des applications en bio-imagerie. Les nanodiamants (NDs) sont photoluminescents grâce à la présence de centres colorés azote-lacune (NV) dans leur maille cristalline.

Le manuscrit est divisé en deux parties. La première concerne l'étude des propriétés optiques des centres colorés NV dans des NDs. Après l'optimisation de la concentration des centres NV, nous comparons la photoluminescence des NDPs à celle des nanoparticules semi-conductrices commerciales; nous concluons qu'elle peut être équivalente, même supérieure dans le cas des NDPs. Pour augmenter le contraste d'imagerie intracellulaire des NDPs, nous avons étudié l'excitation à 2-photons des centres NV. Lors de cette étude avec un laser impulsif, nous avons découvert que le signal de photoluminescence des NDPs excité à un photon chute très fortement lorsque l'impulsion infrarouge est simultanée de l'excitation visible. Nous avons étudié la façon d'utiliser cet effet pour l'imagerie de super-resolution.

La deuxième partie porte sur l'étude des applications des NDPs comme sondes pour la bio-imagerie. Dans le but d'utiliser des NDPs comme véhicules de biomolécules, nous avons étudié leurs mécanismes d'internalisation et avons élucidé leur localisation intracellulaire, en inhibant des voies différentes d'internalisation et par des expériences d'immunofluorescence. De plus, nous avons montré que les NDPs ne sont pas toxiques pour des cellules en culture. Un premier essai de vectorisation a été mené avec de NDPs couverts d'ADN plasmidique.

Mots clés : nanoparticules, diamant, centre coloré, photoluminescence, suivi de particule individuelle, endocytose, cytotoxicité, vectorisation d'ADN

Abstract

This thesis work studies the use of Photoluminescent NanoDiamonds (PNDs) for bio-imaging applications. Nanodiamonds are photoluminescent thanks to embedded nitrogen-vacancy (NV) color centers.

The thesis is divided in two parts. The first part concerns the study of the optical properties of NV color centers in nanodiamonds. After optimization of the NV center concentration, we compared the photoluminescence of PNDs to commercial Quantum Dots (QDs) and conclude that it can be similar or even higher in the case of PNDs. To enhance the imaging contrast of internalized by cells PNDs, we studied the 2-photon excitation properties of NV centers. While implementing a pulsed excitation laser, we discovered that simultaneous one- and two-photon excitation (IR+VIS pulses) quenches the photoluminescence signal of PNDs. We examined how this effect can serve for super-resolution imaging of NV color centers in nanodiamonds.

The second part of the work is devoted to the applications of PNDs as bio-imaging probes. In the prospect of applications of PNDs as drug delivery vehicles, we studied the uptake mechanisms of PNDs and elucidated their intracellular localization by blocking different entry mechanisms and by immunofluorescence experiments. Moreover, we ensured that PNDs are not toxic for cells in culture. As a first try of vectorization we covered PNDs with plasmid DNA and examined the transfection efficiency.

Keywords : nanoparticles, diamond, color center, photoluminescence, single particle tracking, endocytosis, cytotoxicity, DNA vectorization